

546.3'11 V24 m

# METAL HYDRIDES FOR RECHARGEABLE BATTERIES

by

**Lars Ole Valøen**

*Thesis submitted in partial fulfillment of the  
requirements for the degree*

**Doktoringeniør**

Norwegian University of Science and Technology  
Department of Materials Technology and Electrochemistry

March 2000



Universitetsbiblioteket i Trondheim  
Realfagbiblioteket  
7491 TRONDHEIM

---

Doktoringeinørvhandling 2000:30

IME-rapport 2000:13

---

---

Author : Lars Ole Valøen

Address : Department of Materials Technology and Electrochemistry  
Sem Sælands vei 6  
N-7491 Trondheim

E-mail : lov@chembio.ntnu.no

ISBN : 82-7984-052-4

ISSN : 0802-3271

Print : TAPIR Trykkeri, Trondheim, Norway

---



# Preface

The work presented in this thesis has been carried out at the Department of Materials Technology and Electrochemistry, Norwegian University of Science and Technology, NTNU from January 1996 to March 2000. The work has been financed by the Norwegian Research Council through the NYTEK program, with additional funds from Norsk Hydro ASA, and the AMHBAT project, a project financed by the European Union through the Joule III program.

*Professor Reidar Tunold* (Norwegian University of Science and Technology, Norway) has been the main supervisor during the whole period of study. Several other persons have been implicated in this work (in chronological order): *Dr. Svein Sunde* (SINTEF, Norway, now IFE, Halden, Norway) *Dr. Alicja Zaluska* and *Dr. Leszek Zaluski* (McGill University, Montreal, Canada)



# Acknowledgements

I would like to express my thanks to the Research Council of Norway for their financial support through the NYTEK program and also Norsk Hydro ASA, Norway for initiating a new project on metal hydride materials which has contributed directly and indirectly to the financing during the last year of my Dr.ing. work. The following organisations are all acknowledged for travel support: The Memorial Fund of Leif Tronstad, NTNU, Faculty for Chemistry and Biology, NTNU, Norges Tekniske Høgskoles fond, NTNU, The European Union through the Joule III program, and the Japan International Science and Technology Exchange Center (JISTEC). My thanks also go out to the Metal hydride group at McGill University, Montreal, Canada for covering my living expenses during the summer of 1999 and for providing me with the necessary equipment.

A special thanks goes to supervisor *Professor Reidar Tunold* for initiating this project and for giving me the opportunity to take part in it. The years we have been working together have been very fruitful for me, and during this time I have been introduced to many interesting aspects of the electrochemical energy technology.

*Dr. Arnulf Maeland*, Florida, deserves a special thanks for many fruitful discussions and for introducing me to the metal hydride community. His assistance during the period of my Dr.ing. studies has been of great importance.

*Dr. Alicja Zaluska* and *Dr. Leszek Zaluski*, McGill University, Montreal, are gratefully acknowledged for numerous interesting and fruitful discussions and for their hospitality during my stays at McGill University in Montreal. The latter two and *Dr. Hideaki Tanaka* of the Osaka National Research Laboratory, Japan, are gratefully acknowledged for providing the pressure composition isotherms on my arc melted alloys.

*Dr. Svein Sunde* is greatly acknowledged for helping me with the mathematical modeling of the impedance response in metal hydride electrodes and for introducing me to the modelling of the impedance response.

*Dr. Nobuhiro Kuriyama* of the Osaka National Research Laboratory (ONRI), Japan, deserves a special thanks for his hospitality and his helpfulness during my two visits at the ONRI and for sharing his knowledge and experience in the metal hydride field with me. He is also greatly acknowledged for getting me a grant from JISTEC that allowed me to visit the ONRI. Guest researchers *Dr. Daniel Chartouni* and *Dr. Jun Chen* at ONRI are also acknowledged for very interesting discussions regarding crystallographic and electrochemical properties of metal hydrides.

*Professor Andrzej Lasia* of the University of Sherbrooke, Canada, deserves a special thanks for his assistance with modelling the impedance response in porous metal hydride structures. He is also greatly acknowledged for checking parts of the impedance chapters in this thesis.

A special thank also goes to *Dr. J. Oluf Jensen* of The Technical University of Denmark for introducing me to the practical aspects of the laboratory characterization of metal hydride electrodes as well as numerous interesting discussions.

*Colleagues* in the AMHBAT project are all acknowledged for numerous interesting discussions.

My thanks also go out to *Dr. Bjørn Hauback* and *Dr. Volodymyr Yartys* of the Institute for Energy Technology, Norway, for interesting discussions on neutron diffraction and crystallographic properties.

*Ms. Randi Brateng* and *Mr. Sten Egil Johnsen* are acknowledged for their assistance in some electrochemical measurements and for interesting discussions on the kinetics and activation of metal hydride electrodes. Thanks also to *Mr. Kjell Røkke* for his helpfulness in arranging and taking care of some of the the laboratory equipment.

*Dr. Oddmund Wallevik* and *Dr. Christian Rosenkilde* of Norsk Hydro ASA are both greatly acknowledged for their valuable support.

A special thanks to *family, colleagues, and friends* for all encouragement, support and help. A very special thanks also goes to *Suzi* for encouraging me in this work and for her kind assistance in correcting the English in the thesis.

# Contents

<b>Preface</b>	<b>iii</b>
<b>Acknowledgements</b>	<b>v</b>
<b>Summary</b>	<b>xv</b>
<b>1 Introduction</b>	<b>1</b>
1.1 Background . . . . .	1
1.2 Objectives, Scope and Organization of the Thesis . . . . .	3
<b>2 Power Supplies for Portable Applications</b>	<b>5</b>
2.1 Fuel Cells . . . . .	5
2.2 Rechargeable Batteries . . . . .	7
2.2.1 General Properties of Secondary Batteries . . . . .	9
2.2.2 Lithium Based Secondary Batteries . . . . .	10
2.2.3 The Nickel Metal Hydride (NiMH) Battery . . . . .	11
2.3 Combination of Secondary Batteries and Fuel Cell Technology . . .	14
2.3.1 The Nickel Hydrogen Battery . . . . .	14
2.3.2 The Air Metal Hydride Battery . . . . .	15

2.3.3	Batteries Chargeable Electrically and with Hydrogen Gas . . .	16
2.4	Automotive Applications . . . . .	17
<b>3</b>	<b>Applications and Properties of Metal Hydrides</b>	<b>19</b>
3.1	Metal Hydrogen Compounds in General . . . . .	19
3.2	Utilisation of Metal Hydrides . . . . .	21
3.3	Hydrogen Storage . . . . .	23
3.3.1	Binary Metal Hydrides . . . . .	23
3.3.2	Intermetallic Metal Hydrides . . . . .	23
3.3.3	Pressure Composition Temperature Characteristics . . . . .	24
3.3.4	Hysteresis . . . . .	28
3.3.5	Plateau Sloping . . . . .	29
3.4	Hydrogen Storage Alloys of the AB <sub>5</sub> Type . . . . .	30
3.4.1	Structure . . . . .	30
3.4.2	A Site Substitutional Elements . . . . .	32
3.4.3	B Site Substitutional Elements . . . . .	35
3.5	Hydrogen Storage Alloys of Other Types than the AB <sub>5</sub> . . . . .	39
3.5.1	Hydrogen Storage Alloys of the AB <sub>2</sub> Type . . . . .	41
3.5.2	Magnesium Based Hydrogen Storage Alloys . . . . .	42
3.5.3	Other Hydrogen Storage Alloys . . . . .	43
3.6	Charging of of Hydrogen Storage Alloys . . . . .	43
3.6.1	Gas Phase Charging Mechanism . . . . .	43
3.6.2	Electrochemical Charging Mechanism . . . . .	44
3.7	Deterioration from Crack Formation . . . . .	46

3.7.1	Structural Anisotropy . . . . .	48
3.8	Surface Properties for AB <sub>5</sub> Type Alloys . . . . .	50
3.8.1	A Site Elements in Reducing and Alkaline Media . . . . .	50
3.8.2	B Site Elements in Reducing and Alkaline Media . . . . .	51
3.8.3	Surface Treatment and Coating . . . . .	52
3.8.4	Activation . . . . .	53
3.8.5	Self Discharge . . . . .	53
3.9	Diffusion in Metal Hydrides . . . . .	54
3.9.1	State of Charge Dependency of the Apparent Diffusion Coefficient . . . . .	55
3.9.2	Energy Levels . . . . .	56
3.9.3	Diffusion in AB <sub>5</sub> type Alloys . . . . .	57
<b>4</b>	<b>Structural and Related Properties of (La,Ce,Nd,Pr)Ni<sub>5</sub> Alloys</b>	<b>59</b>
4.1	Introduction . . . . .	59
4.2	Experimental Methods . . . . .	60
4.2.1	Factorial Design . . . . .	60
4.2.2	Experimental Procedure . . . . .	62
4.3	Results and Discussion . . . . .	62
4.3.1	Plateau Pressure Changes in (La,Ce,Pr,Nd)Ni <sub>5</sub> Alloys . . . . .	62
4.3.2	Structural Changes and A site Composition . . . . .	66
4.3.3	Structural Anisotropy . . . . .	72
4.3.4	Hysteresis and Van't Hoff Plots . . . . .	73
4.4	Conclusions . . . . .	74

<b>5</b>	<b>Electrochemical Characterization of Metal Hydrides</b>	<b>77</b>
5.1	Electrochemical Characterization Methods . . . . .	77
5.1.1	Electrochemical Cycling . . . . .	78
5.1.2	Open Circuit Voltage Analysis . . . . .	80
5.1.3	Rate Measurements . . . . .	82
5.2	Apparatus . . . . .	84
5.3	Experimental . . . . .	86
5.3.1	Hydride Electrode Construction . . . . .	86
5.3.2	Reference Electrode . . . . .	88
5.3.3	Standard Electrochemical Test for Alloys . . . . .	90
5.3.4	Alloys and Chemicals Used . . . . .	92
5.4	Results . . . . .	93
5.4.1	Electrochemical Cycling of Metal Hydride Electrodes . . . . .	93
5.4.2	Discharge Capacity as a Function of Current Density . . . . .	96
5.4.3	Open Circuit Potential Variations . . . . .	100
5.4.4	Other Potential Measurements . . . . .	101
5.5	Discussion . . . . .	102
5.5.1	Constant Current Cycling . . . . .	102
5.5.2	Open Circuit Potential Measurements . . . . .	104
5.5.3	Rate Measurements . . . . .	104
5.5.4	Other Potential Measurements . . . . .	107
5.5.5	Reproducibility . . . . .	108
5.5.6	Experimental Challenges . . . . .	108
5.6	Conclusions . . . . .	109



<b>6</b>	<b>Electrochemical Properties as a Function of External Pressure</b>	<b>111</b>
6.1	Introduction . . . . .	111
6.2	Experimental . . . . .	111
6.3	Results and Discussion . . . . .	113
6.3.1	Electrochemical Cycling . . . . .	113
6.3.2	Discharge Capacity as a Function of Current Density . . . . .	118
6.3.3	Diffusion Gradients . . . . .	122
6.4	Conclusion . . . . .	124
<b>7</b>	<b>Impedance Modelling</b>	<b>125</b>
7.1	Introduction to Impedance Characterization . . . . .	126
7.1.1	Validation of Experimental Data . . . . .	129
7.2	Rough and Porous Electrodes . . . . .	130
7.2.1	Electrodes with Microscopic Roughness . . . . .	130
7.2.2	The Constant Phase Element . . . . .	131
7.2.3	Transmission Line Approach . . . . .	132
7.2.4	Porous Electrodes Versus Rough Electrodes . . . . .	135
7.3	Hydrogen Evolution in Combination with Hydrogen Absorption . . . . .	135
7.4	Metal Hydride Electrodes . . . . .	136
7.4.1	Introduction . . . . .	136
7.4.2	Previous Work . . . . .	138
7.5	Different Impedance Models . . . . .	139
7.5.1	Theoretical Considerations . . . . .	139
7.5.2	Spherical Diffusion, Sphere Model . . . . .	140

7.5.3	Including Side Processes . . . . .	147
7.5.4	Planar Diffusion Model . . . . .	149
7.5.5	Particle Size Distribution Model . . . . .	150
7.6	Discussion . . . . .	150
<b>8</b>	<b>Impedance Response in Metal Hydride Electrodes</b>	<b>153</b>
8.1	Experimental . . . . .	153
8.2	Model Verification . . . . .	155
8.2.1	Circuit Element Elimination . . . . .	157
8.3	Impedance Model Evaluations . . . . .	157
8.3.1	Reference System . . . . .	158
8.3.2	State of Charge Dependent Response . . . . .	164
8.3.3	Magnesium Based Electrodes . . . . .	169
8.3.4	The Hydrogen Evolution Parallel Reaction . . . . .	173
8.3.5	Amplitude of the Applied Potential . . . . .	174
8.3.6	Impedance Response from Equipment and Electrode Construction . . . . .	176
8.3.7	Contact Impedance . . . . .	178
8.4	Discussion . . . . .	179
8.4.1	State of Charge Dependent Kinetic Variations . . . . .	179
8.4.2	Mechanism . . . . .	181
8.5	Conclusions . . . . .	183

<b>9 Concluding Discussion</b>	<b>185</b>
9.1 Misch Metal Composition in AB <sub>5</sub> Type Hydrogen Storage Alloys . . . . .	185
9.2 Kinetics . . . . .	186
9.2.1 Charge Transfer Step . . . . .	187
9.2.2 Diffusion Step . . . . .	188
9.2.3 Hydride Forming Reaction Step . . . . .	189
9.2.4 Porous Electrode Model . . . . .	189
9.2.5 Side Reactions . . . . .	189
9.3 Recommendations for Further Improvements . . . . .	190
<b>List of symbols</b>	<b>191</b>
<b>Abbreviations</b>	<b>197</b>
<b>Bibliography</b>	<b>198</b>
<b>Index</b>	<b>215</b>
<b>Appendices</b>	<b>A.1</b>
<b>A List of Publications and Presentations</b>	<b>A.1</b>
A.1 List of Published Papers . . . . .	A.1
A.2 List of Presentations . . . . .	A.2
<b>B Determination of Structure Parameters</b>	<b>B.1</b>
B.1 From X-ray Diffraction . . . . .	B.1
B.2 From Neutron Diffraction . . . . .	B.3

<b>C Source Code</b>	<b>C.1</b>
C.1 Spherical Diffusion, Porous Model . . . . .	C.1
C.2 Spherical Diffusion, Size Distribution, Porous Model . . . . .	C.3

# Summary

Rechargeable battery systems are paramount in the power supply of modern electronic and electromechanical equipment. For the time being, the most promising secondary battery systems for the future are the lithium-ion and the nickel metal hydride (NiMH) batteries.

In this thesis, metal hydrides and their properties are described with the aim of characterizing and improving those. The thesis has a special focus on the  $AB_5$  type hydrogen storage alloys, where A is a rare earth metal like lanthanum, or more commonly misch metal, which is a mixture of rare earth metals, mainly lanthanum, cerium, neodymium and praseodymium. B is a transition metal, mainly nickel, commonly with additions of aluminium, cobalt, and manganese.

The misch metal composition was found to be very important for the geometry of the unit cell in  $AB_5$  type alloys, and consequently the equilibrium pressure of hydrogen in these types of alloys. The A site substitution of lanthanum by misch metal did not decrease the surface catalytic properties of  $AB_5$  type alloys. B-site substitution of nickel with other transition elements, however, substantially reduced the catalytic activity of the alloy.

If the internal pressure within the electrochemical test cell was increased using inert argon gas, a considerable increase in the high rate charge/discharge performance of  $LaNi_5$  was observed. An increased internal pressure would enable the utilisation of alloys with a high hydrogen equivalent pressure in batteries. Such alloys often have favourable kinetics and high hydrogen diffusion rates and thus have a potential for improving the high current discharge rates in metal hydride batteries.

The kinetic properties of metal hydride electrodes were found to improve throughout their lifetime. The activation properties were found to be highly dependent

on the charge/discharge current. Fewer charge/discharge cycles were needed to activate the electrodes if a small current was used instead of a higher current. For applications involving the utilisation of high currents, the activation to the required level could be as high as 100 cycles, whereas for low current applications, 5-10 activation cycles could be sufficient when the same current was used for the activation (pretreatment of the alloy might enhance the activation considerably). When an electrode made of an alloy with a relatively high hydrogen equilibrium (plateau) pressure was cycled under a moderate external inert gas pressure, a new activation process was observed when the pressure was increased. This indicated that the activated state was dependent on several factors, which indicated the need of examining each factor individually as well as combined in order to gain a complete understanding of the process.

The characterization of metal hydride electrodes by means of electrochemical impedance spectroscopy, showed that this technique when used properly and in combination with other characterization techniques can be very useful in determining the significance of the different sub-processes in the overall process.

The impedance response for different laboratory metal hydride electrodes were successfully modelled and fitted to experimental data for both  $AB_5$  type alloys and a MgNi type electrode. The following sub processes were found to be significant for the overall reaction rate: charge transfer resistance, double layer capacitance and impedance resulting from hydrogen diffusion within the metal lattice. The diffusion process was best modelled when using a spherical diffusion geometry. To fit the experimental data, equations describing the current distribution in porous electrodes were required.

To account for possible parallel hydrogen evolution during charging, it was necessary to include this step in the model for electrodes having a more negative open circuit potential than the reversible hydrogen evolution potential. Indications of one or more parallel reduction/oxidation processes competing with the electrochemical hydride absorption/desorption reaction were observed.

The results indicated rather large variations in the kinetic parameters for the process at different states of charge of the hydride material. The optimum energy efficiency for an alloy with composition  $MmNi_{3.5-3.7}Co_{0.7-0.8}Mn_{0.3-0.4}Al_{0.3-0.4}$  intended for utilisation in batteries was obtained in the range of 40 to 95% depth of discharge.

# Chapter 1

## Introduction

### 1.1 Background

Today's energy technology is mainly based on fossil fuels, such as coal, oil and natural gas. Since these fuels are present on earth in limited amounts, the future society has to base its energy use on renewable sources. If nuclear energy is dismissed because of environmental and safety considerations regarding nuclear waste, we are left with primary or secondary energy sources like sun, wind and hydropower.

Energy storage is a crucial issue that needs to be addressed in the use of energy from renewable sources, and electrochemical storage in different types of batteries is and will be an important way of intermediate storage of energy. For larger energy storage requirements, hydrogen is an attractive alternative as a fuel, since its reaction with oxygen solely produces water.

Hydrogen may be stored as gas, liquid or in the form of metal hydrides for later use in batteries or fuel cells. Applications of batteries and fuel cells in the transport sector (cars and buses) may contribute to a substantial reduction of pollution in cities.

Rechargeable battery systems are paramount in the power supply of modern electronic and electromechanical equipment. Important applications are communication devices like cellular telephones, electric tools, and "back up" systems for computers and other electronic devices.

One of the potentially largest applications of hydrogen storage alloys is as a part of the technology used for propulsion of zero emission vehicles, as more environmental friendly propulsion systems are needed to improve the air quality, specially in urban areas. The present battery technology for vehicle propulsion is mainly based on advanced lead-acid, nickel cadmium (NiCd) batteries and NiMH batteries. These systems are very reliable and maintenance free. The lead-acid battery, however, has a too low energy density, and the NiCd battery is a pollution hazard due to the high content of toxic cadmium heavy metal. For the time being, the most promising secondary battery systems are the Li-ion and the NiMH batteries. A main problem with all the present battery systems, however, is the very high cost compared to an equivalent gasoline system.

In vehicular applications it is important that the battery can deliver high power in order to give the vehicle acceptable acceleration; and receive high charging currents, which are important during regenerative braking. In this context, NiMH batteries are superior with a very high power density. In addition, the NiMH battery is environmentally acceptable since it does not contain poisonous components. It can be recycled, is safe and robust, has a long cycle life, and has an acceptable energy density, although in this context the present type is inferior to the Li-ion batteries.

We can expect a growing need for hybrid electrical vehicle (HEV) batteries. Commercialization of NiMH batteries in the HEV market will make them very competitive in the EV market as well. There are also several interesting concepts integrating fuel cell and battery technology, as for instance fuel cells with integrated hydrogen storage in metal hydrides.

When fuel cells become commercialized, batteries can operate the car until the fuel cell (and possibly methanol reformer) has warmed up, and it can be recharged during braking, improving the overall efficiency. Both the Daimler Chrysler group and the General Motors company have announced that their fuel cell driven vehicles will be commercially available by 2004.



## 1.2 Objectives, Scope and Organization of the Thesis

This dissertation has been concentrated in four main parts:

1. Production of  $AB_5$ -type metal hydride forming alloys samples and characterization of different properties of these as a function of their composition using structural, thermodynamic and electrochemical techniques.
2. Electrochemical characterization of various metal hydride electrodes where different properties were monitored using a wide range of characterization techniques.
3. Theoretical modelling of the kinetics and transport properties of the electrochemical charge and discharge reactions of the metal hydride electrode.
4. Measurements of the electrode kinetics of metal hydride electrodes and fitting of these results into models developed. The purpose of this is to get a more systematic overview of the variation of the different properties governing the kinetics of this type of batteries and how these properties can be optimized.

This thesis has been divided into nine chapters. In chapter 2, a general overview of different alternatives for power supplies for electronic and electric applications is given. For this overview, the emphasis is on battery systems and systems that combine batteries and fuel cells. General information regarding metal hydrides and their properties are summarized in chapter 3. In chapter 4, effects of the misch metal composition in misch metal based  $AB_5$  type hydrogen storage alloys are elaborated. Electrochemical characterization of metal hydrides in particular is elaborated in chapter 5. The material and methods section in chapter 5 contains general and detailed experimental descriptions on electrochemical measurement techniques used for the characterization of metal hydrides. Chapter 6 deals with how the external pressure affects the properties of the metal hydride electrodes. Different models for the impedance response in metal hydride electrodes are developed in chapter 7. Experimental data fitted to the models developed in chapter 7 are presented in chapter 8. Chapter 9 concludes the study and makes recommendations for further work within the field of characterizing and improving the properties of metal hydride electrodes for use in rechargeable batteries.

A list of the symbols used is given on page 191 and a list of abbreviations can be found on page 197. An index section is included at the end (before appendices) of this thesis. IUPAC notation is used for the elements and all measures are kept within the metric system.

## Chapter 2

# Power Supplies for Portable Applications

*In this chapter, an introduction to electrochemical power sources for portable devices is given. Different power supply devices are compared in terms of energy density and power output.*

The demand for various portable electric devices has increased dramatically over the last decade, as an increased density of transistors in integrated circuits has made it possible to make advanced hand held electronic devices. The environmental drive for low emission vehicles is also larger than ever. As an immediate consequence, interest in non-fossil fuel based power supplies has been on the rise.

### 2.1 Fuel Cells

A fuel cell is a device that converts chemical energy directly into electricity via an electrochemical process. The process also produces heat and water, and carbon dioxide if a hydrocarbon fuel is used.

Fuel cells can be made small enough for consumer electronics applications [1], replacing batteries, as well as large (MW) units for power plants [2]. Fuel cells also offer a promising alternative to the internal combustion engine (ICE) for vehicle propulsion [3], because, in contrary to the ICE, they are not limited by

the Carnot cycle and hence, give a higher fuel efficiency over a wider range of power outputs. There are no harmful  $\text{NO}_x$  emissions from low temperature fuel cells and negligible amounts emitted from high temperature fuel cells. Several fuel cell powered demonstration vehicles have been built in recent years (see Ref [3] for an overview). The operation principle of a fuel cell is shown in figure 2.1. Exhaust will go through the anode outlet if the electrolyte is oxygen conducting,

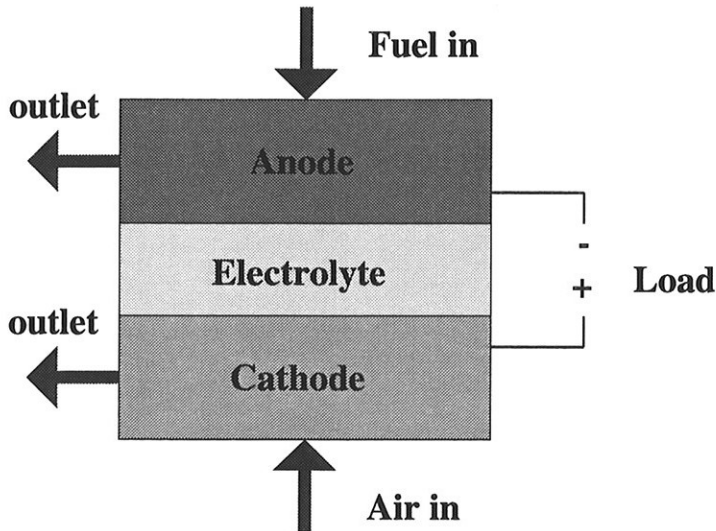


Figure 2.1: Schematic drawing showing main constituent elements and flow in a fuel cell.

and through the cathode outlet if the electrolyte is proton conducting. Several types of fuel cells exist and an overview of fuel cell systems is given in Ref [4]. Each type of fuel cell has its advantages and disadvantages and generally suited for specific applications. Fuel cells are commonly named after the electrolyte, and an overview of the most important fuel cells is given below:

- The alkaline fuel cell (AFC) operates at low temperatures ( $\sim 70^\circ\text{C}$ ), using platinum and/or silver based catalysts. The cell is relatively inexpensive to manufacture, but it requires relatively pure hydrogen as carbon containing fuel can form carbonates with the electrolyte and poison the catalysts. The cell is favourable for use in transportation.
- The phosphoric acid fuel cell (PAFC) is at present the only commercial fuel

cell type and gives reliable systems that operate at moderate temperatures ( $\sim 200^\circ\text{C}$ ). Hydrogen can be supplied from an external reformer. A low power density limits its use to stationary applications due to size. Heat might be utilized to give higher total system efficiencies.

- The proton exchange membrane fuel cell (PEMFC) operates at low temperatures ( $80\text{-}100^\circ\text{C}$ ) and low pressures. The cell has a relatively high fuel efficiency with a small size and a short start-up time, which both favour transportation applications. Pure hydrogen is needed as hydrogen containing traces of carbon monoxide will effectively poison the expensive noble catalysts used. Methanol can be utilized directly in a so called direct methanol fuel cell (DMFC) similar to the PEMFC, but with a somewhat lower efficiency.
- The molten carbonate fuel cell (MCFC) operates at a high temperature ( $> 600^\circ\text{C}$ ), which favours stationary operation. MCFCs can be designed to operate on many different fuels, such as gasified coal and natural gas. Corrosion and material stability is problematic.
- The solid oxide fuel cell (SOFC) operates at a very high temperature ( $> 650^\circ\text{C}$ ), eliminating the need for expensive catalysts. Internal reforming of natural gas is therefore possible. Because of the high operating temperature, the thermal cycling during startup and shutdown can cause material problems. The cell has a very high efficiency and it is well suited for stationary power conversion and co-generation (power and heat).

## 2.2 Rechargeable Batteries

Batteries are divided into primary (non-rechargeable) and secondary (rechargeable) systems.

During the last years different types of metal/air batteries, lithium based "rocking chair"<sup>1</sup> battery systems, and the NiMH battery have shown to be the most promising for future applications. Secondary alkaline metal/air systems are interesting but have low cycle life because of problems associated with the formation of dendrites when charging the metal electrode.

---

<sup>1</sup>During charge/discharge lithium is transported back and forward between two insertion electrodes. This is the reason for the nick name "rocking chair" battery.

Today, several battery types are available on the market and in table 2.1, a general overview of the most important types of secondary batteries is given. The data in the table is mainly taken from the paper by Kordesh and Daniel-Ivad [5] but some data are supplied from various other sources [6–9].

Table 2.1: *Various characteristics of different types of secondary batteries.*

Property		PbO <sub>2</sub> /Pb	NiCd	NiMH	Li-ion
Specific energy ( $E_s$ )	[Wh/Kg]	30-40	40-55	50-70	100
Energy density ( $E_\rho$ )	[Wh/l]	100 [10]	100-140	330[11]	285 [11]
Specific power ( $P_s$ )	[W/kg]	160 [10]	-	180 [10]	180 [10]
OCV	[V]	2.1	1.3	1.3	4.1
Operating range	[V]	2.0-1.8	1.2-1.0	1.2-1.0	3.8-3.0
Peak rate (Li-ion=1)	-	6	10	5	1
Temperature range	[°C]	-30+50	-20+45	-10+40	-20+60
Charge temperature	[°C]	0+45	0+45	0+40	0+45
Final charge voltage	[V]	2.4	1.5	1.5	4.5
Charging time	[h]	2-20	1-3	2-5	3-20
Overcharge protection	-	lim.	yes	yes	no
Overdischarge	-	no	yes	lim.	no
Charge efficiency	[%]	90	85	80	90
Cycle life 30% DOD	-	500	2000	800	2000?
Cycle life 80% DOD	-	200	800	600	800
Cycle life 100% DOD	-	20-50	500	200	200
Self discharge 20°C	%/month	3-5	15-20	20-30	8-15
Self discharge 45°C	%/month	50	60	80	30
self discharge 65°C	%/month	100	100	100	100

The most important secondary battery types at present are the lead acid, the NiCd, the NiMH, and the lithium based battery types. NiMH batteries and Li-ion batteries are replacing the NiCd and lead acid batteries for environmental reasons and because of higher energy storage capacities. The main emphasis in the present chapter is on the NiMH batteries, even though in section 2.2.2 the lithium based batteries are treated shortly. These two technologies will presumably be the main competing technologies in the near future. Currently, NiCd batteries have the largest share of the rechargeable battery market which ex-

cludes automotive applications. NiCd batteries are used in aircrafts, military equipment, telecommunication equipment, home-use portable devices (photography, portable phones, portable computers, camcorders, power tools, toys), and provide standby power in for example emergency lighting and alarms.

### 2.2.1 General Properties of Secondary Batteries

A general description of a secondary battery is given in figure 2.2.

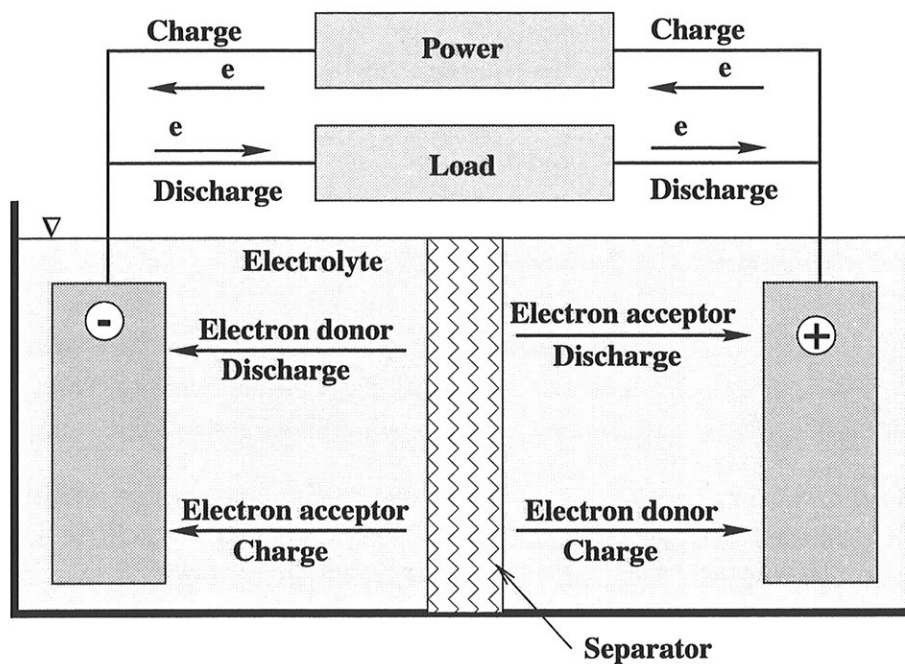


Figure 2.2: *Principal description of a secondary battery.*

As one can see from this figure, rechargeable batteries all have some common components:

**Negative electrode** During discharging a reactant is oxidized, and during charging a species is reduced.

**Positive electrode** During discharging, a reactant is reduced and during charging a species is oxidized.

**Electrolyte** The electrolyte is a charge transport medium with preferably a pure ionic conductivity. It is desirable to have an electrolyte with an as high as possible ionic conductivity.

**Separator** The separator prevents a direct electrical contact. A separator is necessary to ensure pure ionic conductivity between the negative and the positive electrode in liquid electrolyte batteries. The separator is made of sheets of non-conducting fibrous material [12]. The porous structure allows the flow of electrolyte in the batteries. The performance of the separator depends upon the relative magnitudes of their permeability in different directions. The separator must be stable in the electrolyte. For solid electrolyte batteries, the separator can be omitted, since the electrolyte in such a cell acts as both separator and electrolyte because of the higher mechanical stability.

### 2.2.2 Lithium Based Secondary Batteries

Lithium is the lightest metallic element and generates a high voltage versus the standard hydrogen electrode (i.e. -3.04 V [13]). Early attempts used lithium metal in combination with a transition metal oxide or sulphide intercalation compound.

The lithium battery has a great potential due to the high energy density (see table 2.1. In these systems lithium is intercalated in an oxidic or sulfidic positive electrode material like  $\text{TiS}_2$ ,  $\text{MnO}_2$ ,  $\text{LiCoO}_2$ ,  $\text{LiV}_2\text{O}_5$  or  $\text{LiNiO}_2$  [14]. Mixed compounds such as  $\text{LiNi}_{1-x}\text{Co}_x\text{O}_2$  are also used. The negative electrode consists either of pure lithium or a material that can reversibly intercalate lithium. For this purpose, carbon or cyclic organic compounds are used.

A non aqueous electrolyte such as solutions of lithium salts in aprotic solvents or in their mixtures is applied in the lithium ion batteries [15].

Lithium-ion cells do not use metallic lithium or lithium alloys, and lithium is present only in the ionic or intercalated form. This greatly improves the safety of lithium-ion batteries when they are compared to the first generation of lithium batteries containing metallic lithium. As lithium-ion cells are charged and discharged  $\text{Li}^+$  ions are transported between the carbon-based negative electrode and the positive electrode [16], with electrons exchanged as a result of lithium ion insertion and of lithium ion extraction.



The power density in lithium batteries is, however, limited because of a limited conductivity in the non aqueous electrolyte. Using too high currents can therefore produce too much heat, making the battery less safe. Proper control systems are developed, and the lithium battery systems are expected to increase their importance during the next few years.

### 2.2.3 The Nickel Metal Hydride (NiMH) Battery

Since the NiMH battery was commercialized in Japan in 1991 [17], NiMH batteries have entered the international market as replacements for NiCd batteries. As seen from table 2.1, the NiMH battery is very similar to the NiCd battery but has some significant advantages over the latter. One advantage of the NiMH battery is that it has no *memory effect*<sup>2</sup>. The commercial NiMH battery is based on a hydride forming alloy electrode and a nickel counter electrode (NiOOH/NiOH<sub>2</sub> positive electrode<sup>3</sup>) in a 6-8M potassium hydroxide electrolyte. In figure 2.3, the construction of a commercial NiMH battery is given.

To improve the durability of the positive electrode, 0.5-2M LiOH is added to the electrolyte [6]. The Potassium hydroxide electrolyte has a maximum conductivity at a concentration of 6M at room temperature [20, 21]. The energy density in a commercial NiMH battery is very good compared to most other competing battery technologies (see table 2.1). Another feature of the NiMH battery is its environmental friendliness. An incentive for developing NiMH batteries comes from pressing health and environmental concerns to find replacements for the NiCd rechargeable batteries since the NiMH battery does not contain lead or cadmium, which accumulates in the food chain. Satisfactory methods have also been developed for recycling of the relatively valuable metals in the battery [22, 23]. The used batteries can also be used without any preprocessing as additives in the steel production, but problems of separating NiMH and NiCd batteries on a large scale has so far limited an efficient recycling.

The charging of the metal hydride electrode is also relatively uncomplicated be-

---

<sup>2</sup>The property of NiCd batteries that causes them to lose their capacity for full recharging if they are discharged repeatedly the same amount and then recharged without overcharge before they have fully drained. The term derives from the fact that the battery appears to have a memory for the amount of charging it can sustain.

<sup>3</sup>The battery can also be combined with a MnO<sub>2</sub> positive electrode [18] or an intercalating positive electrode [19].

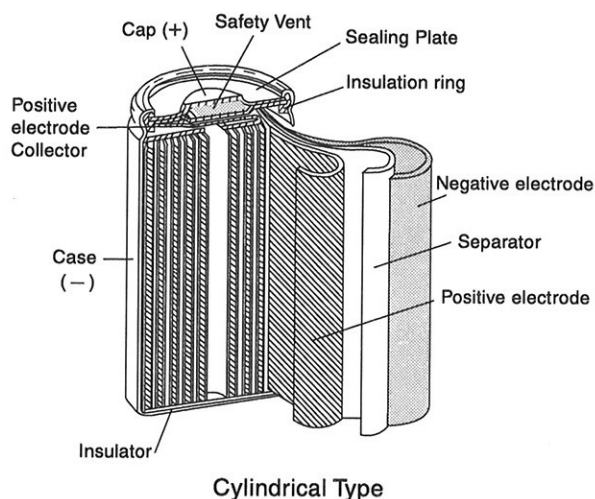
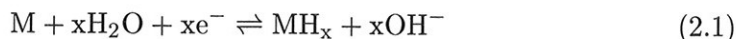


Figure 2.3: *Commercial NiMH battery, spiral wound cylindrical type. The negative electrode is the metal hydride electrode and the positive electrode is made of NiOOH/NiOH<sub>2</sub>.*

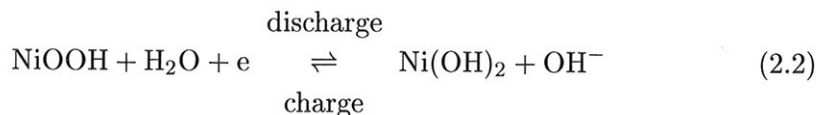
cause of problems associated with dendrite formation are avoided as no metal dissolution deposition takes place.

### Charging/discharging reactions

The following electrochemical reactions take place in the the NiMH battery [9]. At the hydride (negative) electrode:

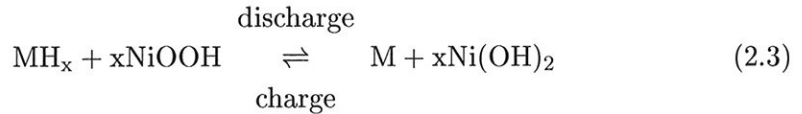


The standard open circuit potential<sup>4</sup> ( $E^\circ$ ) of reaction 2.1 is -0.83 V versus Hg/HgO [6]. At the nickel (positive) electrode:



<sup>4</sup>The open circuit potential is very dependent on the plateau pressure of the hydrogen storage alloy used, see section 5.1.2 for additional details.

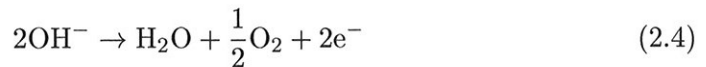
The standard open circuit potential ( $E^\circ$ ) of reaction 2.2 is +0.49 V (versus Hg/HgO)[6]. The total reaction can be summarized as follows:



The open circuit potential of a NiMH battery (reaction 2.3) is the potential difference between the positive and the negative electrode,  $E^\circ = +1.32$  V.

### Overcharge reactions

The NiMH battery has an internal overcharge protection, since the metal hydride (MH) electrode has a higher capacity than the counter electrode which facilitates a gas recombination reaction. This is provided the battery is not completely filled up with electrolyte, leaving adequate space for gas transport and recombination. The overcharge reactions in a NiMH battery are given in Eqs 2.4 and 2.5. Since the overcharge reaction is based on a higher capacity for the MH electrode, the positive NiOOH/Ni(OH)<sub>2</sub> electrode reaches full charge before the MH electrode and produces oxygen.



It is crucial that oxygen can be transported in the gas phase from the counter electrode to the MH electrode, where it produces water according to the following equation:

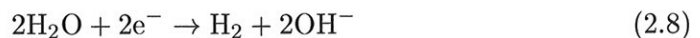


If the metal hydride electrode is overcharged, hydrogen is evolved [24]:



$$E^\circ[V] = 0.000 - 0.0591pH - 0.0295 \log P_{\text{H}_2} \quad (2.7)$$

In alkaline solution,  $\text{OH}^-$  is added on both sides of reaction Eq 2.6 to give



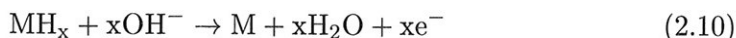
Since the metal hydride electrode is oxidized by oxygen, it is possible to prevent massive hydrogen evolution from the metal hydride electrode and pressure build up by carefully selecting the charge current.

### Overdischarge reactions

When the positive NiOOH/Ni(OH)<sub>2</sub> electrode is overdischarged, hydrogen is evolved at the electrode according to Eq 2.8. The hydrogen evolved at the positive NiOOH/Ni(OH)<sub>2</sub> electrode is transported to the MH electrode by diffusion through the separator and is absorbed<sup>5</sup> by the MH electrode according to the following reaction:



The hydrogen is then discharged from the electrode and forms water:



If the mechanism described does not function properly, the metal hydride electrode material is oxidized:



resulting in a decrease in the maximum discharge capacity.

## 2.3 Combination of Secondary Batteries and Fuel Cell Technology

In this section, the emphasis is put on combinations of components of either an alkaline fuel cell or a polymer electrolyte fuel cell and components of a conventional NiMH battery.

### 2.3.1 The Nickel Hydrogen Battery

The nickel hydrogen battery consists of a fuel cell anode fed with hydrogen gas from a gas storage unit and a nickel cathode [25–31]. The cathode is a nickel cathode similar to the cathode used in NiMH batteries and NiCd batteries. The hydrogen electrode is identical to the anode used in alkaline fuel cells: the thin film electrode consists of an electrocatalyst covered with a hydrophobic gas diffusion membrane. To increase the mechanical strength of a nickel hydrogen battery, the

---

<sup>5</sup>Hydrogen storage materials used for battery electrodes usually have low plateau pressures, facilitating the gas phase absorption reaction.

gas diffusion membrane is put on a substrate [28, 29]. The charge state can be determined by simply measuring the hydrogen pressure at the anode.

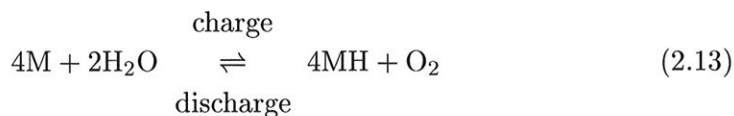
The nickel hydrogen battery is a system that has a very satisfactory cycle life. The battery can be subjected to over 60,000 cycles without degradation [28, 29]. The reason why this battery type has not been used in more applications, is probably low energy density combined with a relatively high cost [26]. Today the nickel hydrogen battery is widely used in space applications because of its long cycle life expectance.

### 2.3.2 The Air Metal Hydride Battery

By replacing the nickel electrode by an air electrode, the energy density can be increased considerably. The reaction in the metal hydride electrode is the same as for the NiMH battery (see Eq 2.1). At the air electrode the following reaction takes place [32]:



Combined with Eq 2.1, this gives the following total reaction [32]:



Several experiments have been performed with air metal hydride batteries. When recharging these for several times [32], there are some major problems associated with these kind of batteries. If natural air is fed to the oxygen electrode  $\text{CO}_2$  and possibly traces of  $\text{CO}$  can contaminate the electrolyte with carbonate compounds, making it necessary to replace the electrolyte on a regular basis. Another problem is the absence of a reversible air electrode that works well at the charging current densities needed. A third electrode therefore has to be added to facilitate the charging reaction. Despite this, an energy density which is considerably higher than that for the NiMH battery has been obtained. However, more controlling devices are needed because of reduced internal protection. The addition of controlling devices increases the total weight of the system, making it less applicable to small scale exploitations.

### **Overcharge reactions**

The overcharge hydrogen evolution reaction in an air metal hydride battery is given by Eq 2.6. The air metal hydride battery has no internal overcharge protection, which can cause a loss of electrolyte if the battery is overcharged.

### **Overdischarge reactions**

The overdischarge reaction in an air metal hydride battery is given by Eq 2.11. In practice, this means that the air metal hydride battery has no internal overdischarge protection which can cause oxidation of the electrode material if it is overdischarged. Since the metal hydride electrode consists of an alloy system, the oxidized electrode material will not retain the lost electrode storage capacity.

It is also possible to replace the alkaline electrolyte with an alkaline solid polymer electrolyte [33, 34], but this type of battery exhibits too low current densities at present.

### **2.3.3 Batteries Chargeable Electrically and with Hydrogen Gas**

The features and the construction procedures for polymer and alkaline fuel cells are described elsewhere [35]. As early as in 1977, the idea of combining fuel cell technology with metal hydride electrodes was proposed by Videm [36]. Experimental efforts in this field were performed in the late seventies by FIAT [37]. Scientists at FIAT tested the system both with anion and cation membranes. The metal hydride alloy associated with cationic membranes dissolved anodically (corroded) during the discharge of the electrodes if the alloy was in direct contact with an acidic membrane. Anion membranes in general have lower conductivities, and will therefore cause too high overpotentials, although the principle is applicable to laboratory scale cells [33].

These types of cells without any membranes have also been tested on laboratory scale [38].

## 2.4 Automotive Applications

Large scale applications of batteries and fuel cells will likely include vehicular applications as well as back up power sources for stationary needs. Stationary applications are usually less sensitive to weight and volume properties and possibly even more cost sensitive. As was mentioned earlier in this chapter, there are many possible future combinations that include batteries and/or fuel cells for future vehicular applications. In table 2.2, promising future propulsion systems are compared with regards to energy density and power output [39].

Table 2.2: *Comparison of promising future propulsion systems with regards to energy density and power output.*

Type (Company)	$E_s$ $\frac{Wh}{kg}$	$E_\rho$ $\frac{Wh}{l}$	$P_s$ $\frac{W}{kg}$	$P_\rho$ $\frac{W}{l}$
High energy NiMH (Ovonic)	70	165	220	520
High Energy Li-ion (SAFT)	126	197	262	410
High energy Li-polymer (3M)	155	220	315	445
PEMFC + MH (Toyota)	188	307	80	131
PEMFC+MH+ NiMH (Toyota)	136	253	231	430
PEMFC+LH <sub>2</sub> (Daimler Chrysler)	253	188	175	140
Air-MH (Hydrocell)	197	266	84	113
Air-MH+ NiMH (Hydrocell)	140	227	238	386

In the table  $E_s$  is the specific energy,  $E_\rho$  is the energy density,  $P_s$  is the specific power and  $P_\rho$  is the power density. The Hydrocell concept is an integrated alkaline fuel cell and hydride storage compartment. When considering the properties mentioned in table 2.2 and the cost (see table 2.1), the combined systems might look like the most promising at this time. In a combined system, the battery can be charged during braking (regenerative braking) and it can also provide peak power. The fuel cell can increase the specific energy and the energy density, giving a considerably longer driving range. It is expected that a lot of interesting developments will be made in the near future.





## Chapter 3

# Applications and Properties of Metal Hydrides

*This chapter emphasizes the applications and properties of metal hydrides and the challenges regarding their characterization.*

The term metal hydride is used to describe a compound of metal and hydrogen that contains some kind of a metal hydrogen bond.

### 3.1 Metal Hydrogen Compounds in General

In figure 3.1, the periodic table in which hydride forming properties for the different elements are highlighted is given [40, 41].

The nature of the metal hydrogen bond is related to the properties of the metal, and metal hydrogen bonds can be classified into the following groups:

**Covalent hydrides** are in general formed from metals to the right of group VIIIB in the periodic table. The properties of covalent hydrides are a reflection of the weak van der Waals forces existing between covalent molecules. The common characteristics of covalent hydrides are typically: low melting and boiling points, liquid or gaseous at room temperature, and solid covalent hydrides are thermally unstable [42].

IA																		VIIIA
H	IIA											IIIA	IVA	VA	VIA	VIIA	He	
Li	Be											B	C	N	O	F	Ne	
Na	Mg	IIIB	IVB	VB	VIB	VIIIB	VIII B				IB	IIB	Al	Si	P	S	Cl	Ar
K	Ca	Sc	Ti	V	Cr	Mn	Fe	Co	Ni	Cu	Zn	Ga	Ge	As	Se	Br	Kr	
Rb	Sr	Y	Zr	Nb	Mo	Tc	Ru	Rh	Pd	Ag	Cd	In	Sn	Sb	Te	I	Xe	
Cs	Ba		Hf	Ta	W	Re	Os	Ir	Pt	Au	Hg	Tl	Pb	Bi	Po	At	Rn	
Fr	Ra																	
		La	Ce	Pr	Nd	Pm	Sm	Eu	Gd	Tb	Dy	Ho	Er	Tm	Yb	Lu		
		Ac	Th	Pa	U	Np	Pu	Am	Cm	Bk	Cf	Es	Fm	Md	No	Lr		





	Forms ionic hydride		Forms metallic hydride, H <sub>2</sub> pressure <1 atm
	Forms covalent hydride		Forms metallic hydride, H <sub>2</sub> pressure >1 atm

Figure 3.1: Periodic system including hydride forming properties for the elements, including the hydrogen equivalent pressure for metallic hydrides.

**Ionic hydrides** are formed from the alkali and alkaline earth metals. The hydrogen has a valence of -1 in ionic hydrides, and the physical properties of these hydrides are often similar to the corresponding halides. Ionic hydrides are often also referred to as *saline* hydrides. Common characteristics of ionic hydrides are: High enthalpy of formation, high melting points, and electronic conductance in the molten state [42]. As seen from figure 3.1. Magnesium hydride occupies a special position, with properties intermediate between the ionic hydrides and the covalent beryllium hydride [42].

**Metallic hydrides** are formed by elements from group IIIB to VIII B in the periodic table (the lanthanides and actinides included). Hydrogen forms in this case a metal bond with the transition metal. In metallic hydrides, hydrogen is in general recognised as an alloying element where the hydrogen electron is transferred to the conduction band of the metal. This results in metallic properties such as luster, hardness and metallic conductivity.

Metallic hydrides are in general much more brittle than metals. Another characteristic of metallic hydrides is a often unusually high deviation from stoichiometry [42].

## 3.2 Utilisation of Metal Hydrides

Metal hydrides can be utilised in a number of different applications [17, 43–48]. Some examples of the different metal hydride applications are given in the following section.

**Hydrogen storage and transport** is probably the most known application of metal hydrides.

- Hydrogen electrodes: NiMH batteries are explained in detail in section 2.2.3. Metal hydrides can also be used as electrodes for electrolyzers (low hydrogen evolution overpotential) and fuel cells.
- Hydrogen gas storage: the hydrogen gas is absorbed at a low temperature and desorbed at a higher temperature, i.e. either hydrogen absorption or desorption is controlled by controlling the temperature. (see section 3.3.3 for an explanation on the operation principles). Metal hydrides can be utilised in stationary hydrogen storage containers, hydrogen carriers, and hydrogen tanks for hydrogen fuelled vehicles.

**Processes.** Absorption and desorption properties of hydrogen can be utilised in several processes.

- Compressors. The working principle of a metal hydride based compressor can be summarized as follows (LaNi<sub>5</sub> type hydrogen storage alloy is assumed): hydrogen gas is absorbed at a low temperature ( $\sim 20^\circ\text{C}$ ), where the equilibrium pressure is low ( $\sim 3$  atm [49]). The hydride is then heated to a higher temperature,  $\sim 140^\circ\text{C}$ , leading to a pressure of about 50 atm. After desorption the pressure drops and the alloy is recharged with hydrogen. The same principle can be used in heat engines (see Refs [48, 50] for additional details).

- **Catalysts.** Many metal hydrides have a very high exchange current densities and may therefore be utilised as catalysts for chemical or electrochemical reactions where hydrogen is one of the reactants.
- **Metallurgical processing.** hydrogenation grinding, and the HDDR<sup>1</sup> process for producing niobium-iron-boron magnets. Hydrogen absorption leads to an expansion and destruction of the metal lattice, causing fine powder to be formed by repeated hydrogenation.
- **Thermal energy applications.** The reaction between hydrogen and the hydride forming alloy is exothermic. The coupling of the absorption-desorption cycles for two different hydrides can be used to transfer heat from a low temperature reservoir to a high temperature reservoir. This can be utilised in thermal energy applications such as heat storage, heat transport, heat pumps, and refrigerators.
- **Other thermal and/or mechanical processes** where heat or mechanical pressure repeatedly needs to be applied.

**Separation technology** The selective absorption of hydrogen in metals can be utilised in separation technology [51]:

- **The separation of hydrogen isotopes.** The absorption rates for hydrogen, deuterium and tritium are different for some hydride forming alloys (see Refs [17, 48, 52] for additional details).
- **Hydrogen separation and the purification of hydrogen;** for example membrane systems for the purification of reformed hydrogen (i.e. hydrogen separators, hydrogen recovery units, high-purity hydrogen generators, hydrogen purification units, see the paper by Sandrock [48] for additional details).
- **Hydrogen fixation.** Metal hydride forming alloys with low plateau pressures easily form hydrides and can therefore be utilised as hydrogen getters, moderators and shielding materials in nuclear reactors.

**Sensors** The temperature dependent equilibrium pressure can be utilised in sensors. The sensitivity area of the alloy used in the sensor is highly dependent on the plateau pressure and temperature (see also section 3.3.3). In practice, this translates into good possibilities for tailoring the sensors to their applications.

---

<sup>1</sup>HDDR: hydrogen-decomposition-desorption-recombination

- Temperature and pressure sensors. The equilibrium pressure for hydrogen increases as a function of temperature (see section 3.3.3). This can be utilised in fire sensors and thermometers.
- Hydrogen sensors. The lattice expansion of an alloy during hydriding can be useful when making tailored hydrogen sensors.
- Switchable optical devices, typically consisting of yttrium/yttrium hydrides. In these hydrides, the degree of transparency changes with the hydrogen content in the metal (please consult the paper by Griessen *et al.* [53] for additional details).

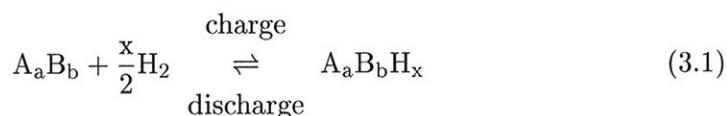
### 3.3 Hydrogen Storage

#### 3.3.1 Binary Metal Hydrides

Binary hydrides are formed by one element from the periodic table and hydrogen. Examples of binary hydrides are  $\text{MgH}_2$ ,  $\text{NiH}$  and  $\text{VH}_2$ . With a few exceptions, binary hydrides are either too stable or too unstable [41].

#### 3.3.2 Intermetallic Metal Hydrides

The metal hydrides of interest for energy storage are formed by a combination of elements in the side groups IIA to IVA in the periodic table. The intermetallic compounds forming hydrides of this type are of the composition  $\text{A}_a\text{B}_b$  where A is a strongly forming hydride element and B is a weakly hydride forming element. A general equation for the hydride formation is described by Eq 3.1.



Intermetallic compounds with formulas like  $\text{A}_2\text{B}$ ,  $\text{AB}$ ,  $\text{AB}_2$ ,  $\text{AB}_3$  and  $\text{AB}_5$  are the most interesting.

In table 3.1, some important hydride forming metals and intermetallic compounds are given [54]. As seen from the table the various compounds have their draw-

Table 3.1: *Some hydride forming metals and intermetallic compounds.*

Family	Model system	Hydride	Disadvantages
A	Magnesium	MgH <sub>2</sub>	Stable, mod. kinetics
AB <sub>5</sub>	LaNi <sub>5</sub>	LaNi <sub>5</sub> H <sub>6.5</sub>	Heavy, expensive
AB <sub>2</sub>	ZrMn <sub>2</sub> , TiMn <sub>2</sub>	ZrMn <sub>2</sub> H <sub>3</sub> , TiMn <sub>2</sub> H <sub>3</sub>	Stable, mod. kinetics
	ZrCr <sub>2</sub> , ZrV <sub>2</sub>	ZrCr <sub>2</sub> H <sub>3.8</sub> , ZrV <sub>2</sub> H <sub>4.9</sub>	Stable, mod. kinetics
AB	TiFe	TiFeH, TiFeH <sub>1.9</sub>	Difficult activation
A <sub>2</sub> B	Mg <sub>2</sub> Ni	Mg <sub>2</sub> NiH <sub>4</sub>	Stable, mod. kinetics
	Ti <sub>2</sub> Ni	Ti <sub>2</sub> NiH	Stable

backs. Several hydrides are too stable and have a too slow kinetics to be used for hydrogen storage applications. In table 3.2, the storage capacities of different metal hydrides are given. For comparison purposes, the hydrogen storage capacities of some other storage media are also given [13, 47].

Table 3.2: *The hydrogen content in different storage media.*

Medium	Density [g/cm <sup>3</sup> ]	N <sub>H</sub> , H-atoms per cm <sup>3</sup> · 10 <sup>-22</sup>	H content wt%
VH <sub>2</sub> (Metal hydride)	4.5	10.3	3.8
MgH <sub>2</sub> (Metal hydride)	1.4	6.7	7.6
Mg <sub>2</sub> NiH <sub>4</sub> (Metal hydride)	2.6	5.9	3.8
LaNi <sub>5</sub> H <sub>7</sub> (Metal hydride)	8.3	7.6	1.6
H <sub>2</sub> (g) (100atm)	8.2·10 <sup>-5</sup>	0.49	100
H <sub>2</sub> (l) (20K)	0.071	4.2	100
H <sub>2</sub> (s) (4.2K)	-	5.3	100
H <sub>2</sub> O, liquid	1.0	6.7	11.2
Ammonia, liquid	0.6	5.3	17.8

### 3.3.3 Pressure Composition Temperature Characteristics

Although the NiMH battery operates with potassium hydroxide electrolyte, much can be learned from studying the reaction of metals with hydrogen gas. Such

studies are always the starting point in the development of new alloys for hydrogen storage. A common method to characterize the properties of metal hydrides is by a graph in which the equilibrium hydrogen pressure ( $P$ ), is plotted as a function of hydrogen concentration ( $C$ ) and Temperature ( $T$ ). The graph reveals the so-called PCT properties of the metal hydride. An idealised version of a PCT diagram is shown in fig 3.2 [6, 54–56].

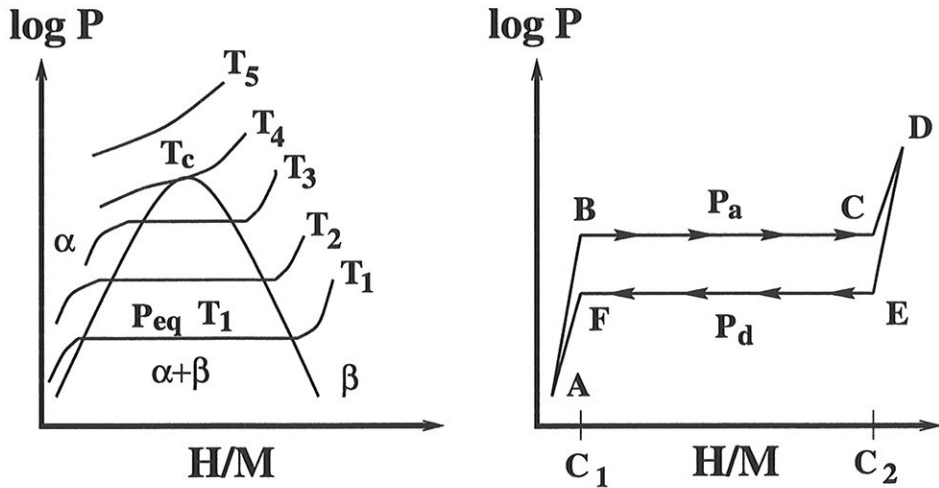


Figure 3.2: Schematic representation of pressure composition isotherms of metal-hydrogen systems ( $T_5 > T_4 > T_3 > T_2 > T_1$ ). The right side of the figure is showing absorption and desorption of hydrogen in a hydrogen storage alloy. A hydrogen absorption-desorption cycle goes in the sequence ABCDEF.

In the figure,  $P$  is the hydrogen equivalent pressure,  $H/M$  the hydrogen to metal ratio,  $\alpha$  the metal phase (with interstitial hydrogen),  $\beta$  the hydride phase,  $P_a$  the hydrogen absorption pressure, and  $P_d$  the desorption pressure. The curves in the figure are called pressure composition (PC) isotherms and give the equilibrium pressure-composition at a given temperature. At temperatures below the critical temperature,  $T_c$ , two-phase regions exist between the solid solution ( $\alpha$  phase) and the hydride ( $\beta$  phase). A two-phase region, as indicated in the figure separates these two regions. For temperatures higher than  $T_c$ , a two-phase region no longer exist. The PC isotherm delineate three distinct sections:

1. Initially the isotherm ascends fast (section A-B) as hydrogen enters the metal lattice and occupies interstitial positions, i.e. solid solution of hydrogen in the metal lattice. By convention, this metal/hydrogen compound is

called the  $\alpha$ -phase. The hydrogen is then dissolved interstitially [6]. Sievert's law [57] can often be applied to this particular section:

$$\frac{H}{M} = K_s \sqrt{P} \quad (3.2)$$

Here  $\frac{H}{M}$  is the hydrogen to metal ratio,  $K_s$  is Sievert's constant, and  $P$  is the equilibrium hydrogen pressure. When the hydrogen content in the metal increases, the hydrogen atoms interact (via the elastic strains introduced in the metal lattice) and the pressure/composition behaviour departs from ideality. This is reflected by a decrease in the slope of the isotherm compared to the ideal Sievert's law behaviour. However, there is a limit in the amount of hydrogen the  $\alpha$ -phase can store.

2. After the  $\alpha$  phase is saturated, a new phase, the hydride phase, ( $\beta$  phase) is starting to form. The saturation level in the  $\alpha$  phase is quite low. There is a discontinuity in the amount of hydrogen that the metal can store: the maximum hydrogen solubility in the  $\alpha$ -phase is  $c_1$  which is significantly lower than the minimum concentration ( $c_2$ ) which can be stored in the  $\beta$ -phase. Typically,  $(\frac{H}{M})_{c_1} < 0.1$  whereas  $(\frac{H}{M})_{c_2} > 1$ . The flat plateau region (section B-C) in the PCT curve corresponds to the coexistence of the  $\alpha$  and  $\beta$  phases. As more hydrogen enters the metal, the fraction of the  $\alpha$ -phase decreases whereas that of  $\beta$ -phase increases. According to Gibbs' phase rule, the equilibrium pressure ideally remains constant in the two-phase region [40, 50]. A possible strain term dependent on the hydrogen content,  $\zeta$ , can also, as suggested by Buschow [50] be added.

$$F = C - P + 2 \quad (+\zeta) \quad (3.3)$$

Here,  $F$  is the degrees of freedom,  $C$  the number of components, and  $P$  the number of phases. As there are three phases present, (i.e. gas phase, hydrogen in solid solution and the hydride phase) only one degree of freedom is left. With constant temperature, the equilibrium pressure ideally has to remain constant. This constant pressure is the plateau pressure of the alloy, and this pressure is highly temperature dependent [58].

3. At the end of the plateau, the entire metal/hydrogen alloy consist of only  $\beta$ -phase. To force more hydrogen into the alloy requires increasing the external gas pressure. This is represented by the rapid increase in the



equilibrium pressure in the C-D region of the PCT curve, indicating solid solution of hydrogen in the  $\beta$  phase [59].

To model the hydrogen absorption and desorption reactions, the shrinking core model is often assumed [60]. The shrinking core model for hydrogen absorption and for hydrogen desorption is illustrated in figures 3.3 (absorption) and 3.4 (desorption).

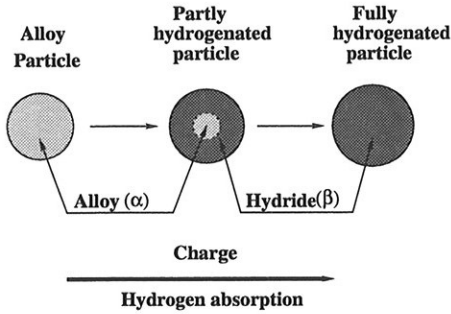


Figure 3.3: *Hydrogen absorption in a spherical shaped hydrogen storage alloy assuming the shrinking core model.*

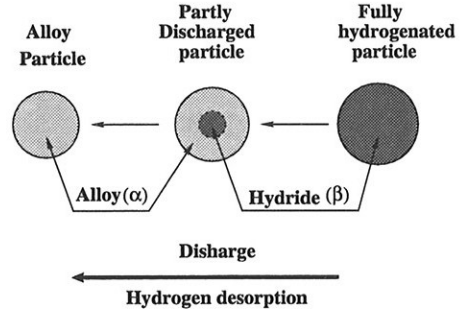


Figure 3.4: *Hydrogen desorption in a spherical shaped hydrogen storage alloy assuming the shrinking core model.*

In practice, the reversible hydrogen storage capacity equals the length of the plateau, and metal hydride hydrogen storage devices are operated in the cycle BCEF (figure 3.2).

The free energy change in the hydrogen absorption/desorption reaction is given by [61, 62]

$$\Delta G = \Delta G^\circ + RT \ln \left( \frac{a_{MH_x}}{(a_{H_2})^{\frac{x}{2}} a_M} \right) \quad (3.4)$$

Here  $\Delta G$  is the free energy change during hydrogen absorption,  $a_i$  the activity of compound  $i$ , and  $R$  and  $T$  the gas constant and the temperature, respectively. If the hydrogen absorption reaction is assumed to be in equilibrium, hydrogen behaves as an ideal gas, and both the metal phase and the hydride phase are in solid state, Eq 3.4 can be rewritten as:

$$\Delta G^\circ = RT \ln p_{H_2} \quad (3.5)$$

Here  $p_{H_2}$  is the equilibrium hydrogen pressure. The correlation between the free energy, the enthalpy, and the entropy is well known [62],

$$\Delta G^\circ = \Delta H^\circ - T\Delta S^\circ \quad (3.6)$$

Here,  $\Delta H^\circ$  is the change in the standard enthalpy, and  $\Delta S^\circ$  the change in the standard entropy during hydride formation. Then Eqs 3.4 and 3.6 can be combined to give the van't Hoff relation, Eq 3.7 [61].

$$\ln P_{H_2} = \frac{\Delta H^\circ}{RT} - \frac{\Delta S^\circ}{R} \quad (3.7)$$

The entropy and the enthalpy of the hydriding reaction can be found from a van't Hoff plot (see figure 3.5). The logarithm of the plateau pressure is plotted versus

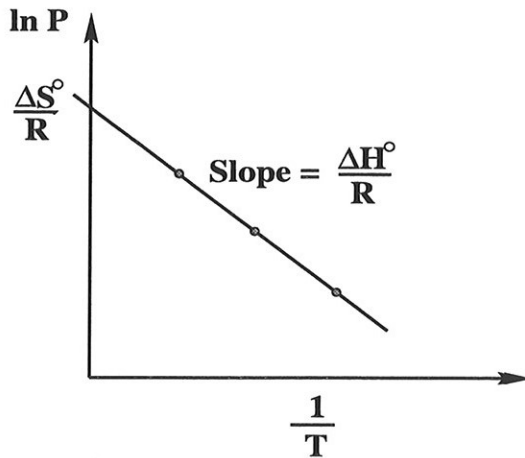


Figure 3.5: Van't Hoff plot for a hydrogen storage alloy where the slope is  $\frac{\Delta H^\circ}{R}$  and where the line crosses the ordinate axes at  $\frac{\Delta S^\circ}{R}$ .

the inverse of the temperature for different temperatures, and subsequently the entropy and the enthalpy are found by linear regression. The hydrogen absorbing reaction is exothermic and the desorption is endothermic. This is an important safety feature because in case there is ever a leak of hydrogen from a hydride hydrogen storage container, and the hydrogen catches fire, the endothermic behavior of the desorption reaction can extinguish the fire.

### 3.3.4 Hysteresis

Hysteresis is commonly observed in metal hydrides. The hysteresis,  $H(T)$ , is temperature dependent and is the logarithm of the ratio between the absorption

and desorption plateau pressure (figure 3.2), Eq 3.8:

$$H(T) = \ln \frac{P_a(T)}{P_d(T)} \quad (3.8)$$

Here  $P_a$  is the absorption plateau pressure and  $P_d$  is the desorption plateau pressure. Hysteresis is believed to be due to the presence of transformation strains during both hydride formation and decomposition. Hysteresis basically represents the conversion of work to heat, i.e. hysteresis must involve irreversible effects and therefore cannot be caused by elastic deformation. The process of accommodation (expansion of the lattice by as much as  $\sim 35\%$  ( $\sim 25\%$  for  $AB_5$  type alloys)) is reasonably represented by elastoplastic analysis. This analysis reveals that the plastic energy created in the metallic phase during the hydride precipitation and decomposition is the major contributor to the energy absorbed during lattice deformations [63]. This lattice deformation require a certain amount of energy which is not entirely recovered as the lattice contracts in desorption [64]. Hysteresis is a very important property and in almost all practical cases a minimum hysteresis is desired [46].

### 3.3.5 Plateau Sloping

Sloping plateaus are frequently observed in intermetallic compound hydrogen systems and can be described by:

$$Slope = \frac{d \ln P_d}{d(\frac{H}{M})} \quad (3.9)$$

The sloping can result from inhomogenities in the intermetallic compounds, but may have a more fundamental origin [64]. According to Gibbs' phase rule, Eq 3.3, the equilibrium pressure for the coexistence of two phases should be independent of the hydrogen concentration when the temperature is below the critical temperature,  $T_c$  (flat plateau). However, experimentally measured plateaus are usually sloping. A considerable part of this sloping results from measurements that have been taken at non-equilibrium conditions. The sloping plateaus could therefore be partly because of the same phenomena as the hysteresis (see section 3.3.4). On the other hand, true equilibrium plateaus also tend to show some sloping [54]. Sloping in alloys of the  $A_aB_b$  type where both A and B are single elements can result from either defects in the lattice or disorders in the atomic arrangement. This may create slightly different energy levels for crystallographic

identical interstitial sites. Increasing lattice strain could also increase the plateau sloping.

In multi component alloy systems the hydrogen pressure is known to increase rather steadily with the amount of hydrogen in the alloy. The reason for this is that element substitution (see sections 3.4.2 and 3.4.3) introduces elements with other properties into the structure. This may change the energy levels of the hydrogen sites in the lattice. New phases and sub phases with different energy levels for the hydrogen in the hydride phase may then appear.

### 3.4 Hydrogen Storage Alloys of the AB<sub>5</sub> Type

Studies of coercivity mechanisms in SmCo<sub>5</sub> permanent-magnet materials at the Philips laboratories in Eindhoven, Netherlands, led to the discovery of the favourable hydrogen sorption properties of the compound LaNi<sub>5</sub>. See the paper by Willems and Buschow [65] for a brief historical overview on this development. Both lanthanum and nickel are partly exchanged by other metals to improve the properties. Substitutional elements for the AB<sub>5</sub> system are treated in sections 3.4.2 and 3.4.3.

AB<sub>5</sub> type alloys, with the A-component being misch metal (a commercial mixture of rare earth elements: lanthanum, cerium, neodymium and praseodymium) and the B-component being nickel (with a variety of other metal additions, such as aluminium, manganese, cobalt, etc.) are widely used as negative electrodes in rechargeable NiMH batteries because of their beneficial kinetic properties, reasonable cost, and long cycle lives.

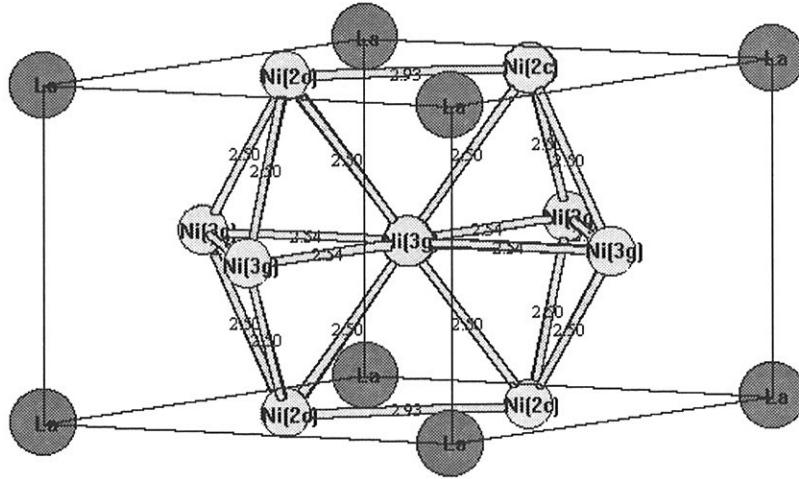
#### 3.4.1 Structure

AB<sub>5</sub> intermetallic compounds tend to crystallise into a hexagonal structure with the designations given in table 3.3 [66, 67].

In figure 3.6, the structure of LaNi<sub>5</sub> with atomic sites indicated is given. The lanthanum atoms occupy the basal plane (*1a*) sites. The nickel(*2c*) sites correspond to the nickel sites in the basal plane, whereas the nickel(*3g*) sites correspond to the nickel sites in the mid plane (The atom plane half way between the lanthanum and nickel(*2c*) sites) [68].

Table 3.3: *Structural designations of  $AB_5$  type compounds, different notations.*

Name	Value
Prototype	CaCu <sub>5</sub>
Pearson	hP6
Space group	P6/mmm (No 191)

Figure 3.6: *The structure of  $LaNi_5$  with indicated atomic sites.*

Two different methods for determination of structure parameters in hydrogen storage alloys are used, X-ray and neutron spectroscopy. These methods are described more in detail in appendix B, and the different features can be summarized as follows:

**X-ray diffraction spectroscopy.** Incoming coherent X-rays are reflected from each plane in the set of parallel planes, and the manner of the diffraction reveals the structure as described in the following section. The characteristic energy increases with increasing atomic number, making the detection of elements with high atomic numbers easy and the detection of elements with low atom numbers (for instance hydrogen) more difficult.

**Neutron diffraction spectroscopy.** By using neutron spectroscopy, the atom cores form the image. The scattering cross section varies independently of the atomic number. Deuterium (not hydrogen) is detected by neutron diffraction, which is extremely useful when determining the hydrogen sites in a metal hydride lattice.

The properties of the hydride phase is known to be strongly influenced by the properties of the corresponding metal phase. Lundin *et al.* [69] presented a general concept of the interstitial hole size, which describes correlations between the free energy of hydride formation and the radius of the tetrahedral hole for  $AB_5$  type hydrides.

Several groups [61, 70, 71] observed a linear relation between logarithm of hydrogen desorption pressure and the unit cell volume for B site substitution. It has been generally concluded that larger volume of the unit cell (resulting from the replacement of nickel by other elements) gives lower equilibrium plateau pressure of the alloy. It is generally adopted that an analogous relation between the unit cell size and the plateau pressure exists also for the A site substitution [6].

### 3.4.2 A Site Substitutional Elements

#### Rare earth element substitution

The A site substitution in  $AB_5$  alloys has one practical reason, namely the low cost of misch metal in comparison to the pure rare earth metals. However, variations in the misch metal composition (resulting from both the ore composition and the manufacturing technology) can result in a serious deterioration of the battery performance. These problems reflect also the economy of the misch metal production, dictated by a growing market for individual rare earth elements (for example: cerium as a catalyst in automotive applications or neodymium in permanent magnets). For these reasons, composition of the misch metal in the battery alloy needs to be adjustable, without sacrificing the electrode performance. Understanding and controlling the effects of rare earth composition is therefore crucial for the real-life performance of the batteries.

When misch metal based NiMH batteries were being developed, one decided to use the metallurgical grade misch metal as this was cheaper than lanthanum.

Since then, the development have mainly taken place using misch metal as the A component in the AB<sub>5</sub> alloy. The misch metal has a typical<sup>2</sup> composition of 20-30% lanthanum, 40-50% cerium, 10-20% neodymium and 5-10% praseodymium [6].

When lanthanum are substituted by other rare earth elements, a solid solution exists in the complete concentration range [68]. Characteristics of possible rare earth A site substitutional elements are given in table 3.4. In the table AW

Table 3.4: *Characteristics of possible rare earth A site substitutional elements.*

Element	AW [g/mol]	$\rho$ [g/cm <sup>3</sup> ]	T <sub>m</sub> [°C]	T <sub>b</sub> [°C]	V <sub>at</sub>	r <sub>cov</sub> [Å]	Structure
Lanthanum	138.9	6.17	920	3469	22.5	1.69	hexagonal
Cerium	140.1	6.67	795	3468	21	1.65	f.c.c.
Praseodymium	140.9	6.77	931	3127	20.8	1.65	hexagonal
Neodymium	144.2	7.00	1024	3027	20.6	1.64	hexagonal
Samarium	150.4	7.52	1072	1900	19.9	1.62	rhombohedr.

represents the atomic weight, T<sub>m</sub> the melting point, T<sub>b</sub> the boiling point, V<sub>at</sub> is the atomic volume and r<sub>cov</sub> the covalent radius. The data in the table are taken from Ref [72]. An increase in the hydrogen plateau pressure (see section 3.3.3) is observed, since the lattice shrinks when lanthanum is replaced by smaller elements.

Rare earth elements, replacing lanthanum in the LaNi<sub>5</sub> structure, substantially change the thermodynamic properties of the alloy. In particular, the equilibrium hydrogen pressure markedly increases as a result of the A site substitution with cerium, praseodymium or neodymium. Uchida *et al.* [73] studied various La<sub>1-x</sub>Re<sub>x</sub>Ni<sub>5</sub> systems (Re = cerium, praseodymium, neodymium, samarium) and found that cerium and samarium are increasing the equilibrium pressure of hydrogen most significantly. Suzuki *et al.* [74] elaborated additions of lanthanum to a cerium-rich misch metal, and concluded that lanthanum should be present in a relatively large amount (more than 30 %) to bring the plateau pressure down to a usable level. It was stressed that a too high plateau pressure (resulting from

<sup>2</sup>Commercial grade misch metal can also contain small amounts of other metals. The most common are some of samarium and/or iron.

high contents of cerium) causes decrease of the charge efficiency. On the other hand, Clay *et al.* [75] found that from the point of view of kinetics of hydrogenation, alloys containing cerium are the best. The authors formulated a qualitative relation for LaNi<sub>5</sub>-based alloys, indicating that "the reaction rate is inversely proportional to the hydride stability". This means that a higher plateau pressure (and consequently lower stability of the hydride), corresponds directly to better kinetics of hydrogenation. These apparently contradicting effects of the A site composition in LaNi<sub>5</sub>-based alloys underline the importance of optimization of the misch metal composition. One clear improvement resulting from the A site substitution is that the presence of neodymium or cerium enhances corrosion resistance of the alloys [6, 76, 77] (praseodymium was not included in this study).

Only a few studies on the misch metal composition have been published. The most comprehensive work regarding misch metal composition has been done by Liu and Huston [78]. They developed an empiric formula for the plateau pressure as a function of the misch metal composition for MmNi<sub>5</sub> alloys. The misch metal composition is limited by the following equation:

$$X_{\text{Ce}} + X_{\text{La}} + X_{\text{Pr}} + X_{\text{Nd}} = 1 \quad (3.10)$$

The desorption plateau pressure in absolute atmospheres at 25°C for an alloy of MmNi<sub>5</sub> ( $P_{e,25}$ ) can then be calculated [78]:

$$\ln P_{e,25} = 10.60 - 5.70X_{\text{Ce}} - 10.03X_{\text{La}} - 8.46X_{\text{Pr}} - 7.40X_{\text{Nd}} \quad (3.11)$$

And the hysteresis can be calculated [78]:

$$\ln \left( \frac{P_a}{P_d} \right) = 1.240 + 0.470X_{\text{Ce}} - 1.026X_{\text{La}} - 0.287X_{\text{Pr}} - 1.361X_{\text{Nd}} \quad (3.12)$$

In Eqs 3.10, 3.11 3.12,  $X_i$  is the weight fraction of element  $i$ . So far, there has been no convincing literature values with regards to the optimum misch metal composition.

### Non rare earth element substitution

Lanthanum can also be substituted with elements such as calcium from group IIA (see figure 3.1) or elements as hafnium and zirconium from group IVB. An overview of some of the properties of these elements are shown in table 3.5 [72].



Table 3.5: *Characteristics of possible non rare earth A site substitutional elements.*

Element	AW [g/mol]	$\rho$ [g/cm <sup>3</sup> ]	$T_m$ [°C]	$T_b$ [°C]	$V_{at.}$	$r_{cov}$ [Å]	Structure
Calcium	40.08	1.55	845	1420	29.9	1.74	f.c.c.
Hafnium	178.49	13.09	2222	5400	13.6	1.44	hexagonal
Zirconium	91.22	6.51	1852	3580	14.1	1.45	hexagonal

According to Jensen [40], calcium substitution is difficult because of the low boiling point of calcium compared to the rare earth metals and the B elements used. (Comparison data for calcium is given in table 3.5, the data for rare earth metals is given in table 3.4, and for B site substitutional elements is displayed in table 3.7). The evaporation of calcium during the alloy production stage makes it difficult to control the alloy composition.

Pure  $\text{CaNi}_5$  has the same  $\text{CaCu}_5$  type structure as  $\text{LaNi}_5$ , and stores even more hydrogen per unit weight than  $\text{LaNi}_5$  because of the considerably lower atomic weight for calcium compared to lanthanum. The problem is a poor cycle life because of calcium corrosion during repeated charge and discharge [40]. A partial substitution of lanthanum in  $\text{LaNi}_5$  by calcium will according to Li *et al.* [79] give the best properties with a stoichiometric content of calcium around 0.4.

### 3.4.3 B Site Substitutional Elements

In recent years, research on  $\text{AB}_5$  alloys has concentrated on modifying the alloy composition by alloying it with various elements. The purposes of these modifications were as follows:

1. Enhancement of the corrosion stability of the alloy, especially under electrochemical cyclic charging/discharging;
2. Decrease of the plateau pressures to enable the reversible charging at ambient conditions of pressure and temperature;
3. Increase of the hydrogen storage capacity; and

4. Increase of the rate at which the hydrogen can be stored or withdrawn from the alloy while maintaining satisfactory electrochemical parameters.

By looking at the structural data for deuterium  $AB_5D_x$  compounds [66, 80], one can see that for an  $AB_5$  type alloy, the differences in the lattice parameters for the hydrided (deuterided) compounds are smaller than for the unhydrided compound. If the lattice is pre-expanded by introducing substitutional elements prior to hydriding, the volume changes during hydriding will be lower. One of the main tasks of a substitution element is therefore to pre-expand the lattice prior to hydrogenation to minimize the lattice stress, decreasing the cracking of the alloy during cycling.

The substitution of nickel in  $LaNi_5$  or  $MmNi_5$  by a transition element leads to important modifications of the crystal structure. In table 3.6 a list of the electrochemical effects of various substitutional elements is given [6]. From the table it can be seen that the selection of substitutional elements is quite challenging, as none of the substitutional elements solely have positive effects.

In table 3.7 data for B elements in the  $AB_5$  system is displayed. The data in the table is taken from Refs [13, 72]. The table shows that there are a lot of possible candidates for B site substitution, which have a wide range of properties. All elements except for boron have a larger atomic volume than nickel, which lowers the plateau pressure for the alloy. According to Uchida and Kuji [81], the decrease is in the order manganese > aluminium > chromium > silicon > iron, zinc, vanadium > cobalt > copper. Compared to the information given in table 3.7, the correlation between the size of the substitution element and the plateau pressure is not unique even though the size of the element will give an indication on the plateau pressure. The hysteresis for  $MmNi_{4.7}Al_{0.3}M_{0.1}$  is reported to decrease in the following order for different M metals: zirconium > cobalt > chromium > titanium=vanadium > copper [82]. The increase in the cycle life is in the following order: chromium < cobalt < silicon [83].

### Single element effects

Below, the effects of B site substitution are given, with an emphasis on structural and kinetic properties. The diffusion properties are discussed in more details in section 3.9.

Table 3.6: *Effects of various alloying elements of a metal hydride electrode made of  $LaNi_{5-x}R_x$  (+, increase, 0 small effect, -, decrease).*

Alloy element	Max capacity	Plateau pressure	Cycle life	High rate properties	Initial activation
Boron	- -	0		+	+ +
Aluminium	-	- -	+	-	-
Silicon	- -	-	+	-	-
Titanium	- -	-	+	-	+
Vanadium	- -	-		+	
Chromium	- -	- -	+	-	
Manganese	+	- -	- -	+ +	+
Iron	-	-	+	-	
Cobalt	-	-	+ +	- -	- -
Copper	-	-	0	-	0
Zinc	-	-	0	-	0
Molybdenum	- -	0		+	+ +
Gallium				-	
Tin		-			

**Boron** is the only element featuring a smaller atomic volume than nickel, which is assumed to be the reason for the very small change in the plateau pressure when boron is substituted for nickel.

**Aluminium** decreases the plateau pressure. Aluminium also increases the temperature range in which the alloy can be used [31, 76, 84]. Aluminium replaces nickel only at the mid plane  $3g$  site [67], inducing a distortion of the  $D(2)$  hydrogen occupation site and a decrease in hydrogen storage capacity. Small amounts of aluminium reduces the volumetric expansion during hydriding considerably as well as the corrosion rate and the maximum storage capacity [85].

**Silicon** improves the melt spinning properties. Silicon tightens the oxide layer and improves the cycle life [86]. Moreover, the self-discharge rate is increased [31, 76, 84]. Silicon decreases furthermore the grain size. Silicon replaces nickel only at the  $3g$  site, causing a distortion of the  $D(2)$  hydrogen occupation site and a resultant decrease in the hydrogen storage

Table 3.7: Characteristics of possible B site substitutional elements.

Element	AW [g/mol]	$\rho$ [g/cm <sup>3</sup> ]	T <sub>m</sub> [°C]	T <sub>b</sub> [°C]	V <sub>at.</sub>	r <sub>cov</sub> [Å]	Structure
Boron	10.81	2.34	2100	2600	4.6	0.82	hexagonal
Aluminium	26.98	2.70	660.1	2467	10.0	1.18	f.c.c
Silicon	28.09	2.33	1410	2355	12.1	1.11	diamond
Titanium	47.88	4.51	1668	3260	10.6	1.32	hexagonal
Vanadium	50.94	6.11	1900	3000	8.35	1.22	b.c.c
Chromium	52.00	7.19	1875	2482	7.23	1.18	b.c.c
Manganese	54.94	7.43	1245	2150	7.39	1.17	cubic
Iron	55.85	7.87	1536	3000	7.1	1.17	b.c.c.
Cobalt	58.93	8.92	1495	2900	6.7	1.16	hexagonal
Nickel	58.69	8.91	1453	2730	6.6	1.15	f.c.c.
Copper	63.55	8.94	1083	2595	7.1	1.17	f.c.c.
Zinc	65.39	7.13	419.5	970	9.2	1.25	hexagonal
Germanium	72.61	5.32	938.3	28.20	13.6	1.22	f.c.c.
Gallium	69.72	5.91	29.78	2403	11.8	1.26	cubic
Molybdenum	95.94	10.22	2610	5560	9.4	1.30	b.c.c.
Indium	114.82	7.31	157	2072	15.7	1.44	tetragonal
Tin	118.71	7.29	232	2270	16.3	1.41	f.c.c.
Antimony	121.76	6.70	631	1587	18.4	1.38	trigonal
Bismuth	208.98	9.78	271	1564	21.3	1.46	monoclinic

capacity.

**Titanium** increases the cycle life, but decreases the maximum storage capacity and give inferior low temperature properties [31, 76, 84].

**Chromium** decreases the maximum storage capacity and improves the cycle life slightly [83].

**Manganese** yields better activation properties but decreases the cycle life [86].

The reason for this decrease assumed to be that manganese precipitates at the grain boundaries [87]. Manganese replaces nickel at the mid plane *3g* sites [67]. Manganese is believed to have certain catalytic properties, which accelerates the electrochemical discharge reaction at low temperatures by

promoting bulk diffusion of hydrogen at low temperatures and by catalysing the reaction of hydrogen and hydroxyl ions at the alloy surface [88].

**Iron** can replace nickel at the  $2c$  site. Iron substitution for nickel in  $\text{LaNi}_5$  does not increase the electrochemical cycle life, but a combination of iron and aluminium does [89]. This is also the case for a combination of iron and cobalt [90]. This allows cost reductions of the NiMH cells without affecting the performance of the alloy [91].

**Cobalt** expands the unit cell in the  $c$  axis direction [92]. Cobalt has a preference for the  $3g$  site in the lattice, but can also occupy the basal plane  $2c$  sites [67]. The latter occurrence might be part of the reason that two plateaus are observed in cobalt containing compounds. The electrochemical cyclic durability is improved without considerable decrease in the discharge capacity [85, 92, 93]. This stabilises the resulting hydride. The use of cobalt also results in inferior high-rate dischargeability and catalytic activity for the hydrogen electrode reaction [92, 94].

**Copper** is one of the few elements that can replace nickel at the  $2c$  site.

**Molybdenum** precipitates at the grain boundaries, forming  $\text{MoCo}_3$  in overstoichiometric  $\text{AB}_5$  type compounds containing cobalt [95]. The  $\text{MoCo}_3$  improves the kinetics considerably [95].

**Germanium** The electrochemical properties of the germanium-substituted alloys show similar trends as the tin-substituted alloys [96], but with more favourable kinetics at high substitutions [97].

**Tin** increases the unit cell volume and reduce the plateau pressure [98]. Tin furthermore replaces nickel at the  $3g$  site [99]. Small additions of tin improves the performance of the metal hydride alloy anode in terms of cycle life, capacity and kinetics [100, 101]. Tin containing  $\text{AB}_{5+x}$  type unstoichiometric alloys have shown very good characteristics for use in battery applications.

### 3.5 Hydrogen Storage Alloys of Other Types than the $\text{AB}_5$

Several types of metal hydrides with different characteristics exists. This section is intended to give a short overview of these alloys, as a complete review is beyond

the scope of this thesis. The main motivation for the desire to replace the  $AB_5$  type hydrogen storage alloy in NiMH batteries is to obtain higher energy storage densities. As seen from table 2.1, the lithium based batteries have a considerably higher storage density than the  $AB_5$  based NiMH batteries. By replacing the  $AB_5$  type hydrogen storage alloy with an alloy with higher storage capacity, a NiMH battery with a higher storage density can be obtained. A lower discharge capacity at high current densities, i.e. poorer kinetics is, however, as well observed for most alternative alloy systems. In figure 3.7, a pie diagram showing the most important contributions to the weight of a NiMH battery is given [21]. From the

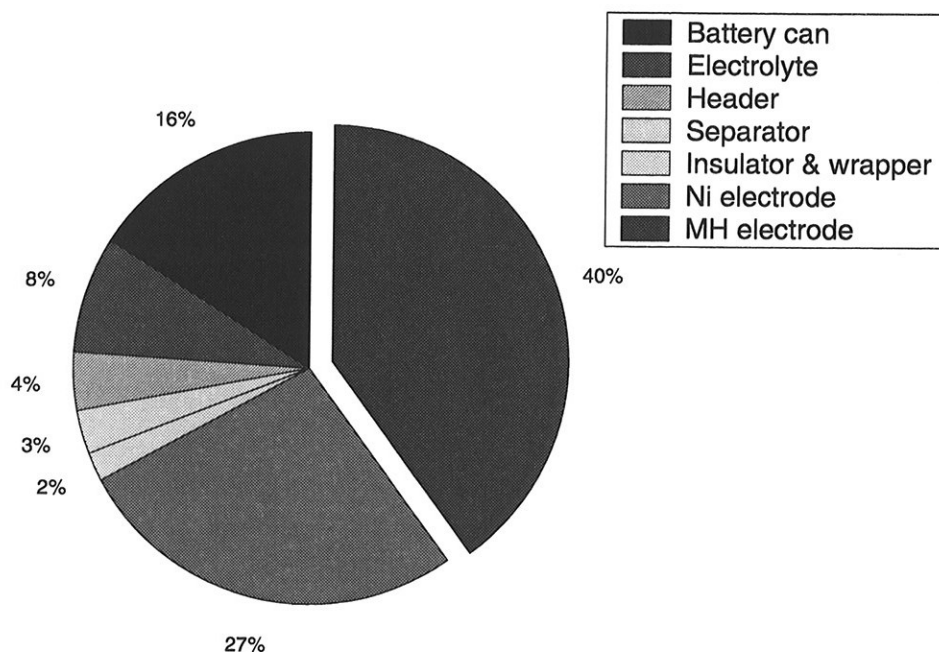


Figure 3.7: Pie diagram showing the most important contributions to the weight of a NiMH battery. The metal hydride electrode is emphasized. The legend labels are ordered counterclockwise, starting on top.

figure, it is visible that the largest contributor to the weight of the battery is the MH electrode. An improvement in the storage capacity of the MH alloy is therefore very beneficial for the battery energy density. In Figure 3.8, a prediction showing the correlation between an increase in the discharge capacity of the metal hydride alloy and the discharge capacity of a battery cell is shown. The figure is

adapted from Zhang [87].

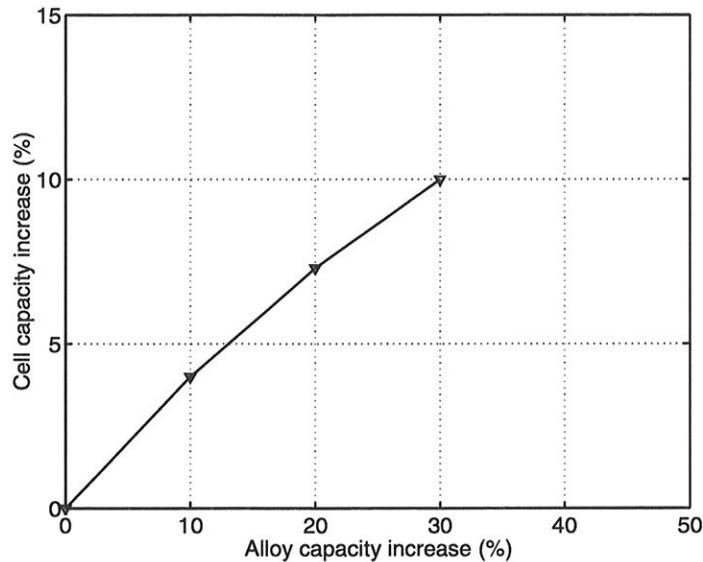


Figure 3.8: *A prediction showing the correlation between increase of the discharge capacity of the metal hydride alloy and the increase of the discharge capacity of a battery cell.*

The reason why the correlation shown in Fig 3.8 is not linear, is that other parts of the cell also contribute to the cell weight. If the capacity of the MH electrode is increased, the capacity of the counter electrode also needs to be increased.

### 3.5.1 Hydrogen Storage Alloys of the $AB_2$ Type

The  $AB_2$  intermetallic system is of great interest since it possesses a higher energy density than the  $AB_5$  system. Besides  $AB_5$  type intermetallic compound, only the  $AB_2$  type has reached commercialization in rechargeable batteries. The  $AB_2$  alloys have a higher storage capacity and a plateau with a higher slope than the  $AB_5$ , and are known to have slower kinetics. Its kinetic properties have been an obstacle to major commercial exploitation. See Refs [102, 103] for additional examples regarding the properties of  $AB_2$  type alloys.

### 3.5.2 Magnesium Based Hydrogen Storage Alloys

Magnesium and magnesium-based alloys are amongst the most attractive materials for hydrogen storage, since their hydrogen storage capacity exceeds all known reversible metal hydrides. Magnesium forms a hydride,  $\text{MgH}_2$ , which contains nominally 7.6 wt% of hydrogen [47, 104].

Magnesium also has a favourable low cost; suggesting an excellent potential for hydrogen related applications. However, to date magnesium hydride tends to be of no practical use for hydrogen storage, neither as hydrogen storage media nor as electrode material in NiMH cells.

The main reason for this is pointed out in table 3.1: the hydride phase is too stable and the kinetics is too slow. Gas storage application at room temperature is therefore not an option for magnesium based alloys. When the temperature increases, the plateau pressure in the alloy increases, and by increasing the temperature, there are good possibilities for using magnesium based materials for hydrogen gas storage. The hydrogen diffusion in magnesium based hydrogen storage alloys is also considerably lower than that for the  $\text{AB}_5$  system. This requires special attention as well. The solution is often to apply material with a very fine grain structure, minimising as such the diffusion path.

To improve the kinetics, there are several options. One can apply very fine grains to maximise the grain border area to compensate for the low specific reactivity, or improve the kinetics by catalysts or surface treatment.

To prepare the required grain structure of magnesium based compounds, ball milling or solid state reactions are often applied (see Refs [40, 104, 105] for additional details about the preparation of magnesium based alloys, and for additional details regarding magnesium based alloys as hydrogen gas storage materials, please consult the paper by Zaluska *et al.* [104]).

For the use of magnesium based alloys in electrochemical applications, magnesium based alloys exhibit a very low open circuit potential because of their low plateau pressure (see section 5.1.2 for additional details). On the other hand, very high theoretical discharge capacities are found for the magnesium base alloys, indicating a very large potential for applications requiring high specific energy storage capacities and low currents. The cycle life for magnesium based alloys has mainly been reported to be quite low, with some exceptions [106]. (For additional details



regarding the electrochemical applications, see Refs [107–109].)

### 3.5.3 Other Hydrogen Storage Alloys

Numerous possible alloy combinations allow for the storage of notable amounts of hydrogen. Among the first intermetallic hydride compounds was the FeTi system discovered at Brookhaven in the 1960s. Demonstration systems using FeTi for hydrogen storage have been built. Prior to the misch metal based AB<sub>5</sub> systems, the FeTi system was the lowest priced when compared to other hydrogen storage alloys, whereas today its price is comparable to the AB<sub>5</sub> system (for additional information regarding the FeTi systems, please consult the paper by Reilly [52]). The FeTi system can also be combined with magnesium based compounds [110].

Other actual and interesting alloys are combinations of titanium, vanadium, magnesium and nickel. An example the TiNi system described by Wang *et al.* [111, 112]. Solid solution alloys (storage in  $\alpha$  phase) [113] is another type of hydrogen storage alloys. The complex hydrides exhibit features very promising for hydrogen storage.

## 3.6 Charging of of Hydrogen Storage Alloys

Hydrogen storage alloys might be charged both from the gas phase and by an electrochemical process. The total mechanism is different since the interfacial steps are different. The steps taking part in the bulk phase are the same, however.

### 3.6.1 Gas Phase Charging Mechanism

The absorption and desorption of hydrogen by a metal involves a number of important steps. For the hydrogen absorption process these include:

1. Transport and adsorption of molecular hydrogen onto the metal surface.



2. Dissociative adsorption of molecular hydrogen into atomic hydrogen at the surface.



3. Transfer of atomic hydrogen through the surface layer, Eq 3.18.

A more detailed description is given in Refs [54, 114]. When the hydrogen is transferred into the lattice, the same reaction path as for hydrogen absorbed by an electrochemical reaction (section 3.6.2) is followed.

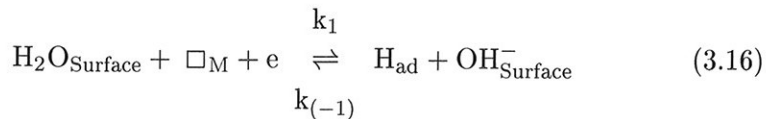
### 3.6.2 Electrochemical Charging Mechanism

The absorption and desorption of hydrogen by a metal involves a number of steps. For the charging (absorption) process these include:

1. Transport of  $\text{H}_2\text{O}$  molecules to the electrode surface.



2. A Volmer reaction, i.e. charge transfer and adsorption of hydrogen atoms at an active site,  $\square_M$ , on the surface.



Here  $\text{H}_{\text{ad}}$  is adsorbed hydrogen and  $\square_M$  is an active site at the surface of the hydrogen storage alloy. The  $\text{OH}^-$  ions are then transported away from the surface:



The Volmer reaction can be either uniform or catalytically enhanced, and in the latter case the reaction takes place only on designated active surface sites. An illustration of the transport of  $\text{H}_2\text{O}$  molecules to the electrode surface and the displacement of  $\text{OH}^-$  molecules away from the surface and the Volmer reaction (Eqs 3.15, 3.16 and 3.16) is given in figure 3.9

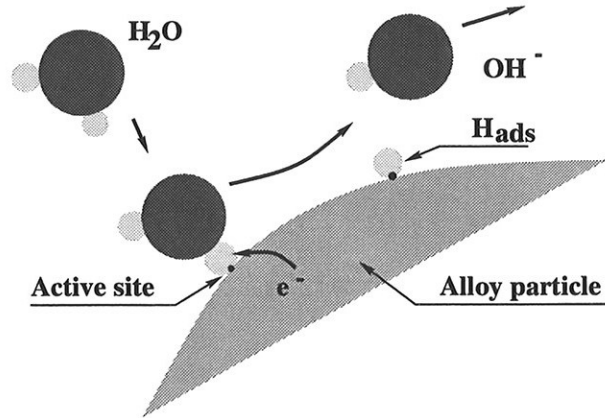


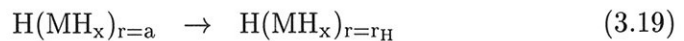
Figure 3.9: An illustration of the transport of  $H_2O$  molecules to the electrode surface and transport of  $OH^-$  molecules away from the surface and the Volmer reaction (Eqs 3.15, 3.16 and 3.16).

3. Transfer of atomic hydrogen through the interface forming interstitial hydrogen in the metal lattice:



Here  $\square_i$  is an empty interstitial hydrogen position.

4. The interstitial hydrogen then diffuses through the  $\beta$  phase and to the interface between the  $\beta$  and  $\alpha$  phase where the hydride phase is formed (figures 3.3 and 3.10).



Here  $r_H$  is radius of the reaction zone for hydride formation and  $a$  is the radius of the metal hydride particles.

5. Nucleation and growth of the hydride phase in the bulk, Eq 3.21



During growth of the hydride  $\beta$  phase, there is a hybridization between the electron orbitals of the hydrogen atom going in and the electron orbitals

of the metal atoms. New electronic states below the Fermi level are also formed and according to Switendick [115], a partial transfer of the  $s$  electron is taking place.

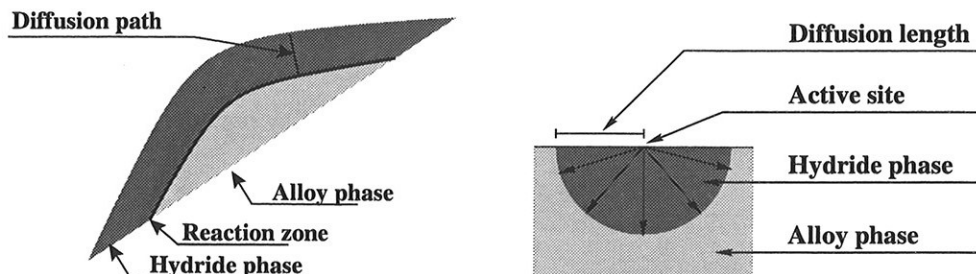


Figure 3.10: Diffusion of hydrogen through the bulk (Eq 3.20). Left: assuming uniform Volmer reaction (Eq 3.16), i.e. shrinking core model, Right: assuming localized Volmer reaction and low density of catalytic surface sites.

The phase changes (see section 3.3.3) which occur during this reaction are identical to those that take place in the gas phase hydrogen storage [30, 116]. Hydrides will initially be formed in the surface layer, and subsequently hydrogen atoms are transported through this hydride layer. The hydrogen desorption can be regarded as the reverse process.

Although the initial properties of metal hydrides formed by either electrolytic or gas charging are similar, hydrogen storage alloys used as electrodes in batteries have a much shorter life time, since they are exposed to a corrosive environment. The rate controlling mechanism may therefore not necessarily be the same as for gas phase absorption and desorption.

A side reaction for both the electrolytic and the gas phase absorption is the recombination of adsorbed hydrogen to form gaseous hydrogen. During the electrochemical charging of metal hydride electrodes at high current densities and especially for nearly fully charged electrodes this process will be more prevalent.

### 3.7 Deterioration from Crack Formation

Along with the equilibrium pressure and hydrogen storage capacity, corrosion resistance (expressed by cycling stability) is one of the basic properties of the

electrode materials. Cycling stability is generally related to two main features: chemical properties of the electrode (surface activity, oxidation and passivation, see section 3.8) and "intrinsic" mechanical properties (volume changes upon hydrogenation, which may cause formation of cracks in the alloys during cycling and in consequence faster corrosion). Because the electrolyte forms an oxide layer on each new surface, eventually a large amount of the alloy become oxidized, reducing the storage capacity [117]. An increase in the temperature results in an increase in the deterioration rate [118]. In this section the focus is on the crack formation problems only, and it is tried to relate them to the structure changes resulting from substitution. However, it needs to be stressed that chemical properties of the surface may be often dominant, and cannot be neglected in the final determination of the electrode performance.

The process of crack formation is related to the volume changes ( $\Delta V/V$ ) resulting from introduction of hydrogen into the  $AB_5$  structure. In general, the smaller the volume expansion (and in consequence less cracking) the higher the resistance to corrosion [6, 65, 119].  $LaNi_5$  exhibits very poor performance in regard to corrosion, because of the large lattice expansion upon hydrogenation. Substitution can reduce the volume changes, and therefore multicomponent  $AB_5$  alloys are more resistant to corrosion than  $LaNi_5$ . Substitution with cobalt is especially effective [66, 93]. In the paper of Adzic et al. [93] it is shown that the reduction of volume changes is directly related to the amount of cobalt in the alloy. In another paper, Züttel *et al.* [90] confirmed the general tendency of cobalt to reduce the volume expansion, but the relation between cobalt content and corrosion resistance was not so straightforward. Similar results have been reported for tin, which was also reported to be able to reduce volume expansion of the alloys [99].

It is still not clear however why certain additions are able to substantially reduce the volume changes caused by hydrogenation (cobalt or tin), and others change it to a lesser extent (as for example aluminium or manganese) and some have no effect at all (copper, zinc). In general, a smaller relative volume expansion ( $\Delta V/V$ ) could be expected for alloys having expanded unit cell (i.e. with the larger unit cell volume,  $V_{uc}$ ). This is however not always true. Although most "anti cracking" additions indeed increase the volume of the unit cell (as a result of the B site substitution with atoms larger than nickel), there exist alloys which are very resistant to cracking and corrosion and at the same time they have significantly reduced unit cell volume (for example alloys with rare earth additions or misch metal). In fact, the best electrode materials can be found equally

amongst the alloys with large unit volumes (e.g.  $\text{La}_{0.92}\text{Ni}_{4.6}\text{Sn}_{0.30}$ ;  $V_{uc} = 89.646 \text{ \AA}^3$ , [99]) and with small unit cell volumes (e.g.  $\text{MmNi}_{4.6}\text{Al}_{0.4}$ ;  $V_{uc} = 85.2653 \text{ \AA}^3$ , [61]).

### 3.7.1 Structural Anisotropy

In an attempt to find a universal correlation between the structure of the multicomponent  $\text{AB}_5$  alloy and its corrosion resistance (i.e. small  $\Delta V/V$ ) various structure parameters of the alloys were analysed in relation to the relative volume changes during charging. An interesting correlation has been found for the data from Adzic *et al.* [93], Vogt *et al.* [99] and Willems [66], as shown in figure 3.11.

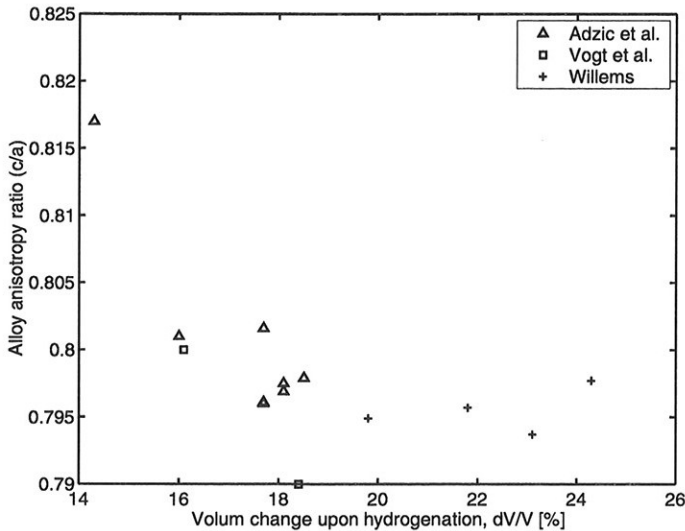


Figure 3.11: The volume changes upon hydrogenation plotted versus the anisotropy ratio of the hexagonal unit cell of the  $\text{AB}_5$  type structure.

The volume changes upon hydrogenation are plotted versus anisotropy ratio of the hexagonal unit cell of the  $\text{AB}_5$  type structure. The anisotropy ratio is defined as a lattice parameter ratio:  $c/a$ , and the ratios used in figure 3.11 are calculated from the  $a$  and  $c$  values listed in Refs [66, 93, 99]. The plot indicates that volume changes *can* be actually correlated with the anisotropy ratio, showing that smaller

volume changes occur when the anisotropy factor is high. Interestingly, the relation includes a variety of alloys with the following additions: cobalt, manganese, aluminium, tin, misch metal, and also non-stoichiometric compositions. One experimental point in the paper by Adzic *et al.* [93], has been omitted in figure 3.11, because of its inconsistency with the volume/corrosion relation. For this alloy ( $\text{MmNi}_{4.3}\text{Mn}_{0.4}\text{Al}_{0.3}$ ), the observed large volume changes did not actually lead to the expected fast corrosion. This fact can be explained by some inaccuracy in the volume change determination for this particular alloy, because on the other hand the alloy exhibited a high structure anisotropy, being consistent with its reported relatively high corrosion resistance.

There exist much more data in the literature indicating that anisotropy can be indeed crucial for the cycling stability of the electrode materials. The best commercial alloys (often with numerous components) always appeared to exhibit a  $c/a$  ratio higher than 0.8, as exemplified in Table 3.8. In contrast,  $\text{LaNi}_5$  has a

Table 3.8: *Anisotropy in various electrode alloys.*

Alloy	$c/a$	Reference
$\text{MmNi}_{3.55}\text{Co}_{0.75}\text{Mn}_{0.4}\text{Al}_{0.3}$	0.817	[93]
$\text{LaNi}_5\text{Sn}_{0.33}$	0.802	[99]
$\text{MmNi}_{4.6}\text{Sn}_{0.4}$	0.8108	[61]
$\text{MmNi}_{4.2}\text{Al}_{0.8}$	0.8143	[61]
$\text{LaNi}_5\text{Cu}$	0.808	[120]

ratio of  $c/a$  equal to only 0.7939.

The concept that corrosion resistance could be related to the anisotropic volume expansion of the  $\text{AB}_5$  type of structure has been previously discussed by Notten *et al.* [119, 120] for non-stoichiometric alloys, and also by Meli *et al.* [121] in the case of substitution of nickel by silicon. It was found that an excess of B-element (nickel or copper) leads to an anisotropic deformation of the unit cell ( $a$  parameter decreases and  $c$  parameter increases), which leads to higher catalytic activity and longer cyclic life of the alloys [95, 119, 122]

An interesting illustration of the correlation between anisotropy and corrosion can be found in the paper by Chen *et al.* [123]. The authors showed that annealing of the alloys leads to a significant improvement of the corrosion resistance. This oc-

curs, however, only for the alloy compositions where an increase of the anisotropy is induced as a result of annealing. This anisotropy change can be clearly seen in the plots illustrating the changes of  $a$  and  $c$  at various temperatures. At certain temperature  $c$  starts to increase and  $a$  to decrease, consequently increasing the anisotropy, which is accompanied by the improved corrosion resistance for these alloys.

In this section it is postulated, however, that the relation between structural anisotropy and corrosion resistance is more universal, and includes not only the non-stoichiometric alloys, but also the A site and the B site substitution. In consequence, standard X-ray diffraction measurements can be very useful in predicting corrosion resistance of the alloys, and the optimization of the alloy composition (in particular replacing cobalt by less expensive additions) could be performed through a combination of various components leading to higher anisotropy of the structure.

### 3.8 Surface Properties for $AB_5$ Type Alloys

Intermetallic compounds often show highly reactive surfaces even after exposure to oxygen or other contaminants. This is due to a reorganisation of the surface [54]. This type of surface property is an intrinsic alloy property, which indicates that surface segregation can be caused by the selective oxidation of certain elements in the alloy.

A poor specific catalytic activity can to some extent be compensated by increasing the total surface area. The latter solution has one drawback though, as also an increased surface is exposed to corrosion. For a more comprehensive treatment of surface properties, see also the paper by Schlapbach [124].

#### 3.8.1 A Site Elements in Reducing and Alkaline Media

If a reducing and alkaline media is assumed<sup>3</sup>, A site elements form hydroxides [24]. When  $LaNi_5$  is exposed to a strong aqueous alkaline electrolyte such as

---

<sup>3</sup>Alkaline electrolyte is applied in NiMH batteries (see section 2.2.3). During electrochemical measurements on metal hydride electrodes, normal potentials are in the range of -0.500 to -1.200V versus the standard hydrogen electrode (SHE) (see sections 5.3.2 and 5.4.1).



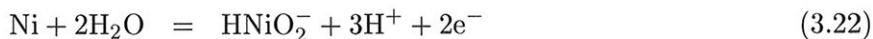
potassium hydroxide at a potential more positive than approximately -2.8V versus SHE,  $\text{La}(\text{OH})_3$  is formed on the surface [6]. For misch metal based  $\text{AB}_5$  type compounds, neodymium and praseodymium will form hydroxides of the  $\text{Re}(\text{OH})_3$  type<sup>4</sup>, whereas cerium forms  $\text{Ce}(\text{OH})_4$  [125] or  $\text{CeO}_2$  [24]. Cerium is the second and most reactive member of the lanthanides. It is very electro-positive and has a predominantly ionic chemistry. (see Refs [126, 127] for additional details concerning the role of cerium in aqueous electrolytes).

The lanthanide hydroxides are non-amphoteric compounds, stable in alkaline solutions and unstable in acid solutions [24]. A nickel enrichment in the surface layer can be observed during charge discharge cycling, attributed to the oxidation or the rare earth compounds (see Refs [124, 128]).

It is also well known that selective corrosion of calcium improves the kinetics in calcium based  $\text{AB}_5$  type alloys.

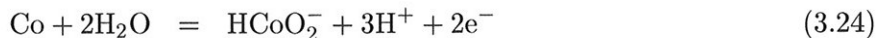
### 3.8.2 B Site Elements in Reducing and Alkaline Media

The most common B site elements are nickel, cobalt, aluminium and manganese. In reducing and alkaline media, B site elements can form hydroxides [24]. Nickel can form nickelite ions,  $\text{HNiO}_2^-$ , according to



$$E^\circ = 0.648 - 0.0886pH + 0.0295 \log[\text{HNiO}_2^-] \quad (3.23)$$

By assuming equilibrium concentration of  $\text{HNiO}_2^-$  on the electrode surface, nickel can form  $\text{HNiO}_2^-$  at more positive potentials than -0.76V versus SHE in 6M potassium hydroxide electrolyte. Cobalt can form dicobaltite ions,  $\text{HCoO}_2^-$ , according to



$$E^\circ = 0.659 - 0.0886pH + 0.0295 \log[\text{HCoO}_2^-] \quad (3.25)$$

By assuming equilibrium concentration of  $\text{HCoO}_2^-$  on the electrode surface, cobalt can form  $\text{HCoO}_2^-$  at potentials more positive than -0.45V versus SHE in 6M potassium hydroxide electrolyte.

---

<sup>4</sup>Re= Rare earth metal.

In reducing and alkaline media at potentials more positive than approximately  $-2.5\text{V}$  versus SHE, aluminium decomposes water with the evolution of hydrogen to form  $\text{AlO}_2^-$  [24].

Manganese is also thermodynamically very unstable in the presence of water. It tends to react slowly with water with the evolution of hydrogen [24]. Manganese forms  $\text{HMnO}_2^-$  at potentials more positive than approximately  $-1.6\text{V}$  versus SHE [24]. Both hexavalent and heptavalent oxidation states can be observed in strong alkaline electrolytes [24].

### 3.8.3 Surface Treatment and Coating

In order to improve both kinetics and cycle life of metal hydride electrodes, various surface modification techniques have been developed:

- Metal coating or micro encapsulating. Micro encapsulating the hydrogen storage alloy with metals, such as nickel [129–131], copper [132–135], palladium [136–138] and cobalt [138, 139] are all reported to improve the properties of metal hydride electrodes. According to Nan *et al.* [140], the coating only improves the initial performance of the electrodes whereas the long term stability is more dependent on the alloy bulk properties.
- Fluorine treatment. Fluorine treatment of alloys is not a metal coating, but fluorine compounds will be formed at the surface. The inventors of this method [141–144] claim that the fluorinated alloys exhibit improved characteristics as: ease of activation, strong resistance against air and gaseous impurities, possibilities for storing the alloys in air or water for a long time.
- Oxidising agents. Treatment of the surface with an alkaline solution with oxidizing agents is reported to improve the kinetics of metal hydride electrodes because of selective corrosion of rare earth metal in the surface, resulting in a nickel enrichment. A  $\text{KOH-H}_2\text{O}_2$  solution has been proven to be very efficient to enhance the activation [145].
- Reducing agents. The surface can also be reduced, leaving a very active surface. A solution of  $\text{KOH-KBH}_4$  was reported to produce a nickel rich surface layer with a high electrocatalytic activity for the electrode reaction for  $\text{Mm}(\text{Ni},\text{Mn},\text{Al})_5$  [146]. The reason for the increase in the electrocatalytic

activity was assumed to be preferential dissolution (i.e. selective corrosion, see section 3.8.2) of manganese and aluminium.

### 3.8.4 Activation

During activation of a metal hydride electrode by cyclic charging and discharging, both the specific discharge capacity and the catalytic properties are increased. Furthermore, there is a repeated crack formation and also an oxidation process going on, resulting in an increase in the total surface area [118]. In the case of  $\text{LaNi}_5$  selective oxidation and removal of lanthanum forms nickel precipitates on the surface [124]. The removal of surface oxides and hydroxides causes a surface enrichment of nickel and a depletion of lanthanum and other rare earth metals in the surface layer [124, 128].

The activation rate will increase with temperature [118] and, is also highly dependent on the plateau pressure of the alloy (see sections 3.3.3 and 5.1.2) as an alloy with a too low plateau pressure will exhibit slow activation<sup>5</sup> [6].

### 3.8.5 Self Discharge

If the plateau pressure (see section 3.3.3) is higher than one atmosphere or the plateau is steep, hydrogen will escape from a fully charged electrode. This will lead to a self-discharge of the battery. The relatively high self-discharge of the metal hydride electrode (see table 2.1) has been a major obstacle for using NiMH batteries as a back up power source, but it can be diminished by applying different principles:

- Designing alloys with a flat plateaus and low plateau pressures [147] (see section 3.3.3).
- Applying hydrogen impermeable separators. The application of hydrogen impermeable separators could stop the self-discharge [147], but oxygen must be allowed to pass through the membrane to prevent the deterioration of the internal over-charge protection (see section 2.2.3). Since the oxygen

---

<sup>5</sup>This observed slow activation process might very well be a result of a lower open circuit potential, shortening the time before the discharge potential reaches the cut off potential (see section 5.1.2 for additional details).

molecule is considerably larger than the hydrogen molecule, this might be difficult in practice.

- Copper micro encapsulation of the alloy is reported to reduce the self-discharge rate [147].
- In a battery, self-discharging can also be enhanced by the separator. In fact, the separator is very important in maintaining the long-term characteristics which includes the resistance to oxidation and a low self-discharge rate. The present separators contain nitric compounds, and self-discharging can be caused by repeated oxidation and reduction of  $\text{NO}_3^-$  ions that have migrated into the electrode. More recent studies indicate that nitrate ions are reduced very fast at a charged MH electrode [21].

### 3.9 Diffusion in Metal Hydrides

The diffusion in  $\beta\text{-LaNi}_5$  is strongly dependent on the temperature and can be approximated by the Arrhenius equation [148].

$$D = D_0 e^{-\frac{E_a}{RT}} \quad (3.26)$$

Here  $E_a$  is the activation energy for diffusion. According to Buschow [50], the assumption of single thermal activated diffusion process in the  $\text{AB}_5$  type hydride is an oversimplification. The hydrogen motion in the  $\text{LaNi}_5$  hydride is rather complicated and involves at least two different diffusion processes with activation energies differing by more than a factor of two. The diffusion process can be associated with the possible movement of hydrogen which involves the crossing of several potential wells of different depths. This is highlighted by the fact that in a  $\text{LaNi}_5$  deuteride, the deuterium atoms occupy more than one interstitial lattice position. These lattice positions are interconnected by a multitude of different jump paths. Further experimental evidence suggest that the analysis of the diffusion related movements in terms of a simple Arrhenius type of activation is not sufficient and can be associated with the fact that for a number of hydrides, the activation energy,  $E_a$ , cannot be taken as temperature independent [50]. For a more detailed explanation, see also the paper by Richter *et al.* [149].

### 3.9.1 State of Charge Dependency of the Apparent Diffusion Coefficient

According to the model developed by Wicke and Brodowsky [150] which was refined by Feldberg and Reilly [151], the diffusion coefficient is dependent on a thermodynamic factor,  $g(\theta_H)$

$$D_{H,\text{measured}} = D_H g \theta_H \quad (3.27)$$

where  $D_{H,\text{measured}}$  is the experimentally determined diffusion coefficient of hydrogen atoms in the metal at a given composition assuming Fickian diffusion;  $D_H$  is the "true" diffusion coefficient of hydrogen atoms in the metal. The hydrogen state of charge,  $\theta_H$  is defined by:

$$\theta_H = \frac{c_H}{c_{H,\text{max}}} \quad (3.28)$$

The thermodynamic factor,  $g(\theta_H)$  can be expressed as follows

$$g(\theta_H) = \frac{d \ln[ a_H ]}{d \ln[ \theta_H ]} = \frac{1}{2} \frac{d \ln[ f_{H_2} ]}{d \ln[ \theta_H ]} \quad (3.29)$$

Here  $a$  is the activity and  $f$  the fugacity. Eqs 3.27 to 3.29 indicates that the true diffusion coefficient is independent on the state of charge, whereas the measured diffusion coefficient decreases with decreasing hydrogen content.

According to the data listed by Richter *et al.* [149], the diffusion coefficient for hydrogen is higher<sup>6</sup> for the  $\beta$  than the  $\alpha$  phase. This is a quite an important finding, since the formation of a hydride phase will not slow down diffusion of hydrogen. It may also be mentioned that for microcrystalline  $\text{LaNi}_{3.94}\text{Si}_{0.54}$  films and also for  $\text{LaNi}_{4.15}\text{Co}_{0.43}\text{Mn}_{0.40}\text{Fe}_{0.02}$ , the diffusivity increased with increasing hydrogen concentration (expanded lattice) in the alloy [152, 153].

---

<sup>6</sup>Only a very few literature values for the diffusion coefficient in  $\alpha$  phase  $\text{AB}_5$  type hydrides were listed.

### 3.9.2 Energy Levels

If the hydrogen diffusion coefficient for diffusion mechanism  $i$  could be calculated using an equation of the type given in Eq 3.30

$$D_i = D_{o,i} e^{-\frac{E_{a,i}}{RT}} \quad (3.30)$$

Where  $E_{a,i}$  is the diffusion energy barrier for mechanism  $i$ ,  $E_{a,i}$  is as follows:

$$E_{a,i} = E^* - E_\beta \quad (3.31)$$

$E^*$  represents the absolute energy for the energy barrier and  $E_\beta$  the energy of the hydrogen site in the lattice. One could imagine a plateau pressure dependence on the transport properties within the metal hydride particles. In an alloy with a high plateau pressure, the hydrogen atom sites in the  $\beta$  phase lattice have a higher energy than alloys with low plateau pressure.

If the absolute energy barrier for the diffusion is either constant or changing less than the energy of the hydrogen sites, the effective diffusion coefficient, will increase when the plateau pressure is increased. This should give higher diffusion coefficients for the high plateau pressure A site substituted alloys than the low plateau pressure B site substituted alloys.

If the diffusion processes influence the overall reaction rates to a large extent, hydrogen will be depleted close to the surface of the metal hydride particle during discharge. This surface depletion is reflected by a decrease in the potential surface potential (see section 5.1.2). As a result, the potential will approach the cut off potential faster than the hydrogen content (DOD) indicates. The rate measurement procedure is therefore indicative of whether there are diffusion limitations in the system or not.

If  $n$  different diffusion mechanisms are assumed, the diffusion flux can then be described as [154]

$$N_H = \sum_{i=1}^n -D_i \nabla c_H = -D_e \nabla c_H \quad (3.32)$$

Here,  $D_e$  is the effective diffusion coefficient.

### 3.9.3 Diffusion in AB<sub>5</sub> type Alloys

The diffusion coefficient for hydrogen in LaNi<sub>5</sub> is reported to be in the range of  $10^{-7}$  -  $10^{-8}$  cm<sup>2</sup>/s [149]. Lundqvist and Lindbergh [155] used a microelectrode technique to determine the diffusion coefficient in AB<sub>5</sub> type electrodes. They found a diffusion coefficient of  $1.3 \pm 0.3 \cdot 10^{-9} \frac{cm^2}{s}$ . As pointed out by Lundqvist [156], there are several experimental challenges with regards to determining the diffusion coefficient. Chen *et al.* [157] measured the diffusion coefficient to be in the order of  $10^{-10}$  cm<sup>2</sup>/s for MmNi<sub>5</sub> system alloys.

The diffusion flux of hydrogen during discharge can be calculated from Eq 3.32. Using an effective diffusion coefficient of  $10^{-8} \frac{cm^2}{s}$ , a maximum diffusion length of 50 μm, and the maximum hydrogen content in LaNi<sub>5</sub> from table 3.2, a diffusion flux of  $9 \cdot 10^{-4} \frac{mol}{cm^2 \cdot s}$  can be calculated.

Aluminium substitution increases the activation energy for diffusion and a subsequent reduction in the apparent diffusion coefficient with two orders of magnitude is observed [158]. The hydrogen diffusion in the α-phase is also slowed down if the cobalt content is increased [92, 94]. The hydrogen diffusion is furthermore reported to increase marginally upon partial substitution of nickel by tin.





## Chapter 4

# Structural and Related Properties of (La,Ce,Nd,Pr)Ni<sub>5</sub> Alloys

*The misch metal composition is a very important parameter in MmB<sub>5</sub> type alloys. In this chapter this issue is treated, with the emphasis on revealing the structural properties.*

Several parts of this chapter have already been published by the author previously [49, 159]<sup>1</sup>.

### 4.1 Introduction

The optimum electrode compositions have been developed mainly through testing of various components and their compositions. At this point the search for improved electrodes requires more understanding of both *action* and *interaction* of various elements in the multi-component alloy in order to better control the properties of the electrodes. The properties of substituted AB<sub>5</sub> type hydrogen storage alloys are also discussed in section 3.4

---

<sup>1</sup>The published parts of this chapter are reprinted with permission from Elsevier Science S.A.

In the present chapter, a new approach to this problem is proposed, namely a factorial analysis of the specifically designed sample series (i.e. samples with two-level variation of composition for three (or more) different components of the alloy, according to the method described Box *et al.* [160]). In this chapter, the first part of the study is described, which includes a systematic determination of the effects of rare earth elements (lanthanum, cerium, praseodymium and neodymium) on the plateau pressure and the alloy structure. Preliminary results on the methodology and on its applicability to multi-variable experimental problems are presented. Future work involves introducing additional variables, i.e. substitution of nickel by other metallic additions, and non-stoichiometric alloys.

In section 3.4.1 different theories regarding the correlations between the structural parameters and the plateau pressure were elaborated. However, not much experimental evidence has been reported so far. Therefore one of the goals of this work was to confirm the correlations, and also to find simple rules for determining and predicting properties of multi-component AB<sub>5</sub> alloys.

## 4.2 Experimental Methods

### 4.2.1 Factorial Design

A factorial design on two levels (described in detail by Box *et al.* [160]) is a method of investigation for multi-variable experimental systems. The method evaluates changes of the system properties, which result from simultaneous introduction of several variables. As a result, it allows us to determine both the "main effects" (caused directly by each variable), and also the "interaction effects" (resulting from a possible interference with other variables). The alloy compositions of the 2<sup>3</sup> factorial design series are listed in Table 4.1. In addition, a basic LaNi<sub>5</sub> compound was also prepared.

The main effect is defined as an average effect of one variable over all conditions of the other variables [160]. The main effect of, for example, cerium, is therefore calculated as follows

$$C_{\text{main}} = \bar{y}_+ - \bar{y}_- = \frac{y_2 + y_4 + y_6 + y_8 - y_1 - y_3 - y_5 - y_7}{4} \quad (4.1)$$

where  $y_i$  is the property affected by cerium (for instance unit cell dimensions or plateau pressure) in various experiments (see also table 4.1). The unit of the

Table 4.1: Alloy compositions of the "2<sup>3</sup>" series. Short notation indicates "low" content (-) and "high" content (+) of cerium, neodymium, and praseodymium, in this order.

Alloy	Short notation	Property
La <sub>0.88</sub> Ce <sub>0.04</sub> Nd <sub>0.04</sub> Pr <sub>0.04</sub> Ni <sub>5</sub>	- - -	y <sub>1</sub>
La <sub>0.74</sub> Ce <sub>0.18</sub> Nd <sub>0.04</sub> Pr <sub>0.04</sub> Ni <sub>5</sub>	+ - -	y <sub>2</sub>
La <sub>0.74</sub> Ce <sub>0.04</sub> Nd <sub>0.18</sub> Pr <sub>0.04</sub> Ni <sub>5</sub>	- + -	y <sub>3</sub>
La <sub>0.60</sub> Ce <sub>0.18</sub> Nd <sub>0.18</sub> Pr <sub>0.04</sub> Ni <sub>5</sub>	+ + -	y <sub>4</sub>
La <sub>0.74</sub> Ce <sub>0.04</sub> Nd <sub>0.04</sub> Pr <sub>0.18</sub> Ni <sub>5</sub>	- - +	y <sub>5</sub>
La <sub>0.60</sub> Ce <sub>0.18</sub> Nd <sub>0.04</sub> Pr <sub>0.18</sub> Ni <sub>5</sub>	+ - +	y <sub>6</sub>
La <sub>0.60</sub> Ce <sub>0.04</sub> Nd <sub>0.18</sub> Pr <sub>0.18</sub> Ni <sub>5</sub>	- + +	y <sub>7</sub>
La <sub>0.46</sub> Ce <sub>0.18</sub> Nd <sub>0.18</sub> Pr <sub>0.18</sub> Ni <sub>5</sub>	+ + +	y <sub>8</sub>

result is the same as the property  $y$ . When the effects need to be related to the amount of each element in the alloy (in atomic%) they are divided by the difference in atomic% between the high and low level of the elemental content.

If two variables do not behave additively, they *interact*. In the case of cerium and praseodymium, a measure of this interaction is given by the difference between the average effect of cerium with low praseodymium content and the average cerium effect with high praseodymium content. By convention, half this difference is called the cerium by praseodymium interaction ( $Ce \times Pr$ ). The  $Ce \times Pr$  interaction is calculated as follows

$$Ce \times Pr = \frac{y_1 + y_3 + y_6 + y_8 - (y_2 + y_4 + y_5 + y_7)}{2} \quad (4.2)$$

The factorial method was applied to design and to analyse a series of AB<sub>5</sub> compositions, in which A was a mixture of lanthanum, cerium, neodymium, praseodymium, and B was nickel (without additions). Three variables were introduced, i.e. the changing contents of cerium, neodymium and praseodymium. The content of each rare earth element was changed at two levels (high and low) and the misch metal composition was varied systematically according to a 2<sup>3</sup> rule (three variables at two levels) [160]. The low-level content was equal to 0.04 atomic%, and the high-level content to 0.18 atomic%. The content of lanthanum was calculated for each composition to complement the total amount of misch

metal, up to the right proportion of misch metal and nickel (i.e. 1:5), and varied from 46 to 88 atomic% lanthanum.

#### 4.2.2 Experimental Procedure

The alloys were prepared by arc melting using a water cooled copper crucible, using elements of high purity (lanthanum - 99.99% (Johnson Matthey, cerium - 99.12%, Treibacher, praseodymium - 99.12%, Treibacher, neodymium - < 99.7%, Treibacher, nickel, 99.95+%, Johnson Matthey). The alloys were melted under argon for at least five times to ensure homogeneity. Each composition was characterized by X-ray diffraction (XRD) using a Nicolet-Stoe powder diffractometer (copper K $\alpha$  radiation). Unit cell parameters of the structure were determined from X-ray diffraction patterns as described in appendix B. For this purpose, reflections with certain Bragg's indices ( $h$ ,  $k$ , or  $l$ ) equal zero were selected, preferably at as high as possible diffraction angle for better accuracy.

Pressure composition (PC) isotherms were measured at 273K, 296 K, 298K and 323K, using a volumetric method. Some of the measurements were performed at McGill University, and some at ONRI, using computer controlled gas titration systems. The equilibrium pressures as a function of hydrogen content obtained in the two laboratories for the same samples exhibited very high reproducibility and therefore all results (independently on the gas titration apparatus) were included in the analysis. Some differences were noted for maximum hydrogen storage capacity, but the values for the average plateau pressures were taken at the midpoint of the isotherm, giving comparable results. Hysteresis was evaluated as  $\ln(\frac{P_a}{P_d})$  where  $P_a$  and  $P_d$  are absorption and desorption plateau pressures respectively.

### 4.3 Results and Discussion

#### 4.3.1 Plateau Pressure Changes in (La,Ce,Pr,Nd)Ni<sub>5</sub> Alloys

The series of AB<sub>5</sub> alloys with varying composition of rare earth elements (lanthanum, praseodymium, neodymium, cerium) were measured in order to determine changes of the equilibrium plateau pressure in dependence of the alloy composition. For comparison, the basic LaNi<sub>5</sub> alloy has also been characterized.

Figure 4.1 shows an example of the pressure-composition isotherm measured for the  $\text{La}_{0.74}\text{Ce}_{0.04}\text{Nd}_{0.04}\text{Pr}_{0.18}\text{Ni}_5$  (- - +) alloy. The first sign in the symbol representing the alloy denotes whether the cerium level is low (4 atomic% ) or high (18 atomic% ), the second one describes the neodymium level and the third one the praseodymium level.

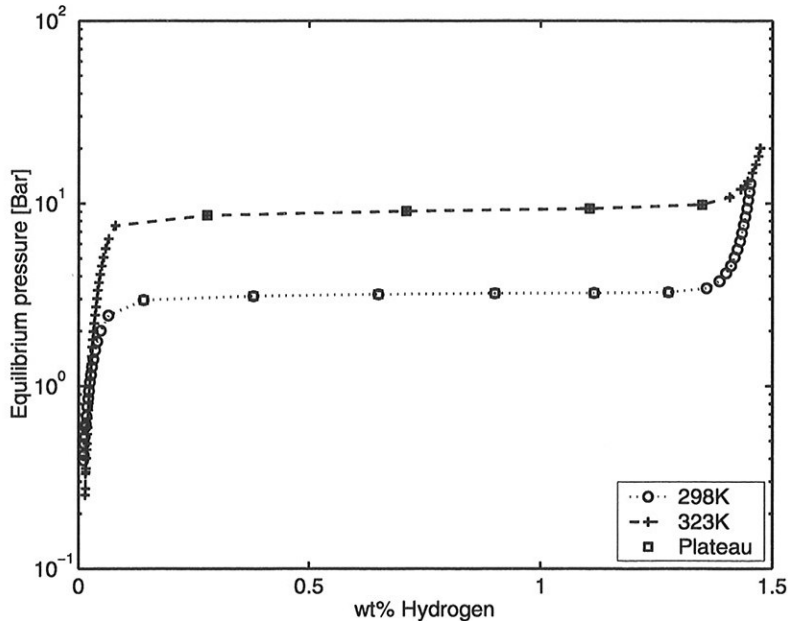


Figure 4.1: *Examples of PC isotherms for hydrogen desorption measured at two temperatures: 25° C and 50° C for  $\text{La}_{0.74}\text{Ce}_{0.04}\text{Nd}_{0.04}\text{Pr}_{0.18}\text{Ni}_5$  ( - - +).*

It has been found that the substitution of lanthanum by praseodymium, neodymium and cerium does indeed change the equilibrium pressure of hydrogen considerably, and the change depends mainly on the total amount of the lanthanum being substituted by other elements. The higher the total content of praseodymium, neodymium or cerium in the alloy, the higher the equilibrium pressure. When compared to the B site substitution, these alloys exhibit not only an opposite change of the plateau pressure (increase of the plateau as opposed to the decrease caused by the B site substitution), but also a different behaviour of the isotherm sloping. As a result of the B site substitution, usually a significant inclination of the slope was observed, whereas in the present series of samples the sloping was always very small. For samples with lanthanum substitution not exceeding about 25 at.%, almost no slope was seen in the isotherms, which increased only slightly as the amount of lanthanum was further decreased.

In addition, there was no significant loss of hydrogen storage capacity of the alloys as a result of the substitution, which remained comparable with the basic LaNi<sub>5</sub> alloy. The effects of substitution on the equilibrium pressure are summarized in table 4.2.

Table 4.2: Gas charging properties for various alloys, all pressures in bar, at 0, 23, 25 and 50° C. Subscripts: a, absorption, d, desorption, e, empirical value calculated from Eq 3.11 and H is taken as  $\ln \frac{P_a}{P_d}$ .

Alloy	P <sub>d,0</sub>	H <sub>0</sub>	P <sub>d,23</sub>	P <sub>d,25</sub>	H <sub>25</sub>	P <sub>d,50</sub>	H <sub>50</sub>
LaNi <sub>5</sub>	0.5	0.79	1.7	1.7	0.69	4.9	-
- - -	-	-	2.2	2.3	0.73	6.7	-
+ - -	1.2	1.04	3.9	-	-	11.1	0.78
- + -	-	-	-	3.9	0.64	-	-
+ + -	2.0	0.88	5.8	6.1	0.83	15.7	-
- - +	1.1	0.83	3.2	3.3	0.68	9.2	-
+ - +	1.8	0.89	5.8	6.0	0.77	15.1	0.51
- + +	1.8	0.54	-	5.4	0.51	-	-
+ + +	3.0	0.96	8.2	-	-	20.9	-

The factorial analysis of the results (presented in table 4.3) shows both the main effects of each rare earth element and the interaction effects on the plateau pressure.

Table 4.3: Quantified main and interaction effects of rare earth metals.

Element effect	a [Å]	c [Å]	c/a -	v <sub>uc</sub> [Å <sup>3</sup> ]	P <sub>d,25</sub> Bar	ΔH [kJ/mol]	ΔS [J/K·mol]
Ce	-0.020	0.005	0.0043	-0.57	2.4	1.6	-0.14
Nd	-0.008	-0.002	0.0008	-0.32	2.1	0.6	-0.05
Pr	-0.008	0.001	0.0016	-0.25	1.7	0.6	-0.05
Ce×Nd	0.002	-0.001	-0.0005	0.06	0.2	-0.2	0.01
Ce×Pr	-0.002	0.000	0.0004	-0.07	0.5	0.2	-0.01
Nd×Pr	-0.002	-0.001	0.0003	-0.09	0.2	0.2	-0.02
Ce×Nd×Pr	0.001	0.002	0.0003	0.07	-0.1	-0.1	0.00

The results confirm previous findings about the dominant role of cerium in the change of different properties. The effect of neodymium is smaller, and that of praseodymium is the smallest. The interaction effects indicate that combined introduction of two rare elements which replace lanthanum is more efficient in increasing the plateau pressure than a single metal substitution. The interaction effects are certainly much smaller than the main effects, but they are not negligible and can even reach the value of the difference between the main effect of for example cerium and neodymium, which can be clearly visible in the measured equilibrium pressures. The interference effects depend on the kind of the rare earth elements. Cerium and praseodymium have the strongest synergetic capability for increasing the plateau pressure. The presence of neodymium reduces this synergy, for both cerium and praseodymium. Finally, in the case of mixed alloy consisting of all three substituting metals (cerium, praseodymium and neodymium), the interaction effect is reduced even more.

The relation between composition of rare earth elements and plateau pressure has been previously evaluated by Liu and Huston [78]. An empiric formula based on linear regression analysis for plateau pressure (and also for other properties, such as the heat of hydride formation and hysteresis) has been determined. The plateau pressure for desorption can be calculated for various compositions of  $MmNi_5$  alloys using Eq 3.11.

Although the formula is very useful and appears to be quite accurate, i.e. it fits the experimental data very well, the authors stress that "no physical significance should be directly attributed to the coefficients". The coefficients indicate again that substitution of lanthanum by cerium affects the plateau pressure the most, and the effects of neodymium and praseodymium are smaller. It is important to note that the formula does not include binary compounds and neither does it apply to cerium-rich and neodymium-rich alloys, which confirms that the effects of substitution are not simply additive. Liu and Huston [78] did not observe any significant reduction in hydrogen storage capacity as a consequence of lanthanum substitution (similarly to the results obtained here), in contradiction to the results of Sakai [6], where capacities of alloys containing neodymium or cerium decreased.

As mentioned above, the changes of plateau pressure caused by substitution are commonly interpreted as resulting from the changes of the unit cell volume. Substituting atoms have atomic radii smaller than lanthanum, and therefore a compression of the unit cell can be expected as a result of the A site substitution. This

in turn is assumed to increase the plateau pressure. However, there is actually no simple relation between the size of the rare earth atoms and the plateau pressure. The size of the atomic radius follows the atomic number of the rare earth metal in the following order:  $La_{57} > Pr_{59} \sim Ce_{58} > Nd_{60}$  with atomic radii:  $r_{a,La}=187.7\text{pm}$ ,  $r_{a,Ce}=182.5\text{pm}$ ,  $r_{a,Pr}=182.8\text{pm}$ ,  $r_{a,Nd}=182.1\text{pm}$  [161]. The same relation occurs for covalent radii (see table 3.4). This indicates that neodymium should cause the largest changes in the equilibrium pressure when replacing lanthanum, and cerium the smallest. However, all experimental results show that cerium has the largest effect on the plateau pressure and praseodymium the smallest. It can be concluded therefore that the plateau pressure changes caused by substitution are not directly related to the size of the atoms substituted, even if the substituting atoms appear to be chemically similar (as they are in the case of the rare earth metals). The case of cerium is indeed more complex. In the elemental form, cerium forms a closed packed, f.c.c. (face centered cubic) structure, in contrast to all other rare earth metals, which form a less dense, hexagonal structure [13]. This means that for some reasons cerium has a higher "packing capability" than lanthanum, praseodymium or neodymium, and this property seems to be reflected also in the effects of substitution. Another difference between cerium and the other three elements, lanthanum, praseodymium and neodymium is that cerium is able to have states of mixed valency [126].

#### 4.3.2 Structural Changes and A site Composition

In order to evaluate the relation between unit cell changes and the rare earth composition, lattice parameters of the alloys have been measured by X-ray diffraction. As known from section 3.4.1, there are two basic parameters that describe the  $CaCu_5$  type of structure in  $AB_5$  type alloys, namely parameter  $a$  (base parameter) and parameter  $c$  (height of the hexagonal prism). In this study, all alloys in the series exhibited a single-phase diffraction pattern, similar to the basic pattern of  $LaNi_5$ . Figure 4.2 shows an X-ray diffraction pattern obtained for alloy composition  $La_{0.60}Ce_{0.18}Nd_{0.04}Pr_{0.18}Ni_5$ , (+ - +).

However, the positions of the Bragg's reflections were slightly shifted, as compared to the original  $LaNi_5$  compound, indicating changes of the unit cell parameters caused by substitution. Table 4.4 presents lattice constants and unit cell volumes for the investigated series of compositions, and table 4.3 their factorial analysis.



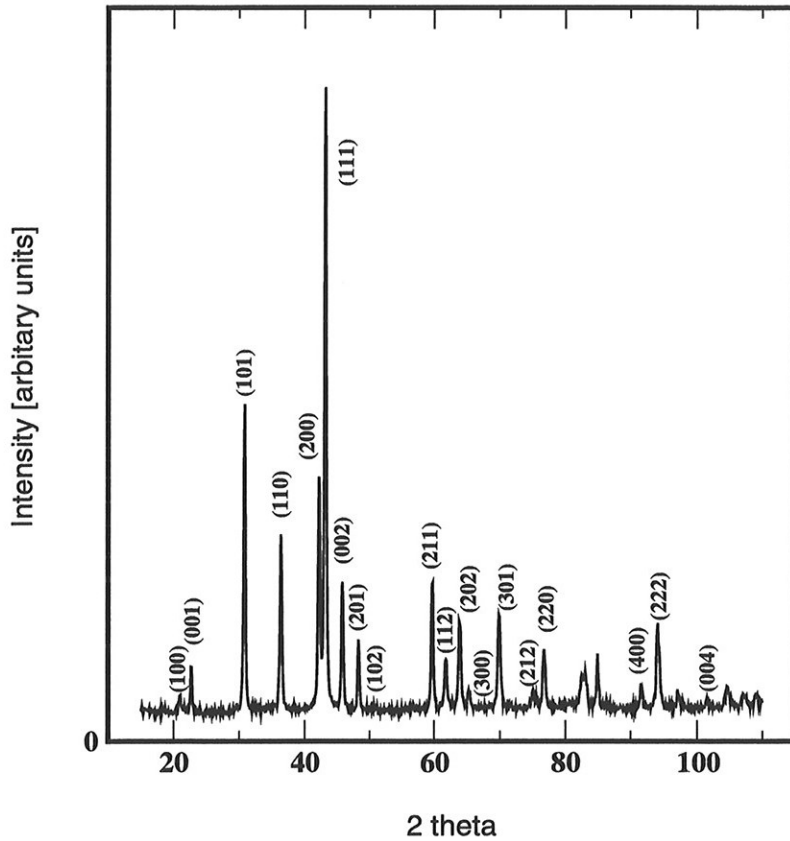


Figure 4.2: X-ray diffraction pattern for  $La_{0.60}Ce_{0.18}Nd_{0.04}Pr_{0.18}Ni_5$  (+ - +) .

All rare earth elements (praseodymium, neodymium, cerium) cause a decrease of the base parameter  $a$  of the  $LaNi_5$  unit cell. Substitution by cerium resulted in the largest changes (although cerium is not the smallest atom, as mentioned above). However, the height of the unit cell ( $c$ -parameter) did not decrease for cerium, but increased slightly. The same tendency was observed for praseodymium, but not for neodymium. This difference between neodymium and cerium (or neodymium and praseodymium) may actually cause the "amplifying" effect of the plateau pressure changes for  $Ce \times Pr$ , an effect that diminished in the presence of neodymium. Although the increase of the unit cell parameter as a result of the substitution by smaller atoms may seem surprising, it can be simply explained.

Table 4.4: Lattice parameters and thermodynamic properties for the studied alloys.  $a$  is the base parameter,  $c$  is the axial parameter,  $V_{uc}$  is unit cell volume. Thermodynamic data are given for desorption of hydrogen.

Alloy	$a$ [Å]	$c$ [Å]	$c/a$ -	$v_{uc}$ [Å <sup>3</sup> ]	$\Delta H$ kJ/molH <sub>2</sub>	$\Delta S$ J/K·molH <sub>2</sub>
LaNi <sub>5</sub>	5.005	3.970	0.7932	86.10	32.7	114.8
- - -	4.992	3.970	0.7953	85.66	31.7	114.7
+ - -	4.972	3.978	0.8001	85.17	30.2	114.6
- + -	4.984	3.971	0.7967	85.44	31.2	114.7
+ + -	4.968	3.973	0.7998	84.92	29.9	114.6
- - +	4.989	3.973	0.7965	85.64	31.5	114.7
+ - +	4.964	3.977	0.8014	84.87	29.5	114.5
- + +	4.975	3.970	0.7979	85.11	30.5	114.6
+ + +	4.956	3.976	0.8023	84.58	29.0	114.5

Introducing smaller atoms (cerium, praseodymium, neodymium) instead of lanthanum into the basal plane causes reduction of the basal parameter  $a$ . Based on simple geometric relations, this compression would induce closer atomic distances between A-atoms and B-atoms (which occupy  $2d$  sites in the structure), if the  $c$  parameter is to be unchanged or smaller as a result of substitution. In order to preserve the proper atomic distances between nickel and rare earth atoms, the  $c$  parameter needs to be extended. In fact, the more reduction of the  $a$  parameter, the more extension of the  $c$  parameter is needed. This observation has direct consequences for the plateau pressure analysis. In the literature concerning the B site substitution, the relation between the structure and the plateau pressure for LaNi<sub>5</sub>-based alloys is usually depicted in regard to the unit cell volume (for example [82, 162]) However, the changes of unit cell volume do not necessarily correspond to the changes of the interstitial hole for hydrogen, especially when the two basic parameters of the structure change in opposite directions, as above. An extreme example of such a situation is presented by Sandrock [163] and Wang et al. [71], where Ca <sub>$x$</sub> Mm<sub>1- $x$</sub> Ni<sub>5</sub> alloys have been described. In this case, calcium suppresses the plateau pressure, which normally should correspond to an increase of the unit cell volume. However, in contrast to this general rule, calcium caused *compression* of the unit cell [71], or no significant change of the volume [163]. At the same time, however, the  $a$  and  $c$  parameters changed significantly,

but in opposite directions  $a$  increased and  $c$  decreased, which as a consequence compensated the resulting volume changes, or even resulted in the reduction of the volume. From this example it is clear that volume changes cannot be directly correlated with the plateau pressure, especially for A site substitution. The problem lies in the fact that as pointed out by Lundin *et al.* [69] the question of the size of a tetrahedral site for hydrogen in the  $AB_5$  structure is not trivial, and requires rather complicated calculations.

Therefore, as in the case of  $Ca_xMm_{1-x}Ni_5$  alloys, the equivalent pressure and the volume of the tetrahedral site may not correspond directly to the total volume change. However, the relation between the plateau pressure and the  $a$  parameter is valid as shown by Sandrock [163], i.e. the larger the  $a$  parameter, the lower the equilibrium pressure. The relation between  $a$  and the plateau pressure is shown in figure 4.3 for the series of samples.

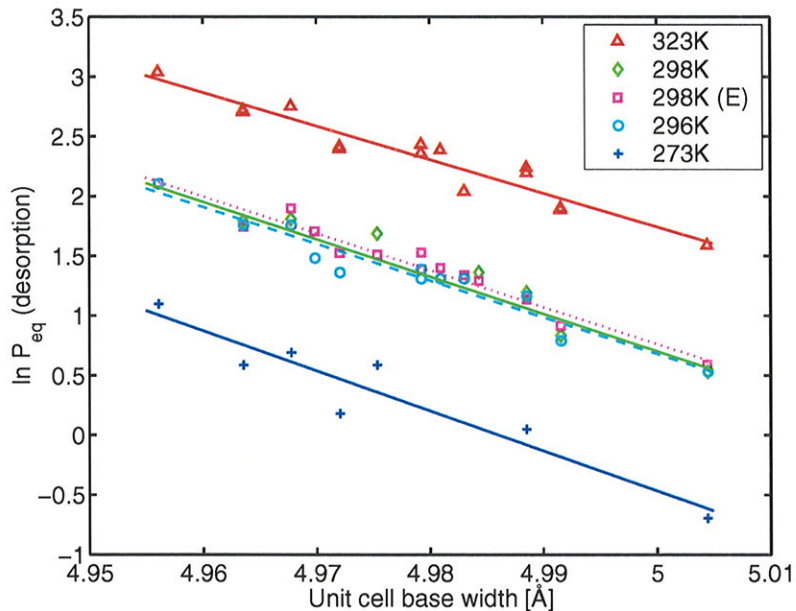


Figure 4.3: Desorption plateau pressure as a function of the base parameter,  $a$ . Dotted line indicates analysis based on Eq 3.11 (square points) and dashed line indicating analysis based on data obtained at  $23^\circ C$  (296K).

The correlation has a linear character, with a relatively satisfactory fit to a straight line. Additional experimental points measured in this study for alloys which did not belong to the  $2^3$  series are also included in the plot.

The relation between unit cell volume and the plateau pressure is shown in figure 4.4 for the series of samples. In figure 4.4, results obtained as well as the results

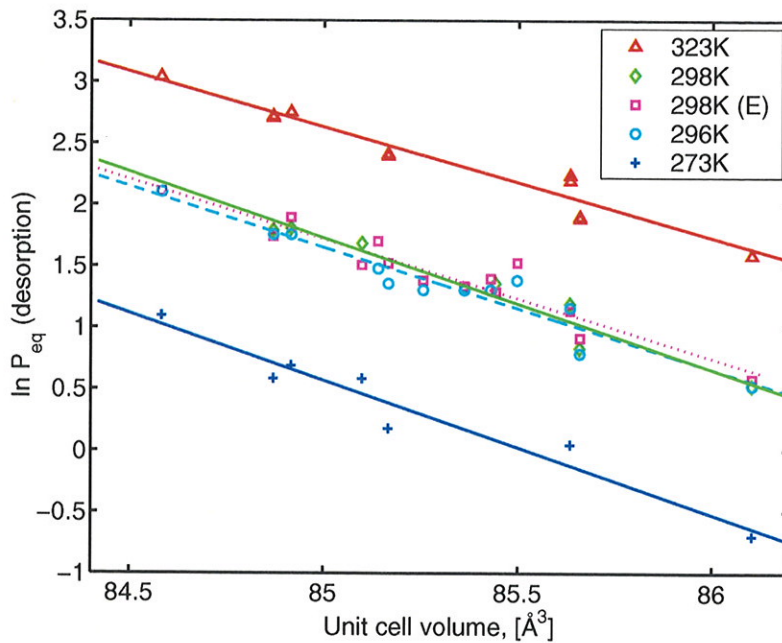


Figure 4.4: Desorption plateau pressure as a function of unit cell volume. Dotted line indicating analysis based on Eq 3.11 (square points) and dashed line indicating analysis based on data obtained at 23° C (296K).

from the formula of Liu and Huston (Eq 3.11) are also included .

It was found that the correlation with volume changes was actually much worse. The average standard deviation for the volume fit was about 30% higher than for the corresponding fit for the  $a$  parameter, which confirms that the  $a$  parameter is more desiccative for the changes of plateau pressure than the volume. The plateau pressure in turn does not exhibit any correlation with the  $c$  parameter, as shown in figure 4.5. (This is obviously caused in part by a relatively large error resulting from the small absolute changes of the  $c$  parameter).

The values of the equilibrium pressures for the alloy compositions calculated by use of Eq 3.11 are plotted versus the  $a$  parameter measured in this study for each alloy. This "hypothetical" relation is represented by the dashed line in figure 4.3, which compares surprisingly well with the actual pressure measurements. It shows that although Liu and Huston claimed that the formula does not have any

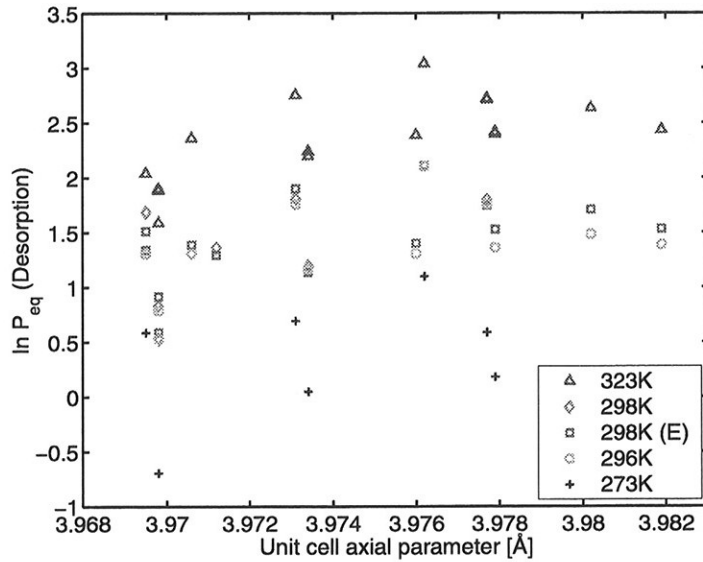


Figure 4.5: *Desorption plateau pressure as a function of unit cell height, c.*

direct physical meaning, the equation can be explained by the simple correlation with the  $a$  parameter. Eq 3.11 represents therefore a simplified, phenomenological form of the correlation between the unit cell dimensions and the equilibrium pressure for A site substitution with rare earth elements.

Although the use of the  $a$  parameter instead of the unit cell volume may seem quite obvious for the A site substitution (because of the opposite changes of  $a$  and  $c$ ), a similar problem is also worth considering for the B site substitution. As mentioned above, literature results usually show plots of equilibrium pressure versus volume changes for the B site substitution, as for example by Balasubramaniam *et al.* [61]. It appears however that even in this case a much better linear correlation can be obtained when using the  $a$  parameter instead of the unit cell volume.

The average standard deviation for the volume fit shown in Ref [61] was about 50% whereas the average standard deviation for the fit based on the  $a$  parameter was only about 8%, indicating a much better fit when using the  $a$  parameter instead of the unit cell volume. However, no correlation could be found including *all* types of substitution, i.e. A site, B site and "mixed" substitution. There is no simple relation that includes simultaneously the present results, along with the results of Refs [61, 99] obtained for alloys with additions occupying the mid-

plane *3g* sites, e.g. aluminium, manganese, tin), and also commercial alloys with cobalt and copper (which represent a "mixed" type of substitution [67, 68]. It is clear that linear relation between structure parameters and plateau pressure occurs only within one type of substitution, i.e. when the additions occupy the same structure sites. This conclusion has a practical consequence, because these linear correlations, which can be derived from standard X-ray and PCT measurements, can be used for an approximate determination of the effect of the type of substitution (either A site or B site) in new alloys.

### 4.3.3 Structural Anisotropy

A site substitution seems very attractive for controlling the anisotropy in AB<sub>5</sub> type alloys, because (as discussed above and in section 3.7.1) the A site substitution often leads to anisotropic changes of the unit cell (in consequence of the "opposite" changes of *a* and *c*). Moreover, in contrast to the B site substitution, it does not necessarily reduce the hydrogen storage capacity, and both high hydrogen storage capacity and high corrosion resistance can be maintained simultaneously. In the present work, the anisotropy factor in relation to the A site substitution was studied. In table 4.4 the values of *c/a* for the series of alloys presented in this chapter were listed. The factorial analysis of the anisotropy effects were given in table 4.3. The tables show that all rare earth elements cause an increase of the anisotropy factor, which explains why replacing lanthanum with other rare earth metals or their mixtures always enhances cycling stability of the alloys. Cerium causes the largest effects, and neodymium the smallest. Interaction effects show that from the point of view of anisotropy the presence of praseodymium is positive, when accompanied by either cerium or neodymium, or both of them. The above results confirm that anisotropy effects are cumulative. This also explains previous findings that corrosion resistance can be increased when A site substitution (misch metal) is combined with B site substitution (aluminium, cobalt) [6, 66].

It is clear from the above that a much more systematic study on the relation between the anisotropy and the corrosion resistance of the electrodes is required. Effects of each addition need to be evaluated in order to design optimised alloys for electrodes. The best materials are expected to be obtained as a result of applying all three ways of the controlled anisotropy: A site substitution, B site substitution and non-stoichiometry.



#### 4.3.4 Hysteresis and Van't Hoff Plots

The theory regarding the hysteresis and the van't Hoff relation is given in sections 3.3.4 and 3.3.3, respectively.

Although there exist a strong correlation between the plateau pressure and the structure of  $AB_5$ -based compounds (as shown above), hysteresis does not exhibit a similar trend. It is confirmed that cerium significantly increases the hysteresis (as seen also in the paper by Dayan *et al.* [164]) whereas praseodymium and neodymium both reduce the hysteresis (see table 4.2). The interaction effects indicate that the smallest hysteresis is obtained when both cerium and praseodymium are present in the alloy.

The van't Hoff plots for hydrogen desorption, which were used to calculate the thermodynamic parameters, are shown in figure 4.6.

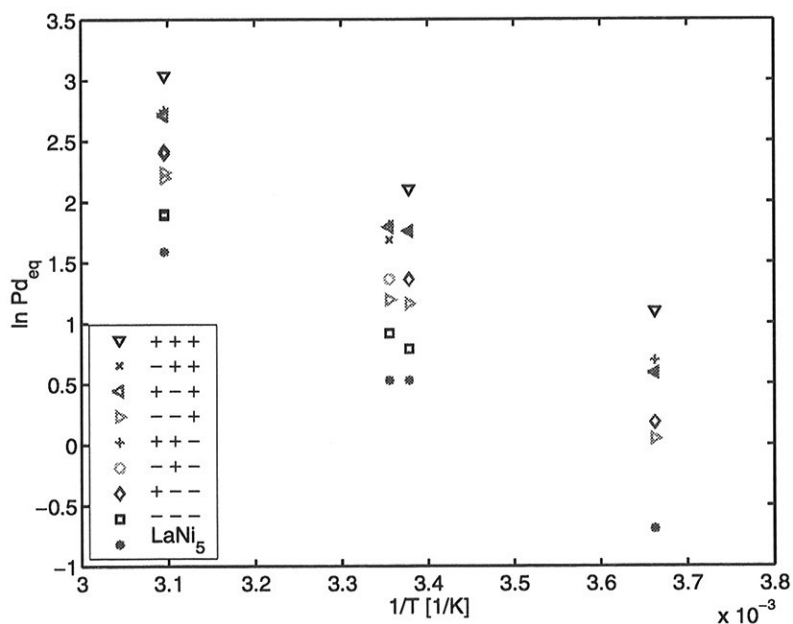


Figure 4.6: Van't Hoff plot for alloys with different rare earth compositions.

The entropy of the hydride decomposition remains rather unaffected with the A site substitution, whereas the reaction enthalpy changes more significantly. Cerium causes the largest change in the enthalpy, leading to more endothermic desorption (and more exothermic absorption). Although neodymium and

praseodymium seem to have similar effects on the enthalpy of the hydride formation, they exhibit different interaction effects with cerium. The conclusions about the enthalpy changes have however only an indicative character, because the plots are based on only three points (temperatures).

## 4.4 Conclusions

The A site substitution in the LaNi<sub>5</sub>-based structure has been studied. Although the substituting elements (cerium, praseodymium, neodymium) have similar chemical and physical properties to lanthanum, their effects on the alloy properties are significant. The basic effect of substitution is attributed to the geometric changes of the unit cell of LaNi<sub>5</sub>, resulting from replacing lanthanum by the smaller atoms of cerium, praseodymium or neodymium. The hydrogen storage capacity is not significantly affected by the A site substitution, but the equilibrium pressure is very sensitive to these changes, in particular to the basal parameter  $a$ . Factorial analysis allowed us to conclude that the effects of the A site substitution are more complex than simply additive. Some synergetic interaction has been observed, in particular between cerium and praseodymium, which resulted in larger equilibrium pressure changes than those extrapolated from the contribution of each element alone.

The results of this work demonstrate that each rare earth element exhibits always advantages in certain areas, and at the same time disadvantages in others. For example, cerium is the most effective in increasing the structural anisotropy, which may lead to higher corrosion stability, but also increases the plateau pressure the most. The plateau pressure needs therefore to be reduced by the B site additions, which in turn reduces the capacity. In consequence, the optimum A site composition should represent a proper balance of all these factors, i.e. plateau pressure, structural anisotropy and hydrogen storage capacity. With regards to this, praseodymium seems to be an effective substitution for lanthanum. Praseodymium does not increase the plateau pressure as much as cerium, and praseodymium-rich alloys exhibit flat isotherms. Also, praseodymium does not cause significant increase of the hysteresis, in contrast to cerium. At the same time, praseodymium does cause anisotropy, although not to such an extent as cerium. The advantages of praseodymium have already been indicated by Chen *et al.* [123], where it was shown that praseodymium-rich alloys exhibited higher



hydrogen storage capacity, better discharge characteristics and longer cycle life. Moreover, misch metal with high praseodymium content may actually become much less expensive, being a residue after extraction of cerium for automotive applications and neodymium for permanent magnets.

For the purpose of alloy optimization, factorial analysis is shown to be very useful. It provides more information about the effects of each alloy component than when changing one variable at a time, and gives a unique possibility to evaluate the interaction effects of the variables.



## Chapter 5

# Electrochemical Characterization of Metal Hydrides

*Metal hydrides can be formed either by a gas phase reaction or by an electrochemical reaction. This chapter has its emphasis on the electrochemical properties of metal hydrides.*

### 5.1 Electrochemical Characterization Methods

Metal hydride electrodes are subject to special characterization challenges. The main purpose of elaborating metal hydride electrodes using various electrochemical techniques can be summarized as follows:

- Characterize the cycle life behaviour; i.e. understand how the corrosion processes deteriorate the metal hydride forming alloy.
- Characterize the kinetics of the electrodes, understand and model the processes and sub processes involved in the hydrogen absorption and desorption process. It is of great importance to understand how different substitution elements act during this process and how to apply systematic search for applicable catalysts.

- Characterize the hydrogen diffusion in the hydrogen storage alloy in the electrode and understand the influence of the hydrogen storage alloy composition.
- Characterize the transport of ions in the porous electrode structure and understand the influence of the electrode construction and using this knowledge to maximise heat, electron and ion flow rates in the electrode.

Several electrochemical techniques have been developed to characterize hydrogen electrodes and the most important of those are presented in the subsequent sections.

### 5.1.1 Electrochemical Cycling

Cycle life characterization is one of the most common ways of characterizing new materials intended for battery purposes.

The cycle life characterization provides information about the following parameters:

- The maximum hydrogen storage capacity at a given set of charge/discharge conditions
- The hydrogen storage capacity as a function of the number of charge/discharge cycles. i.e. information about the stability of the tested alloys against corrosion and general deterioration.

The amount of hydrogen in the electrodes can be controlled either via the potential [165], by potentiostatic charging, or by controlling the charge flow [66]. For all practical purposes, constant current cycling of the electrodes are used to be able to compare the cycle life of different alloys.

Table 5.1 gives an overview of the parameters that can be varied in a standard cycle life test, and, figure 5.1 gives a schematic representation of the potential and the current changes during a standard charge/discharge cycle.

A charge cycle consists of four different steps. Just when the charge current is turned on, the potential jumps from the open circuit potential to a slightly

Table 5.1: Overview of the parameters that can be varied during a charge/discharge cycle life test of a metal hydride electrode.

Step	Parameters that can be varied
Constant current charging	$I_c$ [mA] and time of charge [s]
Break, zero current	Length of the break [s]
Constant current discharge	$I_{dc}$ [mA] The cutoff potential, $E_C$ [V], determines when the discharge is stopped
Break, zero current	Length of the break [s]

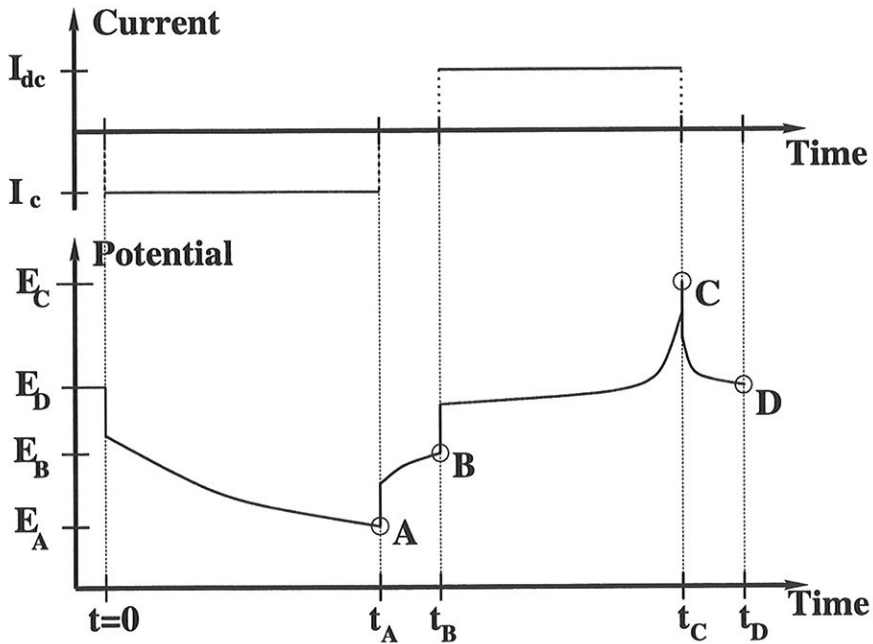


Figure 5.1: Schematic representation of the potential and the current changes during a standard charge/discharge cycle.  $I_c$  is the charge current,  $t_A$  the charge time.  $I_{dc}$  the discharge current,  $(t_C - t_B)$  the discharge time,  $E_B$  the open circuit potential of a charged electrode,  $E_C$  the cut off potential and  $E_D$  the open circuit potential after discharge of the electrode.

more negative potential. The reason for this is the charge overpotential and the ohmic resistance in the electrolyte (please refer to chapter 8 for additional details

regarding the contributions to the potential loss). During charging there is a rather steady shift towards a more negative potential. After cutting the charge current after a predefined amount of charge is transferred to the electrode, the potential momentarily shifts to the open circuit potential. Then there is a rather steady shift towards a slightly more positive potential, i.e. the equilibrium open circuit potential for the charged electrode,  $E_B$ . The steady change is characterized by the equilibrating of concentration gradients in the electrode and desorption of adsorbed hydrogen at the electrode surface. The amount of hydrogen bubbles formed on the surface is highly dependent on the current density (and of the potential) during the charge.

At the onset of the discharge, there is a sudden shift in the potential, indicating the discharge overpotential. The discharge is then continued to a cut off potential, represented by  $E_C$ . The discharge capacity can be computed using Eq 5.1

$$C_{dc} = I_{dc}(t_C - t_B) \quad (5.1)$$

The symbols in the equation refer to the symbols used in figure 5.1. After the discharge is stopped, the potential reaches the equilibrium open circuit potential for a discharged electrode,  $E_D$ , as possible concentration gradients are equalized.

The currents are often related to the maximum discharge capacity of the electrode using the *C-rate*. The C-rate can be calculated using Eq 5.2:

$$C_{rate} \left[ \frac{1}{h} \right] = \frac{I \text{ [mA/g]}}{C_{max,dc} \text{ [mAh/g]}} \quad (5.2)$$

The maximum discharge capacity is highly alloy dependent and the cycle life is usually highly dependent on the conditions selected from table 5.1. A careful selection of the parameters described in table 5.1 is therefore crucial.

### 5.1.2 Open Circuit Voltage Analysis

The equilibrium potential varies as a function of the hydrogen content. The open circuit potential analysis technique contains information about the following properties:

- Plateau pressure for the alloy; and

- Plateau slope of the alloy.

Since this technique provides the same information as the gas phase PCT analysis, it is often referred to as an electrochemical PCT measurement. However, it must be pointed out that electrochemical PCT measurements are less accurate than a gas phase PCT measurements [6].

According to Sakai *et al.* [6] an equilibrium potential,  $E_{eq}(H)$ , can be related to the equilibrium pressure,  $P_{eq}$ , by using the Nernst equation. The relationship can be described

$$E_{eq} = E^\circ(H) + \frac{RT}{2F} \ln \left( \frac{a(H_2O)}{\gamma(H_2)P_{eq}(H_2)} \right) \quad (5.3)$$

Here,  $\gamma(H_2)$  is the fugacity of hydrogen in the hydrogen storage alloy and  $a(H_2O)$  the activity of water. Experimental data at 20°C will yield an empirical correlation as the one given in Eq 5.4 [6].

$$E_{eq}[V] = -0.9324V - 0.0291V \cdot \log(P(H_2)) \quad (5.4)$$

See also the paper by Wang *et al.* [166] for a more detailed discussion of this topic. From Eq 5.4 one can see that a pressure change of one order of magnitude corresponds to a potential change of 29 mV at 20°C. This highlights the importance of this technique, as very high (or low) equivalent pressures can be applied with a minimum safety risk, as long as the hydrogen evolution potential (or metal oxidation potential) is not reached. It is worthwhile to notice the similarities with the equation for the hydrogen evolution reaction (Eq 2.6) as the equilibrium potential of an alloy with a plateau pressure of 1 bar gives the hydrogen evolution potential at 1 bar (-0.93V versus Hg/HgO).

In figure 5.2, a schematic drawing showing the potential versus the discharge capacity for two alloys with different plateau pressures is given.

In the figure, E is the voltage, C the discharge capacity, and  $\eta$  the overvoltage. Subscripts *oc* and *dc* are open circuit and discharge respectively. Subscript *l* denotes an alloy with a low plateau pressure and a sloping plateau, whereas subscript *h* denotes an alloy with a high plateau pressure and also lower plateau slope. The overpotentials are very dependent on the current densities.

From the figure it is seen that the maximum discharge capacities are the same for the two alloys. Even if the overvoltages are the same for both alloys the measured

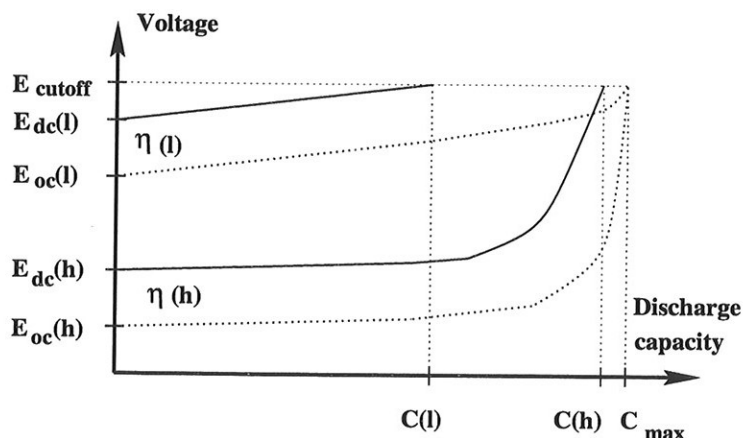


Figure 5.2: Schematic drawing showing the potential versus the discharged capacity for two alloys with different plateau pressures.

discharge capacities differ. (The overvoltage is decreasing with decreasing current density and increasing catalytic activity [154].)

A rough estimate for the minimum equivalent hydrogen pressure that is acceptable for an alloy intended for battery purposes can be calculated using Eq 5.4. An alloy with an open circuit potential in discharged state more negative than the cut off potential ( $E_C$ , see figure 5.2) is in principle useable in batteries. If a cut off potential of  $-0.65\text{V}$  versus  $\text{Hg}/\text{HgO}$  is assumed, an alloy with a plateau pressure of more than  $10^{-9.7}$  bar is in principle applicable for battery purposes. This is, however, provided that an extremely low discharge current is used, i.e. very low overvoltage, and also a very low ohmic loss in the electrolyte.

A good battery alloy will therefore have a plateau pressure that is so high that good kinetics can be expected and low enough so that hydrogen evolution during charging does not result in a considerably lower charge efficiency.

### 5.1.3 Rate Measurements

Another important characterization method for metal hydride electrodes are rate measurements, i.e. the discharge capacity as a function of the discharge current. The procedure for the rate measurement is given in figure 5.3. From figure 5.3 it



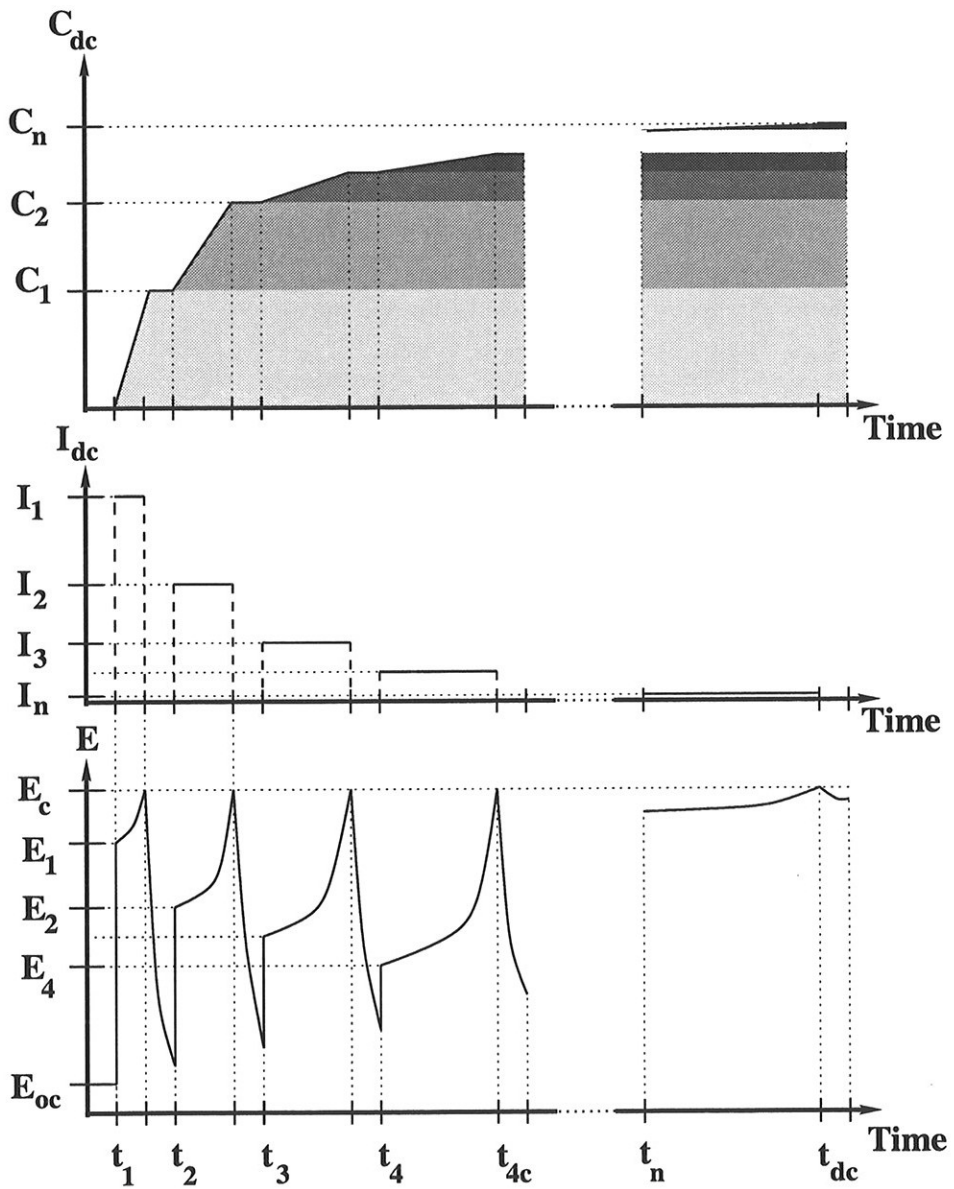


Figure 5.3: Illustration of the measurement procedure for rate measurements using  $n$  different steps.  $E$  is the potential,  $I_{dc}$  the current and  $C_{dc}$  the accumulated discharge capacity. The same overpotential during discharge is assumed for both alloys.

is seen that first, a very high current is applied, giving a very large overpotential. After a short time, the cut off potential is reached. Although the time is short, the current is so high that a quite substantial amount of the capacity can be discharged from the electrode. After a short break, a smaller discharge current is applied and the electrode is again discharged to the cut off potential. Since a smaller current is applied, the overpotential is lower. This procedure is repeated for  $n$  times with a lower discharge current each time. The deep discharge capacity is then given as the accumulated capacity for the current  $n$ .

$$C_{max} = \sum_{i=1}^n C_i \quad (5.5)$$

Here  $C_i$  is the capacity contribution from discharge step  $i$  and  $C_{max}$  is the maximum discharge capacity. For high power applications such as power tools, a high current performance is essential. Rate measurements will allow to obtain the following information:

- Discharge capacity as a function of discharge current; and
- The maximum discharge capacity, which is defined as the discharge capacity using an infinitesimal low current (no concentration gradients and a very low discharge overpotential).

## 5.2 Apparatus

In figure 5.4, a cross sectional view of the experimental setup that was used for the electrochemical measurements is shown and in figure 5.5 a top view is shown. The whole setup was placed inside a teflon compartment. As electrolyte 6M potassium hydroxide was used, giving a pH of 14.78 [24]. Teflon was chosen to avoid corrosion from the strong alkaline electrolyte. PPS is poly phenyl sulfide, which is resistant to strong alkaline electrolytes.

The figure shows a system containing three electrodes: one working hydride electrode, a platinum counter electrode, and a mercury/mercury oxide (Hg/HgO) reference electrode. The working electrode construction used is further detailed shown in figure 5.6. Please refer to section 5.3 for more detailed descriptions of the electrodes. It is crucial to have separate compartments for the working,

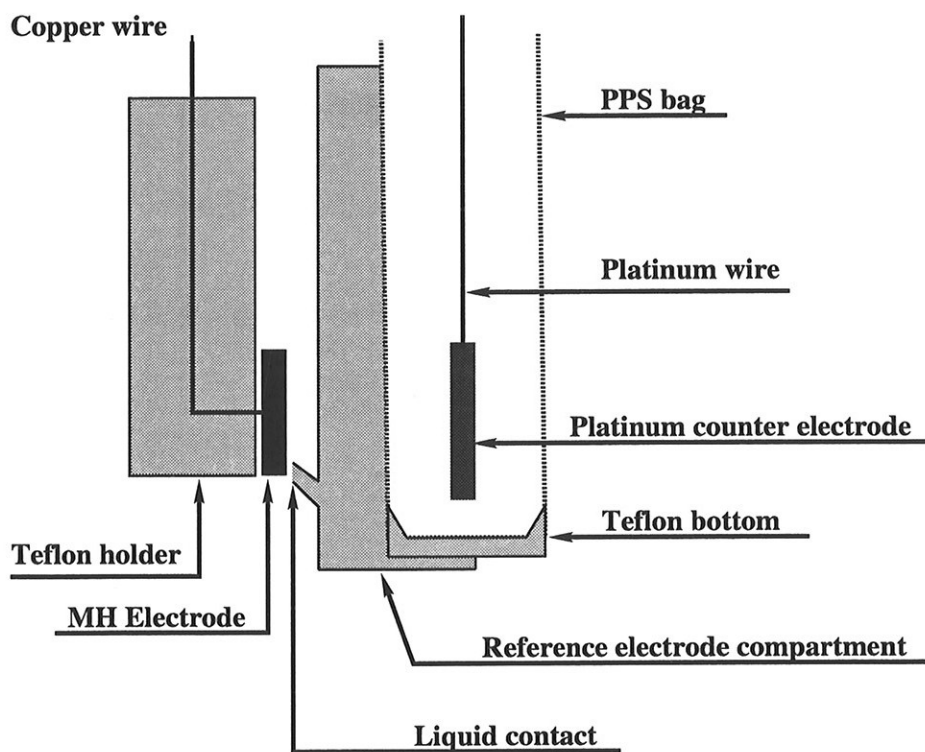


Figure 5.4: *Experimental setup, cross section view. The working electrode is located to the left, the reference electrode compartment in the middle (behind) and the counter electrode compartment to the right. The liquid contact provided contact between the electrode surface and the reference electrode compartment. This ensures correct potential measurements.*

reference, and counter electrodes. There are two reasons for the latter; to prevent undesired voltage changes as a result of contamination, and, to prevent mixing of possible hydrogen evolved at the hydride electrode and oxygen formed at the platinum counter electrode during charging. The potential was measured as close to the hydride electrode surface as possible, i.e. the tip of the reference electrode compartment were placed as close to the MH electrode surface as possible without disturbing the current flow.

Because the electrolyte can dissolve components of glass equipment, all parts in contact with the electrolyte were made of materials resistant to strong alkaline solutions. Teflon was chosen because of a proved good stability, both at ambient and at elevated temperatures in strong alkaline electrolytes.

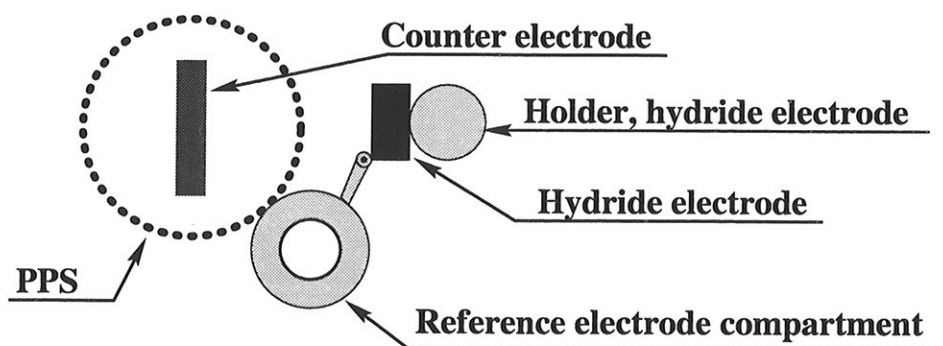


Figure 5.5: Top view of the cell shown in figure 5.4.

Cycle life tests, open circuit voltage measurements and rate measurements were all performed using an Arbin BT2000 16 channel galvanostat/potentiostat controlled by MITS'97 software.

## 5.3 Experimental

### 5.3.1 Hydride Electrode Construction

The electrodes were constructed especially for laboratory use. Two of those electrode constructions are shown in figure 5.6.

Common for each construction was that the metal hydride forming alloy powder was kept under argon until just before electrode pressing. This was necessary since the powder was susceptible to oxidation and consequently possibilities for giving inferior reproducibility if stored in air.

#### Sandwich electrode configuration

1. The hydride forming alloy was mixed with copper powder using a mass ratio of 1:4 ( $\sim 20$  wt% hydride forming alloy).
2. This mixture was transferred to a cylindrical pressing equipment and the surface was smoothed using an appropriate tool.

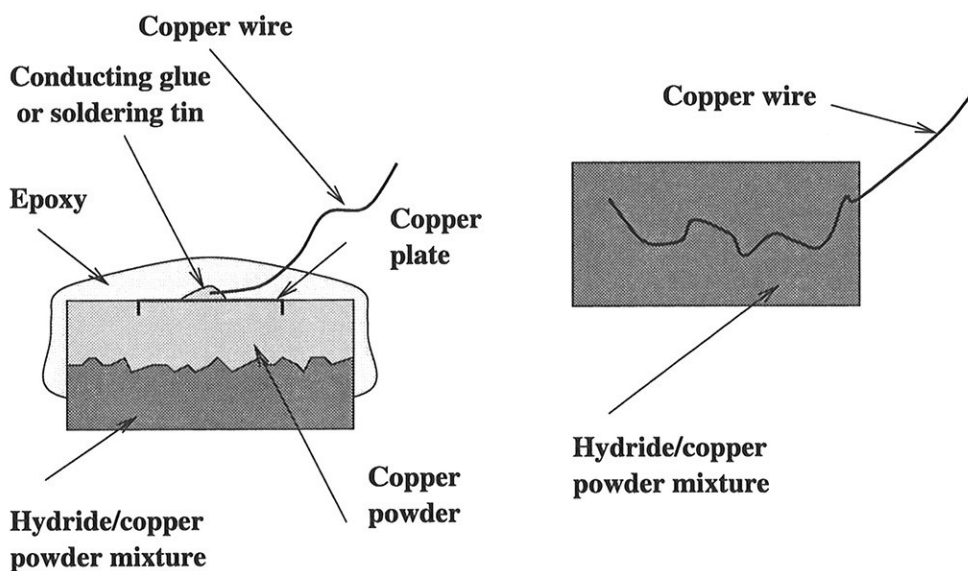


Figure 5.6: *Left: hydride laboratory electrode, sandwich configuration. Right: hydride laboratory electrode, integrated configuration.*

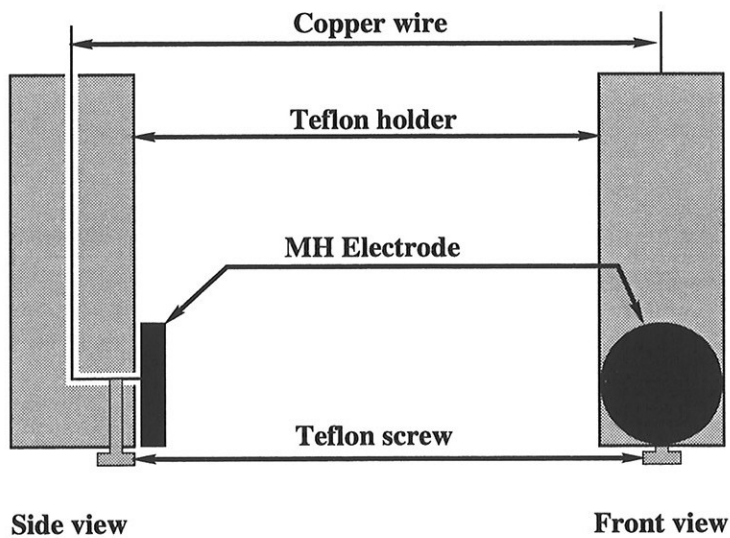


Figure 5.7: *Cross section view from the side and front (facing counter electrode) of how the integrated electrode was mounted in the cell.*

3. Approximately the same amount of copper powder as in the mixture was then transferred to the pressing equipment and the surface was smoothed gently.
4. A copper plate with rough edges to ensure good electrical contact was placed on top of the mixture.
5. The tablet electrode was pressed together using a pressure of  $4 \cdot 10^8$  Pa. This yielded a porosity of approximately 30% [66].
6. A copper wire was soldered or glued to the copper plate, and the connection point was sealed with epoxy.
7. When the epoxy was hardened, the electrode was mounted in the cell as shown in figure 5.4.

### **Integrated electrode configuration**

1. A hydride forming alloy was mixed with copper powder in a mass ratio of 1:4 ( $\sim 20$  wt% hydride forming alloy).
2. The copper wire end was formed as a spiral to improve contact with electrode.
3. The mixture of copper powder and the hydrogen storage alloy in powder form was transferred to the pressing equipment.
4. The tablet electrode was pressed together using a pressure of  $4 \cdot 10^8$  Pa and removed very gently from the pressing equipment.
5. The electrode was then placed in the cell as shown in figures 5.4 and 5.7.

### **5.3.2 Reference Electrode**

Contrary to all other parts of the cell, the reference electrodes were made of glass. The reason for this was that teflon did not have the required mechanical strength, and neither the transparency. If teflon was used, it would also be impossible to seal the electrode with epoxy (see figure 5.8). As for reference electrodes used in alkaline solutions, the Hg/HgO reference electrode is stable, relatively easy to

fabric and reliable [154, 167]. The potential for the Hg/HgO reference electrode is given by [24]:

$$E^{\circ}[\text{V}] = 0.926 - 0.0591\text{pH} \quad (5.6)$$

The potential of the Hg/HgO reference electrode versus the standard hydrogen electrode (SHE) for 6M potassium hydroxide can then be calculated to 0.053V. As such, the Hg/HgO has a potential of 930mV more positive than the reversible hydrogen electrode (RHE) for 6M potassium hydroxide [66]. Two Hg/HgO reference electrode configurations are shown in figure 5.8. No potential differences

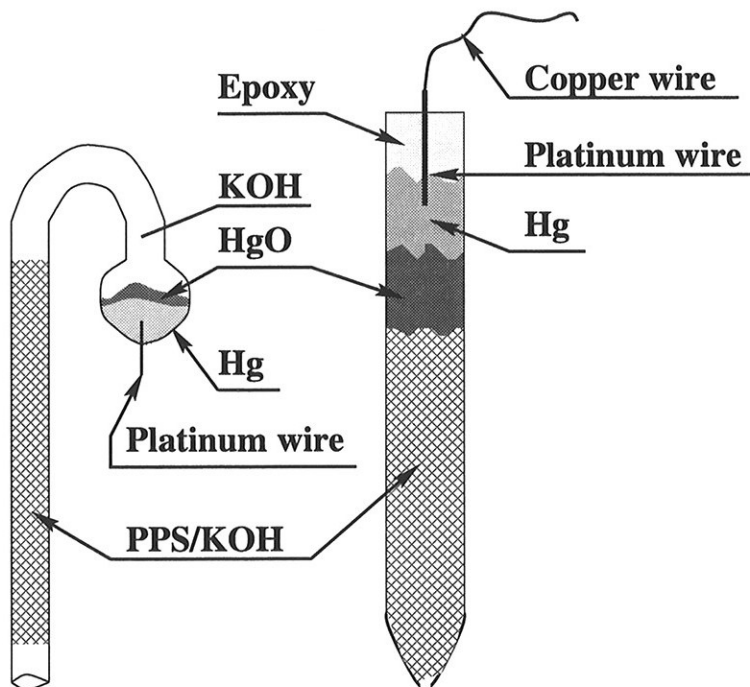


Figure 5.8: *Left: reference electrode, bulb configuration. Right: reference electrode, tubular configuration.*

were detected between the tube and the bulb configuration. The tubular configuration was far the most easy way to make the reference electrodes. The only disadvantage of the tubular configuration compared to the bulb configuration was that only high impedance voltmeters could be used in combination with the tube configuration, indicating higher ohmic resistance. The bulb configuration was less sensitive to the type of voltmeter used. One important parameter for

the bulb configuration was the necessary vacuum created before the electrolyte was filled into reference electrode. To prevent the presence of air bubbles in system, the pressure should be around 1Pa before the electrolyte was added. This would induce the formation of an air bubble with an approximate size of  $10^{-5}$  of the volume of the interior of the reference electrode. This was assumed to be acceptable in order to preserve the ionic conductivity through the upper part.

### **Tubular construction**

The construction of a tubular reference electrode was done as follows: a glass tube was filled with the desired amount of PPS to prevent convection, and then a layer of mercury oxide was placed on top of the PPS. Subsequently a layer of mercury was placed on top of the mercury oxide layer. A platinum wire was then dipped half way down in the mercury. The tube was then sealed with epoxy and potassium hydroxide was finally added by vacuum impregnation.

### **Bulb construction**

The construction of the bulb reference electrode configuration was done as follows: a special piece of glass (see figure 5.8) was used. The platinum wire was mounted in the glass piece. Afterwards, the mercury and the mercury oxide were added using a syringe with a hose mounted on its tip. Subsequently PPS was added. Potassium hydroxide was lastly added by the use of vacuum impregnation.

### **5.3.3 Standard Electrochemical Test for Alloys**

All alloys were tested according to various procedures, which included electrochemical cycling, open circuit voltage measurements, and kinetic measurements.

#### **Electrochemical cycling**

Electrodes were charged and discharged using currents of 300 mA/g active material. All breaks were 5 minutes. The electrodes were charged with 300 mAh/g and discharged to a cut off voltage of -0.6V versus Hg/HgO unless otherwise



noted. Maximum discharge capacity used to calculate C-rates was defined as 300 mAh/g for all alloys unless otherwise noted.

### **Open circuit voltage (OCV) analysis**

As for gas phase PCT, measurements were mostly carried out during desorption (discharge of the metal hydride electrode). The most precise measurements were obtained by discharging the electrode with a low current for a short while. The current would be set to zero and at the end of that discharge. Since relatively large potential differences existed with respect to the state of charge, an empirical formula was elaborated to determine when the open circuit potential was reached. The formula took into account both the scientific reliability as well as the desire to minimize the time of the experiment. For all experiments presented in this thesis, the open circuit potential was defined to have been reached when the variation of the measured potential was less than 0.9mV over a period of time for more than 10 minutes. After the open circuit potential was reached, the electrode was furthermore discharged for a new period and this process continued until the predefined cutoff potential was reached. For a standard test, a current of 50 mA/g in 432s was chosen as this would give 50 discharge steps for an alloy with a discharge capacity of 300 mAh/g. These criteria yielded a measurement time of up to 24h. Several different criteria were applied, and the above presented empirical criteria showed the best reproducibility and reliability.

### **Rate measurements**

The procedure for performing the rate (kinetic) measurements was described in detail in section 5.1.3. For each kinetic measurement, five currents levels per decade were applied to a minimum (deep discharge) current of 0.001 C (0.3 mAh/g). Each discharge was continued until the potential reached the cutoff potential (-0.6V versus Hg/HgO).

### **Measurement combination setup**

In table 5.2, an example of the first 100 cycles in a procedure for alloy testing is given.

Table 5.2: Example of the first 150 cycles in a procedure for alloy testing. Non commented cycle numbers refer to normal charge/discharge cycling.

Cycle No	Action	Note
1-9	Potential logged	Monitor activation process
10	Kinetic measurement	Monitor activation process
15	Potential logged	Monitor activation process
20	Open circuit measurement	Before corrosion
30	Kinetic measurement	Kinetic properties
40	Kinetic measurement	Monitor high current activation
50	Potential logged	For reference
80	Kinetic measurement	Monitor high current activation
100	Potential logged	For reference

After 100 cycles passed, the procedure was continued with cycling, occasional kinetic measurements and logging of the potential was performed for every 50 or 100 cycles.

### 5.3.4 Alloys and Chemicals Used

In table 5.3 a list of the chemicals and alloys used is given. The Hydralloy F

Table 5.3: Chemicals and alloys used.

Chemical	Supplier	Comment
Cu powder < 3 $\mu$ m	ONRI, Japan	-
Cu powder < 64 $\mu$ m	Merck	p.a.
HgO	Riedel de H�en	-
Hydralloy F 30/9C	GfE Metallurgie	Commercial alloy
KOH	Merck	p.a.
LaNi <sub>3.4</sub> Co <sub>1.2</sub> Mn <sub>0.1</sub> Al <sub>0.3</sub>	Shin-etsu Chemical Co.,Ltd.	-
MmNi <sub>3.7</sub> Mn <sub>0.3</sub> Al <sub>0.4</sub> Co <sub>0.7</sub>	H�gan�s AB	-
MmNi <sub>3.7</sub> Mn <sub>0.3</sub> Al <sub>0.4</sub> Co <sub>0.7</sub>	GfE Metallurgie	-

30/9C was used as a reference alloy for several of the measurements shown in

this chapter as well as most of the impedance measurements shown in chapter 8. This alloy had a composition of  $MmNi_{3.5-3.7}Co_{0.7-0.8}Mn_{0.3-0.4}Al_{0.3-0.4}$ . All Hydralloy F 30/9C electrodes were made out of the same batch of this alloy to ensure comparable results.

## 5.4 Results

### 5.4.1 Electrochemical Cycling of Metal Hydride Electrodes

#### Potential-time relations

In figure 5.9, the potential time relations for an electrode made of Hydralloy F 30/9C for various cycle numbers are given.

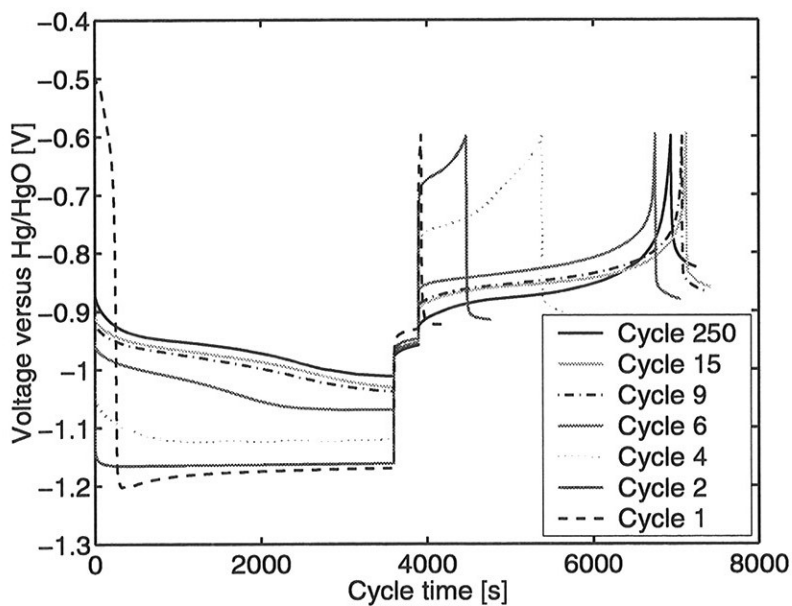


Figure 5.9: *Voltage versus time plots for an electrode made of Hydralloy F 30/9C at various cycle numbers.*

The onset charging potential for the first cycle usually was around -450 mV

versus Hg/HgO. This was the Cu/Cu<sub>2</sub>O potential (see section 5.5.1 for additional details).

For the subsequent cycles, the charge potential started around -850 and ending up in the range of -1000 mV to -1150 mV versus Hg/HgO. As one can see from figure 5.9, the potential-time behaviour changed during the activation of the electrode. During the first cycles, the overpotential was quite high and remained stable during charging. This stable high potential corresponded to the hydrogen evolution potential for the alloy. After a few cycles, the charging potential was changing rather steadily with time. The slope of this potential change was reflected in the slope of the PCT curve (see section 5.1.2) indicating that the overpotential reached a more or less constant value.

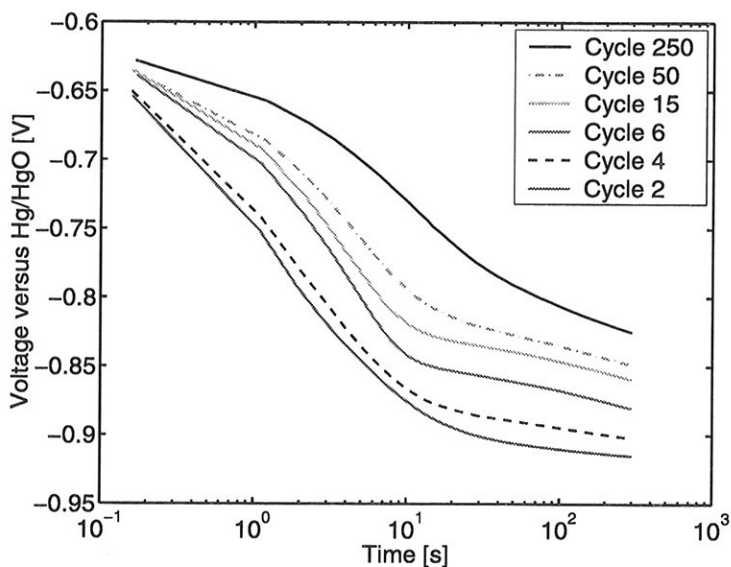


Figure 5.10: Plot of the surface potential versus time during the break after discharge for various cycle numbers.

After the break, the electrodes were discharged until they reached the cutoff voltage. Subsequently the discharge capacity was computed using Eq 5.1. As can be seen from the figure, the discharge overpotential decreased while the discharge capacity increased significantly during the first cycles. It is also visible in the figure that the differences between the absolute values of the charge and the

discharge overpotentials were small.

Another break, equalizing of the hydrogen concentration in the electrode before the next charging is then visible. In figure 5.10 a plot of the potential versus time during this break is shown. From the figure, it appears that the concentration gradients of hydrogen in the electrode are higher before the electrode is activated. The difference in the equilibrium potential is also more than 100mV. This is reflecting the amount of hydrogen left in the electrode after discharge, and according to Eq 5.4 this corresponds to more than three decades of equivalent hydrogen pressure.

### Discharge capacity as a function of number of charge/discharge cycles

In figure 5.11, the discharge capacity as a function of number of charge/discharge cycles for three different alloys are given. The alloys are charged and

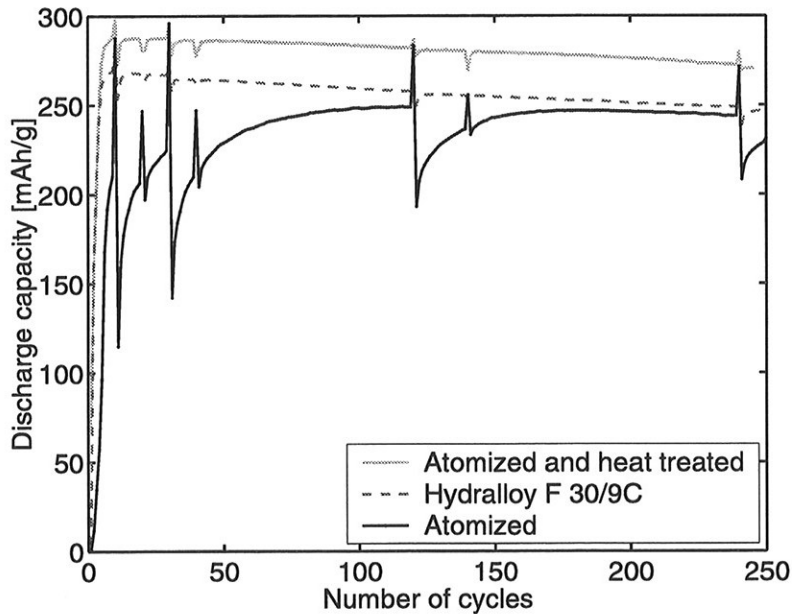


Figure 5.11: *Discharge capacity as a function of number of charge/discharge cycles for three different alloys. Capacity peaks on the curves are deep discharge and equilibrium potential measurements.*

discharged using 200 mAh/g. Capacity peaks on the curves are deep discharge

and equilibrium potential measurements. One alloy is the reference alloy, Hydralloy F 30/9C. The other alloys are made by gas atomizing. One is heat treated and the other is not, and both gas atomized samples had a composition of  $MmNi_{3.7}Mn_{0.3}Al_{0.4}Co_{0.7}$ . In practice this means that the all alloys had the same plateau pressure, with possible differences in the plateau slope. From figure 5.11 one can see that the discharge capacity behaviour was different for each of the alloys. The atomized and heat treated sample and Hydralloy F 30/9C showed considerably faster activation than the non heat treated atomized sample. It is also visible in the figure that the reactivation period after deep discharge for the non heat treated atomized sample was considerably longer than for the other samples. The same deep discharge capacity was observed for both atomized samples, indicating that the performance differences were purely related to kinetics or transport processes.

#### 5.4.2 Discharge Capacity as a Function of Current Density

In figures 5.12 and 5.13, the discharge capacity as a function of current density for Hydralloy F 30/9C is given. The alloys are charged and discharged using 200 mAh/g. The data in the two figures are the same but for the latter figure a logarithmic scale was used for the current, and this figure therefore emphasizes the low current region.

In figure 5.14, the discharge capacity as a function of the number of charge/discharge cycles for different charge discharge current densities of a commercial  $AB_5$  type alloy (Hydralloy F 30/9C) is given.

As can be seen from figures 5.12, 5.13 and 5.14 the discharge capacity was strongly dependent on both the current density and the number of cycles. Contrary to the plot of the discharge capacity versus number of charge/discharge cycles (figure 5.11), the high rate discharge capacity was increasing throughout the whole period the alloy was cycled electrochemically. This indicates that there may be kinetic changes going on within a battery throughout its whole lifetime. The findings here does also not contradict the results given by Chartouni *et al.* [168]. As can be seen from the deep discharge capacity curve in figure 5.14, a continuous decrease of the deep discharge capacity was taking place, although the high current discharge capacity was increasing at the same time. The decrease in the deep discharge capacity was assumed to be a result of continuous oxidation of the

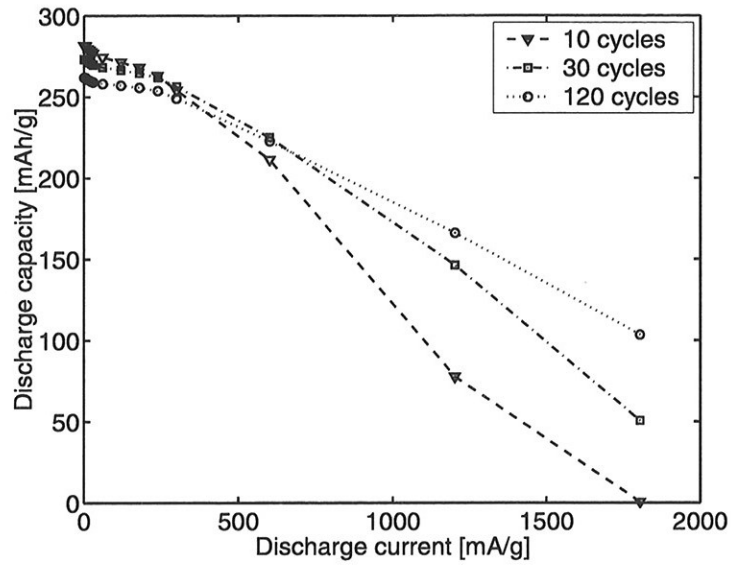


Figure 5.12: *Discharge capacity versus current density for Hydralloy F 30/9C.*

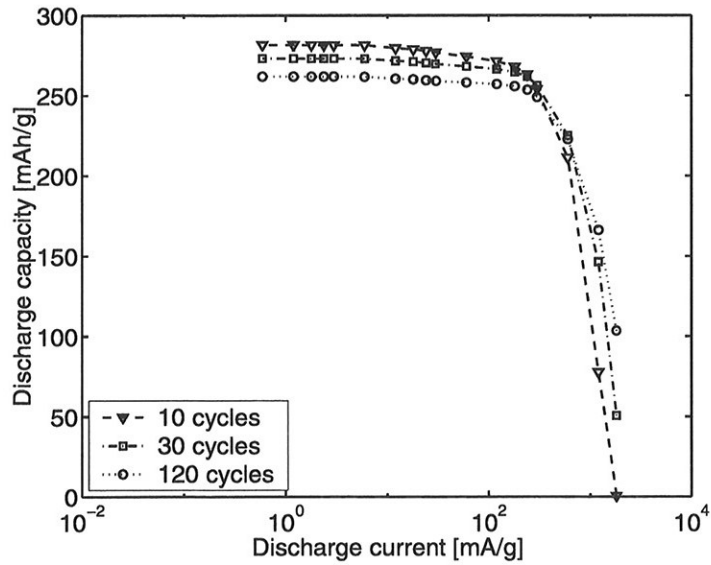


Figure 5.13: *Discharge capacity versus current density for a Hydralloy F 30/9C, logarithmic scale.*

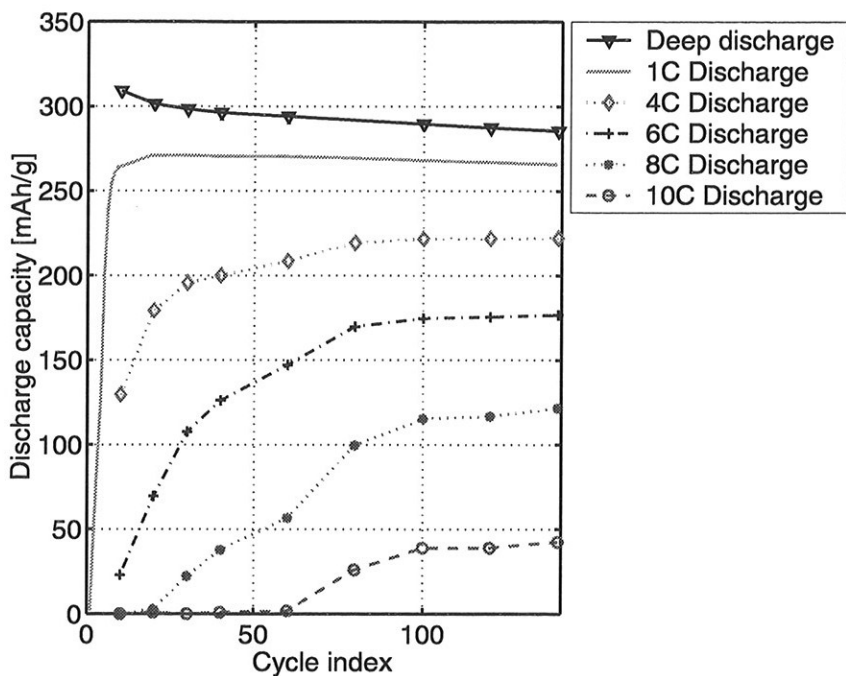


Figure 5.14: Discharge capacity as a function of the number of charge/discharge cycles for different charge discharge current densities of a commercial  $AB_5$  type alloy (Hydralloy F 30/9C).

surface, whereas the increase in the high rate discharge capacity was assumed to be a result of a higher catalytic activity, which resulted in increased activation of the alloy. The latter indicates that different factors governed the high rate discharge capacity and the deep discharge capacity.

In figure 5.15, the discharge capacities as a function of current densities for several  $AB_5$  type alloys with compositions  $(MmNi_{3.7}Mn_{0.3}Al_{0.4}Co_{0.7})$  are given. The alloys are prepared differently: two samples were made by induction melting, one heat treated and the other not. Two samples were made by gas atomizing, one of the latter samples was crushed and heat treated and the other was utilised as raw powder. The alloys are charged and discharged for 10 cycles using 200 mAh/g. In figure 5.16, the discharge capacities as a function of the current density after 240 charge/discharge cycles for the same alloys as shown in figure 5.15 are given.



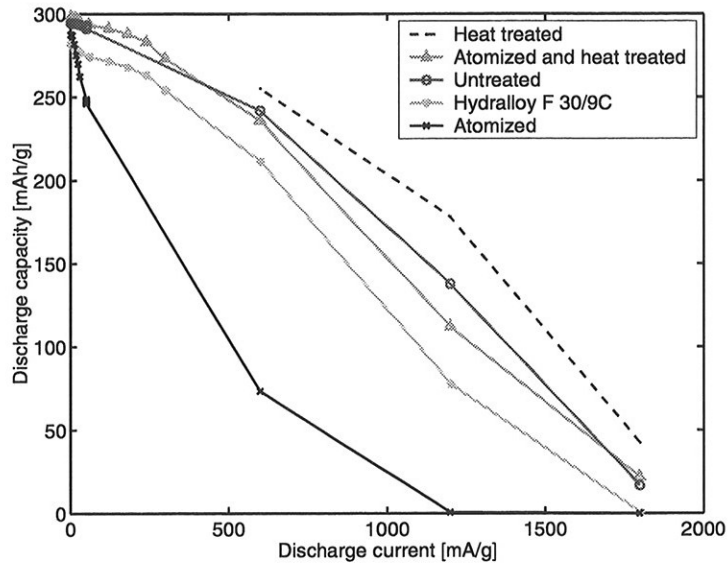


Figure 5.15: Discharge capacity versus current density after 10 cycles for  $AB_5$  type alloys with compositions  $MnNi_{3.7}Mn_{0.3}Al_{0.4}Co_{0.7}$ , prepared differently.

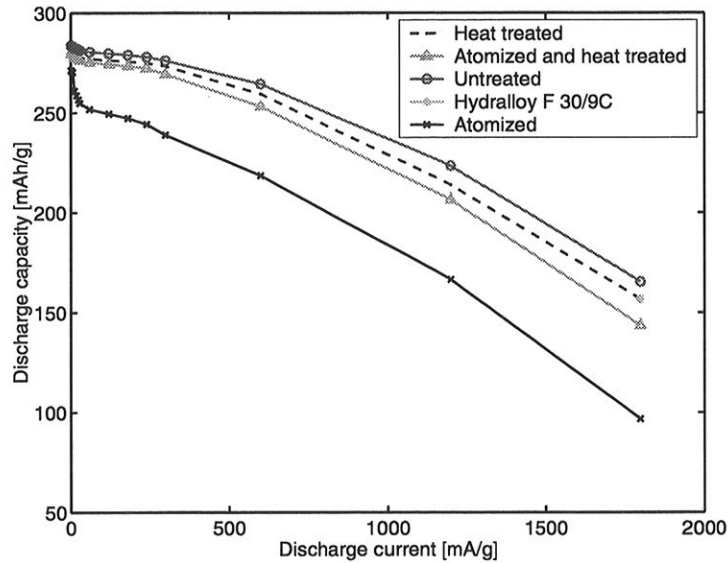


Figure 5.16: Discharge capacity versus current density after 240 cycles for differently prepared  $AB_5$  type alloys with composition  $MnNi_{3.7}Mn_{0.3}Al_{0.4}Co_{0.7}$ .

When comparing figures 5.15 and 5.16, it can be seen that the alloy preparation method was very important for the performance of the electrode during the first charge/discharge cycles. After 240 cycles the differences were negligible if the gas atomized untreated sample was not considered. The reason for the differences between the uncrushed gas atomized sample and the other samples might be that the total surface area per weight was smaller for this sample. A smaller surface area per weight gives a higher current density and consequently a higher overpotential. The figure also clearly indicates that gas atomized alloys should undergo some treatment in order to obtain better performance.

### 5.4.3 Open Circuit Potential Variations

In figure 5.17, the open circuit potential for a commercial  $AB_5$  type alloy (Hydralloy F 30/9C) is given. The depth of discharge is defined with regards to the deep discharge capacity at 20 cycles. As can be seen from figure 5.17, there were no

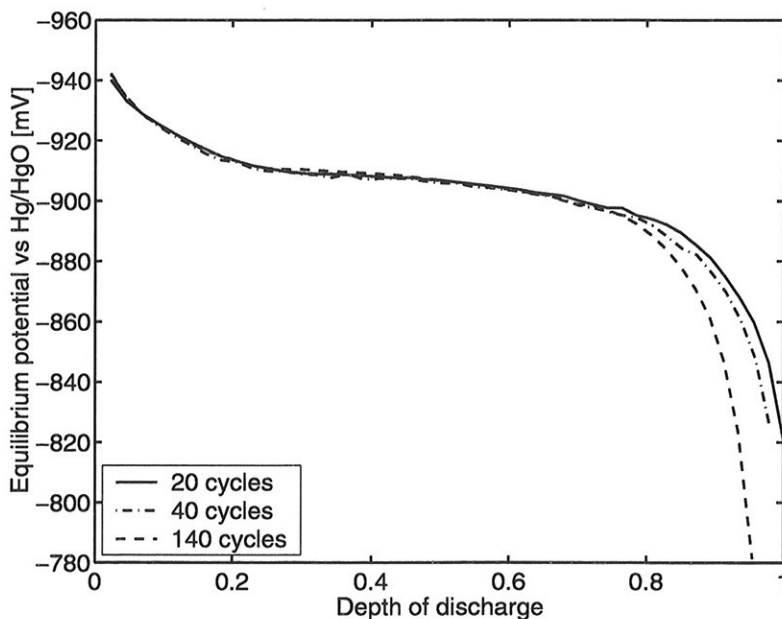


Figure 5.17: *Electrochemical desorption PCT (open circuit potential) diagram for Hydralloy F 30/9C.*

variations in the open circuit potential as a function of the number of charge/discharge cycles. The total discharge capacity did, however, decrease slightly when the electrode was cycled.

#### 5.4.4 Other Potential Measurements

Figure 5.18 shows the variation of the open circuit potential for a completely charged and a completely discharged electrode as a function of the number of charge/discharge cycles executed.

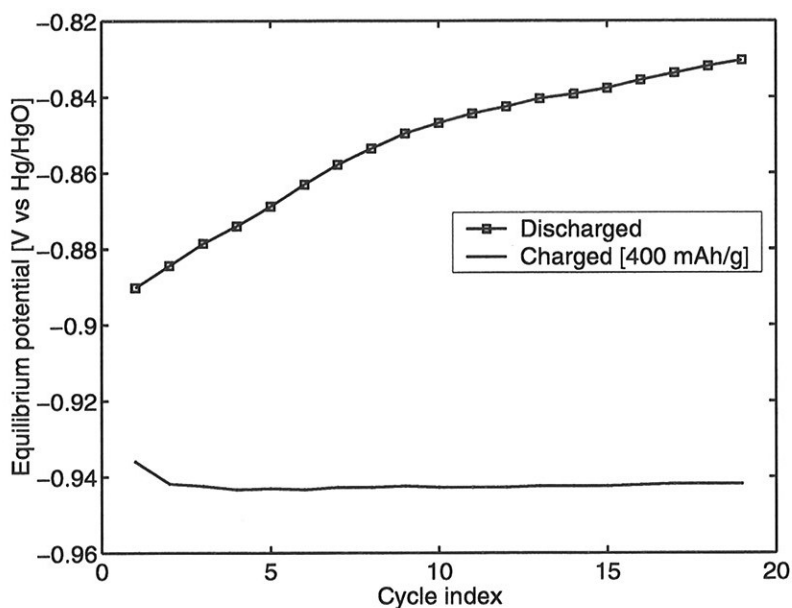


Figure 5.18: Variation of the open circuit potential for a completely charged (400mAh/g,  $E_B$  in figure 5.1) and a completely discharged  $\text{LaNi}_{3.4}\text{Co}_{1.2}\text{Mn}_{0.1}\text{Al}_{0.3}$  electrode (to  $-0.65\text{V}$  versus  $\text{Hg}/\text{HgO}$ ,  $E_D$  in figure 5.1) as a function of the number of cycles.

The electrode was charged with 400 mAh/g ( $\sim 33\%$  overcharge). Charge and discharge currents were 100 mAh/g. Figure 5.18 shows that the open circuit potential for the charged electrode was becoming more negative for the first 2-3 cycles, indicating an increase in the hydrogen content. The open circuit potential for the discharged electrode was increasing rather steadily for the cycles

shown. This indicates that less and less hydrogen was left in the electrode after discharging when the charge/discharge cycling proceeded.

In figure 5.19, the hydrogen evolution potential at the end of the charging period ( $E_A$  in figure 5.1) for  $\text{LaNi}_{3.4}\text{Co}_{1.2}\text{Mn}_{0.1}\text{Al}_{0.3}$  is shown. The electrode is overcharged to 400 mAh/g using currents of 100 mAh/g.

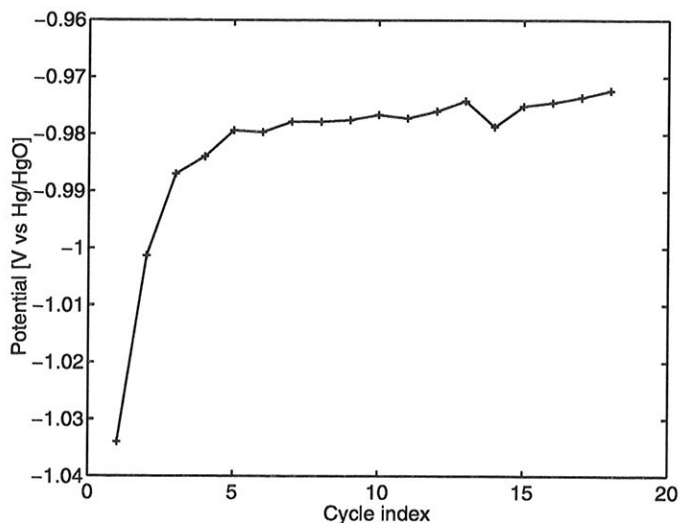


Figure 5.19: End of charge hydrogen evolution potential ( $E_A$  in figure 5.1) for  $\text{LaNi}_{3.4}\text{Co}_{1.2}\text{Mn}_{0.1}\text{Al}_{0.3}$ . The electrode is overcharged using 400 mAh/g, using currents of 100 mAh/g.

The figure shows that the hydrogen evolution potential became less negative (i.e. less overpotential) as the charge/discharge cycling proceeded.

## 5.5 Discussion

### 5.5.1 Constant Current Cycling

As can be seen from figures 5.12 and 5.13 the discharge capacity was strongly dependent on the current density, and from figure 5.14 it is seen that the dependence on the current density changed when the electrode was cycled. During

constant current cycling, the alloys tested were both charged and discharged with relatively high currents (usually in the range of 150-300 mA/g, see section 5.3.3 for additional details). The alloys were with the exception of the experiments shown in figures 5.18 and 5.19 charged up to 300 mAh/g, and no overcharge took place. This yielded a somewhat lower capacity than when electrodes were overcharged and discharged at a lower rate. Since no international standards exist with regards to those parameters, the currents and charging times were chosen to get reliable results in a relatively short time.

By applying Eq 5.4 the reversible hydrogen evolution potential for 6M potassium hydroxide can be calculated to -0.93 V versus Hg/HgO. By comparing with figure 5.9, it can be assumed that the hydrogen evolution reaction can take place during charging at states of charge more than approximately 10% for an activated electrode.

During the first cycle, the potential started at a considerably higher (less negative) value. This was most likely because of reduction of copper, since the copper matrix might have been slightly oxidized before the test is started (the copper oxidation (Cu/Cu<sub>2</sub>O [24]) potential is -460mV versus Hg/HgO[66]). This is shown in figure 5.20, where the potential during charging of a new electrode made of copper (no hydride material) is plotted versus the charge time.

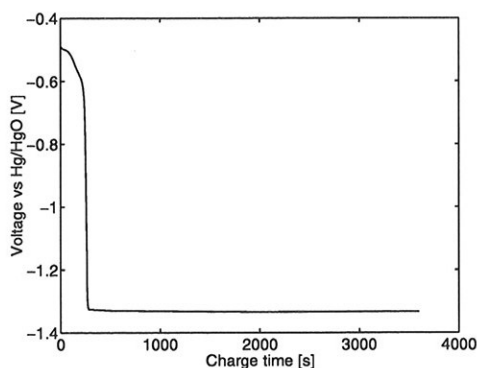


Figure 5.20: *Potential during charging versus the charge time for a copper electrode (no hydride material).*

In figure 5.20, a very similar potential versus time behaviour as for the first cycle in figure 5.9 was observed. This indicates that the oxidized parts of the copper

matrix were reduced during the first minutes of charging. The copper matrix can not be reoxidized during further cycling, since the reversible potential for will not be reached. If using a nickel binder as in batteries, an oxidation of the binder matrix would be possible (see section 3.8.2).

It can also be noted that the slope of the potential relaxation curve (see figure 5.10) is decreasing as the electrode is cycled, indicating that the equalizing times of the concentration gradients are increasing. The change in the equalization times can be resulting from a decrease of the (apparent) diffusion coefficient. If the amount of hydrogen left in the electrode becomes less and less as the electrode is cycled (increased ratio of  $\alpha$  phase), and the diffusion coefficient in the  $\alpha$  phase is lower than in the  $\beta$  phase (see section 3.9 for additional details), this could explain the shape of the curve.

### 5.5.2 Open Circuit Potential Measurements

The open circuit potential plot shown in figure 5.17 indicated that the open circuit potential did not change with the number of cycles, indicating that the chosen procedure gives reproducible results. It also showed that the open circuit potential monitored around cycle No. 20 gives reliable results.

### 5.5.3 Rate Measurements

The kinetic measurements displayed in figure 5.14 show that the kinetics of the alloy was very dependent on the number of charge/discharge cycles performed. When reporting information on the kinetics of the alloy, the number of charge/discharge cycles performed prior to the measurements should always be reported. Both the charge and discharge current used prior to performing the measurements should also be reported, as well as the amount of charge added to the electrode during charging.

The rate measurement procedure is described in detail in section 5.1.3 and also shown in figure 5.3. This procedure enabled a start-up with a high current, preventing oxide formation and possible reactivation processes after discharging with low currents. In figure 5.21, a plot of the discharge capacity during the cycles before, and after two rate measurements for electrodes charged both with 300mAh/g and 400mAh/g is shown.

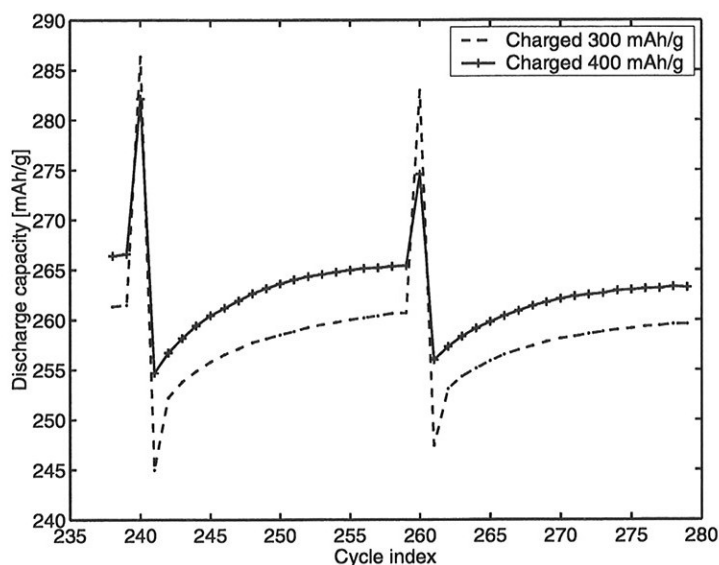


Figure 5.21: Plot of the discharge capacity during the cycles before and after two deep discharge measurement for electrodes charged both with 300mAh/g and 400mAh/g.

From figure 5.21 one can see that some reactivation was required. One could as a first approximation assume that this could be a result of a decrease in the charge transferred to the electrode, but the plot of the 400 mAh/g charged electrode showed the same behaviour. It was therefore assumed that the deactivation of the surface was a result of the oxidation of the surface during the deep discharge. From section 3.8 it is seen that all elements in the  $AB_5$  type alloy except cobalt can oxidize around the  $-0.6V$  versus Hg/HgO cutoff potential. After the deep discharge, the surface is therefore assumed to be cobalt enriched. During the reactivation period, nickel can be electrodeposited during charging, whereas the elements that are easily oxidized are further depleted from the surface region during discharge.

It is also worthwhile to note that the deep discharge capacity was lower for the electrode charged with 400 mAh/g than the electrode charged with 300 mAh/g. The reason for this is assumed to be that the increased rate of hydrogen evolution during overcharging takes electrode material away from the electrode.

In figure 5.22, accumulated discharge capacities versus number of discharge cycles for various discharge currents are shown.

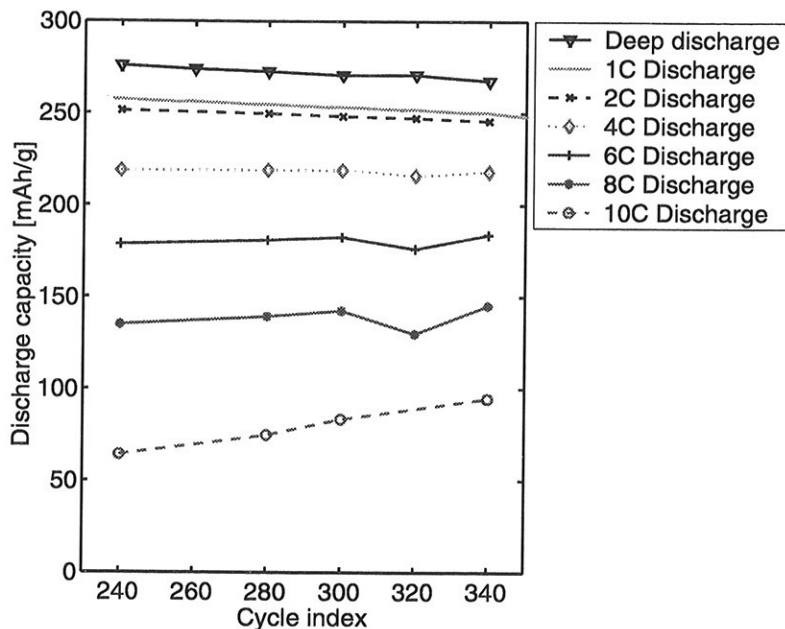


Figure 5.22: Accumulated discharge capacities versus number of discharge cycles for various discharge currents.

As can be seen from figure 5.22, the accumulated 8C discharge was lower when the 10C discharge was not performed before the 8C discharge. Ideally, the line for the 8C discharge should be straight. This was, however, not the case. The way the measurement was done, is described in section 5.3, and it seems clear that the break between the 10C discharge and the 8C discharge smoothed out some concentration gradients. This indicates that diffusion processes, either in the electrode itself or in the electrolyte were of importance for processes requiring a high current over a period of time. The presence of transport phenomena are also visible in the plot of the potential during the break after discharge for a normal charge/discharge cycle, figure 5.10.

The advantages and disadvantages of the method used for kinetic measurements can be summarized as follows:



- The high current capacity showed a very strong dependence upon the number of charge/discharge cycles performed.
- A method with charging between the measurements (i.e. one constant current pulse per cycle) requires special attention. Charging with the same amount for every charge may give a considerable overcharging of the electrode and possibly an higher apparent capacity due to the overcharge. If starting with a low current, reactivation may be required to make the electrode perform normally for high discharge currents. It should furthermore be noted that too much hydrogen evolution may lead to a longer reactivation period and inferior maximum discharge capacity as shown in figure 5.21.
- The discharge of the electrode starts at different depths of discharge, giving a break in the discharge, and consequently a slightly higher total discharge capacity than if the discharge was started at a fully charged electrode for each current.

#### 5.5.4 Other Potential Measurements

The changes in the open circuit potential for the discharged electrode shown in figure 5.18 are quite interesting. The shape of the curve might resemble the surface composition on the metal hydride particles in the electrode. If the surface becomes more and more depleted in rare earth metals and nickel is enriched, the surface potential is expected to change.

If figures 5.17 and 5.18 are compared, there are indications that the open circuit potential is very dependent on the amount of hydrogen in the electrode. The "discharge activation" appears to be slower than the "charge activation". Figure 5.18 furthermore indicates that the main part of the activation is not exposure of new alloy surface to the electrolyte. If the main effect was caused by an area change, the potential changes in figure 5.18 most likely would have been smaller. On the other hand, an increase in the surface area as a result of cracking, would decrease the current density. A lower current density would decrease the overpotential which in turn could lower the amount of hydrogen left in the electrode after discharge.

Figure 5.19 indicates that the catalytic activity for hydrogen evolution increased sharply with the number of charge/discharge cycles during the first cycles.

### 5.5.5 Reproducibility

According to Kuriyama *et al.* [169], vacuum impregnation of the electrolyte before starting the electrochemical cycling or letting the electrode rest in the electrolyte for about half an hour prior to starting measurements, improves the reproducibility of the results obtained during activation of the electrode. When the electrode is activated, the reproducibility is far less dependent on the pretreatment.

No measurements were compared before the 10<sup>th</sup> charge/discharge cycle. Several of the measurements were carried out with two or more parallels. Those experiments showed little or no difference between the parallels.

### 5.5.6 Experimental Challenges

Several experimental challenges are associated with hydrogen metal systems since all kinetic properties are affected by:

- Temperature;
- External pressure, as a pressure build-up in the test cell during measurements could affect the kinetics (see chapter 6 for more details);
- State of charge. The kinetics of the reaction are strongly affected by the state of charge of the electrode (see chapter 8 for more details). The electrode area is also affected by the state of charge (see Eq 5.7 and section 3.7).

The electrode construction gives the surface of the alloy a rough and porous character with a very large electrode surface area (see section 5.3 for a more detailed description on how the electrodes are made). Because of the cracking of the hydride electrode material during cycling, electrochemical techniques based on a known surface area become non-applicable. This limits and complicates the electrochemical characterization of metal hydride electrodes. In addition the properties change with the state of charge and the number of charge/discharge cycles performed [170–172].

The change in surface area due to volume expansion can, when assuming spherical hydride particles, be found by using a simple geometrical consideration<sup>1</sup>

$$A_H = A_M \left( 3 \sqrt{1 + \frac{\Delta V}{V}} \right)^2 \quad (5.7)$$

Here  $A_H$  is surface area of fully hydride phase and  $A_M$  is surface area of metal without any hydrogen. By using Eq 5.7, one can see that for a commercial hydrogen storage alloy with a volume expansion less than 15%, change in surface area will be less than 10%.

In order to obtain reliable, reproducible, and results free from artifacts, all these factors should be controlled and monitored. A further complication is that the electrode is made of pressed hydride forming alloy particles and therefore has an unknown initial surface. During prolonged cycling of the metal hydride electrodes, the surface area increases because of cracking of the metal hydride alloy (see section 3.7 for additional details).

## 5.6 Conclusions

The kinetics of a metal hydride electrode is changing throughout its lifetime and with pre history. The nature of this change is still not clearly known, and plots of the types presented in figures 5.14, 5.18, 5.19, 5.21, and 5.22 have not to the author's knowledge been previously reported in literature. Normally, only a plot of the discharge capacity as a function of the discharge current is shown. As shown in this chapter, this is not sufficient to describe the kinetics of an alloy.

The activation time is highly dependent on the charge/discharge current. The lower the current, the faster the activation. An electrode activated for a low current, however, is not necessarily activated for a higher current. The number of cycles needed for activating an alloy is therefore not a constant figure, but depends on the pre history of this electrode. For high current applications, the activation might need as much as 100 cycles, whereas for low current applications, only 5-10 activation cycles might be needed with the same current used for activation. Pretreatment of the alloy might enhance the activation considerably. The activation is also dependent on the amount of charge transferred to the metal hydride material.

<sup>1</sup>Applying  $V_{\text{sphere}} = \frac{4}{3}\pi r^3$  and  $A_{\text{sphere}} = 4\pi r^2$  [173].



## Chapter 6

# Electrochemical Properties as a Function of External Pressure

*Until now the application of relatively high inert gas pressure to characterize the electrochemical properties of metal hydride electrodes has to the authors knowledge not previously been reported in literature. In the following, a first introduction is given.*

### 6.1 Introduction

The characterization of alloys with high plateau pressures<sup>1</sup> can be performed under high inert gas pressure. In this chapter it is shown that the application of high external inert gas pressures more precisely suppresses the hydrogen evolution reaction during charging. This reaction normally interferes with the characterization of metal hydride electrodes.

### 6.2 Experimental

Alloys were prepared as described in section 4.2, and various properties of the alloys are shown in section 4.3. The electrodes were prepared as described in

---

<sup>1</sup>High plateau pressures are in this chapter limited to pressures higher than ambient pressure, but lower than 30 bar.

section 5.3. A standard electrochemical setup (as the one shown in figure 5.4) was mounted inside an autoclave as shown in figure 6.1. An external pressure

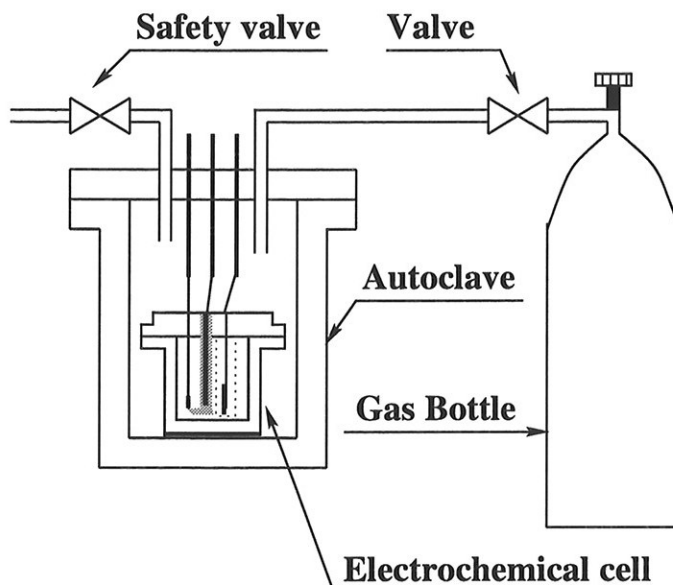


Figure 6.1: *The electrochemical setup used for measurements under elevated pressures.*

was applied inside the autoclave using a gas bottle. Argon was used to pressurize the autoclave in all experiments. For electrochemical cycling, the electrodes were all charged with 300mAh/g. This is below the maximum storage capacity for  $\text{LaNi}_5$ . For safety reasons the overcharging and consequently the hydrogen evolution reaction was minimized during charging. Simultaneous hydrogen evolution from the metal hydride electrode and oxygen evolution from the platinum counter electrode could in the presence of platinum be a possible security hazard. In addition small flow of inert gas through the autoclave was maintained continuously during all measurements to remove hydrogen from the autoclave atmosphere. Electrochemical cycling was performed as described in section 5.1.1. For the experiments with  $\text{MmNi}_5$  alloys, 200 mA/g were applied for charge/discharge, whereas for the  $\text{LaNi}_5$  experiments, 300 mA/g were applied. Rate measurements were performed as described in section 5.3.3.

## 6.3 Results and Discussion

### 6.3.1 Electrochemical Cycling

#### Activation pressure relation

In figure 6.2, the discharge capacity as a function of the number of charge/discharge cycles for  $\text{La}_{0.60}\text{Ce}_{0.18}\text{Nd}_{0.18}\text{Pr}_{0.04}\text{Ni}_5$  at different argon pressures is given. The alloy has a desorption plateau pressure,  $P_{d,25}$ , of 6.1 bar and an absorption plateau pressure,  $P_{a,25}$ , of 14 bar at 25°C (see table 4.2). From the figure it can

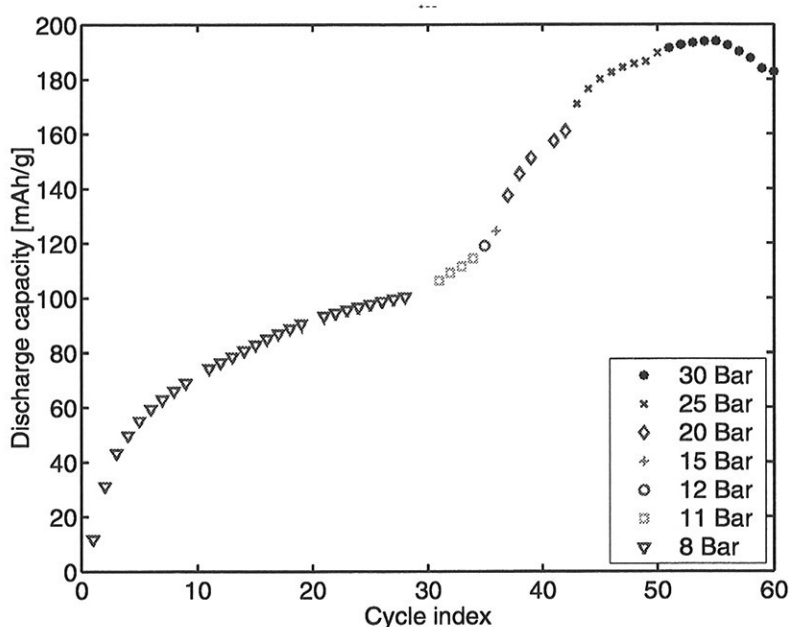


Figure 6.2: Discharge capacity as a function of the number of charge/discharge cycles for  $\text{La}_{0.60}\text{Ce}_{0.18}\text{Nd}_{0.18}\text{Pr}_{0.04}\text{Ni}_5$  ( $P_{a,25}=14$  bar,  $P_{d,25} = 6.1$  bar) when the pressure is gradually increased.

be observed that an activation period succeeded every pressure increase, until the alloy started to corrode. Some of the decrease of the discharge capacity for the highest pressure could also be a result of a decrease of the external pressure because of difficulties maintaining the pressure. The valve shown in figure 6.1

started leaking when pressures above approximately 27 bar were applied. The true pressure might therefore likely have been slightly lower than 30 bar. The 30 bar discharge capacity after 60 cycles was below the 25 bar discharge capacity after 48 cycles, so some corrosion or electrode deterioration was assumed to have taken place. The figure shows that the question whether the electrode is activated or not, can not simply be answered by yes or no, but requires additional explanation (see also the discussion of the kinetic measurements given in section 5.5.3). From figure 6.2 it can be seen that the electrode is not activated solely for a certain current, but also for a certain external pressure. It is likely that new parts of the hydrogen storage alloy are activated when the pressure is increased.

### Discharge capacity

Figure 6.3 is a plot of the discharge capacity for  $\text{LaNi}_5$  as a function of the number of charge/discharge cycles for four different pressures (3.5, 7.5, 15, and 25 bar) is shown. All electrodes were charged with the same amount of charge,

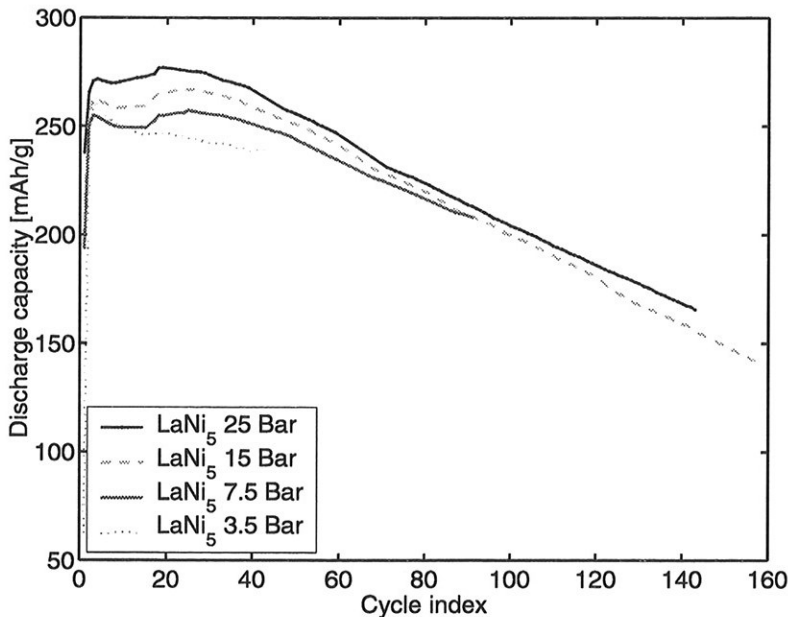


Figure 6.3: Discharge capacity for  $\text{LaNi}_5$  as a function of the number of charge/discharge cycles for four different pressures (3.5, 7.5, 15 and 25 bar).



300 mAh/g. As can be seen from the figure, the discharge capacity was higher when the external pressure was higher. This was assumed to be a result of an improved charge efficiency when charging at higher pressures. More specifically, the hydrogen evolution side reaction appeared to be suppressed when the external pressure was increased.

In figure 6.4, the PC absorption and desorption isotherms at 25°C for LaNi<sub>5</sub> are given. The  $\beta$  phase region is emphasized.

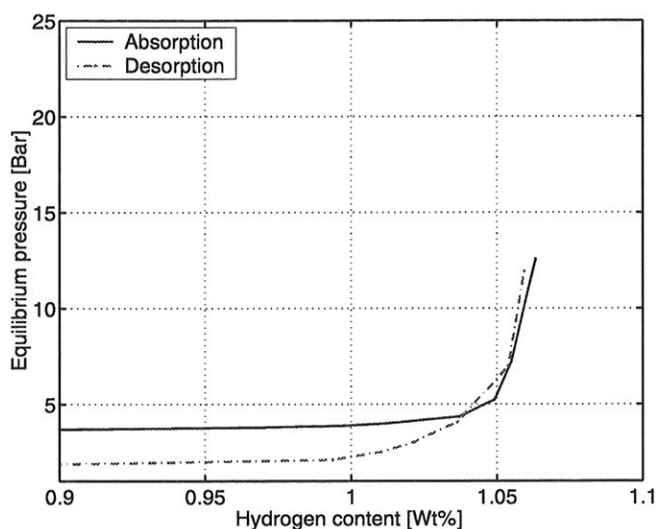


Figure 6.4: PC absorption and desorption isotherms at 25°C for LaNi<sub>5</sub>. The  $\beta$  phase region is emphasized.

From the figure, the additional hydrogen storage as solid solution in the  $\beta$  phase can be estimated to have been in the range of 2-4% of the total storage in the  $\beta$  phase. For an alloy with a discharge capacity of approximately 260 mAh/g, this additional storage will be in the range of 5-10 mAh/g. The maximum hydrogen storage capacity in figure 6.4 is quite low ( $\sim 1$  wt%), but a parallel measurement showed a maximum hydrogen content of 1.4 wt%, which is closer to the literature value given in table 3.2. This other measurement did not, however, provide the absorption isotherm.

The theoretical discharge capacity of LaNi<sub>5</sub> is 375 mAh/g [6]. The discharged capacities for all pressures were well below that number. It is therefore not certain

whether solid solution of hydrogen in the  $\beta$  phase was ever reached during the measurements.

Since all electrodes were charged with the same amount of charge, it is reasonable to assume that the differences in the discharged capacities were solely due to hydrogen evolution during the charging process. In Eq 2.7, the reversible hydrogen evolution potential is given as a function of the hydrogen pressure. If the hydrogen pressure in the electrolyte is assumed to equal the applied pressure, the pressure difference between 3.5 bar and 25 bar corresponds to a difference in the reversible hydrogen evolution potential of approximately 25 mV. By comparing figure 5.17 and Eq 2.7, the hydrogen evolution reaction can be assumed to be a side reaction even for low plateau pressure alloys above approximately 10% charged.

In table 6.1, the discharge capacities for for  $\text{LaNi}_5$  for the first charge/discharge cycles for four different pressures (3.5, 7.5, 15 and 25 bar) are given.  $C_1$ ,  $C_2$  and

Table 6.1: *Discharge capacities for for  $\text{LaNi}_5$  for the first charge/discharge cycles for four different pressures (3.5, 7.5, 15, and 25 bar).*

Pressure Bar	$C_1$ mAh/g	$C_2$ mAh/g	$C_3$ mAh/g
3.5	62.5	246.7	261.6
7.5	194.1	250.3	254.9
15	206.4	255.4	262.7
25	237.9	265.8	270.9

$C_3$  are the discharge capacities for cycles one, two and three respectively. As can be seen from the table, an increased external pressure led to a faster activation even though the lowest pressure is above the hydrogen absorption pressure (3.4 bar).

In figure 6.5, the discharge capacity as a function of the number of charge/discharge cycles for  $\text{La}_{0.60}\text{Ce}_{0.04}\text{Nd}_{0.18}\text{Pr}_{0.18}\text{Ni}_5$  for two different external pressures is displayed (atmospheric and 25 bar). The alloy had an absorption plateau pressure,  $P_{a,25}$ , of 9.0 bar, and a desorption plateau pressure,  $P_{d,25}$ , of 5.3 bar at 25°C. Figures 6.2, 6.3 and 6.5 illustrate that the plateau pressure for hydrogen storage alloys used for metal hydride electrodes in ambient pressure conditions

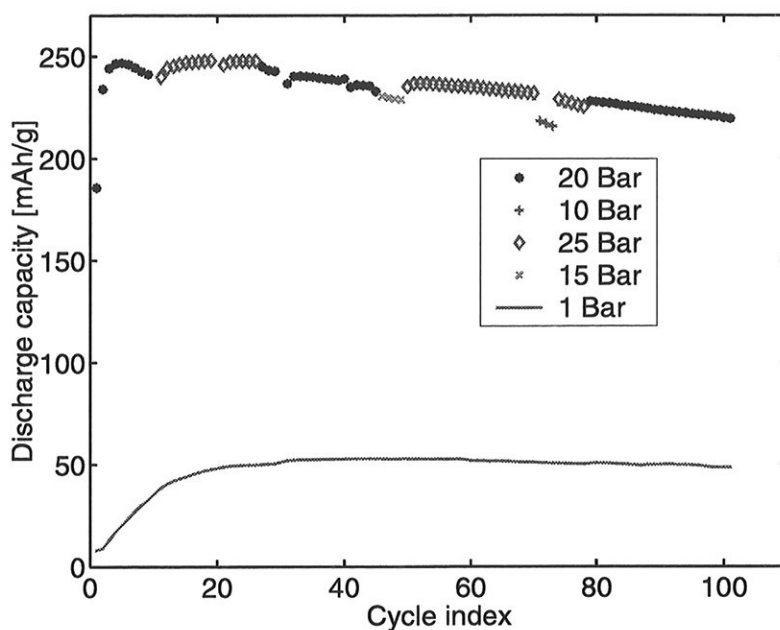


Figure 6.5: Discharge capacity as a function of the number of charge/discharge cycles for  $\text{La}_{0.60}\text{Ce}_{0.04}\text{Nd}_{0.18}\text{Pr}_{0.18}\text{Ni}_5$  electrodes for 1 and  $\sim 25$  bar.

should be well below 1 bar. This is necessary as a higher plateau pressure will give an enhanced hydrogen evolution rate and consequently a lower discharge capacity. If the pressure is below the plateau pressure of the alloy, the  $\beta$  phase will never form (charge/discharge of the  $\alpha$  phase), and naturally an increase in the hydrogen evolution rate is to be expected.

The plateau slope influence the discharge capacity in two ways: first, a high plateau slope will enable some  $\beta$  phase hydrogen storage even for external pressures well below the average plateau pressure (consult the curve for 1 bar external pressure curve in figure 6.5). Secondly, the maximum storage capacity becomes dependent on the external pressure even for pressures well above the plateau pressure. It is important to remember though, that some hydrogen may be stored as solid solution in the  $\beta$  phase (path C-D-E in figure 3.2).

### 6.3.2 Discharge Capacity as a Function of Current Density

Figure 6.6 shows how the discharge capacity versus discharge current of  $\text{LaNi}_5$  after 10 charge/discharge cycles depend on the external pressure.

From the latter figure, it can be denoted that the high rate discharge capacity for  $\text{LaNi}_5$  at 10 charge/discharge cycles increased when the external pressure was increased. The maximum storage capacity was also higher at higher pressures. This might be explained by a more rapid activation at higher pressures.

In figure 6.7, the discharge kinetics after 40 charge/discharge cycles is shown.

From the figure, it can be denoted that even though there is no significant difference in the maximum discharge capacity, the rates were higher at higher pressures. The electrode pressurized at 3.5 bar was activated completely since the maximum discharge capacity was reached. This indicates that a higher external pressure (within limits) did not have any negative effect on the properties of the electrode, and due to an enhanced activation, the high current performance was as well better.

In figure 6.8 the discharge capacity as a function of the number of charge/discharge cycles for  $\text{LaNi}_5$  at two different pressures is shown.

Figures 6.7 and 6.8 show that the high current discharge capacity for  $\text{LaNi}_5$  at 3.5 bar induced a more marked decay of the high current discharge capacity than the discharge capacity at 25 bar. This observation is of importance as it indicates that the catalytic activity decays when the hydrogen evolution rate increased. This is an indication that the hydrogen evolution created convection, and possibly removed catalytic sites from the alloy surface. It is worthwhile to notice that the deep discharge capacity remained unchanged. The observed trends in figure 6.8 furthermore indicate that there were diffusion limitations in the system for  $\text{LaNi}_5$ , which has a considerably higher diffusion coefficient than the  $\text{LaNi}_{5-x}\text{B}_x$  system. (See sections 3.9 and 5.5.3 for additional details concerning diffusion and evaluation of rate measurements.)

In table 6.2 the open circuit potential and the discharge overpotential for an A site substituted and a B site substituted alloy is shown.

In the table,  $E_{oc}$  is the open circuit potential for a charged electrode ( $E_B$  in figure 5.1) and  $\eta$  is the discharge overpotential at onset of discharge ( $t=t_B$  in

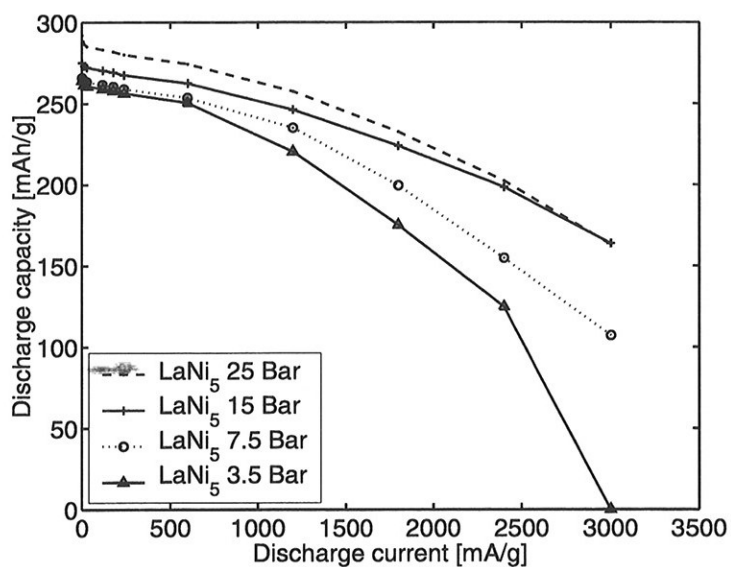


Figure 6.6: Discharge capacity versus discharge current after 10 charge/discharge cycles for  $\text{LaNi}_5$  at various pressures.

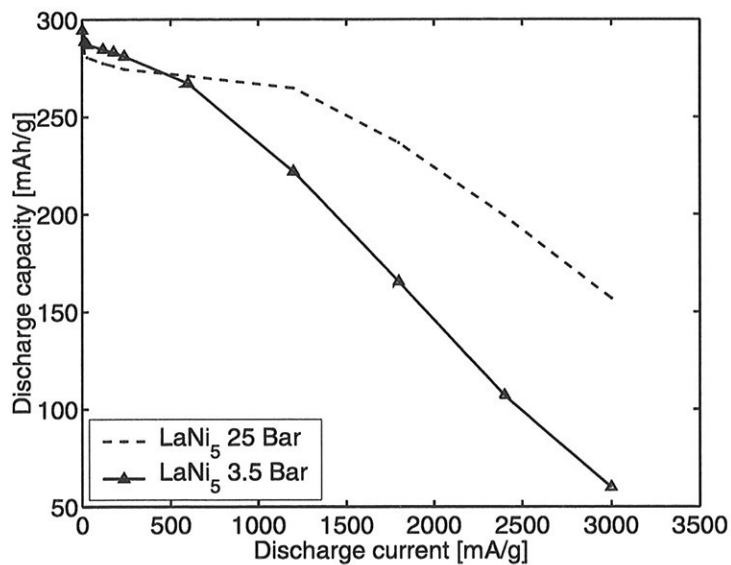


Figure 6.7: Discharge capacity versus discharge current after 40 charge/discharge cycles for  $\text{LaNi}_5$  at different pressures ( $P_a=3.4$  bar, see table 4.2).

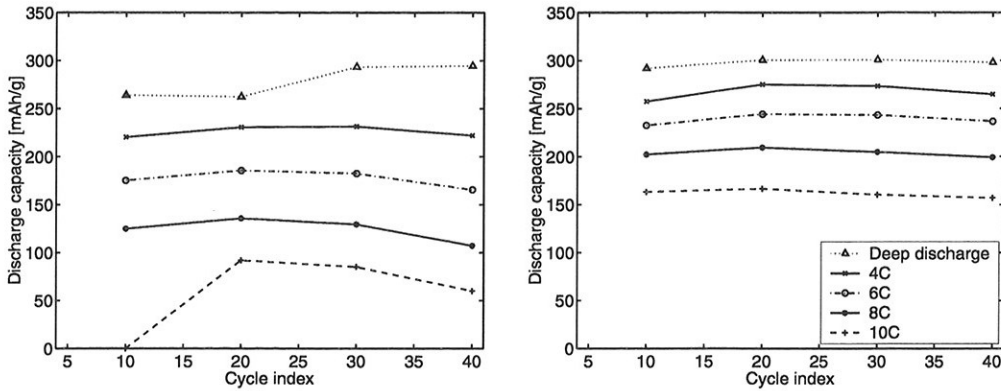


Figure 6.8: Discharge capacity as a function of the number of charge/discharge cycles for  $\text{LaNi}_5$  at two different pressures. Left: 3.5 bar. Right: 25 bar (same legend for both graphs).

Table 6.2: Open circuit potential and the discharge overpotential for an A site substituted and a B site substituted alloy.

Alloy composition	$E_{oc,50}$ [mV]	$\eta_{50}$ [mV]	$E_{oc,100}$ [mV]	$\eta_{100}$ [mV]
$\text{La}_{0.60}\text{Ce}_{0.04}\text{Nd}_{0.18}\text{Pr}_{0.18}\text{Ni}_5$	-982.3	23.3	-982.5	19.7
$\text{MmNi}_{3.7}\text{Mn}_{0.3}\text{Al}_{0.4}\text{Co}_{0.7}$	-949.5	27.3	-950.7	23.9

figure 5.1). Subscript 50 and 100 represents values for 50 and 100 charge/discharge cycles respectively. When comparing the overpotentials in table 6.2, it can be deduced that the B site substituted alloy showed a reduced catalytic activity of the surface compared to the A site substituted alloy even though the A substituted alloy had a very low cerium content. This indicates that catalytic surface sites have a high nickel content, i.e. that nickel is a better catalyst than the B-alloy ( $\text{Ni}_{0.74}\text{Mn}_{0.06}\text{Al}_{0.08}\text{Co}_{0.14}$ ).

It is seen, however, that the differences in the overpotentials were relatively small compared to the differences in the open circuit potentials.

The difference in the open circuit voltage between the two alloys is assumed to be more important for the performance of the alloy. This difference in open circuit potential is a result of the difference in the plateau pressure between the two

alloys. The relation between the plateau pressure and the open circuit potential was elaborated in section 5.1.2.

In figure 6.9, relative capacity discharged versus discharge current density for different alloy systems<sup>2</sup> at different external pressures after 30 charge/discharge cycles are shown.

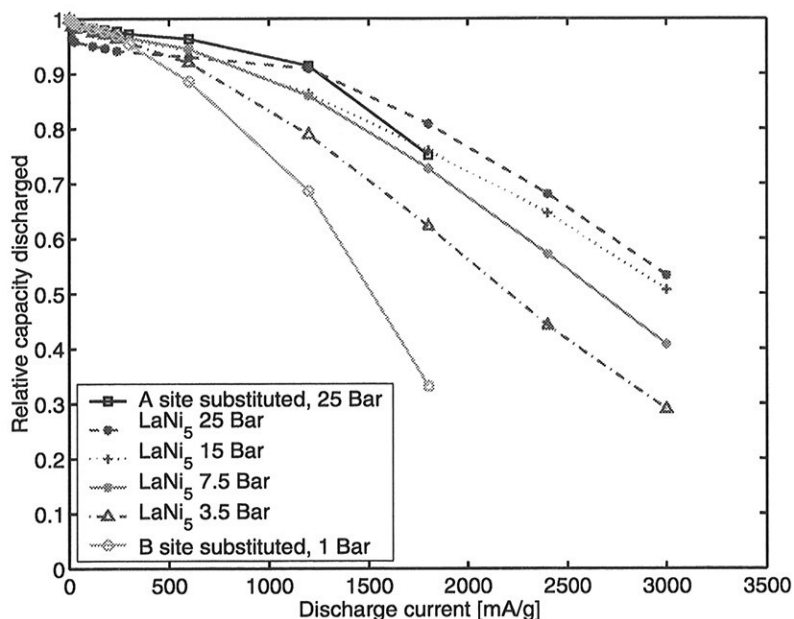


Figure 6.9: *Relative capacity discharged versus discharge current density for different alloy systems at different external pressures after 30 charge/discharge cycles.*

When comparing the rate measurements in figure 6.9, it is found that B site substitution reduced the high rate discharge capability. From that comparison it can be seen that A site substitution did not decrease the high rate discharge capability compared to LaNi<sub>5</sub>. This indicates that the presence of other rare earth metals than lanthanum is good for the discharge performance of metal hydride electrodes. Unfortunately, the high rate discharge measurements on A and B site substituted alloys were not performed for the highest discharge currents.

<sup>2</sup>A-site substituted alloy composition: La<sub>0.60</sub>Ce<sub>0.04</sub>Nd<sub>0.18</sub>Pr<sub>0.18</sub>Ni<sub>5</sub>; B site substituted alloy composition: MmNi<sub>3.7</sub>Mn<sub>0.3</sub>Al<sub>0.4</sub>Co<sub>0.7</sub>

By comparing with the discussion in section 5.5.3 it can be assumed that the discharge capacity at 1800 mAh/g would have been slightly higher for the A and B substituted alloys if the same test procedure as for the LaNi<sub>5</sub> samples was used. Furthermore, it can be assumed that the best comparison between the high rate discharge performance of all the different alloys is done at approximately 1200 mAh/g.

The differences in the high rate dischargeability for LaNi<sub>5</sub> with different applied external pressures are notable. One could expect that the same alloy had the same high rate discharge capacity, regardless of the external pressure. There are two differences that might explain this. Firstly, faster activation was observed for electrodes cycled under higher pressure, and the alloys cycled under lower pressures could as such be less activated

Secondly, in section 6.3.1 it is shown that the differences in the reversible hydrogen evolution potential is around 25mV for the pressures applied. This difference is about the same as the overpotential for the discharge reaction<sup>3</sup> shown in table 6.2. It is therefore reasonable to assume that the rate of the hydrogen evolution was quite different for the different external pressures applied. For a fractured electrode surface formed by selective oxidation of elements (such as lanthanides) in the hydride forming alloy, even a small increase in the hydrogen evolution rate could rearrange the surface structure. Such a rearrangement would most likely smoothen the electrode surface, giving a smaller effective surface area. Hydrogen bubbles remaining in the electrode structure after charging could also block parts of the electrode surface. A smaller surface would give a higher overpotential for the same current, lowering the discharge capacity.

### 6.3.3 Diffusion Gradients

After the electrodes were discharged to the cutoff potential, there was a break, equalizing of the hydrogen concentration in the electrode before the next charging. In figure 6.10 a plot of the potential versus time during this break is shown for different alloys after 50 charge/discharge cycles.

From the figure, it appears that the concentration gradients of hydrogen in the electrode are higher for B site substituted alloys in general. The B site substituted

---

<sup>3</sup>The overpotential for the charge reaction was assumed to be around the same as the discharge overpotential (see section 5.4.1).



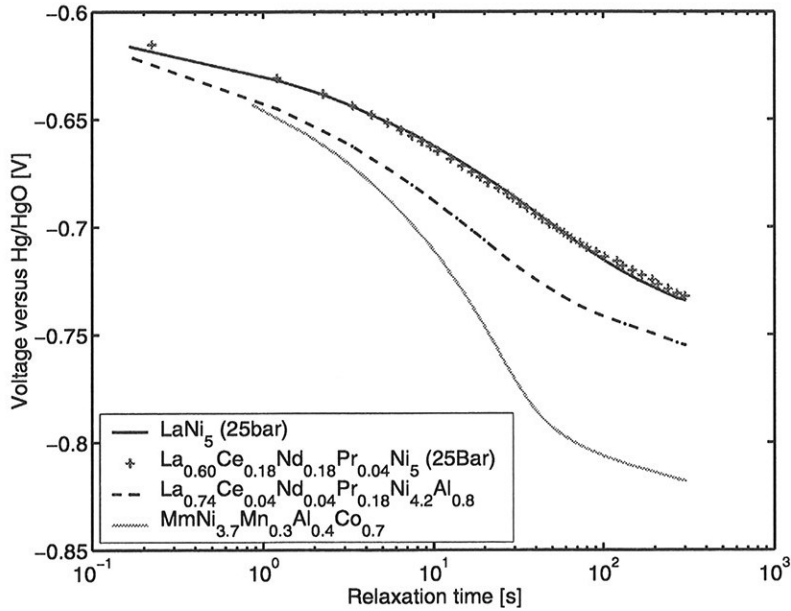


Figure 6.10: Plot of the surface potential versus time during the break after discharge for different alloys after 50 charge/discharge cycles.

alloy containing cobalt had a markedly higher concentration gradient of hydrogen than all the other alloys. As seen from section 3.4.3, cobalt prevents  $AB_5$  type alloys from cracking during cycling. Alloys containing cobalt will therefore have a lower surface to volume ratio compared to alloys not containing cobalt and hence have a longer diffusion path for hydrogen in the metal hydride particles in the electrode.

Since the surface to volume ratio is lower for alloys exhibiting less cracking, the current density during both charge and discharge will also be higher for the cobalt containing alloys. The surface overpotential compared to alloys without cobalt will also be higher since the surface overpotential is proportional to the logarithm of the current density [154].

A comparison of figure 6.9 to the theory regarding the transport properties (section 3.9.2) furthermore indicated that the rate of diffusion of hydrogen might be higher for alloys with a high plateau pressure.

Consequently, there are several effects working in the same direction, but it seems clear that high plateau pressure alloys are discharged more (less hydrogen left in the electrode) during a discharge with the same current. The difference in the hydrogen content in the alloys is approximately 100mV, which corresponds to roughly three decades of equivalent hydrogen pressure.

## 6.4 Conclusion

When an electrode made of an alloy with a relatively high plateau pressure was cycled under a moderate external pressure until the electrode reached a constant discharge capacity, a new activation process was needed when the pressure was increased. This indicates that the activated state was dependent on several factors, which need to be examined individually as well as combined to gain a complete understanding of the kinetics.

An increase of the high rate discharge capacity with increasing external pressure was observed. The results indicate that the overpotential for the discharge reaction increases as the hydrogen evolution rate during charging increase. This increase might either be a result of mechanical rearrangement of the surface during hydrogen evolution or blocking of electrode surface because of remaining hydrogen gas bubbles in the electrode structure after charging.

The results also indicated that that nickel is a better catalyst than the mixture of alloys used instead of nickel in commercial batteries ( $\text{Ni}_{0.74}\text{Mn}_{0.06}\text{Al}_{0.08}\text{Co}_{0.14}$ ). The results also indicated a higher rate of the hydrogen diffusion than B site substituted alloys. Pressurized battery systems with a metal hydride electrode made of an alloy with a high plateau pressure are promising candidates for applications requiring a high discharge capacity at high current densities.

## Chapter 7

# Impedance Modelling

*A very important electrochemical characterization technique is the electrochemical impedance spectroscopy (EIS). In the following, it is shown that the impedance response of metal hydride electrodes can be modelled in a systematic way.*

Some of the impedance modelling given in this chapter has previously been published by the author [174].

Impedance characterization can be used to provide the following information:

- The overall reaction rate;
- The rate of sub processes. An important characteristics of this technique is that the kinetic contribution from sub processes can to a certain extent be separated and evaluated independently. This provides important information about the reaction mechanism; and
- The rate of the overall reaction and the various sub processes as a function of the state of charge.

Furthermore, the EIS technique provides a non-destructive method for elaborating the electrochemical properties of the electrode, as all data are obtained with a minimum polarization of the electrode.

## 7.1 Introduction to Impedance Characterization

A brief introduction to the principles of the EIS technique will be given in the following section. For a more detailed description, see for example the paper by Lasia [175].

EIS is a very sensitive technique, but it is usually not sufficient to solve all the questions which exist with regards to the kinetics. Like any other electrochemical technique, impedance spectroscopy can not be regarded as a "stand-alone" method for model identification because the response of a system to a periodic perturbation does not provide a direct measure of the governing physical phenomena [176]. In figures 7.1 and 7.2, two examples of Complex plane plots and equivalent circuit analysis for two different processes are given [177].

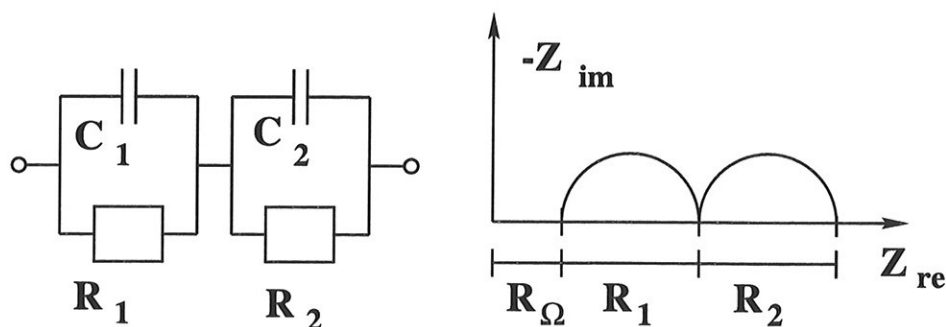


Figure 7.1: *Equivalent circuit and example of a corresponding complex plane plot for an electrode process given by two RC circuits in series. Electrolyte resistance,  $R_{\Omega}$ , added.*

EIS measurements are done by applying a sinusoidal voltage<sup>1</sup> with a low amplitude, typically in the range of 5-15 mV. The expression for this voltage is given by

$$E(t) = E_m \sin(\omega t) \quad (7.1)$$

Here  $\omega (=2\pi f)$  is the angular frequency and  $E_m$  is the amplitude of the applied sinusoidal potential. The measurements are carried out at varying *ac* frequencies,

<sup>1</sup>It is also possible to perform the measurements by applying a sinusoidal current.

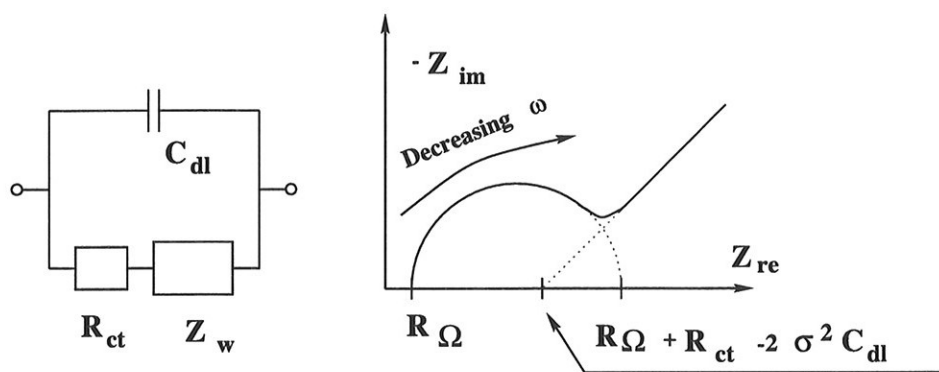


Figure 7.2: *Equivalent circuit and example of a corresponding complex plane plot for an electrode process including charge transfer and infinite diffusion length. Electrolyte resistance,  $R_{\Omega}$ , added.*

hence the name *impedance spectroscopy*. In figure 7.3, the effect of an impedance measurement on a metal hydride system is illustrated.

From figure 7.3, it is seen that during an impedance measurement, hydrogen is both absorbed and desorbed from the hydrogen storage alloy. In addition, the current and the potential are separated in the time domain by a phase angle,  $\phi$ .

Low amplitude is important, and according to Lasia [175], the maximum amplitude,  $\Delta E$  should be lower than  $\frac{8}{n}$  mV, peak to peak, where  $n$  is the number of electrons exchanged in the reaction. In section 8.3.5 it is shown that a particularly low amplitude is desirable for metal hydride electrochemical systems. The measurements are performed with varying angular frequency,  $\omega (=2\pi f)$ , and the current response (Eq 7.2) is monitored.

$$I(t) = I_m \sin(\omega t + \phi) \quad (7.2)$$

Here  $I_m$  is the current amplitude. Eq 7.2 indicates that the current has a phase shift,  $\phi$ , with regard to the voltage. The impedance is described by Eq 7.3

$$|Z| = \frac{E(t)}{I(t)} = \sqrt{Z_{im}^2 + Z_{re}^2} \quad (7.3)$$

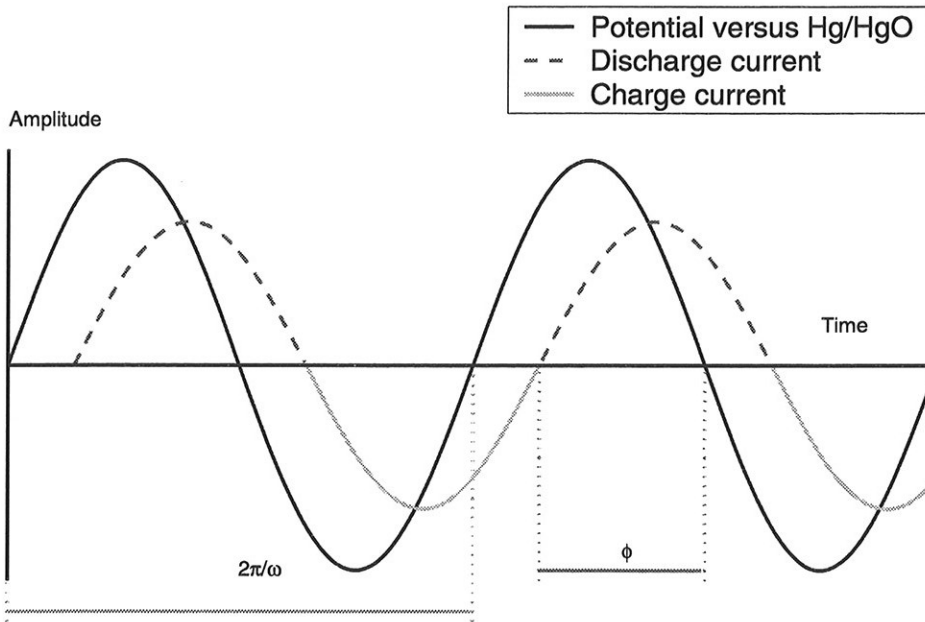


Figure 7.3: Illustration of the potential and current changes in a metal hydride system during an impedance measurement. The metal hydride electrode is during a sinusoidal voltage perturbation both charged (hydrogen absorbed) and discharged (hydrogen desorbed).

The phase angle,  $\theta$ , can be found from Eq 7.4

$$\theta = \arctan\left(\frac{Z_{im}}{Z_{re}}\right) \quad (7.4)$$

Different circuit elements yield different impedance responses

$$Z = \frac{C^\circ}{(j\omega)^n} \quad (7.5)$$

Here  $C^\circ$  is a constant and  $j = \sqrt{-1}$ . The value of  $n$  is unique for each circuit element type. An overview of how the impedance response can be characterized for different  $n$  values is given in table 7.1

The numeric values of the circuit elements are usually determined by a fitting routine, either based on the least square method or the faster Levenbergh-Markhardt

Table 7.1: *Different circuit elements and corresponding  $n$  values according to Eq 7.5.*

Circuit element	Symbol	Unit <sup>2</sup>	$n$ -value [Eq 7.5]
Inductance	L	H (VA <sup>-1</sup> s)	-1
Resistance	R	$\Omega$ (VA <sup>-1</sup> )	0
Warburg diffusion element	W	-	0.5
Constant Phase Element	Q	F (AsV <sup>-1</sup> )	0 - 1.0
Capacitive element	C	F (AsV <sup>-1</sup> )	1

method. Several different fitting routines exist (see the paper by Lasia [175] for an overview).

For a more complete general theoretical treatment of the impedance, there exist several excellent articles and books [175, 178–183].

### 7.1.1 Validation of Experimental Data

The Kramers Krönig transformation is a method to verify the properties of the experimental impedance data. The derivations of the Kramers Krönig transforms are based on the fulfillment of some general conditions of the system [175, 177].

**Causality:** The frequency response of the system comes solely from the applied signal.

**Linearity:** The response can be described by a set of linear differential equations

**Stability:** The system must be stable in the sense that it returns to its original state when no signal is applied.

**Finiteness:** The real and imaginary components of the impedance must be of finite value over the entire frequency range.

The conventional Kramers Krönig analysis can not be applied for systems including diffusion since the impedance must be finite for every  $\omega$  from Eq 7.6 and 7.7

---

<sup>2</sup>Where applicable

$$\lim_{\omega \rightarrow 0} Z = \lim_{\omega \rightarrow 0} \frac{C^{\circ}}{(j\omega)^n} \rightarrow \infty \quad (7.6)$$

$$\lim_{\omega \rightarrow \infty} Z = \lim_{\omega \rightarrow \infty} \frac{C^{\circ}}{(j\omega)^n} \rightarrow 0 \quad (7.7)$$

A way to perform the Kramers Krönig analysis on systems with an impedance response from diffusion is to use the admittance instead of the impedance.

## 7.2 Rough and Porous Electrodes

All electrode surfaces will have roughness to some extent. This is in particular true for metal hydride electrodes. De Levie [184] defines different degrees of roughness. Geometric effects will be called *macroscopic* when they are caused by geometries with dimensions in the order of millimeters or larger. *Microscopic* characterizes roughness of typical dimensions of around 0.01 to 100  $\mu\text{m}$ . *Atomic roughness* deals with steps, kinks and other kinds of atomic scale unevenness, typically in the order of nanometers. The metal hydride electrodes typically have both atomic and microscopic roughness in addition to a porous structure with pores of different shapes and lengths. The roughness and porosity in metal hydride electrodes are very dependent on the electrode construction and on the temperature and pressure used to make the electrodes. The porosity of laboratory scale electrodes which are made as described in section 5.3 is in the range of 15-30% [66, 169].

### 7.2.1 Electrodes with Microscopic Roughness

There have been several attempts to explain and simulate the impedance response for rough and porous electrodes. In the absence of a *dc* current, it can be assumed that the faradaic impedance is independent of the distance within the pore. It is then possible to obtain an analytical solution of the problem [185]. When *dc* current is passing, the potential will change as a function of the depth within the pore due to changes in the current distribution [186]. Numerical methods will then have to be employed to calculate the distribution of potential and current in the pores, which has been done for instance by Lasia [186]. The potential and



current distribution is highly dependent on the exchange current density for the electrode material. According to Lasia [186] a porous electrode giving a perfect semi-circle in the complex plane plot when no current is applied, gives a deformed ellipse when the faradaic impedance is potential dependent. Typical for rough and porous electrodes is also linear segment in the complex plane plot at high frequencies. The relative length of this linear segment increases when the exchange current or overpotential increases [186]. For a description of rough electrodes, the analogy of porous electrodes can be used, but these approximations are only successful when the radius of the pores is small compared to the depth.

### 7.2.2 The Constant Phase Element

Constant phase element<sup>3</sup> (*CPE*) behaviour is frequently observed in electrochemical systems. According to Brug *et al.* [188] the *CPE* is generally believed to originate from inhomogeneities of the interfacial capacitance. For multi-substituted alloys (for example the commercial AB<sub>5</sub> type alloys) one can imagine a distribution of the various surface properties along the surface. The surface will consist of a relatively large number of metals and their oxides and hydroxides. The equation for the *CPE* is given in Eq. 7.8

$$Z_{CPE} = \frac{Y^\circ}{(j\omega)^n} \quad (7.8)$$

Here  $Y^\circ$  is the characteristic parameter for the *CPE* with units  $s^n/\Omega$ . The power  $n$  value will be an expression for the frequency dependence of the constant phase element. For the *CPE*,  $n$  has a value between 0 and 1.0. It usually lies in the narrow region between 0.75 and 0.95 [184], and for these values of  $n$ , the constant phase element is close to being a capacitive element. Analytical results based on shapes of the surface roughness derived using Fourier transformations, have provided *CPE* behaviour with a large range of the exponent  $n$  in Eq 7.8 [189]. The article by Jacquelin [189] establishes the theoretical basis for the "CPE approach" where the double layer capacitance,  $C_{dl}$ , is replaced with a *CPE* element if the surface is rough.

The work by Brug *et al.* [188] points out another possible explanation for the *CPE* element: the idea that it is just an intrinsic property of the electrical double-layer,

---

<sup>3</sup>The phenomenon can also be denoted as fractional power frequency dependence, *FPPD* [187].

the atoms, molecules and ions in it being subject to extremely high electric field strengths with fluctuations. The expression for the connection between the double layer, solution resistance and the charge transfer resistance becomes [186, 188]:

$$Y_o = (C_{dl})^n \left[ R_{\Omega}^{-1} + R_{ct}^{-1} \right]^{1-n} \quad (7.9)$$

By use of Eq 7.9, the double layer capacitance,  $C_{dl}$  can be predicted from fitting to a *CPE* equivalent circuit within an error of 25% [190].

It is, however important to emphasize that one should be careful when using the *CPE* element for all depressed semicircles seen experimentally, because the *CPE* element has the potential of hiding inadequacies in a model.

### Roughness shape dependence

In a theoretical approach, Jacquelin [189] use Fourier series to predict the theoretical impedance response as a function of the shape of the roughness. Relatively smooth roughness profiles may result in a *CPE* type of impedance response. (See the paper by Keiser *et al.* [191] for additional details regarding the impedance response from different pore shapes.)

### 7.2.3 Transmission Line Approach

In the transmission-line approach, the following assumptions are made [192]: the pores are of uniform cross section and of semi-infinite length, homogeneously filled with electrolyte, and without cross links, a large amount of inert electrolyte is present, the electrode material has no resistance, and finally any curvature of the equipotential surfaces within the pores may be neglected.

The transmission-line approach is used for porous electrodes. Under an applied *ac* voltage, the ionic current flows into and out of the pores periodically while experiencing the electrolyte resistance. The amount of charge stored at the double layer inside each pore also oscillates when the ionic current terminates at the electrolyte/electrode boundary. To calculate the interfacial impedance, the pore is approximated by a RC transmission line, where the resistance per unit length is determined by the resistivity of the electrolyte and the pore cross section. The corresponding capacitance per unit length is determined by the double layer

capacitance per unit area and the boundary area per unit length. To complete the model, transmission lines are constructed according to the geometry and porous structure of the electrode/electrolyte interface [193]. This method will lead to a relatively large number of circuit elements, both in series and in parallel. A transmission-line<sup>4</sup> circuit adapted from de Levie [185, 192] is shown in fig 7.4.

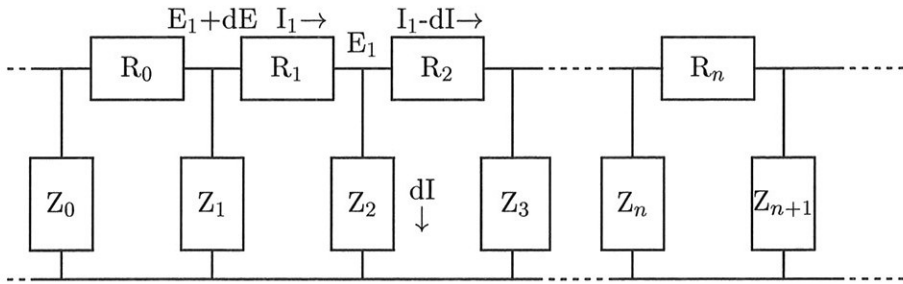


Figure 7.4: *Transmission line equivalent circuit.*

Here the resistances,  $R_i$ , is the solution resistance for segment  $i$  inside the pore, and the impedance,  $Z_i$ , is the electrode impedance for segment  $i$  of the pore. It should be noted that the impedance of the electrode in general depends both on potential (electrode reaction) and on time (diffusion) [192]. It is important to note, however, that impedance measurements can be done in steady state only.

Assuming small amplitudes, the impedance,  $Z_i$ , is only dependent on the angular frequency,  $\omega$ . Then the following equations will describe the transmission line in Fig 7.4:

$$dE = -IRdZ \Leftrightarrow \frac{dE}{dZ} + IR = 0 \quad (7.10)$$

$$dI = -\frac{E}{Z}dZ \Leftrightarrow \frac{dI}{dZ} + \frac{E}{Z} = 0 \quad (7.11)$$

Eqs 7.10 and 7.11 can be further developed, and the pore behaves as an impedance  $\sqrt{ZR}$  and the following conclusions can be reached [192]:

1. The phase angle of the impedance of a porous electrode is half that of the equivalent flat electrode.

<sup>4</sup>A transmission-line network may also be called a ladder network.

2. The absolute magnitude of the impedance of a porous electrode is proportional to the square root of that of a smooth, non porous electrode made of the same electrode material.

According to Fleig and Maier [194] the analytical transmission-line models usually consider the current one-dimensional in the electrolyte. The neglect of currents in the electrolyte perpendicular to the transmission-line restricts these models to pores with a depth much larger than their width. These models will also fail to describe the impedance response in the electrodes if some parts of the electrode surface are smooth.

### Porous Electrodes with Deep Cylindrical Pores

In a model with deep cylindrical pores (i.e. semi-infinite channel formed pores) the impedance can according to Los *et al.* [195] be given by:

$$Z = R_{\Omega} + \frac{Z_p}{n} \quad (7.12)$$

Here  $R_{\Omega}$  is the electrolyte resistance and  $n$  is the number of pores. The porous impedance,  $Z_p$ , can be expressed by [195]:

$$Z_p = \frac{1}{\pi r} \sqrt{\frac{\rho Z_o}{2r}} \coth\left(\sqrt{\frac{2\rho l^2}{r Z_o}}\right) \quad (7.13)$$

Here  $Z_o$  is the specific impedance per unit area of the flat surface in a cylindrical pore,  $\rho$  is the solution resistivity,  $r$  and  $l$  the pore radius and pore length respectively. In an electrode with semi-infinite channels, the total equation for the impedance is [175]:

$$Z = R_{\omega} + \frac{R_{\Omega,p}}{\sqrt{\Lambda}} \coth(\sqrt{\Lambda}) \quad (7.14)$$

Here  $\Lambda$  is the dimensionless electrode admittance for a corresponding flat electrode ( $\frac{1}{Z_{el}}$ ) and  $R_{\Omega,p}$  is the electrolyte resistance along the pore axis and can be expressed by Eq 7.15.

$$R_{\Omega,p} = \frac{\rho l}{n\pi r^2} \quad (7.15)$$

Consequently, the complex plane plot becomes a deformed semicircle [195]. It is worthwhile to mention that this approach does not account for the electrolytic diffusion of ions in the pores in electrode.

#### 7.2.4 Porous Electrodes Versus Rough Electrodes

According to de Levie [184] the first efforts to describe roughness used the analogy with porous electrodes. A transmission-line model work fine for electrodes with small pore diameters. The transmission line models become unreliable when the pore diameter becomes larger than the effective signal penetration depth,  $\sqrt{\frac{Z'}{R'}}$ .  $Z'$  and  $R'$  are here the interfacial impedance and solution resistance, each per unit pore length. This is because the analytical transmission-line models usually consider the current one-dimensional in the electrolyte [194]. Electrode roughness typically involves quite shallow interfacial protrusions and depressions, and this makes the transmission-line approach less applicable for describing rough electrodes.

### 7.3 Hydrogen Evolution in Combination with Hydrogen Absorption

Harrington and Conway [181] developed theoretical models of the *ac* impedance of faradaic reactions involving electrosorbed intermediates, neglecting the diffusion processes. They showed that interpretation of *ac* impedance measurements directly in terms of components of an intuitively assumed equivalent circuit rarely is correct. One exception is in the case of underpotential deposition of an adsorbed species, where no continuous faradaic current pass. Harrington and Conway also developed a physical model for faradaic reactions involving electrosorbed intermediates and proposed equivalent circuits based on the theoretical models fitting these reactions under various conditions.

In figure 7.5, the equivalent circuit for an electrode with one adsorbed species is given. It is assumed that the adsorption reaction is faster than the desorption

reaction. If it is assumed that the desorption is faster, the equivalent circuit contains an inductive loop as shown in figure 7.6.

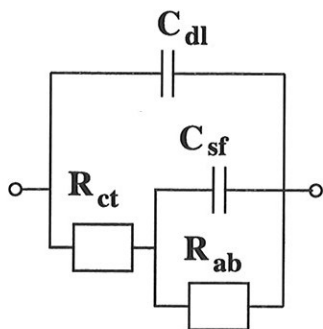


Figure 7.5: *The equivalent circuit for an electrode with one adsorbed species. It is assumed that the adsorption reaction is faster than the desorption reaction.*

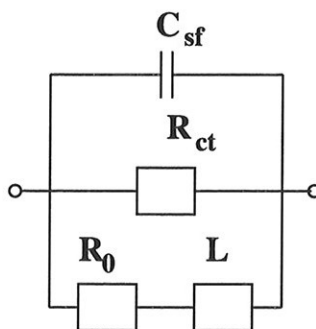


Figure 7.6: *The equivalent circuit for an electrode with one adsorbed species. It is assumed that the desorption reaction is faster than the adsorption reaction.*

As seen from figures 7.5 and 7.6, one can, using the electrochemical impedance technique on systems including adsorbed species determine whether the adsorption or the desorption is the fastest. For a more comprehensive treatment of various issues related to impedance response for electrochemical reactions involving one adsorbed species, please consult Refs [175, 181]. It is important to note, however, that for the Volmer-Herovskiy reaction mechanism, one can not distinguish which step is the rate determining, i.e. the hydrogen *adsorption* and *absorption* can not be separated (see the paper by Lasia [190] for additional details).

## 7.4 Metal Hydride Electrodes

### 7.4.1 Introduction

To optimize MH electrode with regard to electrochemical properties, it is necessary to know the microstructure of the electrode and the kinetic mechanisms governing the electrode. Once the microstructure and the kinetic properties are known, one can make electrodes tailored for certain purposes.

The first part in this process is to identify different steps in the mechanism.

Once the steps are known, a theoretical model for the electrode could be made. The model should then be verified experimentally using suitable electrochemical techniques for a range of different research parameters. This verification has to be done *in situ*. Two methods can be considered, either the potential step method or the electrochemical impedance spectroscopy (EIS) method. In this thesis, the EIS method is chosen because this method will not affect the electrodes too much while measuring. Another feature of this technique is that it is possible to identify and separate processes both in series and in parallel, provided that the process have different time constants. Besides, this method will give simpler mathematical expressions than the potential step method.

To be able to present a reliable model for hydrogen absorption and hydride formation, contributions to the overall reaction rate from several phenomena needs to be understood and included in the model:

- Change of surface area during electrochemical characterization, see section 5.5.6. Because of experimental uncertainties and the contribution from the binder material in the electrode, one cannot measure surface area by simply measuring change in double layer capacitance.
- Charge/discharge of the electrode during impedance measurements (see figure 7.3 for explanations). In section 8.3.5 this is further discussed in terms of the applied potential amplitude.
- Diffusion geometry; The hydrogen diffusion within the metal hydride is modelled both as planar and spherical geometry, model equations for different geometries are given by Jacobsen and West [196].
- Porous structure. The porous structure will increase the possibilities of concentration gradients in the electrolyte.
- Metallurgical inhomogenities, especially for melt-spun materials. This can result in micro inhomogenities resulting in variations in current densities due to differences in electrocatalytic activity.
- The selective corrosion of rare earth metals in  $AB_5$  type metal hydride electrodes, will change the surface as the electrode is cycled.

### 7.4.2 Previous Work

Several groups have given valuable contributions to important issues of modelling impedance response in metal hydride electrodes for battery purposes. Previous work has been done to develop mathematical expressions to characterize mechanisms resulting from charging and discharging of metal hydride electrodes. Agarwal *et al.* [197] used a mathematical model to analyse results of EIS studies on a  $\text{LaNi}_5$  solid electrode.

Impedance characterization of metal hydride electrodes for battery purposes generally makes use of equivalent circuits for interpretation of data [198, 199]. Impedance measurements have also been used to obtain variations of the polarization resistance as a function of depth of discharge (DOD) [137, 156, 200–204] and temperature [205]. It was stated in these papers that the reaction impedance was highest for charged electrodes of the  $\text{AB}_5$  type. The variations were a lot smaller for palladium coated alloys, but still the same trend was observed [137].

Durand *et al.* [206] proposed an impedance model for intercalation of hydrogen in a thin film with linear diffusion. Lim and Pyun [207] did the same for a thin metal membrane under permeable conditions.

Zhang *et al.* [199, 208] developed a model for impedance of a metal hydride electrode neglecting concentration gradients. EIS studies were performed on electrodes with three types of binding additives, varying amounts of active material, and two types of alloys as active material. This research demonstrated the importance of developing electrodes with optimum composition and structure to ensure a good electrode performance. An equivalent circuit for the metal hydride electrode reaction was proposed. Zhang *et al.* [199, 208] concluded that rate capability of charge and discharge of the metal hydride electrode is determined by kinetics of charge-transfer reaction at the alloy surface. These responses are mainly represented by EIS responses in the high and medium frequency region. It can be pointed out that the model presented by Zhang *et al.* [199, 208] is not consistent with the model presented by Harrington and Conway [181] even though the same initial equations were used. A careful mathematical survey of the model presented in the paper of Zhang *et al.* [199] reveals, however, that there is a calculation error in that paper. When recalculating the equations, the same equivalent circuit as presented by Harrington and Conway [181] is obtained.

Kuriyama *et al.* [198, 209–211] did a lot of experimental work in this field, as-



signing different segments of the impedance spectra to different sub-processes. The work was done without presenting a mathematical model for the electrode. These authors found that the following processes need to be taken into account: hydrogen content, electrode reactions on alloy particles, double-layer capacitance, and the resistance and the capacitance between alloy particles in the electrode.

Wang [212] has also done both modelling and measurements, both attributing different arcs in the complex plane plot to different sub-processes. Leng *et al.* [213] modelled the impedance in metal hydride electrodes assuming the diffusion processes as Warburg diffusion. The model proved to be working well for frequencies above 0.005 Hz.

Lundqvist and Lindbergh [156, 214] did a comprehensive work by studying the kinetics of a porous metal hydride electrode using EIS, incorporating both a porous electrode structure and also particle size distribution.

## 7.5 Different Models for Metal Hydride Electrodes

### 7.5.1 Theoretical Considerations

When the diffusion process is neglected<sup>5</sup>, and the hydride forming/splitting process is fast, the hydrogen absorption reaction can be considered as a standard one adsorbed species reaction.

The following assumptions are generally made for all models developed taking diffusion into account:

- Spherical diffusion geometry,
- Hydrogen evolution and metal oxidation are the only reactions competing with the hydride formation, and
- For the porous electrode models, semi-infinite channel formed pores are assumed.

The charge transfer step is the same as in the case of electrolytic hydrogen evolution. The main difference between the hydriding reaction and the hydrogen

---

<sup>5</sup>Neglecting the diffusion step means that the diffusion is assumed to be very fast.

evolution reaction is the absorption step. In this thesis, only treatments including diffusion processes is considered. If no diffusion process is considered, the hydriding/dehydriding reaction can be approximated as a normal electrochemical reaction with one adsorbed species, which is well documented in literature (see section 7.3 for additional details regarding the electrode reaction with one adsorbed species).

### 7.5.2 Spherical Diffusion, Sphere Model

This section is to a large extent based on the paper by the author [174]. An assembly of metal hydride particles with dimensions in all directions of similar magnitude is considered. All particles are electrically connected to a current collector and a major part of their surface is exposed to an aqueous solution with no processes competing with hydride forming reaction or hydrogen desorption reaction.

An illustration on how the metal hydride particles in the electrode are modelled to be connected to the current collector is given in figure 7.7.

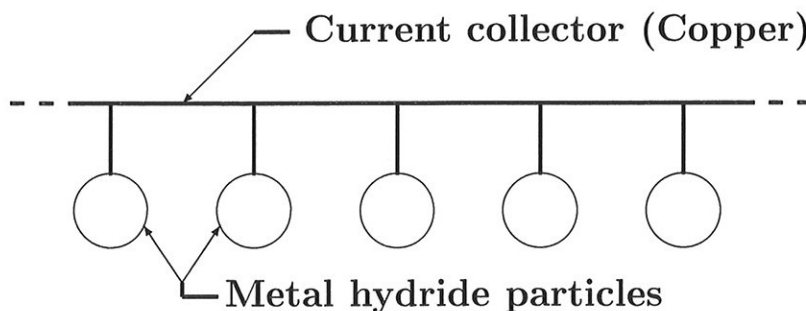


Figure 7.7: An illustration on how the metal hydride particles in the electrode are modelled to be connected to the current collector.

It is furthermore assumed that the electrode reactions at the metal hydride surface can be associated with the processes described in section 3.6.2. In the further development the following assumptions are made:

- The rate of the transport of water and hydroxyl ions in the electrolyte (Eqs 3.15 and 3.16) are high compared to the rate of the diffusion of hydrogen within the metal lattice.
- The metal hydride forming reaction (Eq 3.21) is in equilibrium.
- The rate of diffusion is about same both in the  $\alpha$  and  $\beta$  phase. This means that formally diffusion takes place in a continuum.

The diffusion is further modelled by assuming spherical diffusion, hence the radial diffusion of hydrogen in the hydride can be expressed by Ficks 2. law [215]:

$$\frac{\partial c_H}{\partial t} = D_H \left( \frac{\partial^2 c_H}{\partial r^2} + \frac{2}{r} \frac{\partial c_H}{\partial r} \right) \quad (7.16)$$

Here  $D_H$  is the hydrogen diffusion coefficient in the alloy. By defining  $u_H = c_H \cdot r$  [215] the diffusion equation in spherical coordinates can be written

$$\frac{\partial u_H}{\partial t} = D_H \frac{\partial^2 u_H}{\partial r^2} \quad (7.17)$$

If the potential applied to the metal hydride electrode is the sum of a steady-state value and a harmonic contribution applied at  $t > 0$ ,  $u_H$  may be expressed as

$$u_H = u_H(r, 0) + \tilde{u}_H(r, t) \quad (7.18)$$

Here  $u_H(r, 0)$  is the steady state value. The frequency of the harmonic contribution,  $\tilde{u}_H$ , will be the same as the applied signal provided that the amplitude of the latter is small enough that system is in the linear range for such perturbations. The partial derivative of  $u_H$  with respect to the time gives the following expression:

$$\frac{\partial u_H(r, t)}{\partial t} = \frac{\partial \tilde{u}_H(r, t)}{\partial t} = D_H \left[ \frac{\partial^2 \tilde{u}_H(r, 0)}{\partial r^2} + \frac{\partial^2 \tilde{u}_H(r, t)}{\partial r^2} \right] \quad (7.19)$$

Laplace transforming [216] Eq 7.19 gives

$$s\mathcal{L}\{\tilde{u}_H(r, t)\} - \tilde{u}_H(r, 0) = \frac{D_H}{s} \frac{\partial^2}{\partial r^2} \mathcal{L}\{\tilde{u}_H(r, t)\} \quad (7.20)$$

Rearranging Eq 7.20 gives

$$\left( \frac{\partial^2}{\partial r^2} - \frac{s}{D_H} \right) \mathcal{L}\{\tilde{u}_H(r, t)\} = -\frac{1}{D_H} \tilde{u}_H(r, 0) - \frac{1}{s} \frac{\partial^2}{\partial r^2} \tilde{u}_H(r, 0) \quad (7.21)$$

Solving Eq 7.21 for  $\mathcal{L}\{\tilde{u}_H(r, t)\}$  and using  $\alpha = \sqrt{\frac{s}{D_H}}$  gives:

$$\begin{aligned} \mathcal{L}\{\tilde{u}_H(r, t)\} &= A^\circ \sinh(\alpha r) + B^\circ \cosh(\alpha r) \\ &+ \frac{D_H}{s} \left[ \frac{1}{D_H} \tilde{u}_H(r, 0) + \frac{1}{s} \frac{\partial^2}{\partial r^2} \tilde{u}_H(r, 0) \right] \end{aligned} \quad (7.22)$$

Here,  $A^\circ$  and  $B^\circ$  are constants. To find these constants, the boundary conditions need to be applied. If it is assumed that the hydrogen concentration in the middle of the particles is constant, the boundary condition can be expressed as

$$\tilde{u}_H(0, t) = 0 \quad (7.23)$$

Applying the boundary condition to Eq 7.22 gives the following expression

$$0 = B^\circ + \frac{D_H}{s} \left[ \frac{1}{D_H} \tilde{u}_H(0, 0) + \frac{1}{s} \frac{\partial^2}{\partial r^2} \tilde{u}_H(r, 0) \Big|_{r=0} \right] \quad (7.24)$$

Solving Eq 7.24 for  $B^\circ$  and applying the boundary condition given in Eq 7.23 gives

$$B^\circ = \frac{D_H}{s^2} \frac{\partial^2}{\partial r^2} \tilde{u}_H(r, 0) \Big|_{r=0} \quad (7.25)$$

By assuming that the local changes in the hydrogen concentration at the onset of the measurement is limited to the surface and sub-surface region,  $B^\circ$  in Eq 7.25 will be zero. Eq 7.22 can then be simplified to the following expression:

$$\mathcal{L}\{\tilde{u}_H(r, t)\} = A^\circ \sinh(\alpha r) \quad (7.26)$$

By replacing  $\tilde{u}_H$  with the alternating part of the hydrogen concentration,  $\tilde{c}_H(r, t)$ , one gets:

$$\mathcal{L}\{\tilde{c}_H(r, t)\} = \frac{1}{r} \mathcal{L}\{\tilde{u}_H(r, t)\} \quad (7.27)$$

The rate of the reaction Eq 3.18,  $v_2$ , can be divided in a stationary and an alternating component:

$$v_2 = v_{2,ss} + \tilde{v}_2 \quad (7.28)$$

Here,  $v_{2,ss}$  is the stationary component and  $\tilde{v}_2$  is the alternating component of the rate of the reaction Eq 3.18. The mass balance for hydride particle at the surface ( $r = a$ ) can then be combined with the hydrogen concentration in the particle:

$$\frac{d\mathcal{L}\{\tilde{c}_H\}}{dr} \Big|_{r=a} = \frac{\mathcal{L}\{\tilde{v}_2\}}{D_H} \quad (7.29)$$

Combining Eqs 7.26 and 7.29 gives

$$\frac{\mathcal{L}\{\tilde{v}_2\}}{D_H} = -\frac{1}{a^2}\mathcal{L}\{\tilde{u}_H(a, t)\} + \frac{1}{a}A^\circ\alpha \cosh(\alpha a) \quad (7.30)$$

Solving Eq 7.30 for  $A^\circ$

$$A^\circ = \frac{\mathcal{L}\{\tilde{v}_2\}}{D_H\left[\frac{\alpha}{a}\cosh(\alpha r) - \left(\frac{1}{a^2}\right)\sinh(\alpha r)\right]} \quad (7.31)$$

Combining Eqs 7.26, 7.27, and 7.31 gives

$$\begin{aligned} \mathcal{L}\{\tilde{c}_H\} &= \frac{\mathcal{L}\{\tilde{v}_2\} \sinh(\alpha r)}{rD_H\left[\frac{\alpha}{a}\cosh(\alpha r) - \left(\frac{1}{a^2}\right)\sinh(\alpha r)\right]} \\ &= \frac{\mathcal{L}\{\tilde{v}_2\}}{rD_H\left[\frac{\alpha}{a}\coth(\alpha r) - \left(\frac{1}{a^2}\right)\right]} \\ &= \mathcal{L}\{\tilde{v}_2\}\mathcal{L}\{G(s, r, a, D_H)\} \end{aligned} \quad (7.32)$$

The faradaic current density ( $i_f$ ) from Eq 3.16 is divided into a stationary ( $i_{f,ss}$ ) and an alternating ( $\tilde{i}_f$ ) component:

$$i_f = i_{f,ss} + \tilde{i}_f \quad (7.33)$$

By the use of Taylor-evolution and linearisation, the alternating component of the faradaic current can be expressed by:

$$\tilde{i}_f = \nabla i_f = \sum \tilde{c}_i \left[ \left( \frac{\partial i_f}{\partial c_i} \right)_{c_j, \varphi} \right] + \left( \frac{\partial i_f}{\partial \varphi} \right)_{c_j} \tilde{\varphi} \quad (7.34)$$

Here,  $c_i$  and  $c_j$  are the concentrations of species  $i$  and  $j$  respectively,  $\varphi$  is the electrode potential, and  $\tilde{\varphi}$  is the alternating component of the electrode potential. If the concentrations of  $H_2O$ , and  $OH^-$  are considered constant and the activity of the adsorbed hydrogen is proportional to the surface coverage, the alternating part of the current can be expressed by

$$\tilde{i}_f = \Gamma \tilde{\theta} \left[ \left( \frac{\partial i_f}{\partial \theta} \right)_{\varphi, c_{H_2O}, c_{OH^-}} \right] + \left( \frac{\partial i_f}{\partial \varphi} \right)_{\theta} \tilde{\varphi} = A\tilde{\theta} + B\tilde{\varphi} \quad (7.35)$$

Here,  $\theta$  is the surface coverage of hydrogen. The functions  $A$  and  $B$  are defined by Eq 7.35 and can be assumed to be constant as long as the temperature and pressure are constant<sup>6</sup>. Laplace transforming both sides of Eq 7.35 gives

$$\mathcal{L}\{\tilde{\varphi}\} = \frac{\mathcal{L}\{\tilde{i}_f\} - A\mathcal{L}\{\tilde{\theta}\}}{B} \quad (7.36)$$

The reaction rate (Eq 3.18) is dependent both on the hydrogen concentration and on the surface coverage. The alternating component of the reaction rate can therefore be expressed as:

$$\tilde{v}_2 = \nabla v_2 = \Gamma \tilde{\theta} \left( \frac{\partial v_2}{\partial \theta} \right)_{c_H} + \tilde{c}_H \left( \frac{\partial v_2}{\partial c_H} \right)_{\theta} = C \tilde{\theta} + D \tilde{c}_H \quad (7.37)$$

Here,  $C$  and  $D$  are defined by Eq 7.37 and they can both be assumed to be constant as long as the temperature and pressure are constant. Both sides of Eq 7.37 are then Laplace transformed and combined with Eq 7.32 to give

$$\mathcal{L}\{\tilde{v}_2\} = \frac{C\mathcal{L}\{\tilde{\theta}\}}{1 - D\mathcal{L}\{G\}} \quad (7.38)$$

The mass balance (Eqs 3.16 and 3.18) for the surface can be expressed as:

$$\Gamma \frac{\partial \theta}{\partial t} = - \left[ \frac{i_f}{nF} - v_2 \right] = - \left[ \frac{i_{f,ss}}{nF} + \frac{\tilde{i}_f}{nF} - v_{2,ss} - \tilde{v}_2 \right] \quad (7.39)$$

Here  $\Gamma$  is the surface coverage when  $\theta$  is unity. The number of electrons transferred in the electrode reaction (Eq 3.16),  $n$  is 1. By assuming equilibrium for  $t=0$ , Eq 7.39 can be expressed as:

$$\Gamma \frac{\partial \theta}{\partial t} = - \left[ \frac{\tilde{i}_f}{F} - \tilde{v}_2 \right] \quad (7.40)$$

Laplace transforming the mass balance for the surface (Eq 7.40) gives

$$\Gamma s \mathcal{L}\{\tilde{\theta}\} = - \frac{\mathcal{L}\{\tilde{i}_f\}}{F} + \mathcal{L}\{\tilde{v}_2\} \quad (7.41)$$

Combining Eqs 7.38 and 7.41 and solving for  $\mathcal{L}\{\tilde{i}_f\}$  gives:

$$\mathcal{L}\{\tilde{i}_f\} = F \mathcal{L}\{\tilde{\theta}\} \left( -\Gamma s + \frac{C}{1 - D\mathcal{L}\{G\}} \right) \quad (7.42)$$

<sup>6</sup>  $A$  and  $B$  are not related to  $A^\circ$  and  $B^\circ$ .

The faradaic impedance,  $Z_f$ , is now calculated as the ratio between the Laplace transformed potential and the current, defining  $s=j\omega$ . Combining Eqs 7.42 and 7.36 gives

$$Z_f = \frac{\mathcal{L}\{\tilde{\varphi}\}}{\mathcal{L}\{\tilde{i}_f\}} = \frac{1}{B} \left[ 1 + \frac{\frac{A}{F}}{\Gamma s - \frac{C}{1-D\mathcal{L}\{G\}}} \right] \quad (7.43)$$

Rearranging Eq 7.43 gives the following expression:

$$Z_f = \frac{\mathcal{L}\{\tilde{\varphi}\}}{\mathcal{L}\{\tilde{i}_f\}} = \frac{1}{B} + \frac{1}{\frac{B\Gamma s}{A} - \frac{BCF}{A-AD\mathcal{L}\{G\}}} = \frac{1}{\left(\frac{\partial i_f}{\partial \varphi}\right)_\theta} + Z'_f = R_{ct} + Z'_f \quad (7.44)$$

Eq 7.44 defines the charge transfer resistance,  $R_{ct}$  and the impedance,  $Z'_f$ . The expression for the charge transfer resistance is:

$$R_{ct} = B^{-1} = \left[ \left(\frac{\partial i_f}{\partial \varphi}\right)_\theta \right]^{-1} = \left(\frac{\partial \varphi}{\partial i_f}\right)_\theta \quad (7.45)$$

As seen from Eq 7.45, the charge transfer represents the ratio between the change in the potential and the faradaic current, when a constant coverage of hydrogen on the surface is assumed. From Eq 7.44 it is also seen that the faradaic impedance,  $Z_f$ , can be interpreted as a series circuit with  $R_{ct}$  and the impedance  $Z'_f$ . By substituting  $s = j\omega$ , the inverse of the impedance  $Z'_f$  can furthermore be expressed as:

$$\frac{1}{Z'_f} = +j\omega \frac{B\Gamma}{A} - \frac{BCF}{A-AD\mathcal{L}\{G\}} = \frac{1}{Z'_{f,a}} + \frac{1}{Z'_{f,b}} \quad (7.46)$$

Eq 7.46 can be recognised as a parallel circuit of the two impedances  $Z'_{f,a}$  and  $Z'_{f,b}$  and can be expressed as:

$$Z'_{f,a} = \frac{A}{j\omega B\Gamma} = \frac{1}{j\omega C_1} \quad (7.47)$$

Here,  $C_1$  can be recognised as a capacitance given by:

$$C_1 = \frac{\Gamma F \left(\frac{\partial i_f}{\partial \varphi}\right)_\theta}{\left(\frac{\partial i_f}{\partial \theta}\right)_\varphi} \quad (7.48)$$

$C_1$  may therefore be related to the effect of the surface coverage on the faradaic reaction.  $Z'_{f,b}$  in Eq 7.46 can be expressed as:

$$Z'_{f,b} = -\frac{A-AD\mathcal{L}\{G\}}{BCF} = \frac{AD\mathcal{L}\{G\}}{BCF} - \frac{A}{BCF} = Z_D + R_1 \quad (7.49)$$

Here,  $R_1$  is a constant given by:

$$R_1 = -\frac{1}{F} \left( \frac{\partial i_f}{\partial \theta} \right)_\varphi \left( \frac{\partial v_2}{\partial \theta} \right)_{C_H}^{-1} \left( \frac{\partial i_f}{\partial \varphi} \right)_\theta^{-1} \quad (7.50)$$

$R_1$  may be related to a product of partial derivatives of the rates of different reaction steps with respect to surface coverage and the potential. Eq 7.49 is recognised as a series circuit of  $Z_D$  and  $R_1$ . By combining Eqs 7.32 and 7.49 and using  $\alpha = \sqrt{\frac{j\omega}{D_H}}$  the variable part of Eq 7.49 can be expressed as:

$$Z_D = \frac{AD\mathcal{L}\{G\}}{BCF} = \frac{\sigma}{\frac{rD_H}{a} \left[ \sqrt{\frac{j\omega}{D_H}} \coth\left(\sqrt{\frac{j\omega}{D_H}} r\right) - \frac{1}{a} \right]} \quad (7.51)$$

Here  $\sigma$  is a constant. Further simplification gives for ( $r=a$ ):

$$Z_D = \frac{\sigma}{\sqrt{j\omega D_H} \coth\left(\sqrt{\frac{j\omega}{D_H}} a\right) - \frac{D_H}{a}} \quad (7.52)$$

From 7.52 it is seen that  $Z_D$  is dependent on both frequency, particle radius and the diffusion coefficient of hydrogen in the alloy.  $Z_D$  may therefore be interpreted as a diffusion impedance.

Using regular chemical and electrochemical kinetics [154] renders all circuit elements positive.

Eq 7.43 may then be rearranged to give the circuit shown in figure 7.8. It should be noted that Eq 7.43 and figure 7.8 both are in absence of hydrogen evolution reaction (HER).  $R_{ct}$  refers to the charge transfer resistance, defined by Eq 7.44,  $C_1$  is defined by Eq 7.48, and  $R_1$  by Eq 7.50.  $Z_D$  is the impedance resulting from the diffusion of hydrogen within the alloy particles, defined by Eq 7.52.

The alternating part of the total current can if the hydrogen evolution reaction is neglected be expressed as:

$$\mathcal{L}\{\tilde{i}\} = \mathcal{L}\{\tilde{i}_f\} + \mathcal{L}\{\tilde{i}_{nf}\} \quad (7.53)$$

Here,  $\tilde{i}_{nf}$  is the non-faradaic current which can be expressed by

$$i_{nf} = \frac{dq}{dt} = \sum \left[ \left( \frac{\partial q}{\partial \varphi} \right)_{c_i} \frac{\partial \varphi}{\partial t} \right] = \frac{\partial \varphi}{\partial t} \sum \left( \frac{\partial q}{\partial \varphi} \right)_{c_i} \quad (7.54)$$



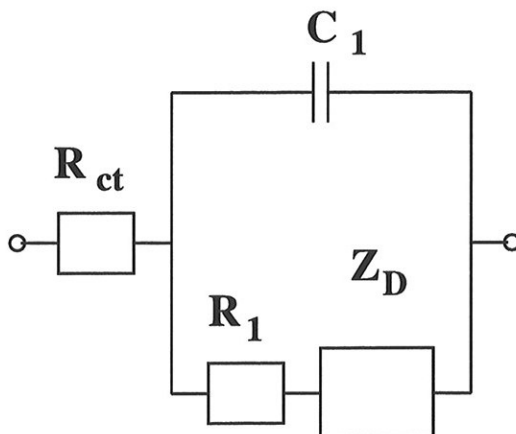


Figure 7.8: *Equivalent circuit representation of Eq 7.43.*

Here,  $q$  is the differential non faradaic charge of the double layer. Laplace transforming both sides of Eq 7.54 gives

$$\mathcal{L}\{\tilde{i}_{nf}\} = s\mathcal{L}\{\tilde{\varphi}\} \sum \left( \frac{\partial q}{\partial \varphi} \right)_{c_i} = sC_{dl}\mathcal{L}\{\tilde{\varphi}\} = j\omega C_{dl}\mathcal{L}\{\tilde{\varphi}\} \quad (7.55)$$

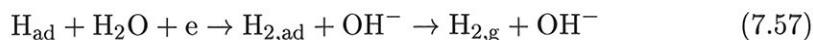
Here,  $C_{dl}$  is a constant. The non faradaic impedance,  $Z_{nf}$ , is now calculated as the ratio between the Laplace transformed potential and the current.

$$Z_{nf} = \frac{\mathcal{L}\{\tilde{\varphi}\}}{\mathcal{L}\{\tilde{i}_{nf}\}} = \frac{1}{j\omega C_{dl}} \quad (7.56)$$

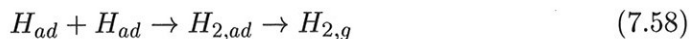
The double layer capacitance,  $C_{dl}$ , can therefore be added in parallel to the calculated faradaic equivalent circuit. This is shown in figure 7.9.

### 7.5.3 Including Side Processes

There exist also the possibility of side reactions like hydrogen evolution and metal oxidation. The hydrogen evolution reaction during charging can follow either the Volmer Herovskys reaction path



Or the Volmer Tafel path



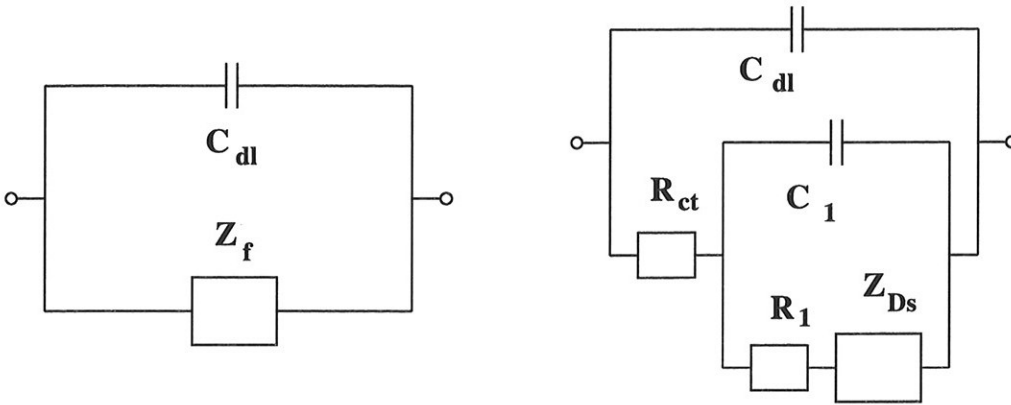


Figure 7.9: For electrolytic processes a double layer capacitance,  $C_{dl}$  is added in parallel to the calculated faradaic equivalent circuit to account for the true capacitance in the physical sense. Right: resulting equivalent circuit, faradaic response shown in detail.

several groups [217, 218] has reported that the Volmer Herovsky reaction is dominant for hydrogen evolution on nickel electrodes. In the further development it is therefore assumed that the hydrogen evolution reaction follows the Volmer Herovsky reaction path. The mass balance for the current, Eq 7.40 must therefore be rewritten as

$$\Gamma \frac{\partial \theta}{\partial t} = - \left[ \frac{\tilde{i}_f}{F} - \tilde{v}_2 - \tilde{v}_{H_{ev}} \right] \quad (7.59)$$

Here  $\tilde{v}_{H_{ev}}$  is the rate of the hydrogen evolution, Eq 7.57. Laplace transforming the mass balance for the surface (Eq 7.40) gives

$$\Gamma_s \mathcal{L}\{\tilde{\theta}\} = - \left[ \frac{\mathcal{L}\{\tilde{i}_f\}}{F} - \mathcal{L}\{\tilde{v}_2\} - \mathcal{L}\{\tilde{v}_{H_{ev}}\} \right] \quad (7.60)$$

Hydrogen evolution will take place in parallel to the hydrogen absorption/desorption and diffusion [219] and may contribute to the surface capacitance. The metal oxidation reaction is assumed to take place in parallel to the charge transfer, Eq 3.16.

An equivalent circuit with hydrogen evolution included is shown in figure 7.10. In figure 7.11 an equivalent circuit including a parallel electrochemical side process such as for instance a metal oxidation and reduction is shown. In figure 7.10,  $R_{ev}$  is the resistance from the hydrogen evolution,  $C_p$  is the resultant capacitance resulting from the hydrogen evolution reaction and  $C_1$  from figure 7.9. In figure

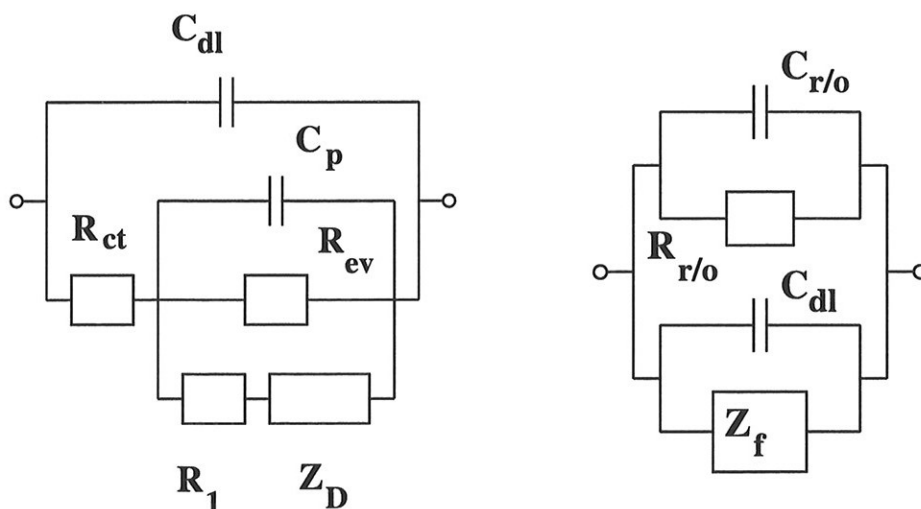


Figure 7.10: *An equivalent circuit for a metal hydride electrode with hydrogen evolution side processes included.*

Figure 7.11: *An equivalent circuit for a metal hydride electrode with a parallel electrochemical side process included.*

7.11,  $R_{r/o}$  the resistance, and  $C_{r/o}$  is the capacitance in a possible parallel electrochemical process such as for instance a metal oxidation and reduction. The lower part of the circuit is similar to the circuit shown in figure 7.9. Since  $C_{dl}$  and  $C_{r/o}$  are in parallel, it will not be possible to distinguish between the two.

#### 7.5.4 Planar Diffusion Model

Assuming a planar diffusion model, the diffusion element is taken to be a Warburg diffusion element. The physical interpretation of the Warburg impedance is discussed [220], and it is observed whenever a reaction is under partial or complete mass control by diffusion. The term *Warburg diffusion* is reserved for the special case of semi-infinite linear diffusion. A planar diffusion path would change all the mass balances in section 7.5.2. A planar diffusion path with no porous contribution seems very unlikely to represent the system of a pressed porous electrode. Changing the geometry from spherical to planar (Warburg), only affects the diffusion term, a circuit describing planar diffusion can therefore be represented by the circuit shown in figure 7.9 with a planar diffusion geometry given by [219]

$$Z_W = \frac{\sigma_w}{\sqrt{j\omega D}} \coth \left[ \sqrt{\frac{j\omega}{D}} X_L \right] \quad (7.61)$$

Here,  $Z_W$  is the mass transfer impedance for finite length diffusion and reflecting interface.  $D$  the diffusion coefficient,  $X_L$  the diffusion length.

### 7.5.5 Particle Size Distribution Model

The metal hydride particles in a metal hydride electrode will naturally have a particle size distribution. This will affect the contribution from diffusion elements given in previous models as other contributions to the impedance only depend on the total surface area. A simple way to consider this effect, is to use a particle size distribution model for diffusion impedance. The total diffusion impedance for a metal hydride electrode consisting of  $n$  distinct particle fractions is given by Eq 7.62

$$\frac{1}{Z_D} = \frac{X_1}{Z_{D,1}} + \frac{X_2}{Z_{D,2}} + \dots + \frac{X_{n-1}}{Z_{D,n-1}} + \frac{X_n}{Z_{D,n}} = \sum_{i=1}^n \frac{X_i}{Z_i} \quad (7.62)$$

Here  $X_i$  is the fraction of particles of the  $i$  size. The simplest way to incorporate a particle size distribution model is to use a discrete distribution of metal hydride particles with a very limited number of fractions.

## 7.6 Discussion

It is very likely that the hydriding surface mechanism is a more complicated process for electrochemical hydriding than for gas phase hydriding. For hydriding via gas phase, the hydrogen bond needs to be broken, and the hydrogen atoms are then more or less free to enter the hydrogen storage alloy lattice. For the desorption process, adsorbed hydrogen is recombined to form gaseous hydrogen.

During the electrolytic process, an electron is transferred from the hydrogen storage alloy (metal hydride) to the water molecule during charging. After this step, the hydrogen atom can be adsorbed on the surface and subsequently can be absorbed into the lattice. During discharge an electron is transferred from the hydroxyl ( $\text{OH}^-$ ) ion to the alloy and adsorbed hydrogen is desorbed and forms water. The electrolytic process as such involves more subprocesses in addition to

an extra barrier in the electrical double layer. Electronic conductivity is also important to facilitate optimum conditions for the hydriding/dehydriding reaction. An optimum reaction rate for the electrolytic hydriding/dehydriding reaction therefore requires additional optimization compared to the gas phase reaction.

The mathematical modelling of a misch metal based hydride electrodes is a complex process because the electrode consists of several metal hydride forming alloy components and particles. The particles may be pressed together with a binder material or pasted into a foam material.

Several assumptions are taken during development of the impedance model.

When modelling impedance the following assumptions were made:

- Spherical shaped reaction zones are uniformly distributed on the metal hydride particles. The shapes of the hydride particles used for the impedance measurements were highly irregular. They were furthermore multi-grained which make modelling of the diffusion process more difficult. For the modelling presented in this thesis, the diffusion coefficient is assumed the same in the bulk metal hydride material and on the grain boundaries.
- A uniform diffusion length. This assumption was used for some of the impedance models presented. In comparisons, the diffusion length distribution models did not fit the experimental data better than the uniform diffusion length models.
- A spherical shaped hydride reaction zone, i.e. spherical hydrogen storage alloy particles. This assumption entailed that the hydride forming reaction started on the alloy surface and moved inwards during the charging of the hydride, giving a reaction zone at a certain radius.

The impedance analysis in this thesis is based on an equivalent circuit analysis. This requires good knowledge of the electrochemical processes taking place in the metal hydride electrodes. If using a conventional impedance fitting tool including only standard elements, neither the hydrogen concentration gradients within the metal hydride particles nor the porous electrode behaviour would have been possible to account for. Special mathematically derived circuit elements were therefore applied to include these processes.



## Chapter 8

# Impedance Response in Metal Hydride Electrodes

*In the following chapter experimental verification of the impedance models developed in chapter 7 is done. The correlation between the electrochemical properties and the state of charge is also discussed.*

Some parts of this chapter have already been published by the author previously [170–172, 174, 221].

### 8.1 Experimental

A similar experimental cell as described in sections 5.2 and 5.3 was used also for the impedance measurements. The cell used for most of the impedance measurements is shown in figure 8.1. The sandwich electrode construction, figure 5.6, was used for most of the impedance measurements. Hydralloy F 30/9C was selected as electrode material because it showed little or no degradation with cycle life for the number of cycles needed to perform the measurements.

The electrolyte was 6M potassium hydroxide (as described in section 5.3) deaerated by N<sub>2</sub>-bubbling to prevent oxygen bubbles interfering with the results. Before measurements, nitrogen were bubbled through the solution, while during the measurements, nitrogen was added *over* the solution. Charging was performed

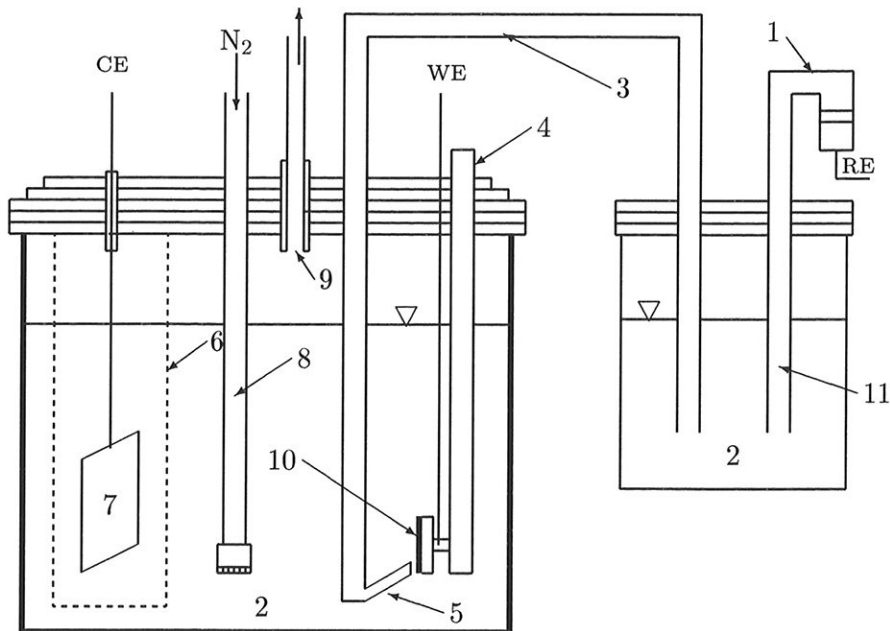


Figure 8.1: *Experimental cell used for impedance measurements. 1) Reference electrode (Hg/HgO), 2) 6M potassium hydroxide, 3) 6M potassium hydroxide, 4) Electrode holder (Teflon), 5) Capillary tube, 6) Diaphragm of polyphenylsulfide (PPS), 7) Counter electrode (platinum), 8) Gas inlet (PTFE) for N<sub>2</sub>-gas, 9) Teflon tube for gas outlet 10) Hydride electrode.*

at a rate of 337.5 mA/g to 297 mAh/g<sup>1</sup>, while discharging was carried out at a rate of 135 mA/g<sup>2</sup> to a cutoff voltage of -600 mV versus Hg/HgO. For the experiments measuring the impedance response as a function of the depth of discharge, discharging was performed at a rate of 1.25C. Hydralloy F 30/9C was used as electrode material unless otherwise noted.

MgNi type electrodes were prepared as follows: magnesium and nickel were mechanically alloyed to form nanocrystalline Mg<sub>2</sub>Ni as described by Jensen [40]. This nanocrystalline Mg<sub>2</sub>Ni and nickel were alloyed to form amorphous MgNi (Mg:Ni = 1:1) The active layer in the electrode was 0.20 g Mg-Ni alloys sieved below 45 μm mixed with 0.80g copper (<44 μm). The active layer was pressed

<sup>1</sup>Corresponds to a rate of 1.25C with 10% overcharge if assuming a maximum discharge capacity of 270 mAh/g (see Eq 5.2).

<sup>2</sup>Corresponds to a rate of 0.5C.



together with a backing layer the same way as the electrodes of the  $AB_5$  type hydrogen storage alloy (for additional details regarding the preparation of the electrode and the electrode material, see the thesis of Jensen [40]). Charging was performed at a rate of 40mA/g, and discharging was carried out at the same rate to a cutoff voltage of -600 mV versus Hg/HgO.

Before any measurements were taken, the electrodes were activated during at least 20 charge/discharge cycles. Measurements were taken at different depths of discharge (DOD). Unless otherwise noted, for each measurement, the electrode was kept at the equilibrium open circuit potential of the electrode after discharging it to the actual depth of discharge (DOD). Impedance measurements were taken after discharge to ensure maximum accuracy in determining the state of charge, since the hydrogen evolution side reaction could interfere with the determination of the state of charge.

The impedance response was monitored in the frequency range of 10 kHz to 0.1 mHz (amplitude 5 mV), using a combination of the Schlumberger Solartron 1250 impedance gain phase analyser and either an EG&G 273 or an EG&G 273a, combined galvanostat/potentiostat. The spectra shown in figures 8.12, 8.13, 8.16, and 8.17 were obtained using an Autolab multipurpose electrochemical measurement instrument, Pgstat 20, in combination with a FRA2 unit.

Constant current charge and discharge were carried out using either an EG&G 273 or an EG&G 273a combined galvanostat/potentiostat.

For the measurements performed at different depths of discharge (DOD), the charged state was defined to be reached as follows (after activation of the electrode):

- Discharge of the electrode to -0.6V versus Hg/HgO,
- Cycle (charge/break/discharge/break) one time, and
- Charge 297 mAh/g.

## 8.2 Model Verification

The verification of the impedance models was usually done using the circuit shown in figure 8.2. The circuit includes the placement of an inductance,  $L$ , an

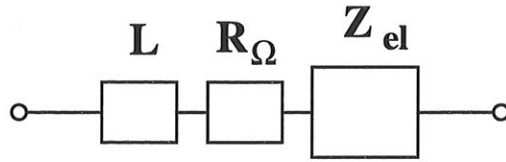


Figure 8.2: Contributions from inductance and ohmic resistance in the system are added in series to the electrode impedance  $Z_{el}$ .

electrolyte resistance,  $R_{\Omega}$ , in series with the electrode impedance,  $Z_{el}$ .

For the magnesium based electrodes, an additional resistance representing the contact between the current collector and the metal hydride particles was included in some of the simulations. the placement of the contact impedance contribution is shown in figure 8.3 As seen from the figure, contact impedance equivalent to

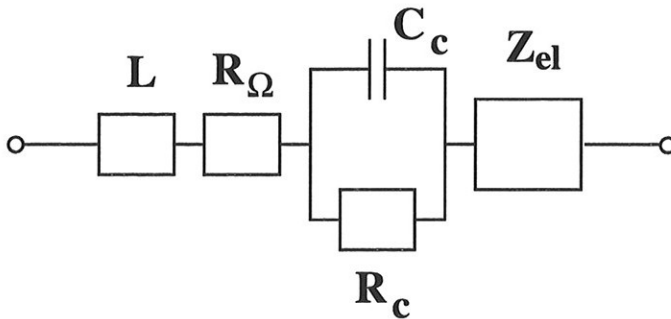


Figure 8.3: Contribution from inductance and ohmic resistance in the electrolyte and contact impedance between the current collector and the metal hydride alloy particles are all added in series to the electrode impedance  $Z_{el}$ .

an RC circuit was be added in series with the electrode impedance,  $Z_{el}$ .

The application of models that fit experimental data includes both a statistical and a graphical part. For the former, the relative standard deviations of the circuit parameters are compared for the different models. The graphical part, on the other hand, involves the following plots:

- Complex plane plots, showing the imaginary part  $Z_{im}$  of the impedance

versus the real part  $Z_{re}$ .

- Bode plots showing impedance ( $Z_{im}$ ,  $Z_{re}$  or  $|Z|$ ) versus the frequency or the logarithm of the frequency.
- The phase angle,  $\theta$ , versus the frequency. This plot gives perhaps the best indication of whether the model simulates the processes in the system or not.
- Residual plots where the difference or the relative difference between the estimated model frequency response and the experimental data are plotted versus the frequency. These graphs show whether possible deviations are systematic or not.

### 8.2.1 Circuit Element Elimination

As mentioned in section 7.5, many sub-processes can be included in an impedance model. By including all possible sub-processes, one is able to fit almost any impedance data. One needs however to be careful not to include an excessive amount of circuit elements, as this will render the obtaining of any conclusion more difficult.

It is essential that the reduction of circuit elements is not done in an arbitrary way. The best way of determining the number of circuit elements is by using a program with error estimates for the circuit elements. For simple circuits, the program developed by Boukamp [178], is user friendly. For metal hydride electrode processes, there is no reasonable alternative to the LEVM fitting routine [222]. The latter is the only program for fitting and simulating impedance response that offers flexibility and the possibility to go beyond the included standard circuit elements [175].

## 8.3 Impedance Model Evaluations

In the subsequent sections, several different impedance models are applied. The equations rendering the spherical diffusion geometry were given in section 7.5.2 and the equivalent circuit for this model was shown in figure 7.9. The planar electrode model was described in section 7.5.4, whereas the inclusion of side reactions

such as hydrogen evolution reaction and a possible parallel reduction/oxidation (redox) side process were described in section 7.5.3. Distribution in the diffusion length was modelled for different discrete particle size distribution as described in section 7.5.5.

As discussed in section 7.2, different models have been developed to account for the impedance response resulting from porous electrode morphology. The model where, deep, cylindrical pores are assumed (section 7.2.3) is used for all porous model simulations.

### 8.3.1 Reference System

For reference purposes, an impedance spectrum for an electrode made of Hydralloy F 30/9C with an intermediate (50%) depth of discharge (DOD) was selected. The simulations were performed as fitting the experimental spectrum to the desired models using a Levenbergh-Markardt fitting procedure based on the LEVM computer program [222] with additional subroutines (the subroutines are given in appendix C).

In table 8.1, the fitting parameters for the reference system (an electrode discharged to 50% depth of discharge) for different impedance models are shown.  $R_{ct}$  refers to the charge transfer resistance, defined by Eq 7.44,  $C_1$  is defined by Eq 7.48, and  $R_1$  by Eq 7.50.  $\frac{D_H}{a}$  is the apparent diffusion coefficient divided by the diffusion length,  $C_p$  is the parallel combination of  $C_1$  and the hydrogen evolution capacitance.  $R_{ev}$ ,  $R_{r/o}$ , and  $R_{\Omega,p}$  are the resistances originating from hydrogen evolution, parallel side processes<sup>3</sup> and the porous morphology<sup>4</sup>, respectively.

In table 8.1, it is also given which processes that were included in the model. For all porous electrode models,  $C_1$  and  $R_1$  were assumed not to influence the electrode processes, as the inclusion of these elements did not improve the fit.

In figure 8.4, the imaginary part of the impedance versus the real part of the impedance response (complex plane plot) for the reference system (an electrode discharged to 50% depth of discharge) for different impedance models is shown. The simulation of the diffusion impedance response is based on two different

---

<sup>3</sup>See section 7.5.3 for additional details.

<sup>4</sup>Deep, cylindrical pores assumed (section 7.2.3).

Table 8.1: *Fitting parameters for different impedance models for an electrode discharged to 50% depth of discharge, reference system.*

Model Geometry	$R_{ct}$ [ $\Omega$ ]	$C_{dl}$ [F]	$C_1$ [F]	$R_1$ [ $\Omega$ ]	$\frac{D_H}{a}$ [ $\frac{m}{s}$ ]	$C_p$ [F]	$R_{ev}$ [ $\Omega$ ]	$R_{r/o}$ [ $\Omega$ ]	$R_{\Omega,p}$ [ $\Omega$ ]
Spherical	0.17	0.032	0.20	0.62	$2.9 \cdot 10^{-9}$	-	-	-	-
Spherical +H <sub>2</sub> evol.	0.17	0.032	-	0.64	$3.7 \cdot 10^{-9}$	0.2	44	-	-
Spherical +porous	0.82	0.24	-	-	$3.3 \cdot 10^{-9}$	-	-	-	0.74
Spherical +porous +H <sub>2</sub> evol.	0.79	0.26	-	-	$4.2 \cdot 10^{-8}$	-	52	-	0.76
Spherical +parallel process	0.80	0.26	-	-	$4.2 \cdot 10^{-9}$	-	-	52	0.76
Planar	0.17	0.035	0.20	0.59	$1.9 \cdot 10^{-8}$	-	-	-	-
Planar +porous	0.93	0.20	-	-	$2.1 \cdot 10^{-8}$	-	-	-	0.64

models, spherical and planar diffusion geometry. Both non-porous and porous electrode morphology were included.

In figure 8.4 it can be observed that a spherical geometry gave a better fit than a planar geometry. The porous model including a parallel process (as described in section 7.5.3) improved the fit in the low frequency region.

Both the advantages and the disadvantages of a complex plane plot are visible in figure 8.4. For electrodes where the diffusion process significantly contributes to the performance of the electrode, the fit in the low frequency region is very important, making the complex plane plot suitable for graphical model evaluations. It is, however, more difficult to determine whether the model fit the data in the high frequency region or not.

In figure 8.5 a plot of the phase angle  $\theta$  versus the frequency is given. The plot includes both a non porous model as described in section 7.5.2. The porous model is based on the model described in section 7.5.2, assuming deep cylindrical

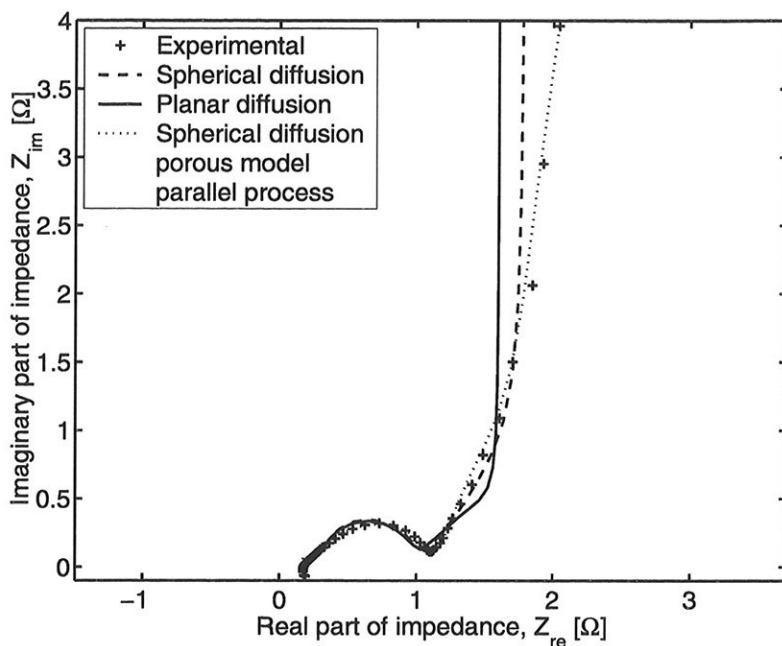


Figure 8.4: Complex plane plot for an electrode discharged to 50% depth of discharge, reference system. The simulation of the diffusion impedance response is based on either spherical or planar diffusion geometry.

pores as described in section 7.2.3. The figure shows that including porosity in the model gave a considerably better fit. For frequencies in the range of 1Hz to 100Hz, the models not including the porous electrode impedance response showed deviations from the experimental data, whereas the model including the porous response fitted the experimental data smoothly.

To account for a possible size distribution in the diffusion length, several size distribution models were developed based on Eq 7.62. The different size distribution models applied are given in table 8.2. In the table,  $X_i$  is the fraction of elements of size  $i$ , defined as the number of particles of size fraction  $i$  divided by the total number of particles, whereas  $a$  denotes the diffusion length in terms of the average particle size,  $a_0$ . All  $a$  values are given in terms of  $a_0$ , the average diffusion length.

As seen from section 7.5.2, the diffusion length, the parameter  $\sigma$  and the diffusion

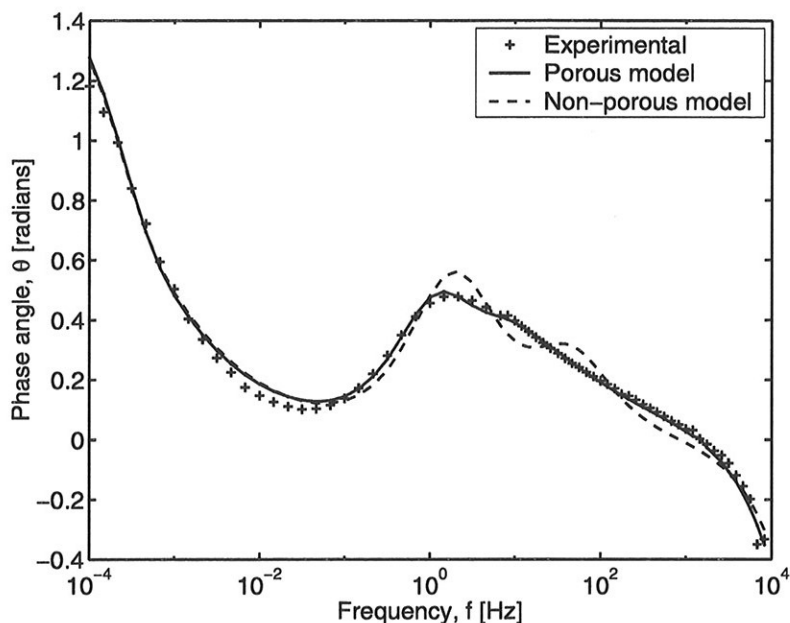


Figure 8.5: Phase angle,  $\theta$ , versus the frequency at 50% depth of discharge for a porous and a non-porous model. Both models have a spherical diffusion geometry.

Table 8.2: Size distribution models applied. All  $a$  values are given in terms of  $a_0$ , the average diffusion length of  $10\mu\text{m}$ . The size fraction  $X_i$  is defined as the number of particles of size fraction  $i$  divided by the total number of particles.

Model	$a_1$	$X_1$	$a_2$	$X_2$	$a_3$	$X_3$	$a_4$	$X_4$	$a_5$	$X_5$
Narrow	0.9	0.1	0.95	0.2	1.0	0.4	1.05	0.2	1.10	0.1
Wide	0.2	0.1	0.6	0.2	1.0	0.4	1.4	0.2	1.8	0.1
Flat	0.2	0.2	0.6	0.2	1.0	0.2	1.4	0.2	1.8	0.2
Sieved	1.2	0.05	1.4	0.15	1.6	0.2	1.8	0.55	2.0	0.05

coefficient are not independent, and it was decided to set the average diffusion length constant ( $10\mu\text{m}$ ) prior to performing the fitting of the data. The first three size distribution models are assumed self explanatory, whereas the last one, sieved, was designed to simulate the size distribution in a sieved powder. The narrow, and wide models are distributed gaussian-like.

In figure 8.6, a Bode plot for the real part of the impedance is shown. The plot shows the size distribution models in table 8.2 fitted to the experimental impedance data. For reference, a model with a uniform size, and a model including a parallel side process are shown. All models assume porous electrode morphology.

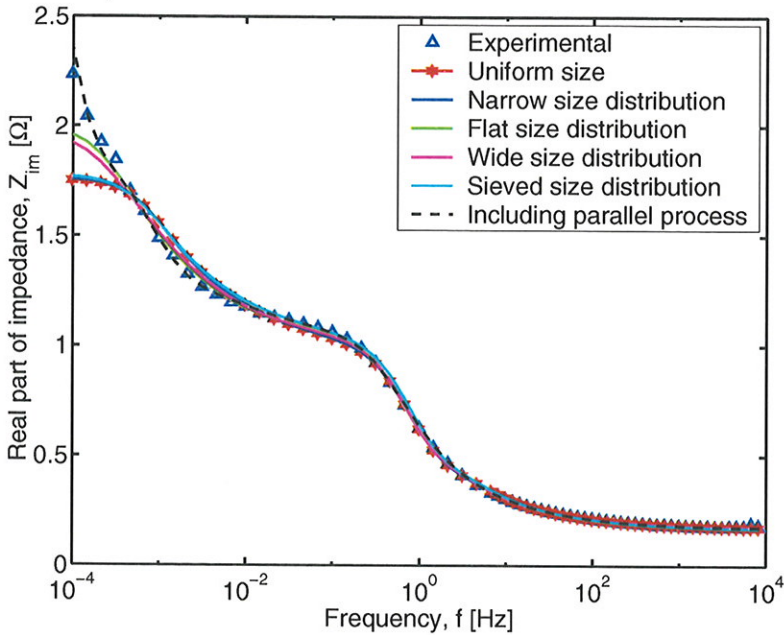


Figure 8.6: Real part of impedance versus frequency (Bode plot) for the real part of the impedance (50% depth of discharge). The plot shows the size distribution models in table 8.2 fitted to the experimental impedance data. For reference, a model with a uniform size, and a model including a parallel side process are shown. All models assume porous electrode morphology.

It is observed that including a size distribution model improves the fit slightly, but less than including the impedance response originating from a process in parallel to the electrochemical metal hydride forming reaction. The magnitude of the determined apparent diffusion coefficient changed when the size distribution models were applied. The relative uncertainty did not, however, decrease.

Considering the shrinking core mechanism shown in figures 3.3 (absorption) and 3.4 (desorption), this observation is of interest as one could have expected the



opposite result for an electrode with several different particle sizes.

In figure 8.7 a plot of the relative residuals of the real part of the impedance versus frequency for three different models assuming a porous electrode morphology is shown.

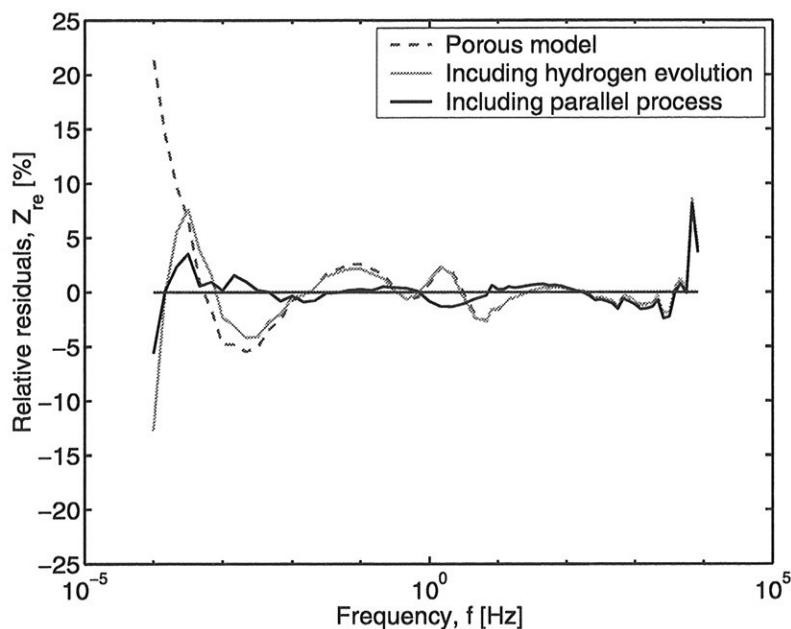


Figure 8.7: *Relative residuals of the real part of the impedance versus frequency for three different models assuming a porous electrode morphology. (50% depth of discharge).*

From the figure one can see that a resistance in parallel to the electrode model for the metal hydride improves the fit for frequencies lower than approximately 20 Hz. This is also seen in figure 8.6, but less pronounced. At higher frequencies, the fit for all three models is similar. The fit including hydrogen evolution also appears to be better than the fit not including this particular process even though the electrode is polarized at a potential less negative than the hydrogen evolution potential.

### 8.3.2 State of Charge Dependent Response

In figure 8.8 a complex plane plot for a fully charged electrode is shown. The

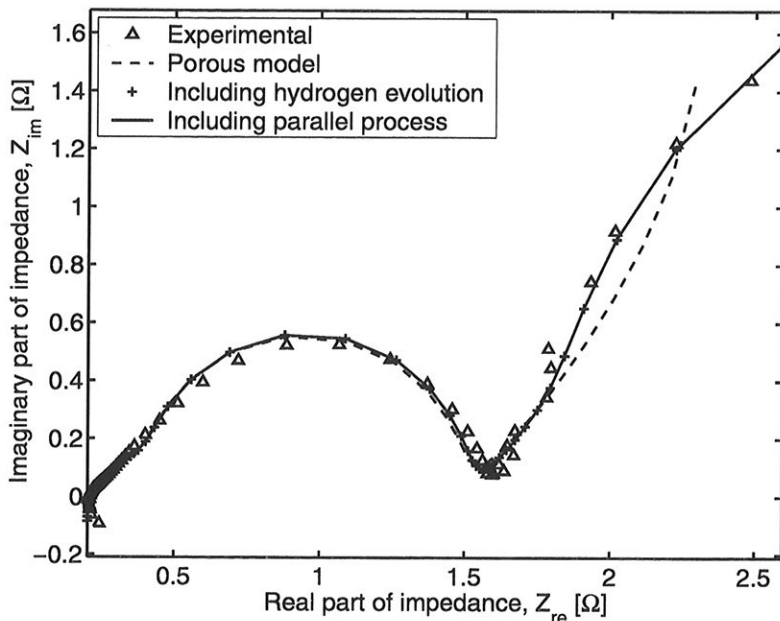


Figure 8.8: *Complex plane plot for a fully charged electrode. The simulation of the impedance response is based on spherical diffusion geometry and porous electrode structure.*

simulation of the impedance response is based on spherical diffusion geometry and porous electrode structure. In the figure it can be observed that including the impedance response from the hydrogen evolution reaction or a parallel redox process gave the best fit.

The fitting parameters for the different impedance models shown in figure 8.8 are given in table 8.3. By comparing the parameter values in tables 8.3 and 8.1, one observes that the charge transfer resistance is considerably higher for the charged electrode. The double layer capacitance is slightly lower for the charged electrode. The open circuit potential for a charged electrode is more negative than the hydrogen evolution potential (compare figure 5.17 and Eq 2.7).

Table 8.3: *Fitting parameters for different impedance models, charged electrode.*

Diffusion Geometry	$R_{ct}$ [ $\Omega$ ]	$C_{dl}$ [F]	$\frac{D_H}{a}$ [ $\frac{m}{s}$ ]	$R_{ev}$ [ $\Omega$ ]	$R_{r/o}$ [ $\Omega$ ]	$R_{\Omega,p}$ [ $\Omega$ ]
Spherical	1.7	0.15	$5.5 \cdot 10^{-10}$	-	-	0.63
Spherical	1.7	0.16	$2.9 \cdot 10^{-9}$	6.6	-	0.64
Spherical	2.2	0.16	$2.9 \cdot 10^{-9}$	-	8.3	0.64

The fitting parameters for an electrode discharged to 10% DOD are given in table 8.4. From the table it can be observed that the charge transfer resistance

Table 8.4: *Fitting parameters for different impedance models, electrode discharged to 10% DOD.*

Diffusion Geometry	$R_{ct}$ [ $\Omega$ ]	$C_{dl}$ [F]	$\frac{D_H}{a}$ [ $\frac{m}{s}$ ]	$R_{ev}$ [ $\Omega$ ]	$R_{r/o}$ [ $\Omega$ ]	$R_{\Omega,p}$ [ $\Omega$ ]
Spherical	1.3	0.16	$8.9 \cdot 10^{-10}$	-	-	0.66
Spherical	1.3	0.17	$2.6 \cdot 10^{-9}$	6.0	-	0.67
Spherical	1.6	0.17	$2.6 \cdot 10^{-9}$	-	7.3	0.67

decreased sharply as the electrode was discharged from 0 to 100% DOD.

The fitting parameters for a discharged electrode are given in table 8.5. From

Table 8.5: *Fitting parameters for different impedance models, discharged electrode.*

Diffusion Geometry	$R_{ct}$ [ $\Omega$ ]	$C_{dl}$ [F]	$\frac{D_H}{a}$ [ $\frac{m}{s}$ ]	$R_{ev}$ [ $\Omega$ ]	$R_{r/o}$ [ $\Omega$ ]	$R_{\Omega,p}$ [ $\Omega$ ]
Spherical	1.9	0.75	$6.0 \cdot 10^{-9}$	-	-	1.1
Spherical	1.9	0.78	$1.7 \cdot 10^{-10}$	12	-	1.2
Spherical	2.1	0.78	$1.7 \cdot 10^{-10}$	-	14	1.2

the table it can be observed that the charge transfer resistance increased when the electrode was discharged from 50 to 100% DOD.

The estimated standard deviations of the parameters were around 15% for the diffusion term and the contribution from possible parallel processes. For the rest of the parameters, an estimated standard deviation of less than 6% was obtained from the LEVM [222] fitting program. It is important to note, however, that the fit obtained is still dependent on the starting parameters. Keeping the uncertainties in mind, the following can be observed from tables 8.1, 8.3, 8.4, and 8.5:

- The diffusion term,  $\frac{D_H}{a}$ , had a lower value for the discharged electrode, indicating a lower apparent diffusion coefficient. The differences are assumed to be smaller than indicated in the tables as also the diffusion length change.
- The porous resistance,  $R_{\Omega,p}$ , was larger for the discharged electrode. By looking at the definition of this element, Eq 7.15, this increase in the porous resistance might be a result of increased pore length for discharged electrodes resulting from volume contractions during discharge.
- The double layer capacitance was lower for the charged electrode and the electrode discharged to 10% DOD. As seen from figure 5.17 compared with Eq 2.7, the open circuit potential for electrodes discharged to less than 12% depth of discharge is higher than the reversible hydrogen evolution potential. Hydrogen bubbles in the electrode structure could decrease the surface area and consequently the double layer capacitance. The fit in the high frequency region was also slightly inferior for fully charged electrodes. It was assumed that both the fit quality and possible hydrogen bubbles contributed to the lower double layer capacitance for charged electrodes. The high double layer capacitance for the discharged electrode might be resulting from volume contractions during discharge, exposing more surface to the electrolyte by reducing possible void space in the electrode.
- The resistances from side processes are highest for medium discharged electrodes, indicating that possible side processes can be both reduction and oxidation processes.

In figure 8.9 the phase angle versus the frequency showing experimental data for a discharged electrode (100% DOD) is shown. From the figure, it can be observed that the porous electrode model simulated the impedance very well also for a discharged electrode. In figure 8.10, the real part of the impedance

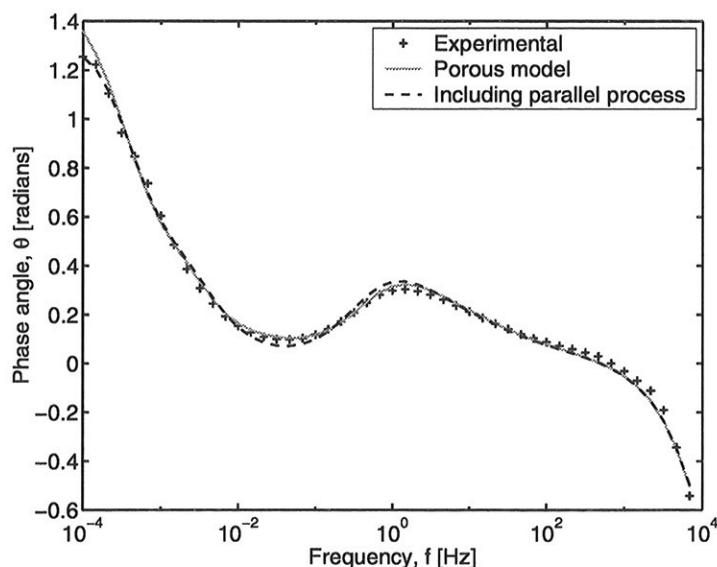


Figure 8.9: Phase angle versus the frequency showing experimental data for a discharged electrode (100% DOD) fitted to two models, both including porous electrode morphology.

versus the frequency (Bode plot) showing experimental data fitted to models both and without particle size distribution for a discharged electrode<sup>5</sup> (100% DOD) is shown. The experimental data is fitted to two models, one model including porous electrode morphology, and one model also including a parallel process.

One observes that including size distribution of the particles did not improve the fit of the impedance data for the discharged electrode. This is a quite notable finding, as the opposite could be expected for a pressed powder electrode consisting of numerous metal hydride forming alloy particles with a wide range of different particle sizes.

The different size distribution models gave the same graphical fit, but with different fitting parameters for the the diffusion impedance. The relative uncertainty in the determined apparent diffusion coefficient increased slightly as the uniform model was replaced with any of the size distribution models. This indicates that

<sup>5</sup>Because of more experimental points in the low frequency region, the impedance response shown in figure 8.10, is taken from another electrode than the other graphs shown in this section.

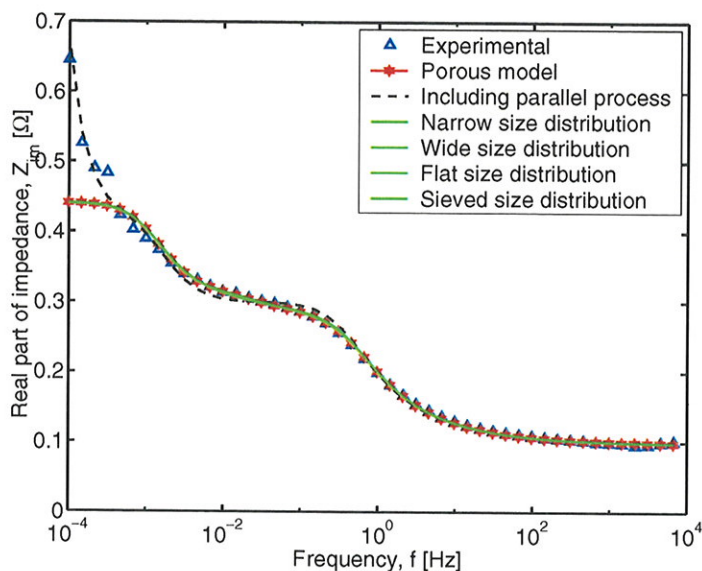


Figure 8.10: *Real part of the impedance versus the frequency (Bode plot) showing experimental data fitted to models both and without particle size distribution for a discharged electrode (100% DOD).*

shrinking core type of model does not describe the processes taking place in an  $AB_5$  type metal hydride electrode properly.

In figure 8.11, the polarization resistance for Hydralloy F 30/9C is shown as a function of the depth of discharge for 4 different runs.

Since the circuit parameters were not found to be completely independent, the polarization resistance is just taken as the width of the arc in the complex plane plot, see for example figure 8.4. The experimental points giving the plot in figure 8.11 are not originating from the same electrode as the data given previously in this section. As seen from figure 8.11, the polarization resistance varied considerably with the DOD. The resistance was relatively high for completely charged electrodes (low DOD), and decreased to a shallow minimum between approximately 40 and 95 % DOD. The shape of the curve is similar to the shapes observed by various other researchers [137, 156, 200–204].

The high resistances observed at the highest depths of discharge are assumed to be caused by partly oxidation of the hydrogen storage alloy in the electrode (see

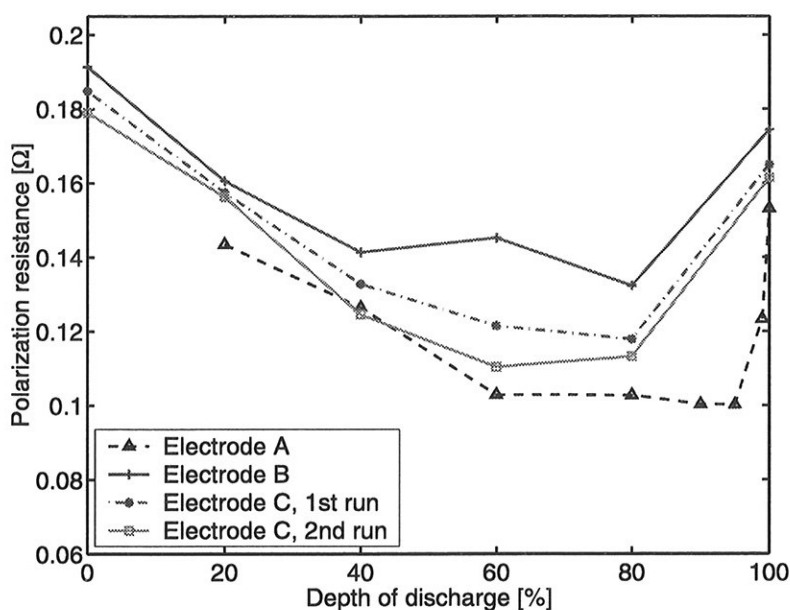


Figure 8.11: Polarization resistance as a function of the state of charge for Hydralloy F 30/9 C.

section 3.8 for additional details regarding the oxidation potentials of the alloy materials). These experimental points should therefore not be taken into consideration when making conclusions about the mechanisms governing the kinetics of the metal hydride electrode.

### 8.3.3 Magnesium Based Electrodes

In figure 8.12, three impedance models were fitted to the experimental data of a charged MgNi electrode. The high frequency region is emphasized. The electrode was made of a ball-milled Mg:Ni (1:1) as described by Jensen [40]. From the figure, it can be seen that the impedance response was similar to that observed for the AB<sub>5</sub> system, indicating that the same processes governed the mechanisms in the electrode processes.

A more detailed comparison between the different models is given in figure 8.13.



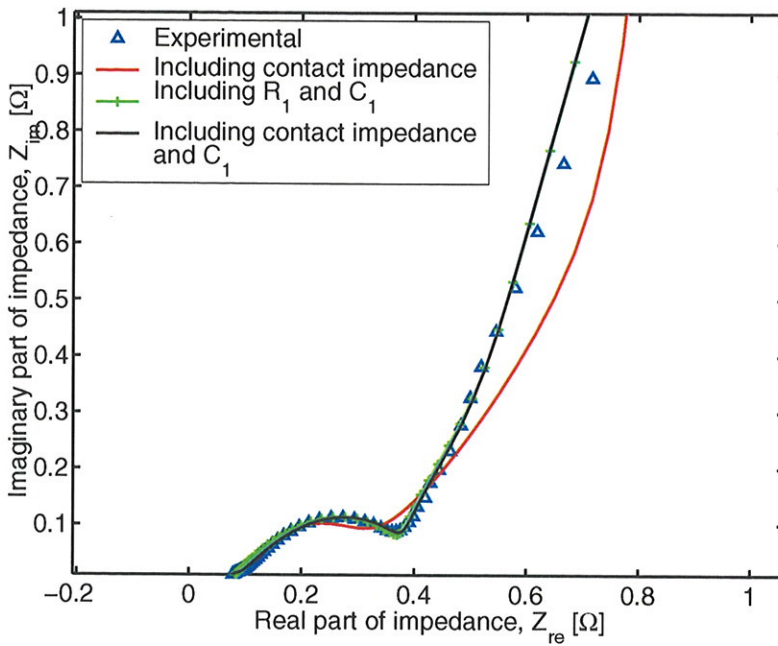


Figure 8.12: Complex plane plot showing impedance response for a charged  $MgNi$  electrode fitted to three different impedance models.  $C_1$  and  $R_1$  are defined by Eqs 7.48 and 7.50 respectively.

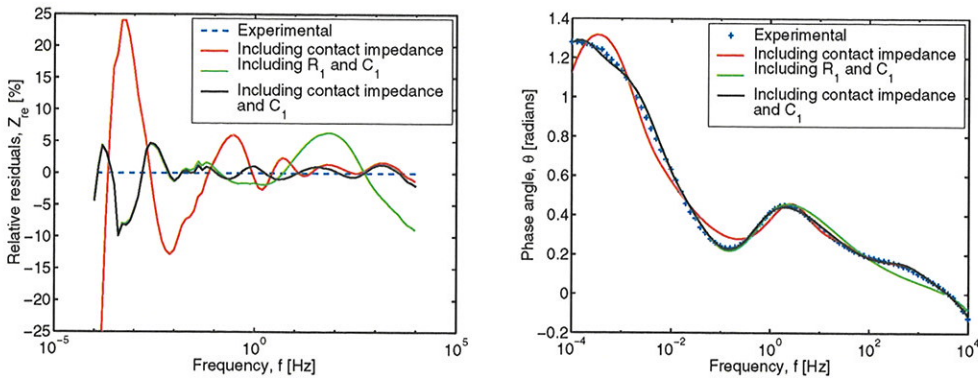


Figure 8.13: Comparison between three different electrode models for  $MgNi$ . Left: residuals of the real part of the impedance versus frequency. Right: phase angle versus frequency.  $C_1$  and  $R_1$  are defined by Eqs 7.48 and 7.50 respectively.



From figure 8.13 it can be observed that, in contrary to the AB<sub>5</sub> system, the high frequency fit was better when the contact impedance was included. In the low frequency region, an improved fit was obtained when the surface capacitance was accounted for. The best fit was obtained when both processes were included.

Since the magnesium nickel metal hydride powder was made by ball milling, the sizes of the hydride particles were considerably smaller than for conventionally made electrodes. In table 8.6, the particle size and quantity of active electrode material are given for the AB<sub>5</sub> type electrodes and the MgNi type electrodes.

Table 8.6: *Particle size and quantity of active electrode material for the AB<sub>5</sub> type electrodes and the MgNi type electrodes.*

Alloy	r [ $\mu\text{m}$ ]	$\rho$ [ $\frac{\text{g}}{\text{cm}^3}$ ]	$m$	$R_p$ [ $\Omega$ ]
MgNi	1	4.9 <sup>6</sup>	0.2	0.3
AB <sub>5</sub>	10	8.3 [47]	0.6	0.14

Here  $r$  is the alloy particle radius,  $\rho$  the alloy density, and  $m$  the active mass. To estimate the particle size of the ball milled MgNi alloy is quite difficult as the particles tend to cluster during ball milling. An average value was therefore estimated from SEM micrographs given by Jensen [40]. The particle size of the AB<sub>5</sub> type alloy is assumed after some cracking during cycling. The polarization resistance is taken as the width of the arc given in figure 8.12 for the MgNi alloy and as an estimated average value of the polarization resistance shown in figure 8.11 for the AB<sub>5</sub> type alloy.

This affected the properties of the hydride electrodes by making the connection to the current collector more difficult and by increasing the reaction area. The connection to the current collector was assumed to be more difficult because the ball-milled particles had a considerably smaller size than the current collector particles [21]. In order to achieve a good current collection, all ball-milled particles should ideally be evenly distributed on the surface of the current collector particles. This is not likely to be the case for an electrode material mechanically mixed together with current collector material. An increase in the contact impedance compared to the AB<sub>5</sub> type electrodes was thus noted. The origin of this impedance might be either cluster formation during the mechanical alloying

<sup>6</sup>Taken as the mass average of Mg<sub>2</sub>Ni and nickel.

or a large difference in the particle size of binder and alloy material. Another possible source of this capacitance could be that magnesium is passive under the conditions used [24], which might influence the contact between the current collector and the metal hydride alloy.

To compare the catalytic activity, the exchange current densities for the different alloys can be compared. The exchange current,  $I_o$ , is the inverse of the polarization resistance and is given by

$$I_o = \frac{RT}{nFR_p} \quad (8.1)$$

Here,  $F$  is Faraday's constant, and  $n$  is the number of electrons transferred.  $R$  and  $T$  are the gas constant and the temperature, respectively. If spherical particles are assumed, the number,  $n$ , of particles can be found from the following equation:

$$n = \frac{m}{\rho V} = \frac{m}{\frac{4}{3}\rho\pi r^3} = \frac{3m}{4\pi\rho r^3} \quad (8.2)$$

Here  $m$  is the active mass and  $V$  is the volume of the active mass in the electrode. The exchange current density can then be expressed as:

$$i_o = \frac{I_o}{A} = \frac{I_o}{n \cdot 2\pi r} = \frac{\rho r}{3m} \cdot \frac{RT}{FR_p} \quad (8.3)$$

Here,  $A$  is the area. If the values given in table 8.6 are assumed, a pure geometrical consideration using spherical particles give a rough indication that says that the catalytic activity for the  $AB_5$  type alloy roughly is 10-12 times higher than the catalytic activity of the MgNi type alloy. The reason for this is assumed to be that in reducing alkaline medium, magnesium passivates [24]. This passivation does not enable for the surface nickel enrichment which is observed for the  $AB_5$  type alloys.

Considering the fact that the charge transfer step is one of the crucial steps governing the total charge/discharge performance of an  $AB_5$  type electrode, it can be noted that the MgNi type electrodes need to be improved considerably before they can be used in batteries.

An improved MgNi type electrode should contain the following properties:

- Better contact between the alloy and the current collector.
- Enhanced surface catalytic properties. The surface should preferably be with a material with higher catalytic activity.

For the measurements with the MgNi electrodes, the accuracy in the state of charge is considerably lower, since the electrodes were charged and discharged with 40 mA/g, which is quite high for MgNi electrodes. Impedance diagrams for MgNi electrodes are therefore given only for one measurement in order to show that the impedance models fit this type of electrodes as well.

### 8.3.4 The Hydrogen Evolution Parallel Reaction

In figure 8.14, a complex plane plot and a plot of the phase angle versus the logarithm of the frequency is given for an electrode polarized at the hydrogen evolution potential.

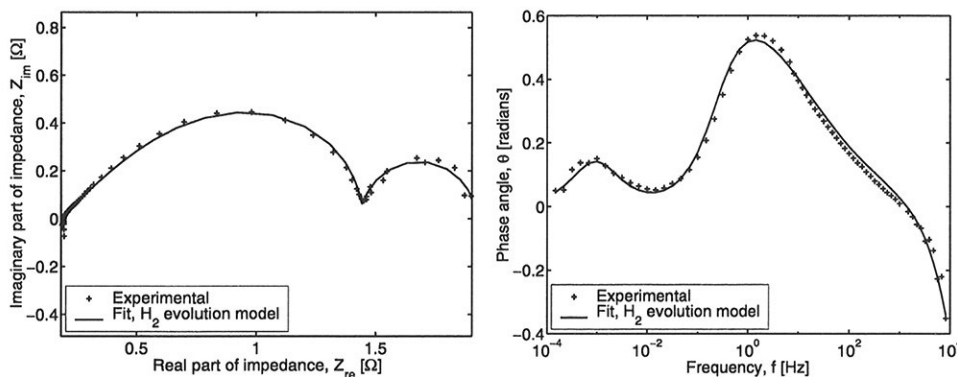


Figure 8.14: *Impedance measurements, electrode polarized at the hydrogen evolution potential fitted to the equivalent circuit given in figure 7.10 with an ohmic resistance and an inductance in series as shown in figure 8.2. Left: complex plane plot. Right: phase angle versus the logarithm of the frequency.*

From the complex plane plot it is observed that the developed porous electrode model described the case of hydrogen evolution on the metal hydride electrode remarkably well. The plot is furthermore similar to the model shown in figure 7.1 with two processes in series. Figure 8.14 furthermore indicates that the diffusion

tail of the impedance diagrams for electrodes polarized at the open circuit potential could be a result of hydrogen diffusion within the metal hydride particle and as such not a result of the diffusion of water molecules or hydroxyl ions in the electrolyte. On the other hand, hydrogen evolution also improves transport of ions in the electrolyte. It is also very important to note that the width of the arcs in the complex plane plot shown in figure 8.14 is very dependent on the potential applied during measurement.

### 8.3.5 Amplitude of the Applied Potential

In figure 8.15 the open circuit potential for intermediate depths of discharge for the most frequently used alloy, Hydralloy F 30/9C<sup>7</sup> is given. The maximum

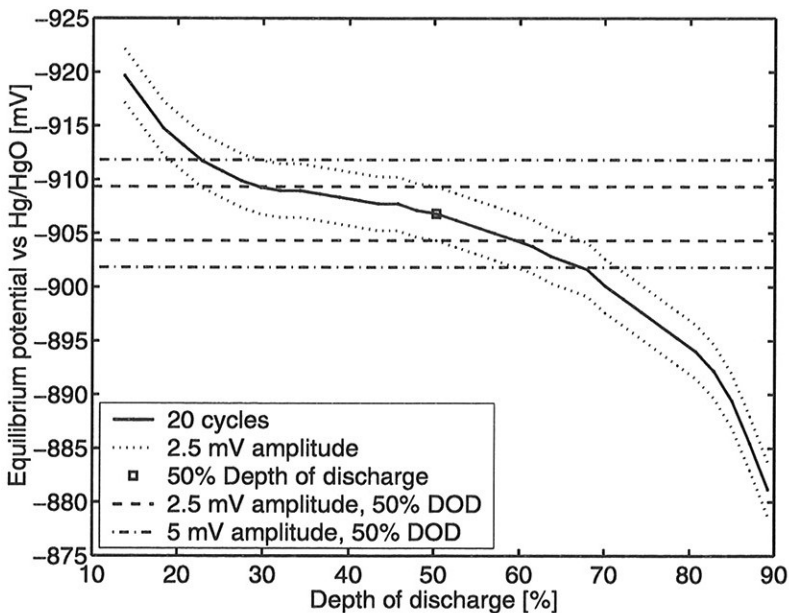


Figure 8.15: *Open circuit (equilibrium) potential versus depth of discharge for an alloy with relatively large plateau sloping (Hydralloy F 30/9C). Maximum potential variations during impedance measurements ( $\pm 2.5\text{mV}$ ) and ( $\pm 5\text{mV}$ ) are indicated.*

<sup>7</sup>The whole diagram from 0-100% DOD is given in figure 5.17.

potential variations during impedance measurements are here defined as polarization of the electrode at the maximum potential amplitude, i.e. an impedance measurement where the frequency approaches zero. As can be observed from the plot of the open circuit for the alloy used in most of the impedance measurements there was no flat plateau region for any depth of discharge.

From figure 8.15 one can also note that it was very important to carry out all the measurements at the right open circuit potential, since the polarization of the electrode at only a couple of mV could induce significant changes in the state of charge for the electrode. The impedance response was very dependent of the state of charge.

Figure 8.15 indicates that the highest possible change in the state of charge was 45% for a 10mV peak to peak amplitude and 30% for a 5mV peak to peak amplitude if the impedance measurements was carried out at approximately 50% depth of discharge. It is reasonable to assume that the actual change was much less than the worst case scenario presented in figure 8.15 because the potential is varied during the impedance measurement (see section 7.1 for additional details). It is important, however, to keep in mind that with less plateau sloping, the impedance at the lowest frequencies could be affected by the change in the state of charge during measurements.

### Flat plateau alloys

In figure 8.16, the impedance response for  $\text{LaNi}_{3.4}\text{Co}_{1.2}\text{Mn}_{0.1}\text{Al}_{0.3}$ , an alloy with a rather flat plateau is given at 50 % DOD.

When comparing the complex plane plot at 50% DOD for an alloy with a high plateau sloping (figure 8.4) and for an alloy with less plateau sloping (figure 8.16), one can observe that in the case of less plateau sloping, the low frequency impedance response shows increased real part. This is reasonable since the real impedance increases by increasing DOD in this range. The shape of the low frequency part of the impedance diagram resembled the shape proposed by Paasch *et al.* [223] for electrodes with charge storage, i.e. an electrode that are charged or discharged during an impedance measurement. The shift is as such assumed to be a result of changes in the state of charge of the electrode during the impedance measurement. In addition, this shift also indicates that the diffusion limitations in the system are related to hydrogen diffusion within the metal hydride particles

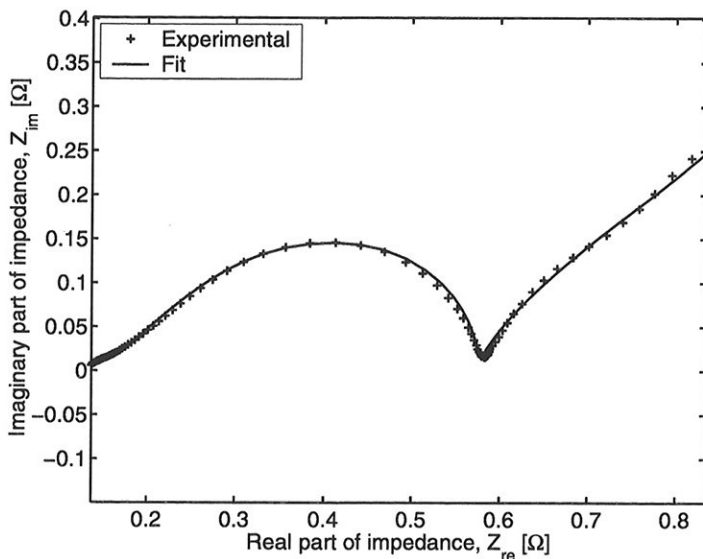


Figure 8.16: Complex plane plot showing impedance response for an alloy with a rather flat plateau ( $\text{LaNi}_{3.4}\text{Co}_{1.2}\text{Mn}_{0.1}\text{Al}_{0.3}$ ) at 50% DOD.

and not diffusion of  $\text{H}_2\text{O}$  and  $\text{OH}^-$  in the electrolyte, since the charge storage possibilities are more limited in the electrolyte. Because the measurements in the flat plateau region were likely to affect the state of charge of the electrode to such an extent that the properties of the metal hydride could change significantly during the measurement, interpretation of the low frequency part of impedance measurements were only possible for either fully charged or fully discharged flat plateau alloys. A possible way of solving this issue, could be to apply current variations instead of potential variations. The amplitude could also be reduced to a minimum. It is, however, very important to keep the amplitude considerably higher than the uncertainty in the potential measurements i.e. noise level.

### 8.3.6 Impedance Response from Equipment and Electrode Construction

According to Edwards *et al.* [224], the combination of a Solartron 1260 and a Solartron 1287 experimental setup will result in an uncertainty exceeding 1% if the maximum frequency goes above 10KHz. This statement is valid for impedances

between approximately  $10\Omega$  and  $1K\Omega$ . Within those impedance limits, the maximum frequency with precise measurements is  $1KHz$ . For impedances less than  $100m\Omega$ , the measurement uncertainty reaches above 1% for all frequencies. If one compares these findings with the experimental data, one observes that the highest frequencies were slightly less precise because of the impedance analyser used.

The copper surface area exposed to the electrolyte contributed to the total electrode capacitance, and thus affected the time constant. In figure 8.17 the impedance response for a pure copper electrode made of a pressed copper powder is given. From figure 8.17, one observes that a linear segment at higher frequen-

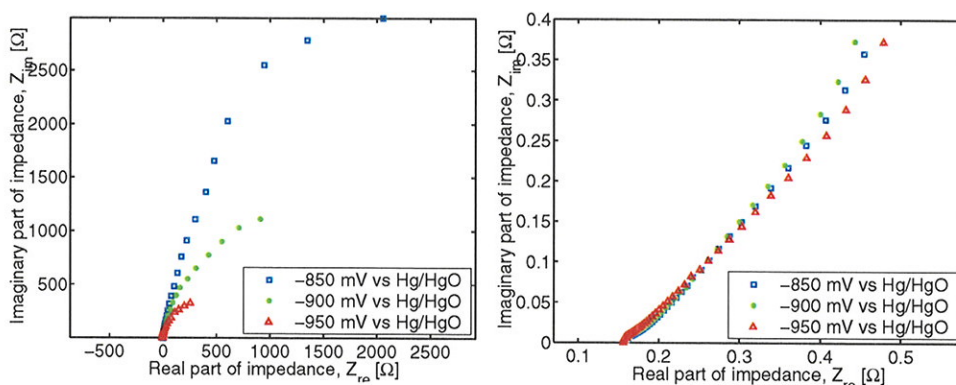


Figure 8.17: *Complex plane plots for a pure copper electrode made of pressed copper powder polarized at different potentials. Left: full spectrum. Right: high frequencies emphasized.*

cies. This linear segment is very similar to the straight-line segment observed at high frequencies for measurements on metal hydride electrodes. This is a strong indication that porous processes really contributed to the impedance response in the electrodes as described in section 5.3. The metal hydride powder has a comparable size to the copper powder, so the porosity will be about the same as in figure 8.17. The low frequency impedance from the copper electrode was a lot larger than for metal hydride electrodes (compare figure 5.20 with for example figure 8.4). It is, however, very likely that the copper surface may contribute significantly to the non faradaic impedance, i.e. the double layer capacitance, rendering analysis of the non faradaic impedance very difficult.

The equilibrium potential for the  $Cu/Cu_2O$  oxidation/reduction reaction is  $-460mV$  versus the  $Hg/HgO$  reference electrode [66]. From figure 8.17, one can



see that the copper powder electrode is not totally blocking and the experimental points for each polarization potential can be connected to form a half circle segment. The diameter in this half circle segment was decreasing as the potential was decreased to more negative values. This indicated that the impedance response was originating from a reduction process. The reversible hydrogen evolution potential is 0.93 V versus Hg/HgO (Eq 5.4). Only for the polarization at -950mV versus Hg/HgO, the reduction process could be hydrogen evolution reaction. For the other two measurements, the shift is assumed to be originating from either adsorption of hydrogen on the electrode surface or from reduction of contaminants in the electrolyte. The shift is, however smaller than for the metal hydride electrodes, indicating that there are parallel processes competing with the electrochemical absorption/desorption reactions. Manganese, which is one of the constituents in Hydralloy F 30/9C, can have several oxidation states and at least two of these exists in the potential range in which the measurements were taken (see section 3.8.2).

### 8.3.7 Contact Impedance

No signs of any contribution from contact impedance were detected for the AB<sub>5</sub> type alloys. The electrochemical setup provided a good contact area between the hydrogen storage alloy and the current collector, since the binder to alloy ratio was high and the particle size of the copper binder and the alloy powder were in the same range. In addition, there were only copper/copper connections from the binder material all the way up to the frequency analyser.

Another way of providing a good contact area is to employ an electrode construction, which has distinct time constants for the current collection steps. This gives extra half circles on impedance diagrams as shown by Kuriyama *et al.* [198, 209–211], and minimizes the possibility that different processes interfere with each other on the impedance diagram.



## 8.4 Discussion

### 8.4.1 State of Charge Dependent Kinetic Variations

The shape of the curve from 0% DOD to 95% DOD shown in figure 8.11 is opposite of what would be expected if the rate of the charge transfer reaction rate was solely controlled by the surface area of the metal hydride particles in the electrode. If the whole metal hydride particle surface was taking place in the charge transfer reaction, (i.e. a uniform catalytic activity) the measured charge transfer resistance would be smaller for completely charged electrodes since those would have the largest surface area.

For other alloy systems, other correlations between the polarization resistance and DOD have been observed. For the MgNi system, for example, the polarization resistance is lowest for completely charged electrodes [106]. The same trends were observed for activated  $\text{Ti}_{0.5}\text{Zr}_{0.5}\text{V}_{2.13}\text{Ni}_{1.15}$  electrodes<sup>8</sup> [225]. The apparently different results for the other systems are indicating that the observed changes in the kinetic properties with the state of charge not are solely due to changes in the electrode as a result of the volume expansion/contractions during charge and discharge. The high resistance of electrodes that had undergone a discharge of less than 50% is therefore notable.

In figure 8.18, an illustration of a nearly fully charged metal hydride particle showing sites still active for hydriding/dehydriding is shown.

From figure 8.18 it can be seen that for an irregularly shaped electrode, some surface sites may be blocked or show at least reduced hydrogen activity when the hydride electrode is nearly fully charged. The diffusion path for hydrogen in the  $\beta$  phase to and from the active surface sites farthest away from the alloy phase (unhydrided center of alloy particles) are so long that essentially, these sites can be excluded from participating in the hydride reaction. An impedance measurement carried out for example on small, uncracked, equally sized gas atomized spherical metal hydride particles with a highly catalytic surface would probably indicate a lower resistance for charged particles (including particles of the  $\text{AB}_5$  type) as observed for other alloy systems.

---

<sup>8</sup>Total resistances (in  $\Omega$ , DOD in parentheses): 0.93 (10%), 1.03 (28%), 1.17 (45%), 1.41 (62%), 1.81 (80%)

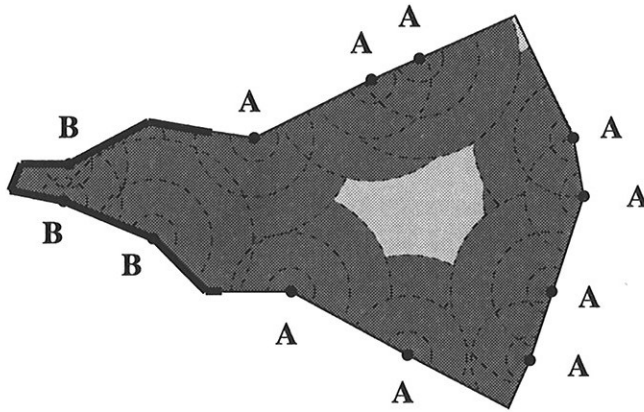


Figure 8.18: *Illustration of a nearly fully charged metal hydride particle showing sites still active for hydriding/dehydriding. The darkened area represents the unhydrided material while the slightly darkened area refers to the hydrided material. Blocked sites are marked with a "B" and active sites with an "A". Active sites may be significantly closer on electrodes than indicated in the figure.*

It is very difficult to perform measurements with a constant particle size throughout the entire electrode, since the metal hydride particles crack down to smaller units during cycling [118].

If surface diffusion of adsorbed hydrogen from the surface sites takes place, the case gets more complicated. If the surface diffusion is slow compared to the bulk diffusion of hydrogen in the  $\beta$  phase, surface site blocking may still occur as shown in figure 8.18. The spherical reaction zones may be replaced with a distribution of spherical reaction zones around the active sites on the surface. The faster the surface diffusion is compared to the bulk diffusion, the more the hydrided zone will resemble the shape of the particle. For example, if the surface diffusion is very fast compared to the bulk diffusion, a shrinking core type of model can very well be used to describe the shape of the hydrided zone as illustrated in figure 8.19. There is no major difference between the hydrided zones when comparing fast surface diffusion and uniform catalytic activity on the alloy surface when the lattice expansion during hydriding is disregarded. When the volume expansion is taken into account the catalytic mechanism and the slow bulk diffusion compared

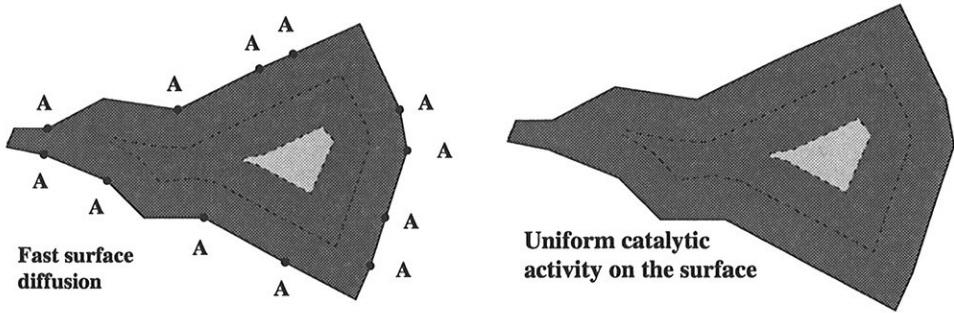


Figure 8.19: *Hydrided zones for nearly fully hydrogenated hydrogen storage alloys. The darkened area represents the unhydrided material while the slightly darkened area refers to the hydrided material. Left: catalytic mechanism assuming fast surface diffusion compared to bulk hydride diffusion; Right: assuming uniform catalytic activity on the surface.*

to the surface diffusion will presumably show very little variation with the state of charge.

No possible reactivation processes after the measurements were taken into account. This is assumed to be a reasonably accurate assumption for the measurements carried out at depths of discharge less than approximately 95% (see section 5.5.3). After the impedance measurements were carried out, the state of charge was recorded. It was found that the sum of the depth of discharge during the measurement, and the remaining charge after the measurement equalled the normal total discharge capacity for the cycles just prior and just after the impedance measurements within a reasonable error.

#### 8.4.2 Mechanism

As seen in previous sections, a size distribution model did not improve the fit to the experimental data. Assuming a catalytically enhanced mechanism, the charge transfer reaction can only take place on active sites at the surface. This translates into replacing the total charge transfer resistance,  $R_{ct}$ , into a collection of individual charge transfer resistances,  $R_{ct}^*$ , in parallel as illustrated in figure 8.20.

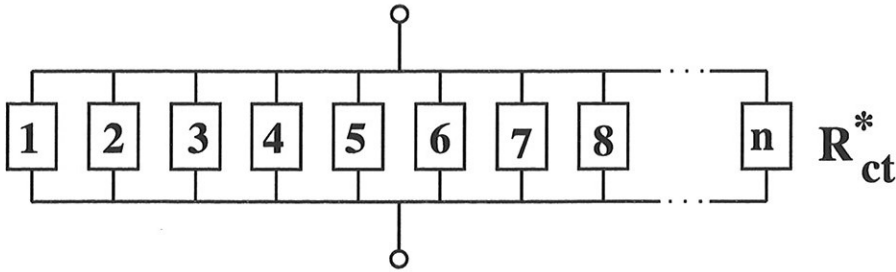


Figure 8.20: Illustration of how charge transfer resistances for active points  $R_{ct}^*$  on the surface combines to the total charge transfer resistance,  $R_{ct}$ .

The total charge transfer resistance can therefore be calculated as follows:

$$\frac{1}{R_{ct}} = \sum_{i=1}^n \frac{1}{R_{i,ct}^*} \quad (8.4)$$

Here  $n$  is the number of active sites on the surface and  $R_{i,ct}^*$  is the charge transfer resistance in active point  $i$ . If the same charge transfer resistance is assumed in each active point, the rate of hydrogen atoms passing this "gate" would be the same for all active sites. The hydrogen would then diffuse through the metal hydride  $\beta$  phase to the reaction zone where new beta phase would be formed.

In figure 8.21, three different possible diffusion paths are compared. As seen from the figure, several possible diffusion paths can exist for hydrogen in the hydrogen storage alloy. If the diffusion speed is the same in all directions, the phase transition will have a spherical shape as shown to the left in the figure. If one direction dominates, the phase border between the  $\alpha$  and the  $\beta$  phase will have a more elliptic shape. If the nucleation centres are not in the surface region, for instance for an inhomogenous alloy with a high plateau slope, the diffusion paths illustrated to the right is the most relevant. With respect to the impedance modelling, it would be impossible to differentiate between the model to the left and in the middle, as for identical starting times for desorption hydrogen atoms would reach the reaction zone at the same time. In the case of multi-grained alloy particles and closely located surface sites, the diffusion paths may be a lot more complicated than those shown in figure 8.21.

Since an active catalytic site is located at the electrolyte interface several oxidation states can exist for the site. A proposed mechanism for the electrolytic

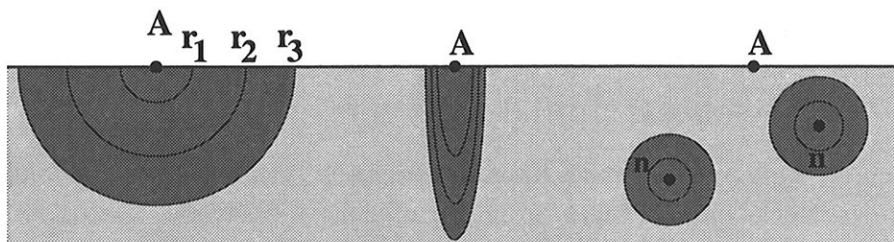


Figure 8.21: *Three possible diffusion paths for hydrogen during discharge (desorption), assuming no surface diffusion of hydrogen. The phase borders are smoothed out. The slightly darkened area represents the unhydrided material while the darkened area refers to the hydrided material. Left: spherical transport path, Middle: elliptic diffusion path. Right: nucleation centres different from surface active site.*

hydriding/dehydriding will therefore have to be elaborated in close relation to the existing data on electrolytic activation of hydrogen storage alloys. It is known that during activation there is a change in the composition of the surface layer, with nickel enrichment on the surface [128]. This indicates that the presence of nickel is important for the charge transfer reaction. This hypothesis is furthermore supported by the fact that an increase in the cobalt content on the B-site in  $AB_5$  type alloys slows the kinetics. This is also the case for most other B site substitution elements (see section 3.4.3).

## 8.5 Conclusions

The electrochemical impedance responses for different laboratory type metal hydride electrodes were successfully modelled and fitted to experimental data for  $AB_5$  type hydrogen storage alloys.

The models fitted the experimental data remarkably well. The fits presented in this chapter differed from fits previously reported in literature by their smooth fit for all frequencies in the range from 10KHz to 0.1mHz. Especially the fit at the lower frequencies was notable.

The different sub-processes taking place during the charge/discharge reaction were identified. The following processes were found to be significant for the overall reaction rate: charge transfer resistance, double layer capacitance, and impedance resulting from diffusion. The diffusion was best modelled when using spherical diffusion geometry. To fit the experimental data, equations describing the current distribution in porous electrodes were needed.

To account for possible parallel hydrogen evolution reaction during charging, it was necessary to include this step in the model for electrodes having an open circuit potential more negative than the reversible hydrogen evolution potential. Indications of one or more parallel reduction/oxidation processes competing with the electrochemical hydride absorption/desorption reaction were observed.

The results furthermore indicated rather large variations in the kinetic parameters for the process at different states of charge of the hydride material. The optimum energy efficiency for a battery electrode of the material used (Hydralloy F 30/9 C) was obtained in the range of 40 to 95% depth of discharge. The results confirmed the usefulness of the impedance method for in situ characterization of hydride electrodes.

## Chapter 9

# Concluding Discussion

*In the following, the findings from the different characterization methods are compared and the study is concluded.*

### 9.1 Misch Metal Composition in AB<sub>5</sub> Type Hydrogen Storage Alloys

To improve the properties of AB<sub>5</sub> type alloys used in NiMH batteries, the misch metal composition should be tailored in order to get the optimum plateau pressure. From chapter 4, one could see that the misch metal composition was very important for the unit cell geometry and consequently the plateau pressure of misch metal based AB<sub>5</sub> type hydrogen storage alloys. Substitution of lanthanum in LaNi<sub>5</sub> with cerium gave a considerably higher plateau pressure than substitution with neodymium and praseodymium. The observed higher pressure could be explained by a contraction of the basal plane parameter. This contraction was to some extent compensated by an increase in the axial unit cell parameter, increasing as such the anisotropy of the unit cell.

LaNi<sub>5</sub> showed a very good high current discharge performance compared to other AB<sub>5</sub> type alloys. In chapter 6 it was shown that the A site substitution of lanthanum by the misch metal did not decrease the high current performance when compared to LaNi<sub>5</sub>. B site substitution of nickel with other transition elements on the other hand substantially reduced the high current performance.

When a higher pressure was used within the cell, a considerable increase in the charge/discharge performance could be attained. A decrease in the cost of the hydrogen storage alloy could be obtained in pressurized cells by applying hydrogen storage alloys with higher plateau pressures.

## 9.2 Kinetics

### Time dependent changes

The kinetics are dependent both on the bulk and the surface properties of the metal hydride material used and are changing throughout its lifetime. The activation properties are highly dependent on the charge/discharge current. For high current applications, the activation might need as high as 100 cycles to reach full capacity, whereas for low current applications, one might need only 5-10 activation cycles with the same current used for activation (pretreatment of the alloy might enhance the activation considerably). The activation time is also dependent on the amount of charge transferred to the metal hydride material and the external pressure. A higher external pressure resulted in a faster activation. The measurements performed indicated that the activated state is dependent on several factors, which need to be examined individually as well as combined in order to gain a complete understanding of the kinetics.

### Impedance characterization

From the characterization of the metal hydride electrodes by means of electrochemical impedance spectroscopy (EIS), it was found that the EIS technique, when used properly and in combination with other characterization techniques, was very useful in determining the significance of the different sub-processes in the overall process. The impedance response for different laboratory metal hydride electrodes were successfully modelled and fitted to experimental data for both electrodes made of  $AB_5$  type alloys and a MgNi type electrode. The models fitted the experimental data remarkably well. The fits differed from previously reported fits by their smooth fit for all frequencies in the range from 10KHz to 0.1mHz. Especially the fit at the lower frequencies (diffusion processes) was notable.



The following sub-processes were found to be significant for the overall reaction rate: charge transfer resistance, double layer capacitance and impedance resulting from diffusion of hydrogen in the alloy. Porous electrode equations were required to fit the experimental data, indicating that the porous structure influenced the performance of the electrode. It was also necessary to include the hydrogen evolution process in the model for discharged electrodes and the metal oxidation process for discharged electrodes.

The results indicated rather large variations in the kinetic parameters for the process at different states of charge of the hydride material. The optimum energy efficiency for an alloy ( $\text{MmNi}_{3.5-3.7}\text{Co}_{0.7-0.8}\text{Mn}_{0.3-0.4}\text{Al}_{0.3-0.4}$ ) intended for utilisation in batteries was obtained in the range of 40 to 95% depth of discharge.

### 9.2.1 Charge Transfer Step

When a comparison was made between the findings from the impedance analysis and the plot of the open circuit potential for charged and discharged electrodes shown in figures 5.10 and 5.18, one could observe that the charge transfer step was very important. The electrode appeared to be fully charged already after 2-3 cycles, whereas the amount of hydrogen left in the electrode after discharge steadily decreased. This indicated that the discharging process may be slower than the charging process. This was as well confirmed by comparing the equivalent circuit analysis done on the electrochemical reactions with a single adsorbed species. When the desorption reaction was faster than the adsorption reaction, it can be observed in section 7.3 that an inductive element parallel to the charge transfer reaction needed to be inserted in the equivalent circuit. No traces of any inductive element in parallel to the charge transfer reaction were observed.

The apparent faster absorption reaction might as well be a result of a lower apparent diffusion coefficient for the  $\alpha$  phase than for the  $\beta$  phase. A possible explanation for this might be that during absorption, hydrogen diffuses through the surface  $\beta$  phase hydride layer to the reaction zone (see figures 3.3 and 3.10). During discharge, hydrogen diffused from the inner hydride phase to the surface (see figure 3.4) through  $\alpha$  phase hydride.

For the first cycles, it is important to note that the overpotential for the hydrogen evolution was considerably higher than for subsequent cycles. During the first cycles, a nickel enrichment of the surface has been observed (see section 3.8).

This nickel enrichment was assumed to be the reason for the enhanced catalytic activity for the hydrogen evolution reaction as the electrode was cycled.

A reduction in the magnitude of the charge transfer resistance would improve the performance of the studied metal hydride electrodes. This reduction in resistance, however, would be coupled with a reduction in the overpotential for hydrogen evolution since the charge transfer step is a common step both for hydrogen absorption and for hydrogen evolution.

### 9.2.2 Diffusion Step

In chapter 8 it is shown that the diffusion was best modelled when using spherical diffusion geometry. However, it was difficult to obtain the diffusion coefficient using electrochemical impedance spectroscopy (EIS). The reason for this was that the determination of the diffusion coefficient required an accurate determination of the diffusion length. During the EIS measurements performed on an electrode at an intermediate depth of discharge, both charge of the surface layer, and discharge of both the charged surface layer as well as the hydrided zone in the middle of the metal hydride particles were assumed to take place. This, as well as inhomogeneous metal hydride particles complicated the precise determination of the diffusion length.

As discussed in section 5.5.3 the diffusion coefficient was important for high, sustained currents. Consequently, the diffusion rate is very important for hydrogen storage alloys intended for vehicular battery use. An alloy with a high diffusion coefficient would allow for the transport of all hydrogen adsorbed at the active surface site to the reaction (hydride nucleation) zone during charging. The fast diffusion would as such be an important factor when it came to reducing the rate of the hydrogen evolution during charging. In section 3.9 it was furthermore emphasized that B-site substituted  $AB_5$  type alloys, with the possible exception of tin substitution, have considerably lower diffusion coefficients than  $LaNi_5$ . Alloys with high contents of aluminium and especially cobalt, had lower diffusion rates, and showed as such increased concentration gradients in the hydride alloy.

### 9.2.3 Hydride Forming Reaction Step

The equations that were used to develop the model equations given in section 7.5.2 did not include any contributions from the hydride forming reaction. To account for the hydride forming reaction, the response could be approximated by an RC circuit following the diffusion step in series with the diffusion and absorption steps in the equivalent circuit used for fitting the data (given in figure 7.10). For an alloy with a very high diffusion rate, it might have been possible to observe some response from the hydride forming step. For the systems described in this thesis, however, no such response was observed for any state of charge. This indicated that the response from this step was small compared to the response from the diffusion step, which was basically the same as for the absorption resistance.

### 9.2.4 Porous Electrode Model

The use of a porous electrode model was crucial for fitting the impedance spectra. The porous response was also observed for pure copper electrodes.

The contribution to the impedance from the porous morphology was a result of the electrical resistivity in the electrolyte. The porous properties of the metal hydride electrode in a commercial NiMH battery may be different because of the absence of large amounts of binder material (copper) used in laboratory scale electrodes.

### 9.2.5 Side Reactions

The hydrogen evolution side reaction was very pronounced while charging during the first charge/discharge cycles. The hydrogen evolution reaction lowered the efficiency of the charge reaction. In chapter 6 it was shown that the hydrogen evolution reaction could be suppressed by applying an external pressure.

For AB<sub>5</sub> type alloys containing misch metal, nickel, cobalt, aluminium and manganese, all elements except cobalt and nickel exhibit active corrosion under discharge conditions at high depths of discharge. At lower depths of discharge (charged electrodes), both nickel and cobalt are immune (see section 3.8.2).

To account for possible parallel hydrogen evolution during charging, it was necessary to include this step in the impedance model for electrodes having an open circuit potential more negative than the reversible hydrogen evolution potential. One or more possible parallel reduction/oxidation processes competing with the electrochemical hydride absorption/desorption reaction were observed. Both hexavalent and heptavalent oxidation states could be observed for manganese in strong alkaline electrolytes [24], which might contribute to lowering the efficiency of the electrochemical hydrogen absorption/desorption reactions.

### 9.3 Recommendations for Further Improvements

To improve the properties of NiMH batteries, metal hydride forming alloys with the following improved properties are needed:

- Fast activation;
- Low rate sensitivity, i.e. low overvoltage at high currents;
- Increased maximum energy storage capacity/density;
- Low corrosion rate, i.e. long cycle life and;
- Inexpensive hydrogen storage alloys, i.e. reduction of the cobalt content.

From chapter 6 it was observed that alloys with a higher plateau pressure than today's most commonly used alloys had a more favourable kinetics. A higher internal pressure within the battery cells might make the use of such alloys possible. Today's alloys contain aluminium and cobalt which both reduces the plateau pressure and give inferior diffusion properties as well as lower catalytic activity on the surface. If the two latter elements are not present, the corrosion properties are known to be inferior. If the  $AB_5$  system is to be used, fine tuning the misch metal composition and also using anisotropical alloys as described in section 3.7.1 might be part of the future solution to the alloy composition issue.

# List of symbols

$a$	Unit cell basal plane parameter
$a$	Radius of metal hydride particles
$a$	Diffusion length, i.e. radius of metal hydride particles
$a_0$	Average diffusion length
$A$	Area
$A$	Constant (section 7.5.2) defined by Eq 7.35
$A^\circ$	Constant (section 7.5.2) defined by Eq 7.22
$A_H$	Surface area of hydride (Eq 5.7)
$A_M$	Surface area of metal phase, hydrogen storage alloy (Eq 5.7)
$B$	Constant (section 7.5.2) defined by Eq 7.35
$B^\circ$	Constant (section 7.5.2) defined by Eq 7.22
$c$	Unit cell axial parameter
$c_1$	Maximum hydrogen concentration in the $\alpha$ phase (section 3.3.3)
$c_2$	Minimum hydrogen concentration in the $\beta$ phase (section 3.3.3)
$c_H$	Hydrogen concentration
$c_j$	Concentration of species $j$
$C$	Number of compounds (only Eq 3.3)
$C^\circ$	Constant
$C$	Constant (section 7.5.2) defined by Eq 7.37
$C_1$	Capacitance defined by Eq 7.48
$C_c$	Contact capacitance
$C_{dc}$	Discharge capacity
$C_{dl}$	Double layer capacitance
$C_i$	Capacity contribution from step $i$ (Eq 5.5)
$C_{max}$	Maximum discharge capacity (deep discharge)
$C_p$	Capacitance ( $C_1$ + hydrogen evolution capacitance)
$C_{rate}$	C-rate (defined by Eq 5.2)

$C_{r/o}$	Capacitance from parallel electrochemical reaction
$C_{sf}$	Surface capacitance
$C_{total}$	Maximum discharge capacity
$d_{hkl}$	Atomic plane distance (Eq B.1)
D	Constant (section 7.5.2) defined by Eq 7.37
D	Diffusion coefficient
$D_o$	Temperature independent term of the diffusion coefficient for hydrogen
$D_e$	Effective diffusion coefficient for hydrogen (Eq 3.32)
$D_H$	Diffusion coefficient for hydrogen
$D_i$	Diffusion coefficient for diffusion mechanism 3.32
$E^*$	Absolute energy for energy barrier
$E^\circ$	Standard potential
$E_a$	Activation energy
$E_A$	Potential after charge, (see figure 5.1)
$E_B$	Open circuit potential, charged electrode (see figure 5.1)
$E_C$	Cut off potential (see figure 5.1)
$E_D$	Open circuit potential, discharged electrode (see figure 5.1)
$E_{eq}$	Equilibrium potential
$E_m$	Voltage amplitude
$E_{oc}$	Open circuit potential
$E_s$	Specific energy
$E_\beta$	Energy of hydrogen site in metal hydride lattice
$E_\rho$	Energy density
F	Faraday constant
F	Degrees of freedom (only Eq 3.3)
$g(\theta_H)$	State of charge dependent thermodynamic factor
H	Hysteresis
$H_0$	Hysteresis at 0°C
$H_{25}$	Hysteresis at 25°C
$H_{50}$	Hysteresis at 50°C
$H_i$	Interstitial hydrogen
$i_o$	Exchange current density
$i_f$	Faradaic current density
$(i_f)_{ss}$	Stationary component of $i_f$
$i_{n,f}$	Non-faradaic current density
$I_o$	Exchange current
$I_m$	Current amplitude

$I_c$	Charge current
$I_{dc}$	Discharge current
$j$	Imaginary 1 ( $j=\sqrt{-1}$ )
$K_s$	Sievert's constant
$l$	Pore length (section 7.2.3)
$L$	Inductance
$m$	Mass
$MH_x$	Metal hydride phase
$n$	Number of
$n$	Number of pores (section 7.2.3)
$N_H$	Diffusion flux of hydrogen (Eq 3.32)
$P$	Pressure
$P$	Number of phases (only Eq 3.3)
$P_{a,0}$	Absorption plateau pressure at 0°C
$P_{a,0}$	Absorption plateau pressure at 0°C
$P_{a,25}$	Absorption plateau pressure at 25°C
$P_{a,50}$	Absorption plateau pressure at 50°C
$P_{d,0}$	Desorption plateau pressure at 0°C
$P_{d,23}$	Desorption plateau pressure at 23°C
$P_{d,25}$	Desorption plateau pressure at 25°C
$P_{d,50}$	Desorption plateau pressure at 50°C
$P_{e,25}$	Empirical value (Ref [78]) for desorption plateau pressure at 25°C
$P_s$	Specific power
$P_\rho$	Power density
$q$	Charge
$r$	Pore radius (section 7.2.3)
$r$	Radius of metal hydride particles
$r_{cov}$	Covalent radius
$r_H$	Radius of the reaction zone for hydride formation
$R$	Gas constant
$R$	Resistance
$R'$	Solution impedance per unit pore length (section 7.2.4)
$R_{ab}$	Absorption resistance
$R_1$	Resistance defined by Eq 7.50
$R_{ct}$	Charge transfer resistance
$R_{ct}^*$	Charge transfer resistance in one catalytic site
$R_c$	Contact resistance

$R_{ev}$	Hydrogen evolution resistance
$R_{r/o}$	Resistance from parallel electrochemical reaction
$R_p$	Polarization resistance
$R_{\Omega}$	Resistance in apparatus and electrolyte
$R_{\Omega,p}$	Porous resistance
$Rate_c$	C-rate
$s$	Laplace variable
$t$	Time
$t_A$	Charge time (see figure 5.1)
$t_B$	Charge time + break time (see figure 5.1)
$t_C$	$t_B$ + discharge time (see figure 5.1)
$t_D$	Full cycle time (see figure 5.1)
$T$	Temperature
$T_b$	Boiling point
$T_m$	Melting point
$v_2$	Reaction rate
$(v_2)_{ss}$	The stationary component of $v_2$
$V$	Volume
$V_{at}$	Atomic volume
$V_{uc}$	Unit cell volume
$X_i$	Size fraction of size $i$ (chapters 7 and 8)
$X_i$	Weight fraction of element $i$
$X_L$	Diffusion length, planar diffusion
$Y^\circ$	Characteristic parameter for CPE
$Z$	Impedance
$Z'$	Interfacial impedance per unit pore length (section 7.2.4)
$Z_o$	Specific impedance per unit area in cylindrical pore
$Z_{CPE}$	Impedance from constant phase element
$Z_D$	Diffusion impedance
$Z_{Ds}$	Impedance from spherical diffusion
$Z_{el}$	Electrode impedance
$Z_f$	Faradaic impedance
$Z_{im}$	Imaginary part of the impedance
$Z_{nf}$	Non-faradaic impedance
$Z_p$	Porous impedance
$Z_{re}$	Real part of the impedance
$Z_w$	Impedance from planar (warburg) diffusion



**Greek letters**

$\alpha$	Alpha phase, metal phase
$\beta$	Beta phase, hydride phase
$\gamma$	Fugacity
$\Gamma$	Coverage of adsorbed hydrogen when $\theta=1$
$\Delta H$	Hydride reaction enthalpy
$\Delta H^\circ$	Standard hydride reaction enthalpy
$\Delta S$	Hydride reaction entropy
$\Delta S^\circ$	Standard hydride reaction entropy
$\frac{\Delta V}{V}$	Relative volume change during hydriding
$\zeta$	Strain term (Eq 3.3)
$\eta$	Overtoltage
$\theta$	Coverage degree of adsorbed hydrogen
$\theta$	Diffraction angle (Eq B.1)
$\theta$	Phase angle
$\theta_H$	State of charge
$\lambda$	Wave length
$\Lambda$	Dimensionless electrode admittance
$\mu$	Chemical potential
$\rho$	Density
$\rho$	Solution resistivity (section 7.2.3)
$\tau_D$	Diffusion time constant
$\tau_k$	Kinetic time constant
$\phi$	Phase shift
$\varphi$	Electrode potential
$\sigma$	Constant defined by Eq 7.51
$\omega$	Angular frequency of ac single

**Subscripts, superscripts and other symbols**

0	0°C
25	25°C
50	50°C
<i>ab</i>	Absorbed
<i>ad</i>	Adsorbed

<i>ct</i>	Charge transfer
<i>eq</i>	Equilibrium
<i>g</i>	Gas
<i>H</i>	Hydrogen
<i>i</i>	Interstitial
<i>l</i>	Liquid
<i>s</i>	Solid
<i>sf</i>	Surface
<i>ss</i>	Stationary component
°	Standard value, i.e. standard state
-	Stationary component
~	Alternating component
→	Adsorption direction
⇌	Reversible reaction
←	Desorption direction
□ <sub><i>i</i></sub>	Empty interstitial position
□ <sub><i>M</i></sub>	Active surface site

# Abbreviations

AC	Alternating Current
AFC	Alkaline Fuel Cell
A.V.	Atomic Volume
AW	Atomic Weight
CPE	Constant Phase Element
CE	Counter Electrode
DOD	Depth Of Discharge
EIS	Electrochemical Impedance Spectroscopy
EV	Electrical Vehicle
FPFD	Fractional Power Frequency Dependence (i.e. CPE)
HDDR	Hydrogen Decomposition Desorption Recombination
HEV	Hybrid Electric Vehicle
ICE	Internal Combustion Engine
ICP	Induction Coupled Plasma
MH	Metal Hydride
MITS'97	Arbin instruments software
Mm	Misch metal (mixture of rare earth metals)
NiCd	Nickel Cadmium
NiMH	Nickel Metal Hydride
OCV	Open Circuit Voltage
PCI	Pressure Composition Isotherm
PCT	Pressure Composition Temperature
PEM	Proton Exchange Membrane
PEMFC	Proton Exchange Membrane Fuel Cell
PPS	Poly Phenyl Sulfide
PTFE	PolyTetraFluorEthylene
RE	Rare Earth

RE	Reference Electrode
RHE	Reversible Hydrogen Electrode
SHE	Standard Hydrogen Electrode
SOC	State Of Charge
SPE	Solid Polymer Electrolyte
WE	Working Electrode

# Bibliography

- [1] C.K. Dyer. *Scientific American*, pp 88–93, (1999).
- [2] A.C. Lloyd. *Scientific American*, pp 80–86, (1999).
- [3] J. Appleby. *Scientific American*, pp 74–79, (1999).
- [4] L.J.M.J. Blomen and M.N. Mugerwa, Ed. *Fuel Cell Systems*. Plenum Press, (1993).
- [5] K. Kordesh and J. Daniel-Ivad. In O. Savadogo and P.R. Roberge, Ed., *Proceedings of the 2nd International symposium on new materials for fuel cell and modern battery systems*, pp 2–13, Montreal, Canada, (1997).
- [6] T. Sakai, M. Matsuoka, and C. Iwakura. In K.A. Gschneider Jr. and L. Eyring, Ed., *Handbook on the Physics and Chemistry of Rare Earths*, vol. 21, pp 133–178. Elsevier Science B.V., (1995).
- [7] E.J. Cairns and F.R. McLarnon. In A.R. Landgrebe and Z-i Takehara, Ed., *Batteries and fuel cells for electric vehicle applications*, vol. 93-8, pp 1–11. The Electrochemical Society, Inc, (1993).
- [8] P.R. Gifford, M.A. Fetccenco, S. Venkatesan, D.A. Corrigan, A. Holland, S.K. Dhar, and S.R. Ovsinsky. In P.D. Bennett and T. Sakai, Ed., *Hydrogen and metal hydride batteries*, vol. 94-27, pp 353–369. The Electrochemical Society, Inc, (1994).
- [9] C. Iwakura and M. Matsuoka. *Progress in Batteries & Battery Materials*, **10**, (1991).
- [10] W Dönöt, G. Gutmann, and P. Urban. In O. Savadogo and P.R. Roberge, Ed., *Proceedings of the 2nd International symposium on new materials for fuel cell and modern battery systems*, pp 14–26, Montreal, Canada, (1997).

- [11] S.R. Ovshinsky, R.C. Stempel, S. Dhar, M.A. Fetcenko, P.R. Gifford, S. Venkatesan, D.A. Corrigan, and R. Young. In *Presented at the 29th international symposium on automotive technology and automation, Florence, Italy*, (1996).
- [12] A.K. Jena and K.M. Gupta. *J. Power Sources*, **80**, 46–52, (1999).
- [13] G. H. Aylward and T. J. V. Findlay. *SI Chemical Data*. Wiley, Australia, 2. Ed., (1974).
- [14] M. Yoshio. *Progress in Batteries & Battery Materials*, **16**, 252–267, (1997).
- [15] B. Scrosati. *Progress in Batteries & Battery Materials*, **13**, 358–362, (1994).
- [16] B. Scrosati. *Progress in Batteries & Battery Materials*, **13**, 355–357, (1994).
- [17] I. Uehara, T. Sakai, and H. Ishikawa. *J. Alloys and Compounds*, **253-254**, 635–641, (1997).
- [18] D. Qu. *J. Applied Electrochemistry*, **29**, 511–520, (1999).
- [19] N. Kamlesh Pandey, N. Lakshmi, and S. Chandra. *J. Power Sources*, **76**, 116–123, (1998).
- [20] Å. Sterten. *Elektro kjemi grunnkurs*. Institutt for teknisk elektro kjemi, NTH, Norway, (1993).
- [21] J. Chen. *High energy storage materials for rechargeable nickel-metal hydride batteries*. PhD thesis, Department of Materials Engineering, University of Wollongong, Australia, (1999).
- [22] J.W. Lyman and G.R. palmer. In P.D. Bennett and T. Sakai, Ed., *Hydrogen and metal hydride batteries*, vol. 94-27, pp 415–431. The Electrochemical Society, Inc, (1994).
- [23] P. Zhang, T. Yokohama, O. Itabashi, Y. Wakui, T.M. Suzuki, and K. Inoue. *J. Power Sources*, **77**, 116–122, (1999).
- [24] M. Pourbaix. *Atlas of electrochemical equilibria in aqueous solutions*. National Association of Corrosion Engineers, Houston, Texas, USA, (1974). Second edition.
- [25] A. Visintin, A. Anani, S. Srinivasan, and H.S. Appleby, A. an Lim. *J. Applied electrochemistry*, **25**, 833–840, (1995).

- [26] A. Visintin, S. Anani, A. Srinivasan, and A.J. Appleby. In D.A. Corrigan and S. Srinivasan, Ed., *Hydrogen storage materials, batteries and electrochemistry*, vol. 92-5, pp 319-332. The Electrochemical Society, Inc, (1992).
- [27] K. Naito, T. Matsunami, K. Okuno, M. Matsuoka, and C. Iwakura. *J. Applied electrochemistry*, **23**, 1051-1055, (1993).
- [28] D. Coates and R.D. Wright. In D.A. Corrigan and S. Srinivasan, Ed., *Hydrogen storage materials, batteries and electrochemistry*, vol. 92-5, pp 199-209. The Electrochemical Society, Inc, (1992).
- [29] D. Coates and R.D. Wright. In D.A. Corrigan and S. Srinivasan, Ed., *Hydrogen storage materials, batteries and electrochemistry*, vol. 92-5, pp 400-416. The Electrochemical Society, Inc, (1992).
- [30] A. Anani, A. Visintin, K. Petrov, S. Srinivasan, J. J. Reilly, J. R. Johnson, R. B. Schwarz, and P. B. Desch. *Journal of Power Sources*, **47**, 261-275, (1994).
- [31] T. Sakai, H. Miyamura, N. Miyamura, A. Kato, K. Oguro, and H. Ishikawa. *J. Electrochem. Soc.*, **137**(3), 795-799, (1990).
- [32] T. Sakai, T. Iwaki, Z Ye, D Noréus, and O. Lindström. In P.D. Bennett and T. Sakai, Ed., *Hydrogen and metal hydride batteries*, vol. 94-27, pp 393-402. The Electrochemical Society, Inc, (1994).
- [33] N. Vassal, E. Salmon, and J.-F. Fauvarque. *J. Electrochem. Soc.*, **146**(1), 20-26, (1999).
- [34] N. Vassal, E. Salmon, J.-F. Fauvarque, and J.-F. Penneau. In C.F. Holmes and A.R. Landgrebe, Ed., *Batteries for Portable Applications and Electric Vehicles*, vol. 97-18, pp 869-880. The Electrochemical Society, Inc, (1997).
- [35] S. Srinivasan, B.B. Davé, K.A. Murugesamoorthi, A. Parthasarathy, and A.J. Appleby. Overview of fuel cell technology. In L.J.M.J. Blomen and M.N. Mugerwa, Ed., *Fuel Cell System*, chapter 2, pp 37-72. Plenum Press, (1993).
- [36] K. Videm. In A.F. Andersen and A.J. Maeland, Ed., *Hydrides for energy storage*. International Association For Hydrogen Energy, Pergamon Press, (1977).

- [37] C. Folonari, G. Iemmi, F. Manfredi, and A. Rolle. *J. Less-Common Metals*, **74**, 371–378, (1980).
- [38] N. Kuriyama, T. Sakai, H. Miyamura, I. Uehara, and H. Ishikawa. In *Hydrogen energy Process X, Proc 10th World Hydrogen Energy Conf*, vol. 10, pp 1713–1718. Int. Assoc. Hydrogen energy, (1994).
- [39] J.O. Jensen and N.J. Bjerrum, Ed. *Development of air metal hydride battery (AMHBAT)*, (1999). Contract JOR-CT97-0193.
- [40] J.O. Jensen. *Anodematerialer til metalhydridbatterier*. Ph.d. thesis, Den Kgl. Veterinær- og Landbohøjskole, Denmark, (1997).
- [41] A.J. Maeland. The storage of hydrogen for vehicular use - a review and reality check. Technical report, Institute for Energy Technology, N-2007 Kjeller, Norway, (1999). IFE/I-99/012.
- [42] A.J. Maeland. In A.F. Andersen and A.J. Maeland, Ed., *Hydrides for energy storage*, pp 19–31. International Association For Hydrogen Energy, Pergamon Press, (1977).
- [43] G.G. Libowitz. In D.A. Corrigan and S. Srinivasan, Ed., *Hydrogen storage materials, batteries and electrochemistry*, vol. 92-5, pp 3–23. The Electrochemical Society, Inc, (1992).
- [44] R. Omachi. *Materials Science Forum*, **30**, 147–154, (1988).
- [45] F.E. Lynch. *J. Less-Common Met.*, **172-174**, 943–958, (1991).
- [46] G. Sandrock, S. Suda, and L. Schlapbach. Applications. In L. Schlapbach, Ed., *Hydrogen in Intermetallic Compounds I*, vol. 67 of *Topics in applied physics*, chapter 5. Springer-Verlag, (1992).
- [47] R. Wiswall. Hydrogen storage in metals. In G. Alefeld and J. Völkl, Ed., *Hydrogen in Metals II, Application oriented properties*, vol. 29 of *Topics in Applied Physics*, chapter 5. Springer-Verlag, (1978).
- [48] G. Sandrock. In Y. Yürüm, Ed., *Hydrogen Energy System. Production and Utilization of Hydrogen and Future Aspects*, vol. 295 of *NATO ASI Series, Series E: Applied Sciences*, pp 253–280. Kluwer academic publishers, (1995).



- [49] L.O. Valøen, A. Zaluska, L. Zaluski, H. Tanaka, N. Kuriyama, R. Tunold, and J.O. Ström-Olsen. Structure and related properties of (La,Ce,Nd,Pr)Ni<sub>5</sub> alloys. Manuscript accepted *J. Alloys and Compounds* (jalcom 5757), (2000).
- [50] K. H. J. Buschow. Hydrogen absorption in intermetallic compounds. In K.A. Gschneider and L. Eyring, Ed., *Handbook on the Physics and Chemistry of Rare Earths*, vol. 6, chapter 47, pp 1–111. Elsevier Science Publisher B.V., (1984).
- [51] W.M. Rutherford. *Materials Science Forum*, **31**, 19–38, (1988).
- [52] J.J. Reilly. *Zeitschrift Für Physikalische Chemie, Neue Folge*, **117**, 155–184, (1979).
- [53] R. Griessen, J.N. Huiberts, M. Kremers, A.T.M. van Gogh, N.J. Koeman, J.P. Dekker, and P.H.L. Notten. *J. Alloys and Compounds*, **253-254**, 44–50, (1997).
- [54] K.J. Gross. *Intermetallic Materials for Hydrogen Storage*. PhD thesis, Institut de Physique, Universite de Fribourg, Fribourg, Switzerland, (1998).
- [55] K.H.J Buschow and A.R. Miedema. In A.F. Andersen and A.J. Maeland, Ed., *Hydrides for energy storage*, pp 235–249. International Association For Hydrogen Energy, Pergamon Press, (1977).
- [56] J. Xiao and P. Li. *Int. J. Hydrogen Energy*, **24**, 741–746, (1999).
- [57] G. Sandrock. In Y. Yürüm, Ed., *Hydrogen Energy System. Production and Utilization of Hydrogen and Future Aspects*, vol. 295 of *NATO ASI Series, Series E: Applied Sciences*, pp 135–166. Kluwer academic publishers, (1995).
- [58] H.H. van Mal and A.R. Midema. In A.F. Andersen and A.J. Maeland, Ed., *Hydrides for energy storage*. International Association For Hydrogen Energy, Pergamon Press, (1977).
- [59] T.B. Flanagan. In A.F. Andersen and A.J. Maeland, Ed., *Hydrides for energy storage*, pp 135–150. International Association For Hydrogen Energy, Pergamon Press, (1977).
- [60] W. Zhang, S. Srinivasan, and H.J. Plohen. *J. Electrochem. Soc*, **143**, 4039–4046, (1996).

- [61] R. Balasubramaniam, M.N. Mungole, and K.N. Rai. *J. Alloys and Compounds*, **196**, 63–70, (1993).
- [62] K. Laidler and J. Meiser. *Physical Chemistry*. Benjamin/Cummings Publishing Company, Menlo Park, California, USA, (1982).
- [63] R. Balasubramaniam. *J. Alloys and Compounds*, **253-254**, 203–206, (1997).
- [64] T.B. Flanagan and W.A. Oates. Thermodynamics of intermetallic compound-hydrogen systems. In L. Schlapbach, Ed., *Hydrogen in Intermetallic Compounds I*, vol. 63 of *Topics in applied physics*, chapter 3. Springer-Verlag, (1988).
- [65] J.J.G. Willems and K.H.J. Buschow. *J. Less-Common Met.*, pp 13–30, (1987).
- [66] J.J.G. Willems. *Philips J. Res. Suppl.*, **39**(1), (1984).
- [67] T. Vogt, J.J. Reilly, J.R. Johnson, G.D. Adzic, and J. McBreen. *J. Electrochem. Soc.*, **146**(1), 15–19, (1999).
- [68] A. Percheron-Guegan and C. Lartigue. *Materials Science Forum*, **31**, 125–142, (1988).
- [69] C.E. Lundin, F.E. Lynch, and C.B. Magee. *J. Less-Common Metals*, **56**, 19–37, (1977).
- [70] G. Busch, L. Schlapbach, and A. Seiler. In A.F. Andersen and A.J. Maeland, Ed., *Hydrides for energy storage*, pp 293–299. International Association For Hydrogen Energy, Pergamon Press, (1977).
- [71] X. Wang, C. Chen, C. Wang, and Q. Wang. *J. Alloys and Compounds*, **232**, 192–196, (1996).
- [72] Alfa Aesar catalog. Johnson Matthey, (1997).
- [73] H. Uchida, M. Tada, and Y.C. Huang. *J. Less-Common Metals*, **88**, 81–87, (1982).
- [74] K Suzuki, N. Yanagihara, H. Kawano, and A. Ohta. *J. Alloys Compounds*, **192**, 173–175, (1993).
- [75] K.R. Clay, A.J. Goudy, R.G. Schweibenz, and A. Zarynow. *J. Less-Common Metals*, **166**, 153–162, (1990).

- [76] T. Sakai, H. Miyamura, N. Miyamura, A. Kato, K. Oguro, H. Ishikawa, and C. Iwakura. *J. Less-Common Metals*, **159**, 127–139, (1990).
- [77] T. Sakai, T. Hazama, H. Miyamura, N. Kuriyama, A. Kato, and H. Ishikawa. *J. Less-Common Metals*, **172-174**, 1175–1184, (1991).
- [78] J. Liu and E. Lee Huston. *J. Less-Common Metals*, **90**, 11–20, (1983).
- [79] Z.P. Li and S. Suda. In P.D. Bennett and T. Sakai, Ed., *Hydrogen and metal hydride batteries*, vol. 94-27, pp 16–23. The Electrochemical Society, Inc, (1994).
- [80] K. Yvon and P. Fischer. Crystal and magnetic structures of ternary metal hydrides: A comprehensive review. In L. Schlapbach, Ed., *Hydrogen in Intermetallic Compounds I*, vol. 63 of *Topics in applied physics*, chapter 4. Springer-Verlag, (1988).
- [81] H. Uchida and T. Kuji. *Int. J. Hydrogen Energy*, **24**, 871–877, (1999).
- [82] Y. Osumi, H. Suzuki, A. Kato, and K. Oguro. *J. Less-Common Met.*, **89**, 287–292, (1983).
- [83] L. Jiang, F. Zhan, D. Bao, G. Qing, Y. Li, and X. Wei. *J. Alloys and Compounds*, **231**(1-2), 635–638, (1995).
- [84] T. Sakai, H. Miyamura, N. Miyamura, A. Kato, K. Oguro, H. Ishikawa, and C. Iwakura. *J. Less-Common Metals*, **161**, 193–202, (1990).
- [85] G.D. Adzic, J.R. Johnson, S. Mukerjee, J. McBreen, and J.J. Reilly. In G. Jerkiewicz and P. Marcus, Ed., *Electrochemical surface science of hydrogen adsorption and absorption*, vol. 97-16, pp 288–300. The Electrochemical Society, Inc, (1997).
- [86] R.S.A. Babu, B. Viswanathan, and S.S. Murthy. *Bulletin of Electrochemistry*, **11**(3), 133–144, (1995).
- [87] L.Y. Zhang. Rare earth based metal hydrides and nimh rechargeable batteries. In R.G. Bautista, Ed., *Rare Earths: Science, Technology and Applications III*, pp 235–257. The Minerals, Metals & materials Society, 1997, (1997).

- [88] S.R. Ovshinsky and M.A. Fetcenko. Electrochemical hydrogen storage alloys and batteries fabricated from Mg containing base alloys. United states patent No 5,506,069, (1996).
- [89] F. Meli, A. Züttel, and L. Schlapbach. *J. Alloys and Compounds*, **231**(1-2), 639-644, (1995).
- [90] A. Züttel, D. Chartouni, K. Gross, P. Spatz, M. Bächler, F. Lichtenberg, A. Fölzer, and N.J.E. Adkins. *J. Alloys and Compounds*, **253-254**, 626-628, (1997).
- [91] J.M. Cocciantelli, P. Bernard, S. Fernandez, and J. Atkin. *J. Alloys and Compounds*, **253-254**, 642-647, (1997).
- [92] C. Iwakura, K. Fukuda, H. Senoh, H. Inoue, M. Matsuoka, and Y. Yamamoto. *Electrochim. Acta*, **43**(14-15), 2041-2046, (1998).
- [93] G.D. Adzic, J.R. Johnson, S. Mukerjee, J. McBreen, and J.J. Reilly. *J. Alloys and Compounds*, **253-254**, 579-582, (1997).
- [94] H. Pan, J. Ma, C. Wang, C.P. Chen, and Q.D. Wang. *Electrochim. Acta*, **44**, 3977-3987, (1999).
- [95] P.H.L. Notten and P. Hokkeling. *J. Electrochem. Soc.*, **138**(7), 1877-1885, (1991).
- [96] B.V. Ratnakumar, S. Surampudi, C. Witham, A. Hightower, R.C. Bowman, and B. Fultz. *37th Power Sources Conference*, pp 440-445, (1996). Cherry Hill, New Jersey, June 17-20.
- [97] C. Witham, A. Hightower, B. Fultz, B.V. Ratnakumar, and R.C. Bowman Jr. *J. Electrochem. Soc.*, **144**(11), 3758-3764, (1997).
- [98] C.K. Witham, B. Fultz, B.V. Ratnakumar, and R.C. Bowman Jr. In P.D. Bennett and T. Sakai, Ed., *Hydrogen and metal hydride batteries*, vol. 94-27, pp 68-77. The Electrochemical Society, Inc, (1994).
- [99] T. Vogt, J.J. Reilly, J.R. Johnson, G.D. Adzic, and J. McBreen. *Electrochem. and Solid State Lett.*, **2**(3), 111-114, (1999).
- [100] B.V. Ratnakumar, S. Surampudi, S. Di Stefano, G. Halpert, C. Witham, A. Hightower, and B. Fultz. In P.D. Bennett and T. Sakai, Ed., *Hydrogen and metal hydride batteries*, vol. 94-27, pp 57-67. The Electrochemical Society, Inc, (1994).

- [101] B.V. Ratnakumar, C. Witham, R.C. Bowman Jr, A. Hightower, and B. Fultz. *J. Electrochem. Soc.*, **143**(8), 2578–2584, (1999).
- [102] J.-M. Joubert, D. Sun, M. Latroche, and A. Percheron-Guégan. *J. Alloys and Compounds*, **253-254**, 564–569, (1997).
- [103] Q.M. Yang, D.H. Ryan, and J.O. Ström-Olsen. *J. Electrochem. Soc.*, (1996). Presented at 190th ECS meeting.
- [104] A. Zaluska, L. Zaluski, and J.O. Ström-Olsen. *J. Alloys and Compounds*, **288**, 217–225, (1999).
- [105] E. Rönnebro. *Structural investigations of some ternary metal hydrides*. PhD thesis, Department of Structural Chemistry, Stockholm University, (1999).
- [106] N. Cui, P. He, and J.L. Luo. *Electrochim. Acta*, **44**(20), 3549–3558, (1999).
- [107] N. Cui and J.L. Lou. *J. Alloys and Compounds*, **265**(1-2), 305–310, (1998).
- [108] N. Cui and J.L. Lou. *Int. J. Hydrogen Energy*, **24**(1), 37–42, (1999).
- [109] N. Cui and J.L. Lou. *Electrochim. Acta*, **44**(5), 711–720, (1998).
- [110] P. Mandal and O.N. Srivastava. *J. Alloys and Compounds*, **205**, (1994).
- [111] C.S Wang, Y.Q. Lei, and Q.D. Wang. *Electrochim. Acta*, **43**(21-22), 3193–3207, (1998).
- [112] C.S. Wang, Y.Q. Lei, and Q.D. Wang. *Electrochim. Acta*, **43**(21-22), 3209–3216, (1998).
- [113] G.G. Libowitz and A.J. Maeland. *Materials Science Forum*, **31**, 177–196, (1988).
- [114] K.S. Nahm, W. Y. Kim, S.P. Hong, and W.Y. Lee. *Int. J. Hydrogen Energy*, **17**(5), 333–338, (1992).
- [115] A.C. Switendick. The change in electronic properties on hydrogen alloying and hydride formation. In G. Alefeld and J. Völkl, Ed., *Hydrogen in Metals I, Basic properties*, vol. 28 of *Topics in Applied Physics*, chapter 5. Springer-Verlag, (1978).

- [116] G. Sandrock. In P.D. Bennett and T. Sakai, Ed., *Hydrogen and metal hydride batteries*, vol. 94-27, pp 1-15. The Electrochemical Society, Inc, (1994).
- [117] A. Anani, A. Visintin, S. Srinivasan, and A.J. Appleby. In D.A. Corrigan and S. Srinivasan, Ed., *Hydrogen storage materials, batteries and electrochemistry*, vol. 92-5, pp 105-119. The Electrochemical Society, Inc, (1992).
- [118] A.H. Boonstra and T.M.N. Bernhards. *J. Less-Common metals*, **161**, 355-368, (1990).
- [119] P.H.L. Notten. Rechargeable nickel-metalhydride batteries: a successful new concept. In F. Grandjean, G.J. Long, and K.H.J. Buschow, Ed., *Interstitial Intermetallic Alloys*, chapter 7, pp 151-195. Kluwer Academic Publishers, Nederland, (1995).
- [120] M. Latroche, P.H.L. Notten, and A. Percheron-Guégan. *J. Alloys and Compounds*, **253-254**, 295-297, (1997).
- [121] F. Meli, A. Züttel, and L. Schlapbach. *J. Alloys and Compounds*, **190**, 17-24, (1992).
- [122] P.H.D. Notten, R.E.F. Einerhand, and J.L.C. Daams. *J. Alloys and Compounds*, **231**(1-2), 221-232, (1995).
- [123] Z.H. Chen, M.Q. Lu, Y.L. Wang, and Z.Q. Hu. *J. Alloys and Compounds*, **231**(1-2), 550-552, (1995).
- [124] L. Schlapbach. Surface properties and activation. In L. Schlapbach, Ed., *Hydrogen in Intermetallic Compounds I*, vol. 67 of *Topics in applied physics*, chapter 2. Springer-Verlag, (1992).
- [125] B.T. Kilbourn. *A lanthanide lanthanology, part I, A-L*. Molycorp, Inc., White Plains, NY, USA, (1993).
- [126] F. Lopez-Aguilar, J. Costa-Quintana, and M.M. Sanchez-Lopez. *Phys. Rev. B*, **56**(3), 1335-1344, (1997).
- [127] B.T. Kilbourn. *Cerium, a guide to its role in chemical technology*. Molycorp, Inc., White Plains, NY, USA, (1992).

- [128] D. Chartouni. *Untersuchung von Metallhydrid-Elektroden mittels in situ Raster-Tunnelmikroskopie, Photoelektrone-Spektroskopie, elektrochemischen und metallurgischen Methoden*. PhD thesis, University of Fribourg, Switzerland, (1999).
- [129] K. Naito, T. Matsunami, K. Okuno, M. Matsuoka, and C. Iwakura. *J. Applied Electrochemistry*, **24**, 808–813, (1994).
- [130] Z.Y. Tang, W.X. Chen, Z.L. Liu, and H.T. Guo. *J. Applied Electrochemistry*, **26**, 1201–1204, (1996).
- [131] C. Jun and Z. Yunshi. *Int. J. Hydrogen Energy*, **20**(3), 235–237, (1995).
- [132] T. Sakai, H. Ishikawa, K. Oguro, C. Iwakura, and H. Yoneyama. *J. Electrochem. Soc.*, **134**(3), 558–562, (1987).
- [133] H. Ishikawa, K. Oguro, A. Kato, H. Suzuki, and E. Ishii. *J. Less-Common Metals*, **107**, 105–110, (1985).
- [134] H. Ishikawa, K. Oguro, A. Kato, H. Suzuki, and E. Ishii. *J. Less-Common Metals*, **120**, 123–133, (1986).
- [135] J.-H. Lee, K.-Y. Lee, and J.-Y. Lee. *J. Alloys and Compounds*, **232**, 197–203, (1996).
- [136] A. Visintin, C.A. Tori, G. Garaventa, and W.E. Triaca. *J. Electrochem. Soc.*, **145**(12), 4169–4172, (1998).
- [137] G. Zheng, B.N. Popov, and R.E. White. *J. Applied Electrochemistry*, **28**, 381–385, (1998).
- [138] M. Matsuoka, T. Kohno, and C. Iwakura. *Electrochimica Acta*, **38**(6), 787–791, (1993).
- [139] N. Kuriyama, T. Sakai, H. Miyamura, H. Tanaka, I. Uehara, F. Meli, and L. Schlapbach. *J. Alloys and Compounds*, **238**, 128–140, (1996).
- [140] J. Nan, Y. Yang, J. You, and Z. Lin. *J. Power Sources*, **79**, 64–68, (1999).
- [141] X. L. Wang and S. Suda. *J. Alloys and Compounds*, **194**(1), 73–76, (1993).
- [142] X. L. Wang, K. Iwata, and S. Suda. *J. Alloys and Compounds*, **231**(1-2), 860–864, (1995).

- [143] X. L. Wang, K. Iwata, and S. Suda. *J. Alloys and Compounds*, **231**(1-2), 829–834, (1995).
- [144] F. J. Liu and S. Suda. *J. Alloys and Compounds*, **231**(1-2), 696–701, (1995).
- [145] N. Kuriyama, T. Sakai, H. Miyamura, H. T. Tanaka, H. Takeshita, and I. Uehara. *J. Alloys and Compounds*, **253-254**, 598–600, (1997).
- [146] W. Chen, Z. Tang, H. Guo, Z. Liu, C. Chen, and Q. Wang. *J. Power Sources*, **74**, 34–39, (1999).
- [147] C. Iwakura, Y. Kajiya, H. Yooneyama, T. Sakai, K. Oguro, and H. Ishikawa. *J. Electrochem. Soc.*, **136**(5), 1351–1355, (1989).
- [148] R.F. Karlicek Jr and I.J. Lowe. *J. Less-Common Met.*, **73**, 219–225, (1980).
- [149] D. Richter, R. Hempelmann, and R.C. Bowman Jr. Dynamics of hydrogen in intermetallic hydrides. In L. Schlapbach, Ed., *Hydrogen in Intermetallic Compounds I*, vol. 67 of *Topics in applied physics*, chapter 3. Springer-Verlag, (1992).
- [150] E. Wicke and H. Brodowsky. Hydrogen in palladium alloys. In G. Alefeld and J. Vökl, Ed., *Hydrogen in Metals II, Application oriented properties*, vol. 29 of *Topics in Applied Physics*, chapter 3. Springer-Verlag, (1978).
- [151] S.W. Feldberg and J.J. Reilly. *J. Electrochem. Soc.*, **144**(12), 4260–4265, (1997).
- [152] Z.X. Zhou, J.S. Huang, W.K. Hu, F.Y. Yao, and Y.S. Zhang. *J. Alloys and Compounds*, **231**(1-2), 297–301, (1995).
- [153] M.M. Popovic, B.N. Grgur, M.V. Vojnovic, P. Rakin, and N.V. Krstajic. *J. Alloys and Compounds*, **298**(1-2), 107–113, (1999).
- [154] J.S. Newman. *Electrochemical systems*. Prentice Hall, Englewood Cliffs, 2 Ed., (1991).
- [155] A. Lundqvist and G. Lindbergh. *J. Electrochem. Soc.*, **145**(11), 3740–3746, (1998).
- [156] A. Lundqvist. *The metal hydride electrode and the nickel metal hydride battery*. PhD thesis, Department of Chemical Engineering and Technology, Applied Electrochemistry, Kungliga Tekniska Högskolan, Stockholm, (1998).



- [157] J. Chen, S.X. Dou, D.H. Bradhurst, and H.K. Liu. *Int. J. Hydrogen Energy*, pp 177–182, (1998).
- [158] R.C. Bowman jr, B.D. Craft, A. Attalla, M.H. Mendelsohn, and D.M. Gruen. *J. Less-Common Met.*, **73**, 227–232, (1980).
- [159] L.O. Valøen and R. Tunold. In *Nordic workshop on hydrogen in electrochemical energy conversion*, Geilo, Secretariat: Energiforskningen, N-1432 Ås, (1999). Nordic Energy Research Program -Electrochemical Energy Conversion.
- [160] G.E.P. Box, W.G. Hunter, and J.S. Hunter. *Statistics for experimenters*. John Wiley & Sons, Inc, New York, United States of America, 1. Ed., (1978).
- [161] J. Emsley. *The elements*. Clarendon press, Oxford, (1989).
- [162] C. Witham, R.C. Bowman Jr, and B. Fultz. *J. Alloys and Compounds*, **253-254**, 574–578, (1997).
- [163] G. Sandrock. In *Proc of the 12th Intersociety Energy Conversion Engineering Conference (IECEC)*, vol. I, pp 951–958, (1977). 779146.
- [164] D. Dayan, M.H. Mintz, and M.P. Dariel. *J. Less-Common Met.*, **73**, 15–24, (1980).
- [165] M.H.J. van Rijswick. In A.F. Andersen and A.J. Maeland, Ed., *Hydrides for energy storage*. International Association For Hydrogen Energy, Pergamon Press, (1977).
- [166] C.S. Wang, X.H. Wang, Y.Q. Lei, C.P. Chen, and Q.D. Wang. *Int. J. Hydrogen Energy*, **22**(12), 1117–1124, (1997).
- [167] D.J.G. Ives and G.J. Janz, Ed. *Reference electrodes, theory and practice*. Academic press, New York and London, (1961).
- [168] D. Chartouni, N. Kuriyama, A. Otto, V. Günter, C. Nützenadel, A. Züttel, and L. Schlapbach. *J. Alloys and Compounds*, **285**, 292–297, (1999).
- [169] N. Kuriyama, T. Sakai, H. Tanaka, H.T. Takeshita, and I. Uehara. Evaluation of electrochemical capacity of hydrogen storage alloy. Presented at MRS fall meeting in Boston, (1997).

- [170] L.O. Valøen, Rh. Edwards, S. Sunde, and R. Tunold. In O. Savadogo and P.R. Roberge, Ed., *Proceedings of the 2nd International symposium on new materials for fuel cell and modern battery systems*, pp 905–907, Montreal, Canada, (1997).
- [171] L.O. Valøen, S. Sunde, and R. Tunold. In T.O. Sætre, Ed., *Hydrogen Power: Theoretical and Engineering Solutions, Proceedings Hypothesis II, Grimstad, Norway*, pp 297–302. Kluwer Academic Publishers, (1998).
- [172] L.O. Valøen, S. Sunde, and R. Tunold. In C.F. Holmes and A.R. Landgrebe, Ed., *Batteries for Portable Applications and Electric Vehicles*, vol. 97-18, pp 761–767. The Electrochemical Society, Inc, (1997).
- [173] S Barnett and Cronin T.M. *Mathematical Formulae*. Longman, Kuala Lumpur, Malaysia, 4. Ed., (1986).
- [174] L.O. Valøen, S. Sunde, and R. Tunold. *J. Alloys and Compounds*, **253-254**, 656–659, (1997).
- [175] A. Lasia. Electrochemical impedance spectroscopy and its applications. In B. E. Conway, J. O'M Bockris, and R.E. White, Ed., *Modern aspects of electrochemistry*, number 32, chapter 2. Kluwer Academic/Plenum Publishers, New York, (1999).
- [176] M.E. Orazem, P. Agarwal, and L.H. Garcia-Rubio. *J. Electroanal. Chem*, **378**, 51–62, (1994).
- [177] D.D. Macdonald. In D.D. Macdonald and A.C. Khandahar, Ed., *High temperature electrode materials and characterisation*, vol. 91-6, pp 1–43. The Electrochemical Society, Inc, (1991).
- [178] B.A. Boukamp. *Equivalent circuit, equivcrt.pas, users manual*. University of Twente, Enschede, Nederland, (1989).
- [179] E. Lindner, K. Tóth, and E Pungor. *Dynamic characteristics of ion-selective electrodes*. CRC Press, Boca Raton, Florida, (1988). Kap 2.
- [180] EG& G Princeton applied research. Basis of electrochemical impedance spectroscopy (eis). Application note AC-1.
- [181] D.A. Harrington and B.E. Conway. *Electrochim. Acta*, **32**(12), 1703–1712, (1987).

- [182] K. Micka. *Introduction into the theory of impedance measurements*. Publishing Department, Institute of Chemical Technology, Prague, 1. Ed., (1995).
- [183] J.R. Macdonald. *Impedance Spectroscopy*. Wiley, New York, (1987).
- [184] R. de Levie. *J. Electroanal. Chem*, **281**, 1–21, (1990).
- [185] R. De Levie. Electrochemical response of porous and rough electrodes. In P. Delahay, Ed., *Advances in Electrochemistry and Electrochemical engineering*, vol. 6, pp 329–397. Interscience, New York, (1967).
- [186] A. Lasia. *J. Electroanal. Chem*, **397**, 27–33, (1995).
- [187] L. Nyikos and T. Pajkossy. *Electrochim. Acta*, **30**(11), 1533–1540, (1985).
- [188] G.J. Brug, A.L.G. Van Deen Eeden, M. Sluyters-Rehbach, and J.H. Sluyters. *J. Electroanal. Chem*, **176**, 275–295, (1984).
- [189] J. Jacquelin. *Electrochim. Acta*, **39**(18), 2673–2684, (1994).
- [190] A. Lasia and D. Grégoire. *J. Electrochem. Soc*, **142**(10), 3393–3399, (1995).
- [191] H. Keiser, K.D. Beccu, and M.A. Gutuar. *Electrochim. Acta*, **21**, 539–543, (1976).
- [192] R. De Levie. *Electrochim. Acta*, **9**, 1231–1245, (1964).
- [193] J.C. Wang. *Solid State Ionics*, **28-30**, 1436–1440, (1988).
- [194] J. Fleig and J. Maier. *Solid State Ionics*, **94**, 199–207, (1997).
- [195] P. Los, A. Lasia, and H. Ménard. *J. Electroanal. Chem*, **360**, 101–118, (1993).
- [196] T. Jacobsen and K. West. *Electrochim. Acta*, **40**(2), 255–262, (1995).
- [197] P. Agarwal, M.E. Orazem, and A. Hiser. In D.A. Corrigan and S. Srinivasan, Ed., *Hydrogen storage materials, batteries and electrochemistry*, vol. 92-5, pp 120–137. The Electrochemical Society, Inc, (1992).
- [198] N. Kuriyama, T. Sakai, H. Miyamura, I. Uehara, H. Ishikawa, and T. Iwasaki. *J. Alloys and Compounds*, **202**, 183–197, (1993).

- [199] W. Zhang, M.P. Sridar Kumar, S. Srinivasan, and H.J. Plohen. *J. Electrochem. Soc.*, **142**(9), 2935–2943, (1995).
- [200] B.N. Popov, G. Zheng, and R.E. White. *J. Applied Electrochemistry*, **26**, 603–611, (1996).
- [201] K. Bundy, M. Karlsson, G. Lindbergh, and A. Lundqvist. *J. Power Sources*, **72**, 118–125, (1998).
- [202] G. Zheng, B.N. Popov, and R.E. White. *J. Electrochem. Soc.*, **143**(2), 435–441, (1996).
- [203] G. Zheng, B.N. Popov, and R.E. White. *J. Electrochem. Soc.*, **142**(8), 2695–2698, (1995).
- [204] G. Zheng, B.S. Haran, B.N. Popov, and R.E. White. *J. Applied Electrochemistry*, **29**, 361–369, (1999).
- [205] G. Zheng, B.N. Popov, and R.E. White. *J. Applied Electrochemistry*, **27**, 1328–1332, (1997).
- [206] R. Durand, J.C. Chen, J.P. Diard, and C. Montella. In B.E. Conway and G. Jerkiewicz, Ed., *Electrochemistry and materials science of cathodic hydrogen absorption and adsorption*, vol. 94-21, pp 207–219. The Electrochemical Society, Inc, (1994).
- [207] C. Lim and S-I. Pyun. *Electrochim. Acta*, **38**(18), 2645–2652, (1993).
- [208] W. Zhang, M.P. Sridar Kumar, A. Visintin, and S. Srinivasan. In S. Srinivasan, D.D. Macdonald, and A.C. Khandkar, Ed., *Electrode materials and processes for energy conversion and storage*, vol. 94-23, pp 92–107. The Electrochemical Society, Inc, (1994).
- [209] N. Kuriyama, T. Sakai, H. Miyamura, I. Uehara, and H. Ishikawa. In P.D. Bennett and T. Sakai, Ed., *Hydrogen and metal hydride batteries*, vol. 94-27, pp 237–248. The Electrochemical Society, Inc, (1994).
- [210] N. Kuriyama, T. Sakai, H. Miyamura, I. Uehara, H. Ishikawa, and T. Iwasaki. *J. Electrochem. Soc.*, **139**(7), L72–L73, (1992). Letter.
- [211] N. Kuriyama, T. Sakai, H. Miyamura, I. Uehara, and H. Ishikawa. *J. Alloys and Compounds*, **192**, 161–163, (1993).

- [212] C. Wang. *J. Electrochem. Soc.*, **145**(6), 1801–1812, (1998).
- [213] Y. Leng, J Zhang, S. Cheng, C. Cao, and Z. Ye. *Electrochim. Acta*, **43**(12-13), 1945–1949, (1998).
- [214] A. Lundqvist and G. Lindbergh. *Electrochim. Acta*, **44**, 2523–2542, (1999).
- [215] J. Crank. *The mathematics of diffusion*. Oxford, 2 Ed., (1975).
- [216] E. Kreyszig. *Advanced engineering mathematics*. Wiley, New York, 6. Ed., (1988). Kap 2.
- [217] H.E.G. Rommal and P.J. Moran. *J. Electrochem. Soc.*, **132**(2), 325–329, (1985).
- [218] A.G. Pshenichnikov. *J. Matr. Chem. Phys.*, **22**, 121–148, (1989).
- [219] A. Lasia. Applications of the electrochemical impedance spectroscopy. To be published. [alasia@courrier.usherb.ca](mailto:alasia@courrier.usherb.ca).
- [220] S.R. Taylor and E. Gileadi. *Corrosion Science*, **51**(9), 664–671, (1995).
- [221] L.O. Valøen, S. Sunde, and R. Tunold. In *3rd Nordic Symposium on Hydrogen and Fuel Cells for Energy Storage, Helsinki*. Nordic Energy Research Program -Electrochemical Energy Conversion, (1997).
- [222] J.R. Macdonald. CNLS, Complex nonlinear least squares immitance fitting program, LEVM Version 7.0, [www.solartron.com](http://www.solartron.com), (1997).
- [223] G. Paasch, K. Micka, and P. Gersdorf. *Electrochim. Acta*, **38**(18), 2653–2662, (1993).
- [224] D.D Edwards, J.-H. Hwang, S.J. Ford, and T.O. Mason. *Solid State Ionics*, **99**, 95–93, (1997).
- [225] D. Chartouni. Measurements of polarization resistance versus the depth of discharge. Personal communication, (2000). [daniel.chartouni@onri.go.jp](mailto:daniel.chartouni@onri.go.jp).
- [226] B.D. Cullity. *Elements of X-ray diffraction*. Addison-Wesley publishing company Inc., (1956).
- [227] D. Chartouni, F. Meli, A. Züttel, K. Gross, and L. Schlapbach. *J. Alloys and Compounds*, **241**, 160–166, (1996).

# Index

- $\alpha$  phase, 25, 26
- $\beta$  phase, 25, 26, 56, 182
- AB<sub>2</sub> type alloys, **41**
- AB<sub>5</sub> type alloys, 3, 30, **30**, 32, 51, 54, 57, 96, 98–100, 131, 155, 168, 171, 172, 183, 186, 188
  - A site, 32–34, 50, 56, 65, 69, 71–74, 120, 121
    - Non rare earth, 34
    - Rare earth, 32
  - B site, 32, 35, 36, 47, 50, 56, 63, 68, 71, 72, 74, 120, 121, 183, B.3
  - Diffusion, 55
  - Misch metal composition, 59
  - Structure, 30, B.1
- Acknowledgements, v
- Activation, 24, 37, 38, 52–54, 57, 92, 94, 96, 98, 107–109, 113, 116, 118, 124, 155, 183, 186, 190
- Air metal hydride battery, **15**
  - Overcharge reaction, 16
  - Overdischarge, 16
- Aluminium, 37, 57
- Apparatus, 84
- Autoclave, 112
- Battery, 7
  - Figure, 9
  - Li-ion, 8, 10, 17
  - Li-polymer, 17
  - Lithium, 10
  - NiCd, 8, 9, 11, 14
  - NiMH, 2, 7, 8, 11, **11**, 12–15, 17, 21, 24, 32, 39, 40, 42, 189, 190
    - Cell reaction, 12
    - Overcharge reaction, 13
    - Weight contributions, 40
- Boron, 37
- C-rate, 80
- Characterization
  - Electrochemical, 77
- Characterization Methods
  - Electrochemical, 77
    - Cycle life, 78
- Chemicals used, 92
  - Table, 92
- Chromium, 38
- Circuit elements expressions
  - Table, 129
- Cobalt, 39
- Constant current
  - Charge, 79
  - Discharge, 79
- Constant phase element, 131
- Copper, 39
  - Powder, 86, 88
- Covalent hydrides, 19
- CPE, 131

- Equation, 128
  - n-values
    - Table, 129
- Critical temperature, 25
- Cycle life, 52, 78, **78**, 79, 80, 86
  - Figure, 79, 95
- Cycling
  - Constant current, 78
  - Electrochemical, 90
  - Standard Procedure
    - Table, 92
- Deactivation, 105
- Diffraction
  - Neutron, B.3
  - X-ray, B.1
- Diffusion
  - Hydride, 54
  - Planar, 149
- EIS, 125, 126, 137–139
  - General, 126
  - Introduction, 126
  - Metal hydride, 136
  - Modeling, 139
- Electrochemical Characterization, 77
- Electrochemistry
  - High pressure, 111
- Electrode
  - Configuration
    - Integrated, 88
  - Construction, 86
    - Sandwich, 86
  - Negative, 9
  - Porous, 130, 132
    - Deep cylindrical, 134
    - Transmission line, 132
    - vs Rough, 135
  - Positive, 9
  - Rough, 130
    - microscopic, 130
    - Shape dependence, 132
    - vs Porous, 135
- Electrode reaction
  - Kinetics, 3, **44**, 51, 52, 77, 82, 104, 108, 109, 124, 169, 183, 186
- Electrolyte, 10
- Energy density, 11
- FPPD, 131
- Fuel Cell, 1, 2, 5, 6, 14, 16, 17
  - Figure, 6
  - PEM, 17
- Germanium, 39
- Greek letters, 195
- Hydride
  - Covalent, 19
  - Diffusion, **54**
    - SOC dependent, 55
  - Forming, **189**
  - Ionic, 20
  - Saline, 20
- Hydride electrode
  - Construction, 86
    - Integrated, 87
    - Sandwich, 87
- Hydride electrodes
  - Electrochemical cycling, 93
- Hydrogen
  - Absorption, 21, 22, 25, 27, 43, 77, 116, 137, 139, 148, 188,  
B.2
  - Desorption, 27, 32, 46, 63, 73, 140, 148

- Diffusion, 55, 56, 104, 106, 123, 174, 184, 188
  - AB<sub>5</sub>, **57**
  - Geometry, 137
  - Limitations, 175
  - Paths, 182
  - Spherical, 140, 184
  - Surface, 180
- Evolution, 16, 81, 82, 94, 102, 105, 107, 111, 112, 115–118, 139, 140, 146, **147**, 148, 149, 155, 173, 174, 187–189
- Storage capacity, 27, 35, 37, 38, 42, 78
- Hydrogen diffusion, 57
- Hydrogen storage alloys
  - Magnesium based, 42, **42**, 43, 154, 169, 171, 172, 179, 186
- Hysteresis, 28
- Impedance
  - Modeling, 125
- Ionic hydrides, 20
- Iron, 39, 43
- Lattice expansion, B.2, **B.2**
- List of Abbreviations, 197
- List of symbols, 191
- Lithium
  - battery, 10
- Lithium battery, **10**
- Magnesium, 42
- Manganese, 38
- Measurements, 91
- Memory effect, 11
- Metal hydrides, **19**
  - Binary, 23
  - Characterization, 43
  - Crack formation, 46
  - Energy storage, 21
  - Intermetallic, 23
  - Metal bond, 20
  - Processes, 21
  - Sensors, 22
  - Separation technology, 22
  - Surface properties, 50
  - Surface treatment, 52
  - Utilisation, 21
- Metal hydrogen bonds, 19
- Misch metal, 30, 32–34, 43, 47, 49, 51, 62, 72, 151, 185
  - Composition, **59**
- Molybdenum, 39
- Neutron diffraction, B.3
- Nickel Hydrogen battery, 14
- Nickel metal hydride battery
  - Electrolyte, 11
- PC isotherm, 25
- PCT, **24**
  - Electrochemical, 80, 91
  - Figure, 25
  - van't Hoff
    - Plot, 28
    - Relation, 28
- Periodic system, 20
- Plateau
  - Sloping, 29
- Rate measurements, 91
- Reactivation, 104, 105, 107, 181
- Reference electrode
  - Construction, 88, 89
  - Bulb, 89



- Tubular, 89
  - Hg/HgO, 84, 88, 89, 177
- Reproducibility, 108
- Saline hydride, 20
- Self discharge, **53**
  - Reduction of, 53
- Separator, 10
- Silicon, 37
- SOC
  - Kinetic variations, 168, 179
- Structural Anisotropy, 48, 72
- Surface
  - Properties, 50
  - Treatment, 52
- Thesis, 3
- Tin, 39
- Titanium, 38
- X-ray diffraction, 31, 50, 62, 66, 67,  
72, B.2



# Appendix



# Appendix A

## List of Publications and Presentations

### A.1 List of Published Papers

- Valøen, L.O., Sunde, S. and Tunold, R.; "An AC impedance model for electrode processes in metal hydride electrodes" *J. Alloys and Compounds* **253-254** pp 656-659 (1997). (Ref [174])
- Valøen, L.O., Sunde, S., Edwards, Rh. and Tunold, R.; "Characterization of the electrode processes in metal hydride electrodes by AC impedance" *Proceedings of the Second International Symposium New Materials for Fuel Cells and Modern Battery Systems* pp 905-907 (1997). (Ref [170])
- Valøen, L.O., Sunde, S. and Tunold, R.; "An impedance model for metal hydride electrodes" In *Batteries for portable applications and electric vehicles*; The Electrochemical Society Inc, PV 97-18, pp 761-767 (1997). (Ref [172])
- Valøen, L.O., Sunde, S. and Tunold, R.; Characterisation of the electrochemical properties of metal hydride electrodes by use of ac impedance -Variation in the properties with state of charge, 3rd Nordic Symposium on Hydrogen and Fuel Cells for Energy Storage, Nordic Energy Research Program -Electrochemical Energy Conversion, Helsinki 1997, (Ref [221])

- Valøen, L.O., Sunde, S. and Tunold, R.; "Characterization of the electrochemical properties of metal hydride electrodes by AC impedance" *Hydrogen Power: Theoretical and Engineering Solutions*, Proceedings, Hypothesis II, Grimstad, Norway, 1997, pp 297-302 (1998). (Ref [171])
- Valøen, L.O. and Tunold, R.; *Effect of the rare Earth composition on the properties of AB<sub>5</sub> type alloys*, Nordic workshop on hydrogen in electrochemical energy conversion, Geilo, 1999, (Ref [159])
- Valøen, L.O., Zaluska, A., Zaluski, L., Tanaka, H., Kuriyama, N., Ström-Olsen, J.-O., and Tunold, R.; *Structure and related properties of (La,Ce,Nd,Pr)Ni<sub>5</sub> alloys*, manuscript accepted for publication in *J. Alloys and Compounds*, January 2000, (Ref [49])

## A.2 List of Presentations

- ORAL PRESENTATION: Nordic metal hydride battery seminar, Copenhagen, March 27-29, 1996: "Characterization of Metal Hydride Electrodes by AC Impedance".
- POSTER PRESENTATION: International Symposium on Metal Hydrogen Systems, Fundamentals and Applications, Les Diablerets, Switzerland, August 25-30, 1996: "An AC impedance model for electrode processes in metal hydride electrodes".
- POSTER PRESENTATION: Second International Symposium New Materials for Fuel Cells and Modern Battery Systems, Montreal, Canada, July 6-10, 1997: "Characterization of the Electrochemical Properties of Metal Hydride Electrodes by use of AC impedance".
- POSTER PRESENTATION: Gordon Conference on Metal-Hydrogen Systems, Henniker, New Hampshire, July 13-18, 1997: "Characterization of the Electrochemical Properties of Metal Hydride Electrodes by use of AC Impedance".
- ORAL PRESENTATION: Hypothesis II, Grimstad, Norway, August 18-22, 1997: "Characterization of the Electrochemical Properties of Metal Hydride Electrodes by use of AC Impedance -Variation in the properties with state of charge".

- ORAL PRESENTATION: 3rd Nordic Symposium on Hydrogen and Fuel Cells for Energy Storage, Helsinki, Finland, September 25-26, 1997: "Characterization of the Electrochemical Properties of Metal Hydride Electrodes by use of AC Impedance -Variation in the properties with state of charge".
- POSTER PRESENTATION: 49th Annual Meeting of ISE, September 13-18, Kitakyushu, Japan 1998: "Electrochemical impedance study of copper coated metal hydride electrodes".
- ORAL PRESENTATION: Symposium on Electrochemical Energy Conversion and Storage (Post-meeting of 49th Annual Meeting of ISE), September 20-21, Osaka National Research Institute, Ikeda, Osaka, Japan, 1998: "Impedance modeling and measurements on metal hydride electrodes".
- ORAL PRESENTATION: Nordic workshop on "Hydrogen in electrochemical energy conversion", March 3-5 1999, Geilo, Norway, "AB<sub>5</sub> type metal hydrides, structural parameters versus properties".
- POSTER PRESENTATION: Hydrogen Electrochemistry and Energetics How far are we from the Hydrogen Society? Trondheim, Norway, June 16-18, 1999: "Structural and thermodynamic effect of the rare earth composition on the properties of (La,Ce,Nd,Pr)Ni<sub>5</sub> alloys".
- POSTER PRESENTATION: Gordon Conference on Metal-Hydrogen Systems, Henniker, New Hampshire, July 18-23, 1999: "Structural and thermodynamic effect of the rare earth composition on the properties of (La,Ce,Nd,Pr)Ni<sub>5</sub> alloys".





## Appendix B

# Determination of Structure Parameters

### B.1 From X-ray Diffraction

A very brief description of the interpretation of XRD patterns is given here. For a more comprehensive and fundamental description and interpretation of X-ray spectra, please consult Ref [226]. For a more practical description, including the interpretation of XRD-patterns and also neutron diffraction patterns on hydrogen storage alloys, Ref [54] should be consulted.

The first step is to identify the diffraction peaks on the X-ray pattern. Figure B.1 shows an X-ray diffraction pattern for  $\text{LaNi}_5$  (the crystal plane diffraction peaks are indicated in the figure).

To calculate the unit cell dimensions, it is preferable to use peaks where either  $h$ ,  $k$  or  $l$  indicating planes in the structure equal zero. To calculate the distance between the crystal planes,  $d$ , Bragg's law, Eq B.1, can be used.

$$n\lambda = 2d_{hkl}\sin\theta \quad (\text{B.1})$$

For this type of structure, and assuming a quadratic basal plane in figure 3.6, parameters are given by Eq B.2.

$$\frac{1}{d^2} = \frac{4}{3} \left( \frac{h^2 + hk + k^2}{a^2} \right) + \frac{1}{c^2} \quad (\text{B.2})$$

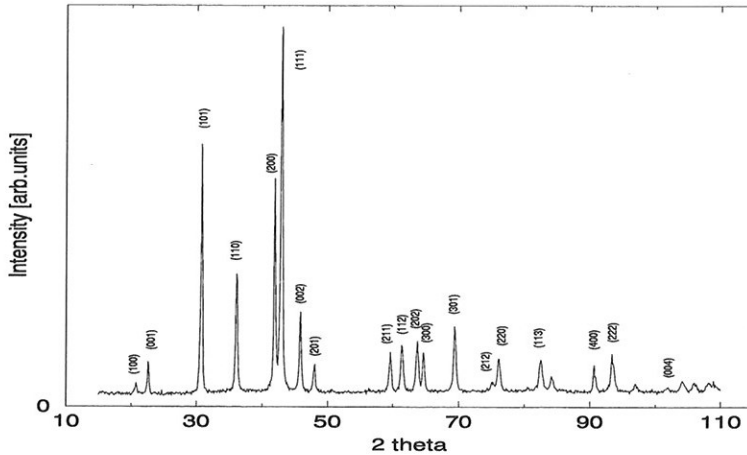
LaNi<sub>5</sub>

Figure B.1: X-ray diffraction pattern for LaNi<sub>5</sub> with crystal plane diffraction peaks indicated. Intensity versus  $2\theta$  [degrees].

Here  $a$  is the basal plane unit cell lattice parameter and  $c$  is the axial unit cell parameter. The accuracy improves as the diffraction angle increases. For the pattern shown in figure B.1, the peaks  $[400]$  and  $[004]$  will give the best accuracy for the cell parameters. The unit cell volume,  $V_{uc}$ , can be found from Eq B.3.

$$V_{uc} = \frac{\sqrt{3}}{2} a^2 \cdot c \quad (\text{B.3})$$

The lattice expansion along the  $c$  axis is expected to have the largest influence on cracking because the alloys have a layer structure with an ABABA stacking sequence [6]. A partial derivation of Eq B.3, however, shows that a 1% change in the  $a$  parameter will affect the unit cell volume by a more than 1% change in the  $c$  parameter. Willems [66] showed that the lattice expansion during hydrogenation is about 8% in the  $a$  direction and about 5% in the  $c$  direction for LaNi<sub>5</sub> based compounds. It is of crucial importance to reduce the lattice expansion during hydrogen absorption, as this is believed to be one of the major reasons for shortened cycle life. The lattice expansion can be reduced by element substitution, as described in sections 3.4.2 and 3.4.3.

## B.2 From Neutron Diffraction

By using neutron diffraction, and by exchanging the hydrogen with deuterium, one can in addition to the metal lattice, also observe the hydrogen sites in the lattice. Structure properties for compounds with small differences in atomic number can be determined with this technique. Different isotopes will also give different scattering<sup>1</sup>.

The  $\text{LaNi}_5$  alloy stores three H atoms at the  $D(1)$  sites in the basal plane and three H atoms at the  $D(2)$  sites in the  $Z=\frac{1}{2}$  plane [6]. Logically this should give two plateau regions (and two different hydride phases) in figure 3.2, however, in  $\text{LaNi}_5$  related compounds the energy of the  $D(1)$  and the  $D(2)$  sites are so similar that one normally observes only one plateau. In alloys with cobalt substitutions on B sites, however, two distinct plateaus are observed [227].

---

<sup>1</sup>Neutrons are absorbed to a very small extent in some materials, for instance aluminium. Sample holders can therefore be constructed of aluminium. This also makes thick samples possible, with possible studies of the bulk properties of the material.



# Appendix C

## Source Code

*In this appendix the source used for circuit elements not included in the standard LEVM [222] non linear least square fitting program is given*

For non-porous models, the subroutine given in section C.1 was used, not incorporating the porous electrode model. For models with planar diffusion geometry, the subroutine given in section C.1 was used, substituting the diffusion element with Eq 7.61.

In section C.2, one of the size distributions given in table 8.2 are given. The other size distribution models were based on the same subroutine, but with different numbers for the size fractions and diffusion lengths.

### C.1 Spherical Diffusion, Porous Model

```
$STORAGE:2
C Hydrogen absorption spherical diffusion geometry
C No problem with units
C © Lars Ole Valøen 1999,2000
C
SUBROUTINE SSUB(M,FREQ,P,F)
IMPLICIT REAL*8(A-H,O-Z)
DOUBLE PRECISION RS,CDL,CP,RCT,RP,RAB,SIGMA,DH,ROMP
DOUBLE PRECISION XL,LS
```

```
DIMENSION P(*),F(*),FREQ(*)
COMPLEX*16 ZT,IOMEGA,YB,YA,ZW,ZA,ZF,CCOTH,XLAMBDA,ZEL,ZL
C
C
Main program
C
RS=P(1)
CDL=P(2)
CP=P(3)
RCT=P(4)
RP=P(5)
RAB=P(6)
SIGMA=P(7)
DH=P(8)
XL=P(9)
PHI=P(10)
LS=P(11)
ROMP=P(12)
DO 100 I=1,M
    OMEGA=FREQ(I)
    IOMEGA=DCMPLX(0.,OMEGA)
    ZW=SIGMA/(SQRT(IOMEGA*DH)*CCOTH(SQRT(IOMEGA/DH)*XL)-DH/XL)
    ZA=ZW+RAB
    YA=IOMEGA*CP+1./RP+1./ZA
    ZF=RCT+1./YA
    ZEL=1./(IOMEGA*CDL+1./ZF)
    XLAMBDA=SQRT(1./ZEL)
    ZL = IOMEGA*LS
    ZT=ZL+RS+ROMP/XLAMBDA*CCOTH(XLAMBDA)
    F(I)=DREAL(ZT)
    F(I+M)=DIMAG(ZT)
100 CONTINUE
C
RETURN
END
C
FUNCTION CCOTH(X)
```

```

COMPLEX*16 X,CCOTH,CDCOTH
CCOTH=CDCOTH(X)/X
RETURN
END
C

```

## C.2 Spherical Diffusion, Size Distribution, Porous Model

```

$STORAGE:2
C Hydrogen absorption spherical diffusion geometry
C No problem with units
C Wide size distribution
C © Lars Ole Valøen 1999,2000
C
SUBROUTINE SSUB(M,FREQ,P,F)
IMPLICIT REAL*8(A-H,O-Z)
DOUBLE PRECISION RS,CDL,CP,RCT,RP,RAB,SIGMA,DH,ROMP
DOUBLE PRECISION XL,LS
DIMENSION P(*),F(*),FREQ(*)
COMPLEX*16 ZT,IOMEGA,YB,YA,ZW,ZA,ZF,CCOTH,XLAMBDA,ZEL,ZL
C
C
Main program
C
RS=P(1)
CDL=P(2)
CP=P(3)
RCT=P(4)
RP=P(5)
RAB=P(6)
SIGMA=P(7)
DH=P(8)
XL=P(9)
PHI=P(10)
LS=P(11)

```

```

ROMP=P(12)
DO 100 I=1,M
  OMEGA=FREQ(I)
  IOMEGA=DCMPLX(0.,OMEGA)
  XLA=0.20*XL
  XLB=0.60*XL
  XLC=1.00*XL
  XLD=1.40*XL
  XLE=1.80*XL
  ZSA=SIGMA/(SQRT(IOMEGA*DH)*CCOTH(SQRT(IOMEGA/DH)*XLA)-DH/XLA)
  ZSB=SIGMA/(SQRT(IOMEGA*DH)*CCOTH(SQRT(IOMEGA/DH)*XLB)-DH/XLB)
  ZSC=SIGMA/(SQRT(IOMEGA*DH)*CCOTH(SQRT(IOMEGA/DH)*XLC)-DH/XLC)
  ZSD=SIGMA/(SQRT(IOMEGA*DH)*CCOTH(SQRT(IOMEGA/DH)*XLD)-DH/XLD)
  ZSE=SIGMA/(SQRT(IOMEGA*DH)*CCOTH(SQRT(IOMEGA/DH)*XLE)-DH/XLE)
  ZW=1/(0.1/ZSA + 0.2/ZSB + 0.4/ZSC + 0.2/ZSD + 0.1/ZSE)
  ZA=RAB +ZW
  ZA=ZW+RAB
  YA=IOMEGA*CP+1./RP+1./ZA
  ZF=RCT+1./YA
  ZEL=1./(IOMEGA*CDL+1./ZF)
  XLAMBDA=SQRT(1./ZEL)
  ZL = IOMEGA *LS
  ZT=ZL+RS+ROMP/XLAMBDA*CCOTH(XLAMBDA)
  F(I)=DREAL(ZT)
  F(I+M)=DIMAG(ZT)
100 CONTINUE
C
RETURN
END
C
FUNCTION CCOTH(X)
  COMPLEX*16 X,CCOTH,CDCOTH
  CCOTH=CDCOTH(X)/X
RETURN
END
C

```